Universidade de São Paulo
Instituto de Física

Estudo da correlação angular entre elétrons oriundos de quarks pesados e partículas carregadas em colisões pp e p-Pb com o detector ALICE

Elienos Pereira de Oliveira Filho

Orientador

Prof. Dr. Alexandre Alarcon do Passo Suaide

Tese de doutorado apresentada ao Instituto de Física da Universidade de São Paulo para a obtenção do título de Doutor em Ciências

Banca Examinadora

Prof. Dr. Alexandre Alarcon do Passo Suaide (orientador) - IFUSP
Profª. Drª. Emi Marcia Takagui - IFUSP
Prof. Dr. Fernando Silveira Navarra - IFUSP
Prof. Dr. Donato Giorgio Torrieri - UNICAMP
Profª. Drª. Sandra dos Santos Padula - IFT/UNESP

São Paulo
2014

University of São Paulo

Institute of Physics

Study of the angular correlation between heavy-flavour decay electrons and charged unidentified particles in pp and p-Pb collisions with ALICE

Elienos Pereira de Oliveira Filho

Advisor

Prof. Dr. Alexandre Alarcon do Passo Suaide

A thesis submitted in partial fulfillment of the requirements for the degree of doctor of philosophy

Thesis committee

Prof. Dr. Alexandre Alarcon do Passo Suaide (orientador) - IFUSP

Prof^a. Dr^a. Emi Marcia Takagui - IFUSP

Prof. Dr. Fernando Silveira Navarra - IFUSP

Prof. Dr. Donato Giorgio Torrieri - UNICAMP

Prof^a. Dr^a. Sandra dos Santos Padula - IFT/UNESP

São Paulo

2014

"That which does not kill us make us stronger."
(Friedrich W. Nietzsche)

ii

Acknowledgements

iv

To my parents

Elienos and Ester

Resumo

O próposito de colisões entre íons pesados relativísticos é investigar as propriedades do plasma de quarks e gluons (QGP, do inglês *Quark-Gluon Plasma*). A transição de fase, de um estado hadrônico para o QGP, ocorre em regimes onde a temperatura e/ou densidade atingem um valor suficientemente alto. Neste contexto, colisões entre íons pesados e leves (por exemplo, p-Pb) permitem acessar efeitos devido à matéria nuclear fria (CNM, do inglês *Cold Nuclear Matter*) e colisões elementares (por exemplo, próton-próton) são usadas como referência para estudos com íons pesados, além de proporcionarem testes para cálculos de QCD perturbativa.

Quarks pesados, isto é *charm* e *bottom*, são ferramentes muito convenientes no estudo e caracterização do QGP. Essas partículas são produzidas através de espalhamento duro nos instantes iniciais da colisão e, portanto, elas atuam como uma sonda externa para o sistema criado na reação.

Esse trabalho consiste no estudo da correlação angular entre elétrons oriundos de quarks pesados e partículas carregadas, em colisões pp ($\sqrt{s} = 2.76$ e 7 TeV) e p-Pb ($\sqrt{s_{\mathrm{NN}}} = 5.02$ TeV), no acelerador LHC (do inglês *Large Hadron Collider*) do CERN, usando o detector ALICE (do inglês *A Large Ion Collider Experiment*). A distribuição angular mencionada foi medida em função da multiplicidade do evento, no caso de colisões p-Pb. Em colisões pp, a contribuição relativa de quarks *charm* e *bottom* para o total de elétrons provenientes de quarks pesados foi estimada usando a função de correlação obtida.

Abstract

The aim of relativistic heavy-ion collisions is to investigate the properties of the Quark-Gluon Plasma (QGP) phase, that is achieved at high-enough temperatures and/or densities. In this context, light on heavy-ion collisions (e. g. p-Pb) are used to assess Cold Nuclear Matter effects (CNM), while elementary hadronic collisions (e. g. proton-proton) provide tests for QCD (Quantum Chromodynamics) based calculations and baseline for studies with heavy-ions.

Heavy quarks, i. e. charm and beauty, are very convenient in the characterization of the QGP. They are produced via initial hard parton-parton scatterings at the early stages of the collision and, therefore, they are a self-generated probe for the system created in the reaction.

In this work the angular correlation between electrons from heavy-flavour hadron decays and charged particles was studied in pp ($\sqrt{s}$ = 2.76 and 7 TeV) and p-Pb ($\sqrt{s_{\mathrm{NN}}}$ = 5.02 TeV) collisions at the CERN Large Hadron Collider, using the ALICE detector. The correlation strengths were evaluated as a function of multiplicity in p-Pb collisions. In pp collisions the relative beauty (and charm) contribution to the total heavy-flavour decay electron yield was estimated using the measured correlation distribution and Monte Carlo templates.

x

Contents

List of Figures

List of Tables

Chapter 1

Introduction

The aim of relativistic heavy-ion collisions is to study the properties of the Quark-Gluon Plasma (QGP) phase, which is expected to occur for high-enough temperatures and/or densities. Calculations from Quantum Chromodynamics (QCD), the field theory of the strong interaction, suggest that the transition from the hadronic matter to the QGP should occur for energy densities of the order of $1 \, \mathrm{GeV \, fm^{-3}}$. During the past $\sim 20 - 30$ years data from many heavy-ion facilities have shown several indications that the QGP is produced in heavy-ion collisions at sufficient high energies. The strongest evidences, that a new state of matter has been indeed formed, were provided by experiments of the Relativistic Heavy-Ion Collider (RHIC), buit at the Brookhaven National Laboratory (BNL) in New York, which began the operations in 2000. Since 2009, heavy-ion collisions can be studied at the highest energies available to date, at the CERN Large Hadron Collider (LHC), localized near the Swiss-French border. In Chapter 2 the physics of the QGP is introduced and some of the most relevant experimental results are reviewed.

In this context, light on heavy-ion collisions (e. g. p-Pb or d-Au collisions) are used to assess Cold Nuclear Matter (CNM) effects, such as saturation at small Bjorken-x. These effects modifies particle production and dynamics in the initial-state, which can be misinterpreted as a property of the medium created in the final state. Furthermore, elementary collisions (e. g. proton-proton or electron-positron collisions) are used as reference for studies with heavy-ions and provide constraints for QCD based calculations, since neither medium nor nuclei effects are present in these collision systems. Part of Chapter 2 is dedicated for this discussion.

Heavy-flavours, i. e. charm and beauty, are very convenient in the characterization of the QGP. These particles are dominantly produced via initial hard parton-parton scattering processes, which occur at the early stages of the collision and, therefore they are a self-generated probe for the system created in the reaction. In other words, they experience the whole system evolution, from the pre-equilibrium phase until the hadronization and freeze-out. Furthermore, due to the large virtuality involved, the production cross-section of heavy-flavours can be estimated through perturbative QCD (pQCD) calculations. Heavy-flavours (or more

generally hard probes) are the subject of Chapter 3.

Among the possible observables, this thesis will focus on two-particle angular correlations. The angular correlation function is defined as the distributions of the difference in azimuth ($\Delta\varphi$) and in pseudorapidity ($\Delta\eta$) between a trigger and an associated particle. The distribution around ($\Delta\varphi = 0, \Delta\eta = 0$) is dominated by the near-side jet, i. e. by the correlation between particles produced in the fragmentation of the same parton (which is one of the partons created in the initial hard scattering). The correlation structure at $\Delta\varphi = \pi$ is due to the back-to-back pair production, i. e. due to the correlation with the away-side jet and, therefore, it is strongly sensitive to the parton-medium interaction. Furthermore, for low transverse momentum the angular correlation is sensitive to the collective flow phenomena. Correlations in the light-flavour sector have been widely studied by experiments at RHIC and LHC. A detailed discussion on two-particle angular correlations as well as a review of the main experimental results from RHIC to the LHC are the subject of Chapter 4.

Angular correlations between electrons from heavy-flavour hadron decays and charged unidentified particles is the subject of this thesis and, it is divided in two (complementary) parts as explained in the following.

In the first part of the work, the correlation distribution was measured in p-Pb collisions at $\sqrt{s_{\mathrm{NN}}} = 5.02$ TeV and in pp collisions at $\sqrt{s} = 7$ TeV, for electrons with $1.0 < p_{\mathrm{T}}^e < 6.0$ GeV/c (in three p_{T} bins) and charged particles, required to satisfy $0.5 < p_{\mathrm{T}}^e < 2.0$ GeV/c. The correlation strengths were evaluated as a function of multiplicity in p-Pb collisions and the results were compared to the pp data as well as MC@NLO simulations, that are implemented in the PYTHIA program. The description of this measurement and results are described in Chapters 6 and 8 respectively.

In pp collisions, the angular distribution between heavy-flavour decay electrons and charged particles can be used to estimate the relative beauty contribution to the total heavy-flavour decay electron yield, using the measured correlation distribution and Monte Carlo templates. This technique is introduced in Chapter 4, where results from the STAR collaboration are shown. In this work, this method was applied to the ALICE data for pp collisions at $\sqrt{s} = 2.76$ TeV and the description of the analysis is the content of Chapter 7.

In the present work, the correlation function is triggered by electrons from heavy-flavour hadron decays, i. e. the trigger particles in the angular correlation distribution are electrons from charm and beauty. The associated particles are charged unidentified tracks. In this text the associated particles are often called hadrons or associated hadrons, since the sample are dominantly composed by hadrons, compared to leptons.

The experimental environment on which this work was developed (i. e. the CERN LHC accelerator, the ALICE experiment and the analysis software) is the subject of Chapter 5, which includes a short description on the main subsystems of ALICE used in this work, the off-line (ALIROOT) framework and the most relevant experimental techniques (particle identification, trigger, multiplicity selection and so on).

Chapter 2

The Quark-Gluon Plasma

2.1 Quarks and gluons

Currently, it is well established that, at the most elementary level matter is made of few particles, which are organized in groups called as quarks, leptons and gauge bosons [1, 2, 3]. For instance, protons and neutrons are not elementary, i. e. particles without internal structure, but they are bound states of quarks.

In addition to this picture, there are four fundamental interactions that occur between elementary particles: gravitational, electromagnetic, weak and strong force. In particle physics, the interaction between two particles is understood as due to the exchange of a third particle, the quantum of the field involved in the interaction.

Photons, for instance, are the quanta of the electromagnetic field and, therefore, the electromagnetic interaction is understood as an exchange of a photon between two charged particles. In analogy, the mediator of the strong interaction is the gluon and it occurs between particles carrying color charge (quarks and gluons). The mediators of the fundamental interactions are spin-1 particles and they are collectively called gauge bosons.

Each fundamental interaction has a specific Quantum Field Theory (QFT) for the description of elementary particle dynamics. The QFT of the electromagnetic force is the Quantum Electrodynamics (QED) and the strong interaction is described by the QCD theory.

A schematic table containing the elementary particles and their properties (mass, electrical charge and spin value) can be seen in Figure 2.1 [4]. In Table 2.1 there is a summary of the fundamental forces, their QFT and boson that mediates the interaction [2].

Table 2.1: Fundamental interactions. Reproduced from [2].

Force	Strength	Quantum Field Theory	Mediator
Strong	10^{43}	Chromodynamics	Gluon
Electromagnetic	10^{40}	Electrodynamics	Photon
Weak	10^{29}	Flavourdynamics	W and Z
Gravitational	1		Graviton

Figure 2.1: Table of elementary particles. Figure from [4].

As aforementioned, hadrons, such as protons and neutrons, are composed by spin-1/2 particles, called quarks. The existence of quarks was proposed in 1964 by Gell-Mann and Zweig to explain the classification of the known hadronic states. Four years later, in 1968, experiments of high-energy electron-proton scattering, known as Deep Inelastic Scattering (DIS), carried out at the Stanford Linear Accelerator Center (SLAC) [2, 3], revealed the internal structure of protons and the results turned out to be consistent with the quark hypothesis [2].

Figure 2.2 shows the Feynman diagram of the inelastic $e^+ -$ proton scattering process [5]. In this process an electron (positron) with 4-momentum k interacts with a proton with 4-momentum P through the electromagnetic force, i. e. by exchanging a (virtual) photon with 4-momentum q[1]. The 4-momentum of the outgoing electron is, therefore, given by $k' = k - q$.

Since the process occurs via electromagnetic interaction, the differential cross-section can be calculated using QED and the result is shown in Equation 2.1 [2], where E and E' are the energies of the incoming and outgoing electron respectively, α is the fine structure constant, θ is the scattering angle, $W_{1,2}$ are two structure functions of the proton, to be determined and x is the fraction of the momentum of the proton carried by the scattered parton [2].

$$\frac{\mathrm{d}\sigma}{\mathrm{d}E'\mathrm{d}\Omega} = \left(\frac{\alpha\hbar}{2E\sin^2(\theta/2)}\right)^2 \left[2W_1(q^2, x)\sin^2(\theta/2) + W_2(q^2, x)\cos^2(\theta/2)\right] \tag{2.1}$$

---

[1] In Figures 2.3 to 2.5, and later in Chapter 3, Q is used to denote the 4-momentum of the virtual photon in the scattering process.

Figure 2.2: Feynman diagram of the inelastic e^+ − proton **scattering process (Deep Inelastic Scattering). Figure from [5].**

Assuming that the proton has an internal structure composed by point-like particles, Bjorken predicted, in the decade of 1960s, that the structure functions $W_{1,2}$ do not depend on the variable q, but only on x. More precisely, he predicted that $W_{1,2}$ should assume the form expressed in Equations 2.2 and 2.3 [2], where M is the proton mass.

$$MW_1(q^2, x) \rightarrow F_1(x) \tag{2.2}$$

$$\frac{-q^2}{2Mc^2x}W_2(q^2, x) \rightarrow F_2(x) \tag{2.3}$$

The prediction expressed in Equations 2.2 and 2.3 is called Bjorken scale. In Figure 2.3 the experimental result for the structure function $F_2(x)$ as a function of q^2 is shown for several values of x [6].

Figure 2.3 shows that experimental data confirms the Bjorken scale for high-x ($x \gtrsim 0.1$) values, which is consistent with the quark model. However, one can also notice that at low-x values the Bjorken scale breaks down, i. e. the structure function F_2 shows a dependence with q^2 (in fact, it rises with q^2). This is understood by the fact that treat protons as composed by three quarks (2 quarks up and 1 down) is oversimplified. In fact it can be shown that only a fraction of the total momentum of the proton ($\approx 50\%$) can be attributed to these quarks, which are known as valence quarks [2].

In addition to the valence quarks, protons contains gluons and a sea of quarks at low Bjorken-x. This sea can be understood thinking that one gluon in the nucleon can split in a quark-antiquark pair. Therefore, at a given moment, the nucleon might contain an extra pair of partons carrying any flavour [2, 1].

Now, coming back to the Figure 2.3, at high-x values, the scattering occurs dominantly from a valence quark and the Bjorken scale is observed. But, for low-x values the contribu-
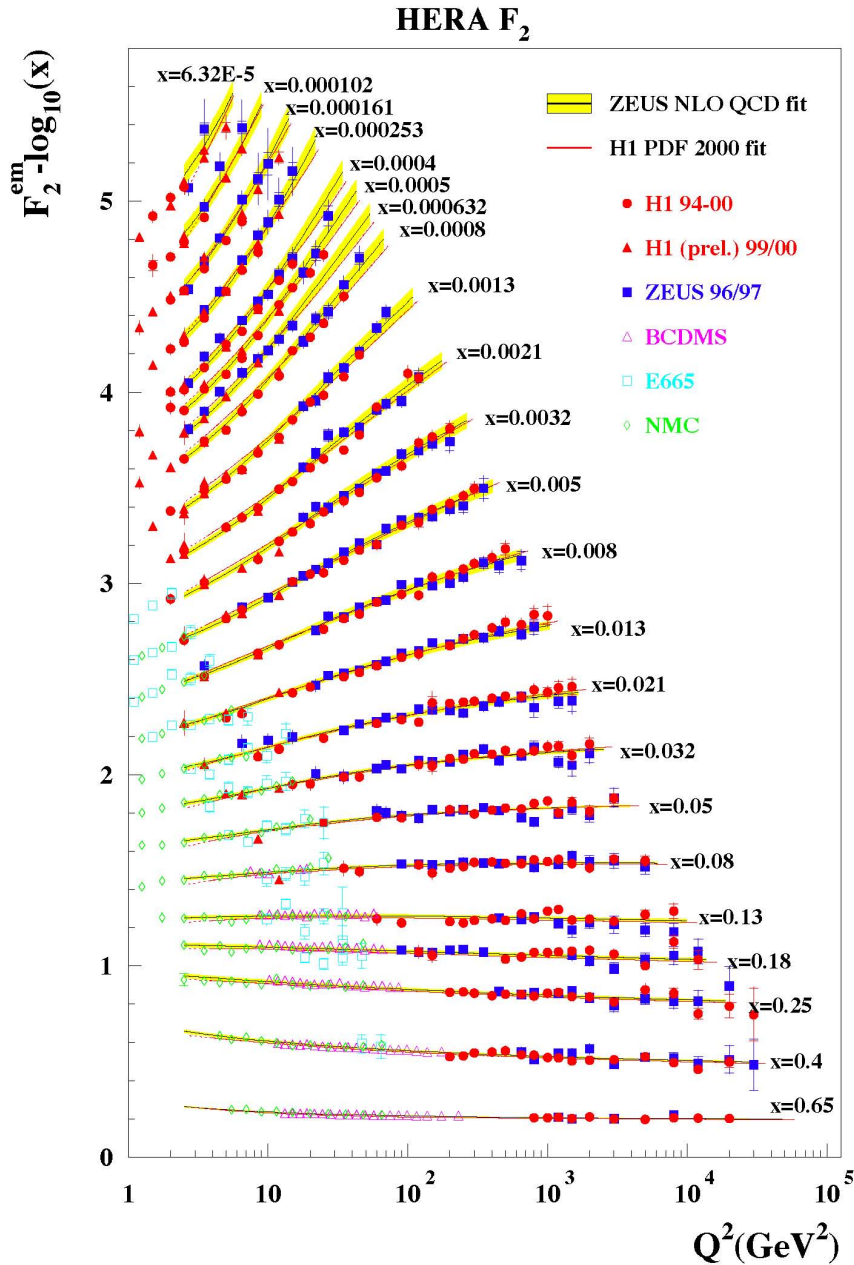
Figure 2.3: The structure function F_2 as a function of q^2 for several values of the Bjorken-x variable. Figure from [6].

tion of gluons and the sea quark to the scattering start to be important and the Bjorken scale, which is based on a three-quark model, breaks down, since these contribution increases with the momentum transfer q^2 [2, 6].

Figure 2.4 shows the Parton Distribution Functions (PDFs) of quarks and gluons in the proton [6]. The bands are fits to the experimental results obtained by the ZEUS and H1 Collaborations at HERA [6]. In this Figure it can be noticed that at high-x the valence up and down quarks dominates and, at low-x values gluons and the sea quarks become the most
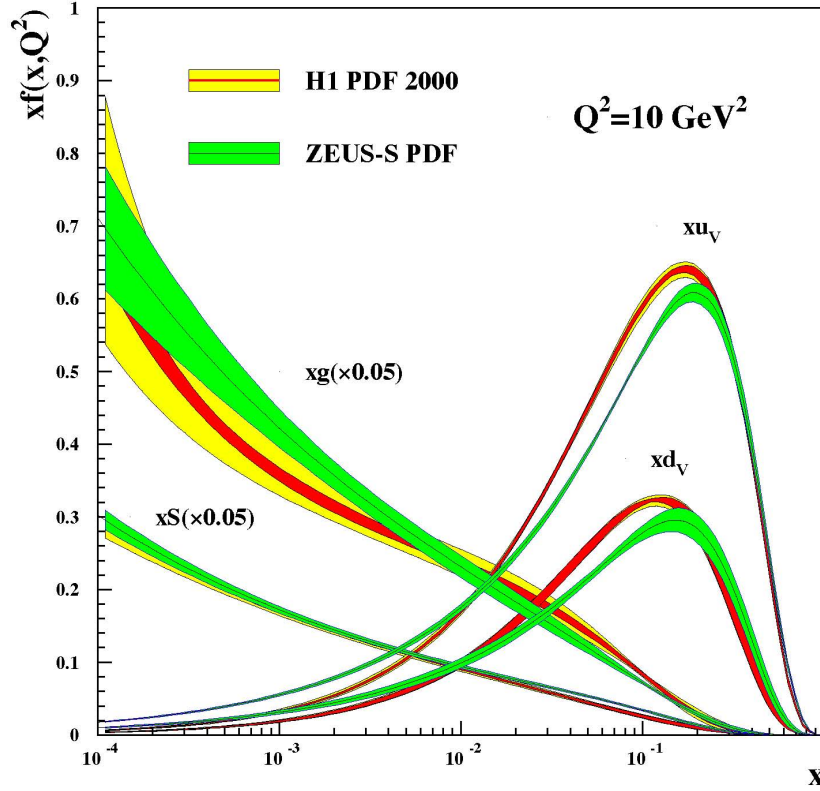
Figure 2.4: Distribution functions of quarks and gluons in the proton ($xf(x, Q^2)$) **as a function of the Bjorken-x, for** $Q^2 = 10$ **GeV^2 . Figure from [6].**

important contribution.

2.2 Quantum Chromodynamics (QCD)

Quantum Chromodynamics is the quantum field theory of the strong interaction, which affects colored particles, i. e. quarks and gluons. One of the main aspects of the QCD is that gluons also carry color charge, unlike QED, on which photons do not carry electric charge. Therefore, in QCD gluons can interact with gluons and this has an important consequence that will be discussed in this section.

For the discussion that will follow it is interesting to look at the coupling constants α of QED and QCD, which can be understood as the strength of the electromagnetic and strong interaction respectively. The coupling constant of the QED and QCD are of the form expressed in Equations 2.4 and 2.5 [2], where $\Lambda_{\mathrm{QCD}} \approx 200$ MeV, known as QCD scale, defines a reference strength of the strong interaction.

$$\alpha_{\mathrm{QED}}(q^2)(\approx \alpha \approx 1/137) \propto \frac{1}{1 - (\alpha/3\pi)\log(q^2/(mc)^2)} \tag{2.4}$$

$$\alpha_s(q^2) \propto \frac{1}{\log(q^2/\Lambda_{\text{QCD}}^2)} \tag{2.5}$$

From Equations 2.4 and 2.5 one can notice the opposite behavior between QED and QCD. In QED, for large energies, or equivalently for short distances, the coupling constant is larger, i. e. the interaction is as stronger as the distances get smaller. Equivalently one can say that, for shorter distances the effective electric charge is larger. The reason of this effect is that at small distances the screening effect of the polarized vacuum is weaker.

In QCD the effect is the opposite. Equation 2.5 shows that for higher energies (shorter distances), α_s decreases and goes *asymptotically* to zero, i. e. for short-enough distances the effective color charge is zero and the partons do not experience the strong interaction. This is one of the main aspects of QCD and it is called *Asymptotic Freedom*. The behave of α_s as a function of q^2 is shown in Figure 2.5 [7]. Qualitatively, the asymptotic freedom can be understood as a consequence of an *anti-screening* effect due to the gluon-gluon interaction [2].
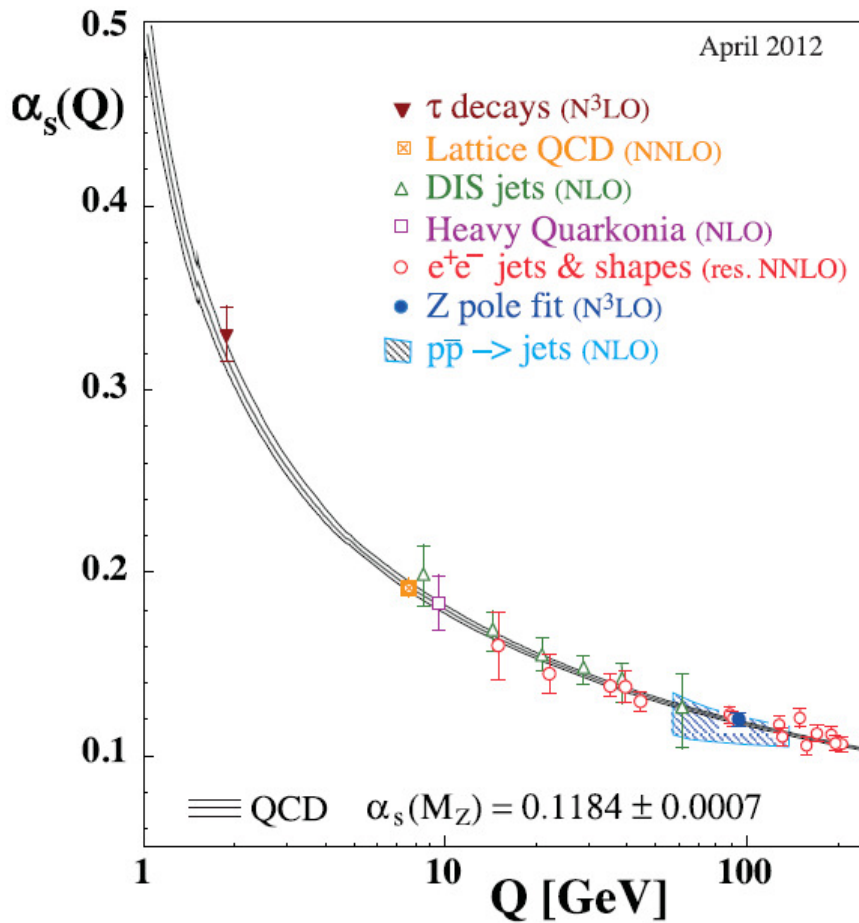
Figure 2.5: Coupling constant of the QCD α_s as a function of the energy scale Q^2. Figure from [7].

Another aspect of the strong interaction (which can be understood as the other *face* of asymptotic freedom) is that colored particles, i. e. quarks and gluons, can not be observed. Rather, they should always be *confined* in hadrons in a configuration leading to a white (or colorless) state. This property is called *confinement* and it is also suggested by Equation 2.5. Since at large distances the strength of the QCD interactions (the α_s) is extremely large, colored particles might be always bound together in colorless states. However, a rigorous proof of confinement is still missing due to the difficult of dealing with the theory in regimes of large α_s [1, 2, 3].

2.2.1 Hard versus soft QCD process

Equation 2.5 defines two QCD regimes called *soft* and *hard* QCD processes. Hard processes are those characterized by large virtualities, i. e. interactions with large momentum transfer ($Q \gg \Lambda_{QCD}$), which implies in a small coupling constant ($\alpha_s < 1$). Therefore, the production cross-section of a hard scatterings can be estimated through perturbative QCD calculations, i. e. by expanding the equation in powers of α_s high-order terms can be neglected [1, 2, 3]. That means, in other words, that only the lowest-orders (i. e. the simplest) Feynman diagrams has to be included in the calculation, depending on the required precision. Therefore, in this regime, also called as *perturbative QCD* (pQCD), predictions are made from first principle analytic calculations and QCD provides these predictions as precise as requested (one can always add one more Feynman diagram in the calculation) [1, 2, 3]. Chapter 3 is dedicated to a more elaborated discussion about hard QCD process and its role in heavy-ion collisions.

In the other extreme, the soft regime corresponds to process characterized by low energy scales ($Q \lesssim \Lambda_{QCD}$). In this case analytical QCD calculations are not possible, since higher-orders Feynman diagrams have a larger contribution to the production cross section. Therefore, it is necessary to look for alternative methods in QCD and rely on effective theories to treat the strong interaction in this regime [3].

Currently, the only way of provide predictions from first principles, i. e. using QCD, in the soft regime is through a technique called *Lattice QCD*, where QCD calculations are numerically performed in a discretized space-time lattice [3]. In this approach the partition function of the system (i. e. built from the QCD Lagrangian) is evaluated through Monte-Carlo methods [3]. However, this technique requires large amounts of computational resources and consumes relatively large times of processing. Furthermore, its accuracy is limited in some aspects due to finite size effects and other technical difficulties [3]. Therefore, in the soft regime phenomenological models play an important role in the description of the strong interaction and, the combination between lattice QCD and phenomenological models often provides reliable predictions. Indeed, lattice QCD results are frequently used as input for phenomenological model calculations providing, for instance, an equation of state [3].

2.3   Deconfined QCD matter: the Quark-Gluon Plasma

At high temperatures and/or densities, calculations from lattice QCD [3, 9, 10, 11, 12], as well as from the MIT (phenomenological) bag model [3, 13, 14], predicts that a phase transition from the hadronic matter to a deconfined state of quarks and gluons, a Quark-Gluon Plasma (QGP), should occur.

In the simplified bag model, hadrons are treated as a bag of non-interacting massless quarks, where the confinement is a consequence of the equilibrium between the internal and external pressures over the bag. With it, the condition of a transition to a deconfined phase is characterized by the Temperature in which the internal pressure are no longer compensated by the external one. This model predicts a first order phase transition, i. e. with an abrupt change in the energy density of the system, to an ideal gas of quarks (and gluons), a weakly-interacting Quark-Gluon Plasma (wQGP), at a critical temperature $T_c \approx 140 - 150$ MeV for a null chemical baryonic potential ($\mu_B = 0$) [3, 13, 14].

A more accurate description of the thermodynamic properties of the Quark-Gluon Plasma (QGP) is provided by lattice QCD calculations. One of the main aspects that is currently in discussion is about the nature of the phase transition and the existence of a critical point separating a first/second-order transition from a cross-over [3]. In lattice QCD the order of the transitions depends on the number of flavours and on the quark masses [3, 11], as can be seen in Figure 2.6, for $\mu_B = 0$ [3, 11].
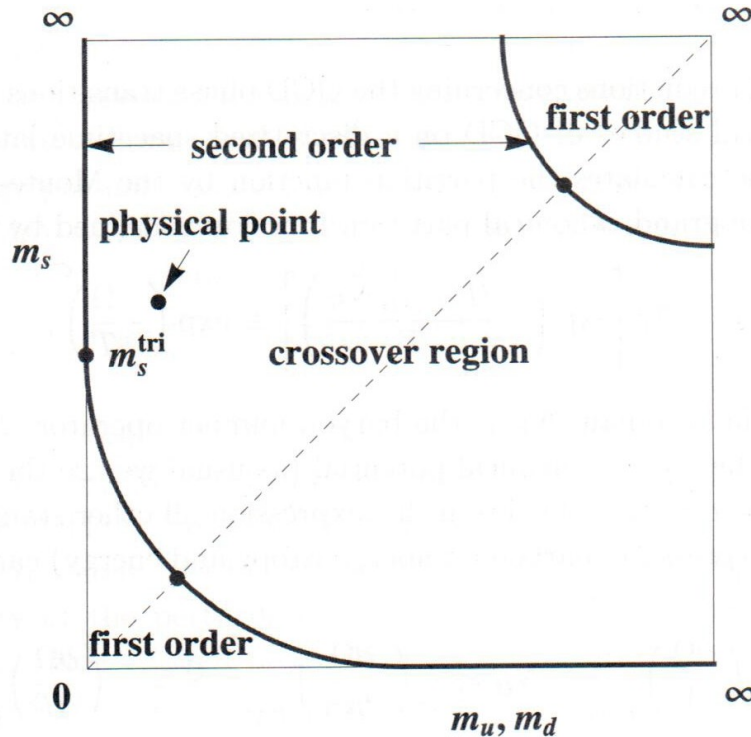
Figure 2.6: Columbia plot. Order of the QCD phase transition to a deconfined state as a function of the quark masses [3, 11]. Figure from [3].

Figure 2.6 shows that lattice QCD predicts a crossover transition for physical masses of the up, down and strange quarks at $\mu_B = 0$. A recent calculation of the equation of state of the QCD matter at μ_B, using realistic quark masses, was reported in [12]. The dependence of the pressure, energy and entropy densities as a function of temperature is shown in Figure 2.7 [12]. In this Figure, the crossover region is indicated by the yellow vertical bar, which corresponds to a critical temperature $T_c = 154 \pm 9$ MeV.
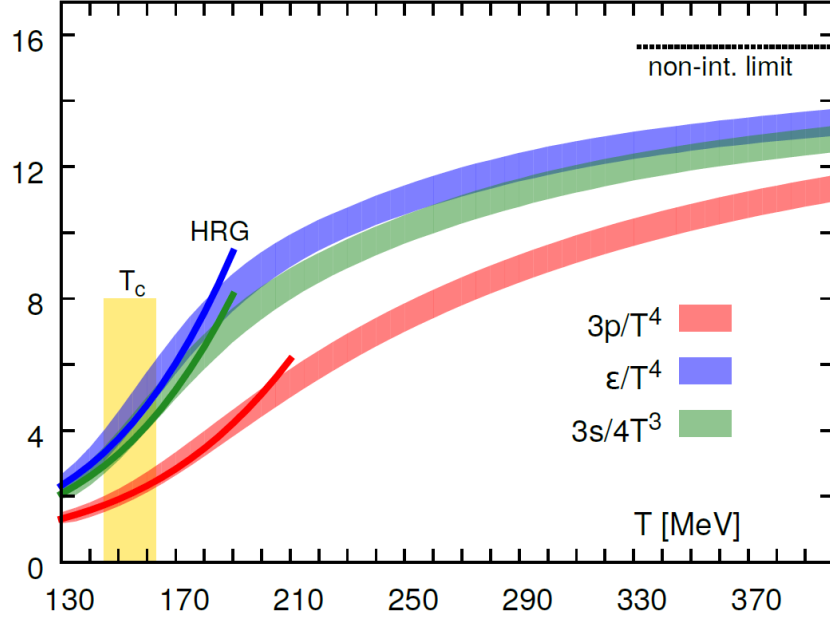
Figure 2.7: Thermodynamics variables (energy density ϵ, pressure p and entropy density s) as a function of temperature T, obtained from lattice QCD calculations using realistic quark masses. The horizontal line shows the ideal gas limit for the energy density and the yellow region at $T_c = 154 \pm 9$ MeV corresponds to the cross over region. Figure from [12].

From the Stefan-Boltzmann law, the ratio of the energy density by the fourth power of the temperature is a constant proportional to the system degrees of freedom ($\epsilon/T^4 \propto N_{d.o.f}$). Therefore the observed increase in this variable, shown in Figure 2.7, can be interpreted as an increase of the number of degrees of freedom, which, after the transition to a deconfined phase, should include the color and flavour degrees of freedom [15, 16]. Furthermore, the smooth-like dependence of ϵ, p and s with T, i. e. the absence of a singularity at the $T = T_c$ (which would be expected for a first-order transition), is a feature of a crossover transition [3].

The behavior of the QCD matter for $\mu_B > 0$ is represented in the (T, μ_B) phase diagram shown in Figure 2.8 [9, 10]. Even though lattice calculations for $\mu_B > 0$ have technicals issues, results suggests that for larger μ_B the transition is of first-order, which also implies the existence of a critical point [3], as illustrated in Figure 2.8.

It is speculated that the early universe, just after the big bang, might have been a Quark-Gluon Plasma with small baryonic density. Therefore, the study of QCD at such extreme tem-
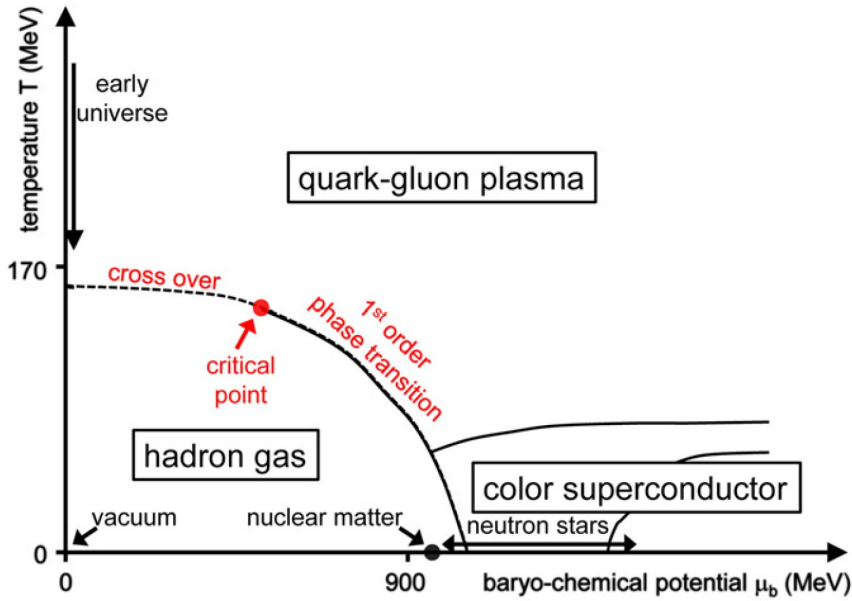
Figure 2.8: The QCD phase diagram. Figure from [8] (see also [9] and [10].

peratures is also important for the understanding of the universe expansion and cooling, as it is for the investigation of the strong interaction itself. Furthermore, theoretical studies suggest that in regimes of large μ_B and low temperatures, which should occur in central regions of compact stars, matter might behave as a color superconductor [9, 10].

In the next Section, it will be presented how QCD can be studied in the laboratory at such extreme conditions. The most common observables are defined and the main experimental evidences for the formation of a deconfined state are presented.

2.4 Characterization of the Quark-Gluon Plasma

In the laboratory the properties of the QGP are investigated through relativistic heavy-ion collisions [3, 16], as it was proposed for the first time by Chin [3, 17]. It can be said that the heavy-ion programs aiming the study of the deconfined QCD matter started with two fixed-target experiments in the decade of 1980 [3, 15]: the Alternating Gradient Synchrotron (AGS) at Brookhaven National Laboratory [18], in the USA, and the Super Proton Synchrotron at the European Organization for Nuclear Research (CERN) [19], in Geneva, Switzerland. These accelerators started the activities working with light-nuclei beams. Beams of ^{28}Si at $\sqrt{s_{NN}} = 14$ GeV and ^{16}O at $\sqrt{s_{NN}} = 60 - 200$ GeV were used at AGS and SPS respectively [3, 15]. In the decade of 1990 AGS and SPS started to accelerate heavy-ions, with ^{197}Au at $\sqrt{s_{NN}} = 11$ GeV at AGS and ^{208}Pb at $\sqrt{s_{NN}} = 158$ GeV at SPS [3, 15].

In fact, results from SPS suggested a transition to the deconfined QCD matter in heavy-ion collisions [21]. However, the discovery of the this new state of matter became well-

established with data from the Relativistic Heavy-Ion Collider (RHIC), at BNL, which started the activities in 2000 providing pp, d-Au and Au-Au collisions at relativistic energies up to $\sqrt{s_{NN}}$ = 200 GeV [20]. Experiments at RHIC, mainly STAR (Solenoidal Tracker At Rhic) [22] and PHENIX (the Pioneering High Energy Nuclear Interaction eXperiment) [23], reported results for several observables, indicating that a new, hot, dense and very dissipative medium has been created. Furthermore, these results were also compatible with a system with flavour and color degrees of freedom.

At the moment one of the aims of the experiments at RHIC and now also at the CERN Large Hadron Collider (LHC) [24], is to detailed characterize the QCD matter that is created in relativistic heavy-ion collisions. Particularly, at the LHC the QCD medium can be studied at the TeV scale, the highest energies available to date. Currently, there are data from LHC for pp at $\sqrt{s}$ = 2.76 and 7 TeV, p-Pb at $\sqrt{s_{NN}}$ = 5.023 TeV and Pb-Pb at $\sqrt{s_{NN}}$ = 2.76 TeV. It is expected that in the next years the LHC will provide pp collisions at $\sqrt{s}$ = 14 TeV and Pb-Pb collisions at $\sqrt{s_{NN}}$ = 5.5 TeV.

In the following it will be introduced the main observables in high-energy heavy-ion collisions and a review of the main experimental results from the RHIC and LHC experiments will be provided.

2.4.1 Space-time evolution of relativistic heavy-ion collisions
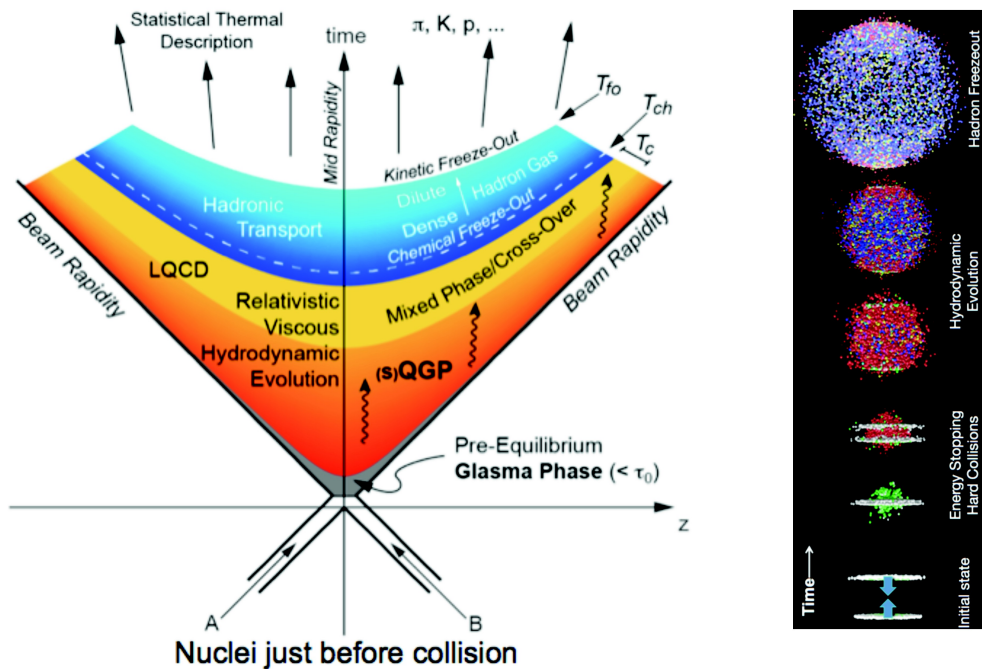
Figure 2.9: Schematic view of the space-time evolution of the system created in relativistic heavy-ion collisions. Figure from [25].

In relativistic heavy-ion collisions, after the reaction the system that is created undergoes

a chain of stages. The space-time evolution of the system is schematically represented in Figure 2.9.

Just after the collision particle production takes place in a pre-equilibrium stage, i. e. before the system reaches thermal equilibrium. After a given time interval τ_0 the medium achieve thermal equilibrium and, for sufficiently high-energy densities, it is expected to be in a deconfined quark-gluon plasma phase. At this stage, global properties (a equation of state) can be estimated from lattice QCD and phenomenological models (e. g. volume, temperature, viscosity and so on). Furthermore, the medium evolution can be described by hydrodynamic models, which treats the system as a relativistic fluid in expansion [3, 31].

The time-scale for the equilibrium stage depends on how interacting is the system. Currently, experimental data supports a strongly interacting medium within equilibrium timescale of the order of $\tau_0 \approx 1$ fm/c [3, 31].

As the system expands and cools down, a cross over transition, expected for a $\mu_B = 0$, from the deconfined matter to a hadron gas occurs. The hadronic system is expected to behave as a strongly interacting system at the beginning with inelastic scattering dominating the interaction between hadrons. In the next step, the hadronic system reaches chemical freeze-out, the stage when inelastic collisions are over and the hadronic yields are well determined. At this moment the medium can be described by thermo-statistical models [3, 31].

In the last stage, called thermo-kinetic freeze-out, elastic collisions are also over. This occur when the typical mean free path of the system is higher than the inverse rate of the interactions and the system behave as an ideal gas of non-interaction hadrons. These hadrons are measured by the detectors placed around the collision point [3, 31].

2.4.2 Global variables

In this Section it will be presented how some of the global properties of the system created in heavy-ion collisions, at equilibrium stage as well as at freeze-out, are estimated from experimental data. Some of the main results from SPS to the LHC will be shown and it will be discussed how these results support the production of a deconfined phase in relativistic heavy-ion reactions.

The energy density of the medium produced in heavy-ion collisions can be estimated using the Bjorken's formula displayed in Equation 2.6 [26], where τ_0 is the equilibrium time discussed in the previous Section, $R_A \approx 1.2A^{1/3}$ fm is the nuclear radius and $\frac{dE_T}{dy}$ is the transverse energy per unity of pseudorapidity [3, 15, 25].

As discussed in the previous Section, the equilibrium time (or formation time) is of the order of 1 fm/c. This short equilibration time is equivalent to a strongly interacting medium and it is supported by experimental data [3]. This will be discussed in Subsection 2.4.3.

Results from RHIC BES (Beam Energy Scan) program, reported by the PHENIX collaboration, for the energy density of the medium created in Au-Au collisions at several energies

is shown in Figure 2.10 [27]. The energy density was evaluated as a function of the number of nucleon participants, for several collision energies, ranging from $\sqrt{s_{NN}} = 7.7$ to 200 GeV. These results shows that the energy density of the matter produced in these collisions is larger than that needed for the transition to the QGP phase, i. e. it is typically several orders of magnitude above the critical value ($\epsilon_c \approx 0.6 - 1$) suggested by lattice QCD calculations [15, 25].

$$\epsilon = \frac{\text{Energy}}{\text{Volume}} = \frac{1}{\pi R_A^2 \tau_0} \left(\frac{\mathrm{d}E_T}{\mathrm{d}y} \right)_{y=0} \tag{2.6}$$
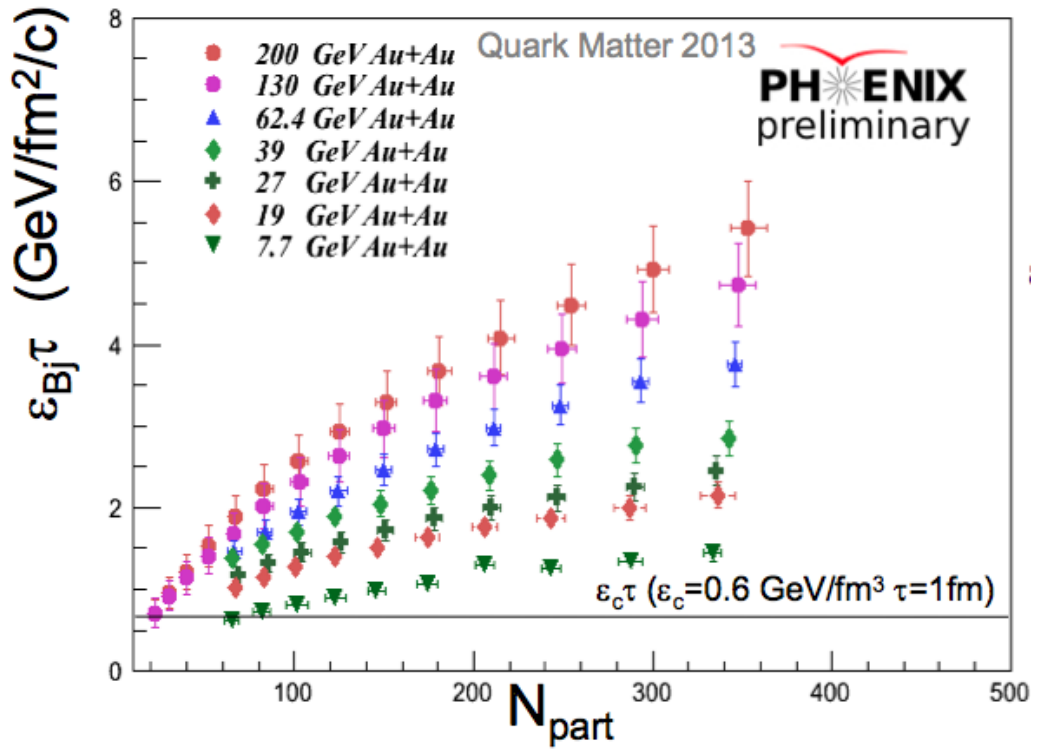
Figure 2.10: Energy density of the system created in heavy-ion collisions as a function of the number of participants, for different collision energies. Figure from [27].

The number of nucleons participants (N_{part}) is related to the collision geometry and increases with the inverse of the collision impact parameter (see Chapter 5). Therefore, Figure 2.10 shows that the medium energy density is as larger as the collision impact parameter decreases and, therefore, the deconfined phase is more likely to occur for small values of the impact parameter.

Figure 2.11 shows the energy density per pseudorapidity unity per number of participants as a function of the center of mass energy, measured by several experiments from SPS to LHC [28]. It can be seen that the energy density is larger by a factor $\approx 3 - 4$ compared to RHIC [25].

Another property that can be evaluated is the temperature of the medium. It can be
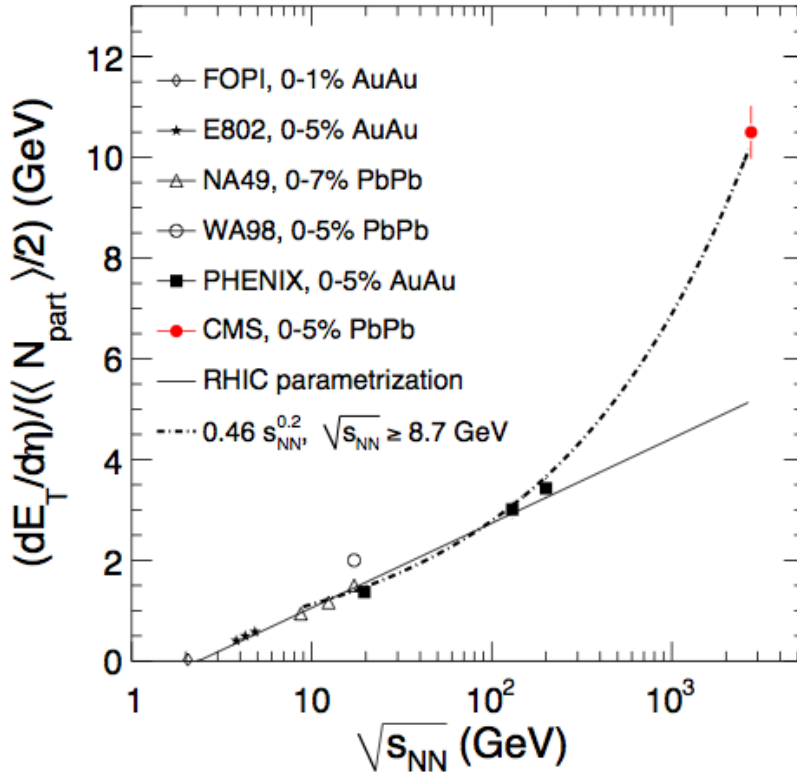
Figure 2.11: Transversal energy per pseudorapidity unity per number of participants as a function of the center of mass energy, measured by several experiments from SPS, RHIC and LHC. Figure from [28].

estimated by measuring the production of direct photons in the experiment, i. e. those that are emitted (created) by the medium. Figure 2.12 shows the invariant yield of direct photons as a function of the transverse momentum [29]. In this spectrum, the low-p_T part are due to thermo photons emitted by the medium and the shape of the p_T dependence can be used to estimated the medium temperature, in analogy to a black-body emission. With it, as displayed in Figure 2.12 the estimated temperature of the QCD matter is $T = 304 \pm 54$ MeV $\approx 2T_c$ for Pb-Pb collisions at the LHC energies [29].

The high-p_T part of the spectrum is due to hard QCD processes and, therefore, is described by pQCD calculations, which is the subject of Chapter 3.

Thermodynamical properties can be also inferred at the chemical freeze-out stage and it is particularly important to determine the nature of the phase transition. Figure 2.13 shows the particle yields of several species, measured in Pb-Pb collisions at $\sqrt{s_{NN}} = 2.76$ TeV, by the ALICE Collaboration [30]. The hadron yields is fitted by a thermo-statistical model with two free parameters (temperature T and baryonic chemical potential μ_B).

As it is displayed in the Figure, from this approach the estimated freeze-out temperature is $T \approx 156 - 164$ MeV, consistent with lattice QCD calculations at $\mu_B \approx 0$ MeV. These results are consistent with the regime of matter at the early universe. Furthermore, at such small
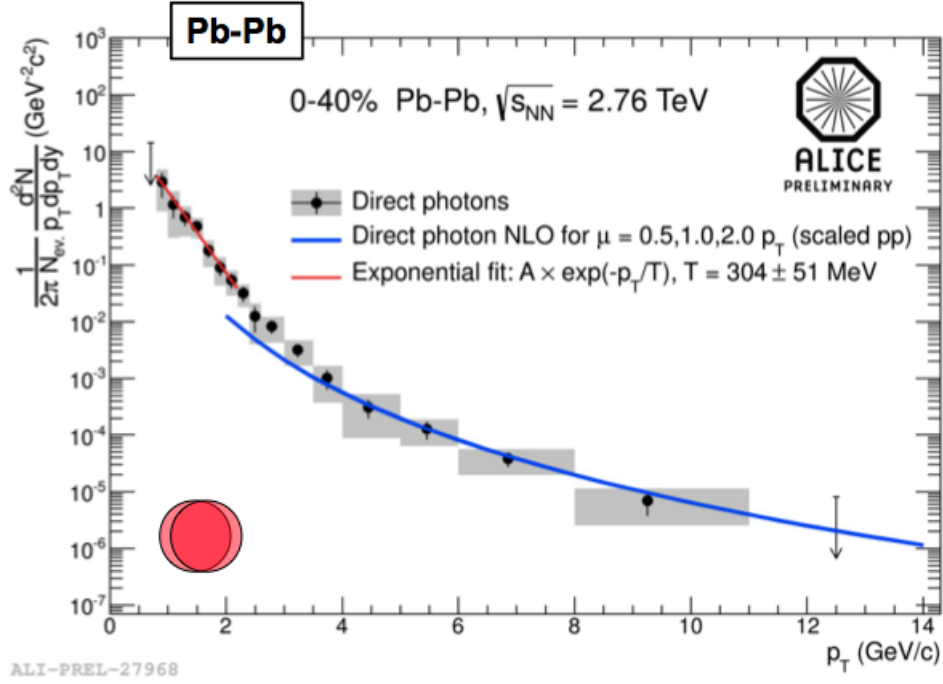
Figure 2.12: Thermal photon production in Pb-Pb collisions at $\sqrt{s_{NN}} = 2.76$ TeV as a function of p_T, measured by the ALICE experiment. Figure from [29].
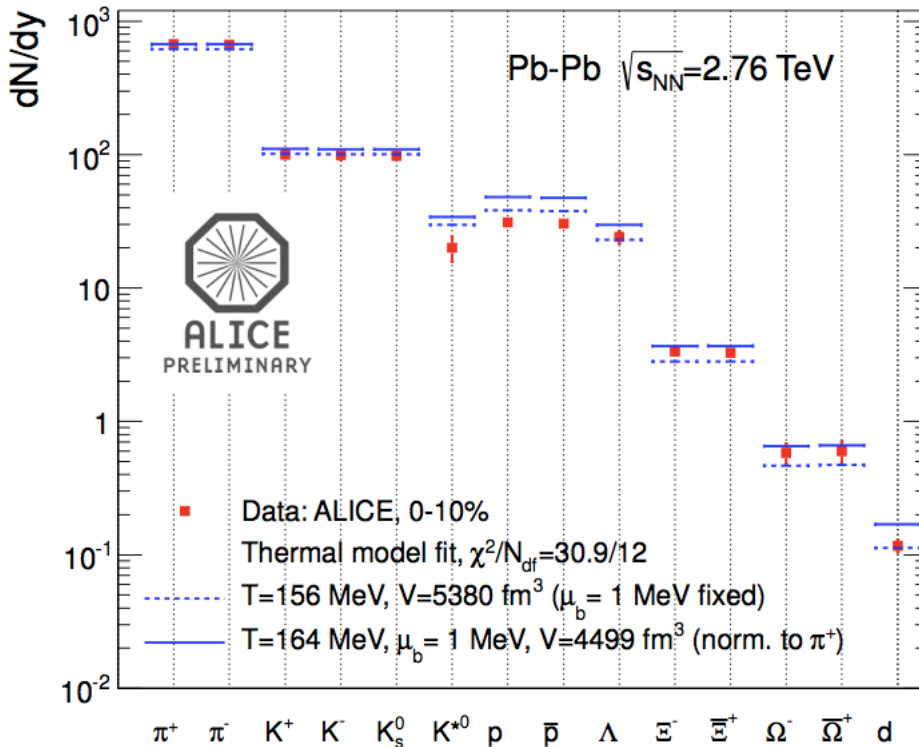
Figure 2.13: Particle yields after chemical freeze-out, measured in Pb-Pb collisions at $\sqrt{s_{NN}} = 2.76$ TeV, with ALICE. Figure from [30].

μ_B lattice calculations provides reliable predictions and, therefore, be used to predict the behavior of the system created in heavy-ion collisions for the RHIC and LHC energies.
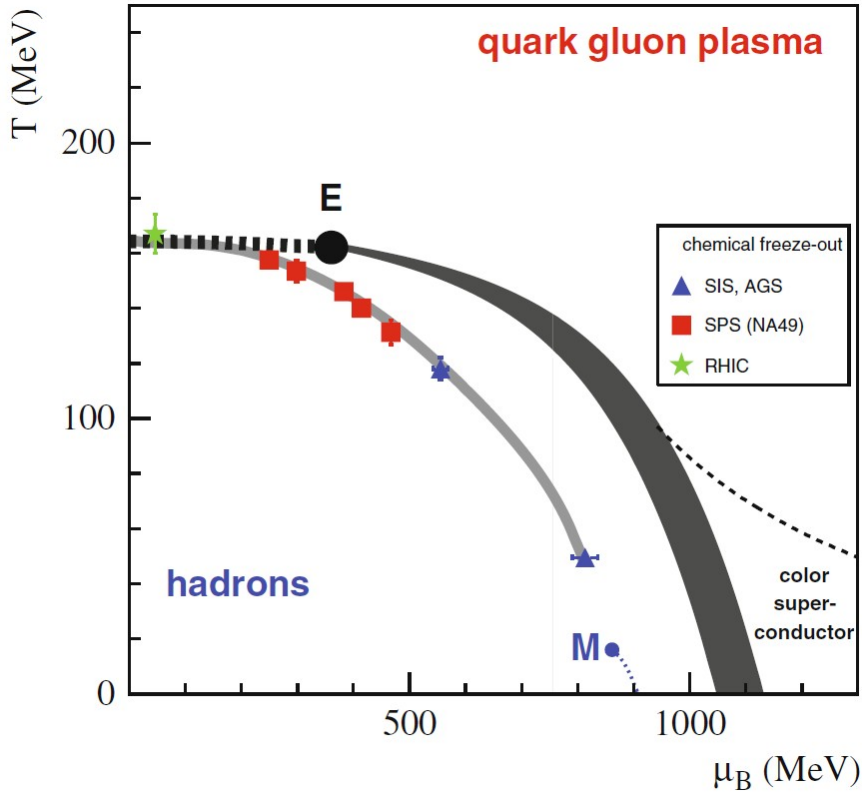
Figure 2.14: Freeze-out temperature as a function of μ_B, evaluated in heavy-ion collisions at AGS (blue triangle), SPS (red squares) and RHIC (green star), along with the QGP-hadronic matter transition line, that is expected from theoretical studies. Figure from [31].

For smaller energies, the collision produces a system with larger μ_B. The chemical freeze-out curve in the (T, μ_B) diagram is shown in Figure 2.14, along with the hadron-QGP transition line, obtained from lattice QCD calculations [31].

2.4.3   Collective flow

Another properties of the medium created in relativistic heavy-ion collisions, observed at RHIC for the first time, is the particle azimuthal anisotropy. That means, the distribution of the particles after kinetic freeze-out in the plane transverse to the beam line is not uniform.

In order to quantify this effect, the particle momentum distribution is expanded in a Fourier series, as represented in Equation 2.7 [3], where ϕ and Ψ_{RP} are the azimuthal angle of the particle and the reaction plane respectively.

$$\frac{dN}{dy d^2 p_T} = \frac{dN}{2\pi p_T dy dp_T} \left[1 + \sum_{n=1}^{\infty} 2v_n \cos(n(\varphi - \psi_{RP})) \right] \tag{2.7}$$

Following from this expansion, the anisotropy is quantified by the Fourier coefficients v_n, defined in Equation 2.8.

$$v_{\mathrm{n}} = \left\langle \cos\left[n\left(\varphi - \Psi_{\mathrm{RP}}\right)\right]\right\rangle \tag{2.8}$$

Of particular interest is the second coefficient (v_2) in the Fourier expansion, which can be qualitatively understood in terms of the collision geometry schematically drawn in Figure 2.15. In a very simplified picture, considering a semi-central collision, in the overlap region between the two nucleus have elliptical form, which are collimated in the reaction plane represented by the XZ plane in the Figure. If the system behave as an ideal gas of quarks and gluons, this initial spacial anisotropy will not have any further implication in the particles distribution. However, in case of a strongly interacting system, due to the interactions the initial spacial anisotropy is transfered to a momentum anisotropy, which result in a positive pressure gradient in the direction parallel to the reaction plane and, therefore, more particles are emitted in this direction compared to the that perpendicular to the reaction plane.
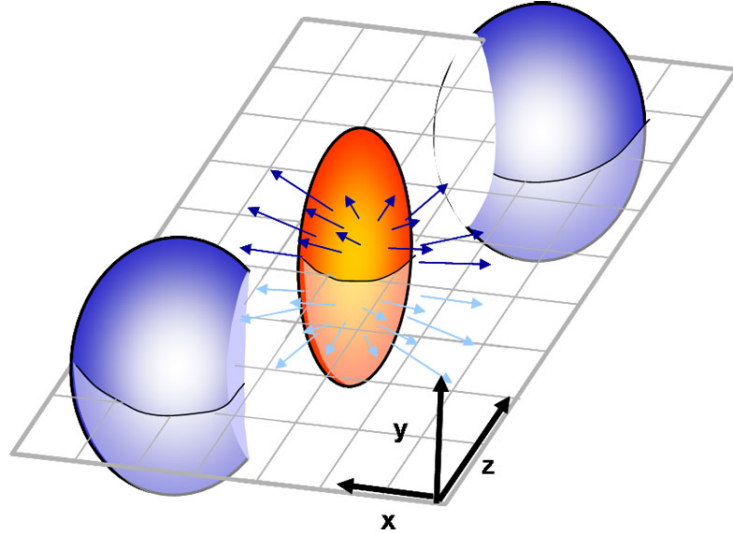
Figure 2.15: Schematic view of the geometry of a semi-central heavy-ion collision. Figure from [31].

Figure 2.16 (top panel) shows one of the first results for the v_2 coefficient measured by the STAR Collaboration at RHIC, in Au-Au collision at $\sqrt{s_{\mathrm{NN}}} = 200$ GeV [32]. The Figure shows a positive v_2 for several particle species at low-p_{T}. As it is displayed in the Figure, these results are described by hydrodynamic model calculations. These hydrodynamic calculations assume a short equilibrium time and, therefore, these results suggest a strongly interacting Quark-Gluon Plasma (sQGP). Furthermore, these models include an equation of state compatible with lattice QCD with a phase transition at $T_{\mathrm{c}} = 165$ MeV, and with a sharp kinetic freeze-out.

Figure 2.16 (bottom panel) shows the result reported by the ALICE Collaboration, for Pb-Pb collisions at $\sqrt{s_{\mathrm{NN}}} = 2.76$ TeV [33, 34]. The results from ALICE are also well described by hydrodynamical model calculations as reported in [34].
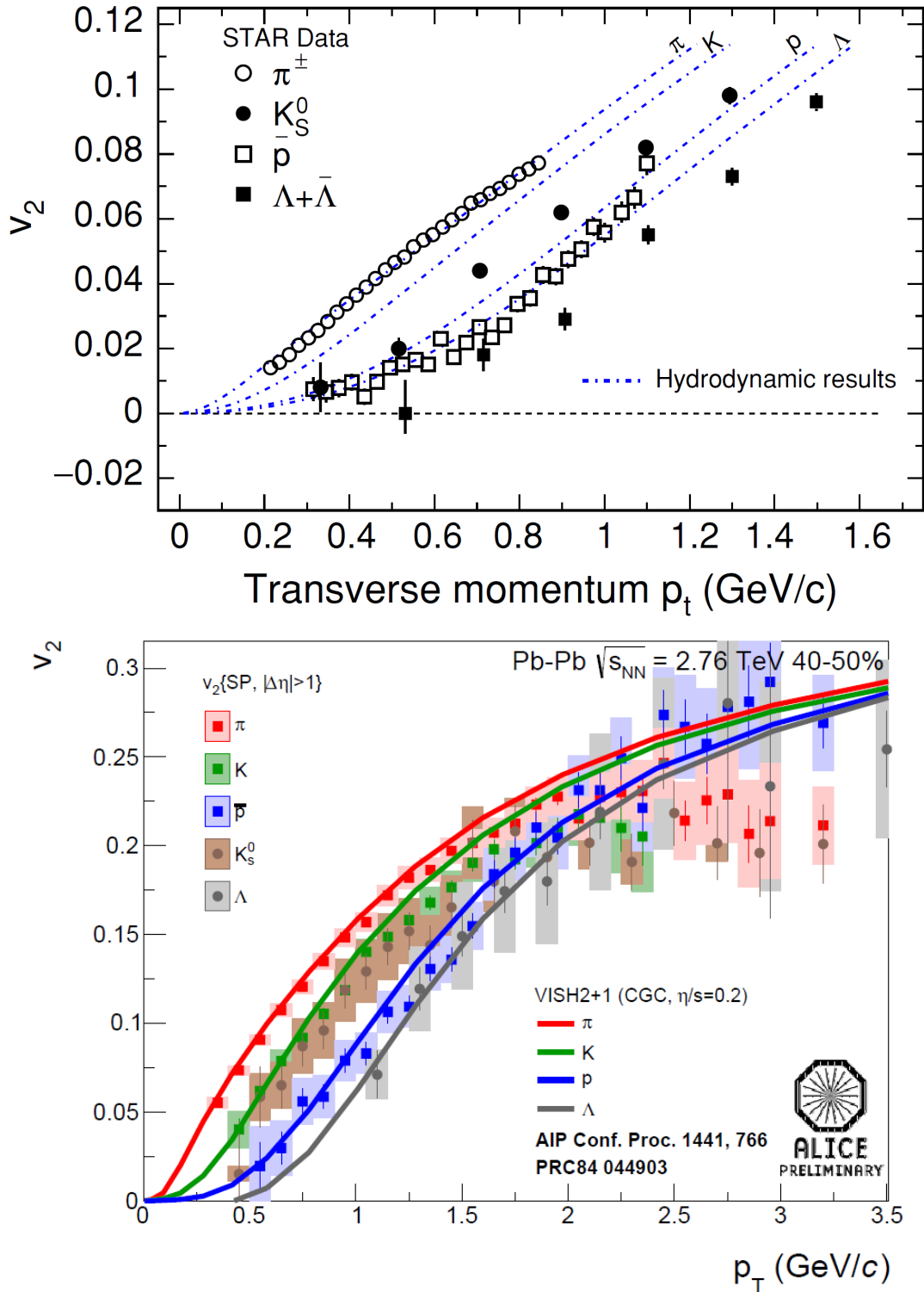
Figure 2.16: Top panel: Elliptic flow coefficient v_2 for several particle species, as a function of transverse momentum p_T, measured in Au-Au collisions at $\sqrt{s_{NN}} = 200$ GeV with STAR. Bottom panel: Elliptic flow coefficient v_2 for several particle species, as a function of p_T, measured in Pb-Pb collisions at $\sqrt{s_{NN}} = 2.76$ TeV with ALICE. Figures from [32] and [33, 34].

Finally, there are indications that v_2 scales with the number of valence quarks [32, 34]. This result (that is shown in Figure 2.17 [32]) suggests that the system created in the collision
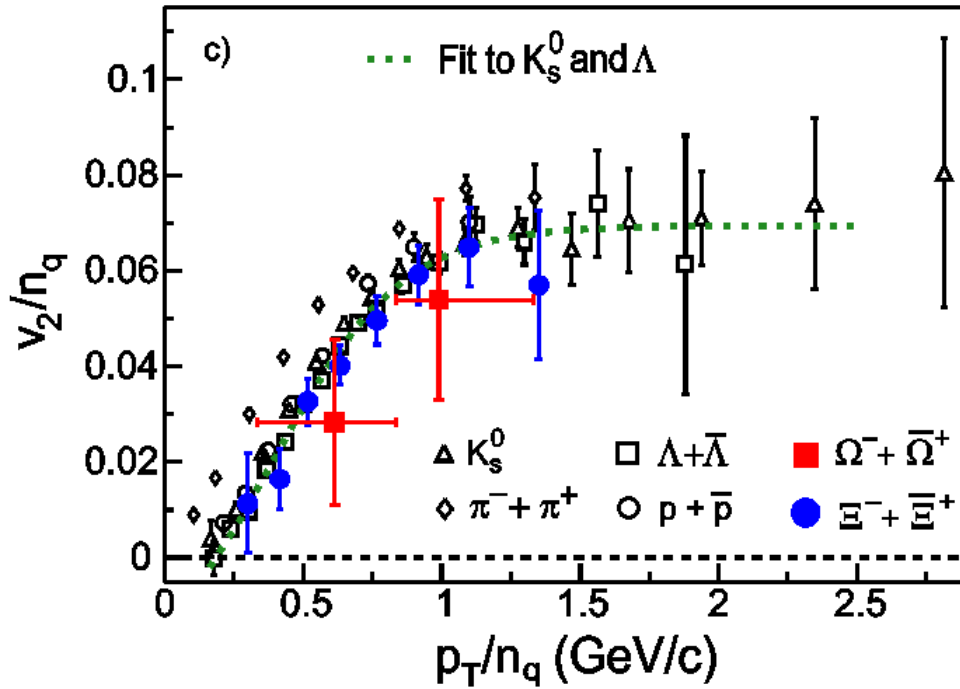
Figure 2.17: Elliptic flow coefficient v_2 of several particle species, scaled by the number of valence quarks n_q, as a function of p_T/n_q, measured in Au-Au collisions at $\sqrt{s_{NN}} = 200$ TeV with STAR. Figure from [32].

includes, indeed, flavour degrees of freedom.

2.5 Cold Nuclear Matter (CNM) effects

In heavy-ion collisions, the colliding nuclei are not just an incoherent superposition of their nucleons. Therefore, the parton flux into the collision and the dynamics of particle production might be modified, in the initial state, by coherent effects [35].

For a proper characterization of the QGP, it is important to separate these initial-state effects of the Cold Nuclear Matter (CNM) from those due to the hot QCD medium created in the final state [35]. This can be addressed through measurements of a given observable in proton-nuclei (or deuteron-nuclei collisions), where an extended QGP phase are not expected to be produced. In the following, the main aspects of the Cold Nuclear Matter will be addressed and a comparison to the experimental data from p-Pb collisions, recently published by the ALICE Collaboration, will be presented to illustrate this aspect.

2.5.1 Low-x physics at the LHC

At the LHC it will be possible to access the parton distribution functions at low Bjorken-x, ≈ 2 orders of magnitude smaller than at RHIC. A clear discussion o this can be found in [15]. As an example, for the production of a quark-antiquark pair with invariant mass $M_{Q\bar{Q}}$, via

gluon fusion ($g + g \rightarrow Q + \bar{Q}$), in a nuclei-nuclei collision at center of mass energy $\sqrt{s_{NN}}$, the Bjorken-x values of the gluons that suffer the scattering are given by Equation 2.9 [15].

$$x_1 = \frac{M_{Q\bar{Q}}}{\sqrt{s_{NN}}}\exp(+y_{Q\bar{Q}}) \qquad\qquad x_2 = \frac{M_{Q\bar{Q}}}{\sqrt{s_{NN}}}\exp(-y_{Q\bar{Q}}) \qquad\qquad (2.9)$$

Therefore, at the middle rapidity region ($y \approx 0$) $x_1 \approx x_2 \approx \frac{M_{Q\bar{Q}}}{\sqrt{s_{NN}}}$. For the case of charm production ($M_{c\bar{c}} \approx 2.4$ GeV) $x \approx 10^{-4}$, which is typically two order of magnitude lower than at RHIC [15, 31]. Figure 2.18 shows the typical x-regions covered by the LHC, RHIC and SPS as a function of the energy scale Q^2 [31].
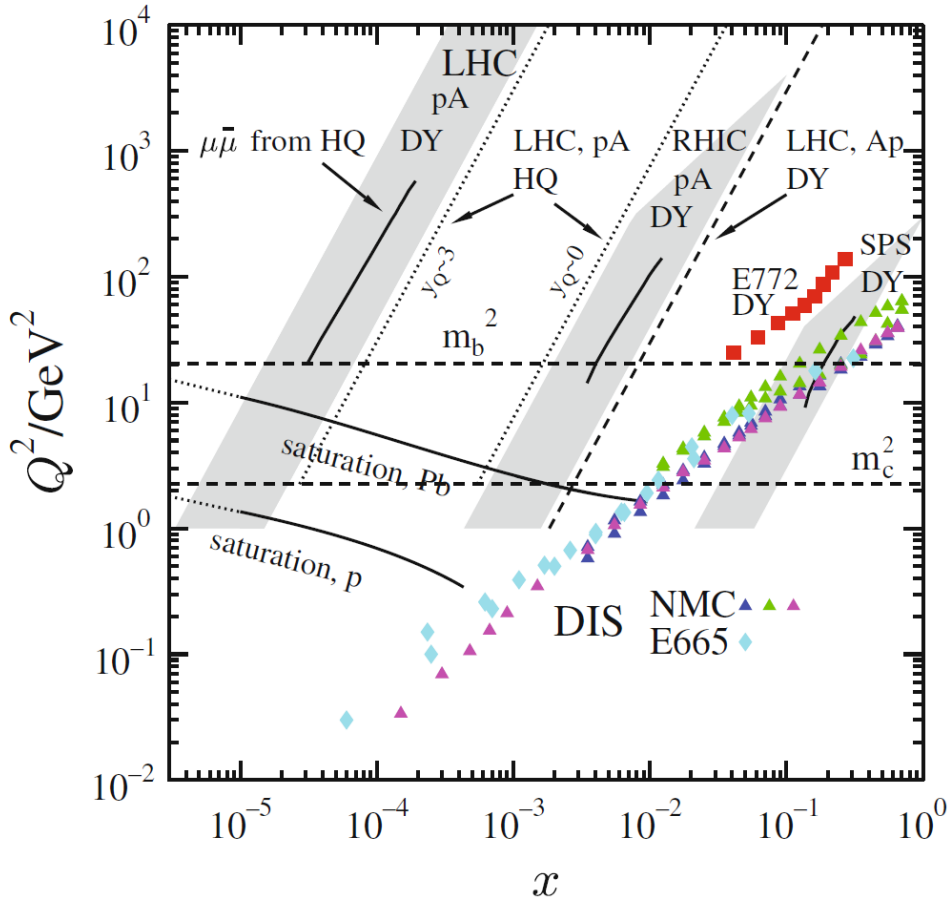
Figure 2.18: **The Bjorken-x as a function of the energy scale Q^2. The filled regions indicates the coverage of LHC, RHIC and SPS. Figure from [31].**

2.5.2   Gluon saturation and color glass condensate

Results from electron-proton DIS show that the gluon density is strongly enhanced at low values of Bjorken-x. This is shown in Figure 2.19 (left panel) [3, 25, 31].

Therefore, at low-x the gluon density is very large. If the energy scale involved Q^2 is high enough, the gluons will fit normally in the finite space of the nuclei. However if Q^2 is smaller than a certain value Q_s^2, i. e. if they are extended enough, the gluons overlap inside the nuclei.
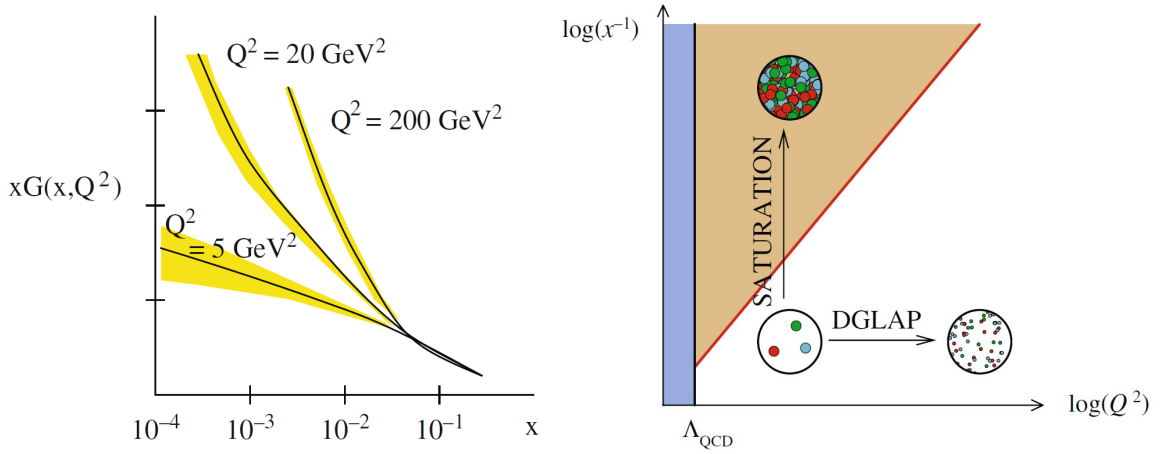
Figure 2.19: Left: Rapidity density of gluons $xG(x, Q^2)$ **as a function of** x **for** $Q^2 = 5, 20, 200$ **GeV**^{2} **[31].**
Right: Schematic view of the saturation phenomena at small Bjorken-x**. Figures from [31].**

This phenomena is called gluon saturation and Q_s^2 is the saturation scale. Figure 2.19 (right panel) schematically represents this situation, and shows the line defining the saturation scale as a function of x [3, 25, 31].

In the saturation regime, since gluons are very close to each other they form a system in the weak coupling limit ($\alpha_{QCD} < 1$), for which was quoted the name Color Glass Condensate (CGC) [3]. Color indicates that the constituents of the medium (the gluons) have color charge, glass refer to the property that low-x gluons evolute slowly compared to other timescales in the problem and condensate is indicating the large number of gluons in the system [3, 25].

2.5.3 Nuclear shadowing

The nuclear shadowing effect is a modification in the parton distribution function of nucleons in a nuclei [15, 25]. This modification is quantified by the shadowing factor, defined as the ratio between the two PDFs, as defined in Equation 2.10 [15].

$$R^{Pb}(x, Q^2) = \frac{g^{Pb}(x, Q^2)}{g^{p}(x, Q^2)} \tag{2.10}$$

The shadowing factors reported by several groups, for the valence quarks, sea quarks and gluons, as a function of x, are shown in Figure 2.20 [36].

The shadowing effect can be qualitatively understood in the following way. Due to the large density of gluons with small x, two small x gluons, with Bjorken-x x_1 and x_2 can merge and produce a single gluons with larger momentum $x = x_1 + x_2$. Therefore the PDF will be reduced at low-x and enhanced at a larger-x range, as one can see in Figure 2.20 [15].
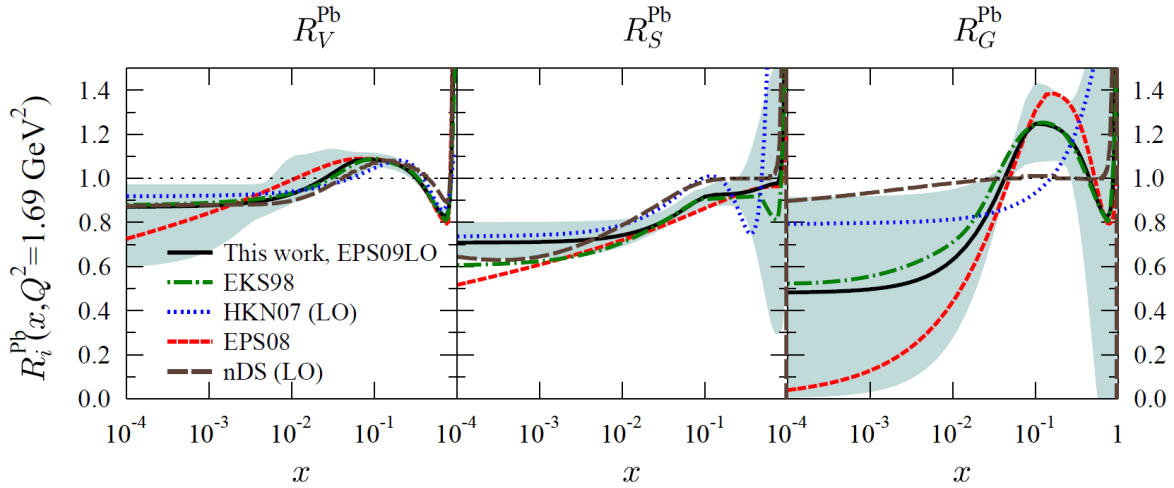
Figure 2.20: Modification of the parton distribution function of nucleons in a nuclei, for valence and sea quarks, and for gluons. Figure from [36].

2.5.4   Control experiments: the role of p-Pb collisions

In Pb-Pb (or Au-Au) collisions, CNM effects, such as saturation at small Bjorken-x, can be misinterpreted as due to properties of the QCD medium created in the collision. Therefore, for a proper characterization of the QGP it is crucial to disentangle initial and final-state effects. This can be addressed through analysis of light on heavy-ion (i. e. p-Pb or d-Au) collisions, where the QGP phase is not expected to occur but nuclei effects are present. In the following an example of this strategy will be provided.

For the example that will follow it is necessary to introduce the nuclear modification factors (R_{AA} and R_{pA}), which are defined in Equation 2.11, where $d\sigma^{AA}/dp_T$ ($d\sigma^{pA}/dp_T$) is the differential cross section in A-A (p-A) collisions, $d\sigma^{pp}/dp_T$ is the differential cross section in pp collisions and N_{coll} is the number of binary collisions in the nuclear collision, which is estimated through the Glauber Model [37]. Defined in this way, in the absence of effects of the medium created in heavy-ion collisions (or due to initial-state effects) on the differential cross section, the nuclear modification factor coincides, by construction, with unity ($R_{AA} = 1$ and $R_{pA} = 1$).

$$R_{AA} = \frac{1}{\langle N_{coll} \rangle} \frac{d\sigma^{AA}/dp_T}{d\sigma^{pp}/dp_T} \qquad R_{pA} = \frac{1}{\langle N_{coll} \rangle} \frac{d\sigma^{pA}/dp_T}{d\sigma^{pp}/dp_T} \qquad (2.11)$$

Figure 2.21 shows the nuclear modification factor of charged particles measured in p-Pb collisions at $\sqrt{s_{NN}} = 5.02$ TeV, with ALICE detectors [38]. The particle spectra has a visible modification at the lower-p_T region, which is well described by Color-Glass-Condensate model calculations as well as by a modified nPDF with pQCD calculations [38]. The lower panel shows also the comparison to several tunes of HIJING Monte Carlo generator [38], with and without shadowing. It is also shown that R_{p-Pb} is compatible with unity at larger

p_T values. The higher p_T part is one of the subjects of the next Chapter.
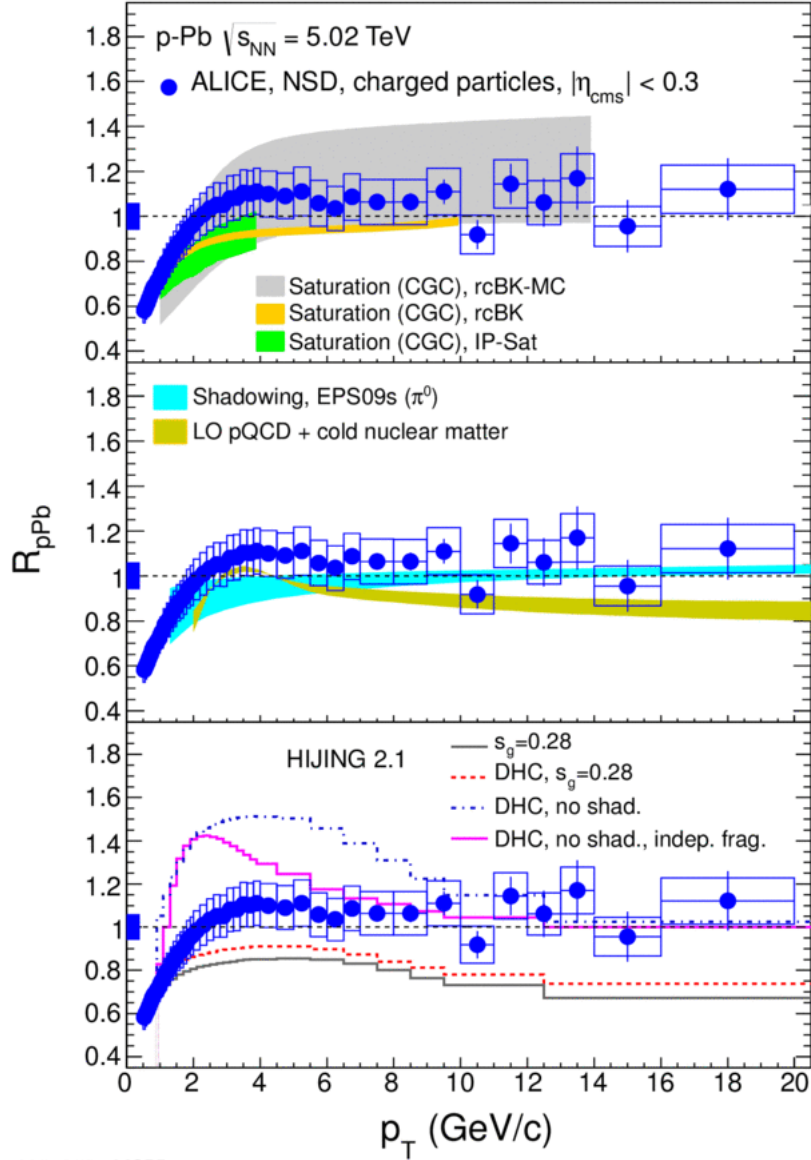
Figure 2.21: Nuclear modification factor of charged unidentified particles in p-Pb collisions at the LHC at $\sqrt{s_{NN}} = 5.02$ TeV, measured with ALICE. The experimental result is compared to CGC model calculations (top panel), shadowing calculations using the EPS09 PDF (middle panel) and to the Decoherent Hard Collision (DHC) model implemented in HIJING (bottom panel). In the legend of the the bottom panel s_g refers to the shadowing parameter. Figure from [38].

Chapter 3

Hard probes

3.1 Introduction to hard probes

In the previous Chapter we have introduced many experimental observables used in the global characterization of the medium created in heavy-ion collisions, i. e. those observables that are used to evaluate global variables such as temperature, volume, energy density and so on. Most of these observables had a common property that they are related to the regime of soft process in QCD and the predictions (and post-dictions) have to rely on non-perturbative lattice QCD calculations, phenomenological and thermo-statistical models. In fact, those measurements are mostly associated with low-p_T particles, produced typically in process with small momentum transfer ($Q \lesssim \Lambda_{\mathrm{QCD}}$).

In this Chapter the subject is on a new group of observables called collectively hard probes. With a hard probe it is possible to "tomographycally" study the QCD matter [31]. In simple words, a hard probe can be defined as a particle produced in a scattering with large momentum transfer (large Q^2) [15, 31]. Here, large means significantly larger than the QCD scale $Q \gg \Lambda_{\mathrm{QCD}} \approx 0.2$ GeV. Following from this definition, hard probes have the following features [15, 25, 31]:

- **Predictions can be made through perturbative QCD calculations**
  Since $\alpha_s(Q^2) \propto \frac{1}{\ln(Q^2/\Lambda_{\mathrm{QCD}}^2)}$, for a hard parton with $Q \gg \Lambda_{\mathrm{QCD}}$ the related coupling constant will be small ($\alpha_s < 1$) and, therefore, higher order Feynman diagrams can be neglected, i. e. the calculations are significantly facilitated by the fact that only lower order diagrams have a significant contribution.

- **Short timescale production**
  Hard partons are produced in the initial hard scattering that occur between partons from the two colliding nucleus, at the very early stages of the collision. Furthermore, the production process occurs typically in a timescale of the order $\tau_{\mathrm{prod}} \approx 1/Q$. As an example, for a process with $Q > 2$ GeV, $\tau_{\mathrm{prod}} \lesssim 0.1$ fm $\ll \tau_0 \approx 1$ fm, where τ_0 is the typical formation (equilibrium) time discussed in the previous Chapter.
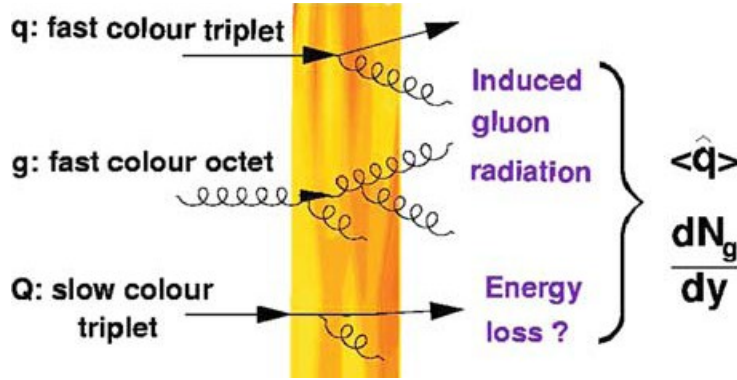
Figure 3.1: Illustration of how hard partons are used to probe the hot and dense QCD medium, in relativistic heavy-ion collisions. Figure [31].

- **Information on initial states and QCD medium effects**
  From the previous property it follows that hard partons carry information about the whole system evolution, from the pre-equilibrium phase until the hadronization and freeze-out. Their production can be affected in the initial state by CNM effects. After that, they can be its kinematics modified due to the interaction with the medium, for instance losing energy. For example, in case of enough re-scattering, they might participate in the collective expansion of the system, leading to a positive v_2 for these particles.

What follows from above discussion is that hard probes are self-generated probes for the system created in heavy-ion collisions. They are well known from pQCD calculations and via data from elementary (pp) collisions. With it, any observed modification in a hard probe related observable should be either a CNM effect or due to the interaction of the hard parton with the hot QCD medium in the final state.

Figure 3.1 [31] illustrates the strategy of using hard partons to probe the hot and dense QCD matter in heavy-ion collisions. The effects of the interaction of the parton with the medium, such as gluon radiation and energy loss, on the final state can be used to evaluate several properties of the medium such as the transport coefficient $\hat{q}$, the initial gluon rapidity density $\frac{dN_g}{dy}$ and so on [31].

In the next Section several relevant experimental results on hard probes will be discussed, focusing on jets, single high-p_T particles and heavy quarks.

3.2   In medium energy loss: suppression of high-p_T particles

A first example of hard probe in heavy-ion collisions are the measurements of charged particles with high transverse momentum ($p_T > 2 - 3$) GeV. These particles are originated in the fragmentation of a hard parton and, therefore, they carry the features described in the previous Section.

Figure 3.2 shows the nuclear modification factor of charged unidentified particles in p-Pb and Pb-Pb collisions at $\sqrt{s_{NN}}$ = 5.02 and 2.76 TeV respectively, measured with ALICE at the LHC [38]. A strong suppression of particles with transverse momentum larger than 3 − 4 GeV is visible for Pb-Pb collisions, not observed for the p-Pb data. In fact, in p-Pb collisions the nuclear modification factor for particles in the high momentum range is consistent with unity. Therefore, the suppression observed for heavy-ion collisions is a final state effect, i. e. due to the medium created in the reaction. Such yield suppression is interpreted as due to energy loss of partons while traversing the QGP [15, 25, 31].

In fact, the measured yield suppression is described by energy-loss models. In Figure 3.3 the nuclear modification factor for central Pb-Pb collisions is displayed in an extended momentum range, along with several models, on which energy loss is included [39].

ALI−PUB−44351
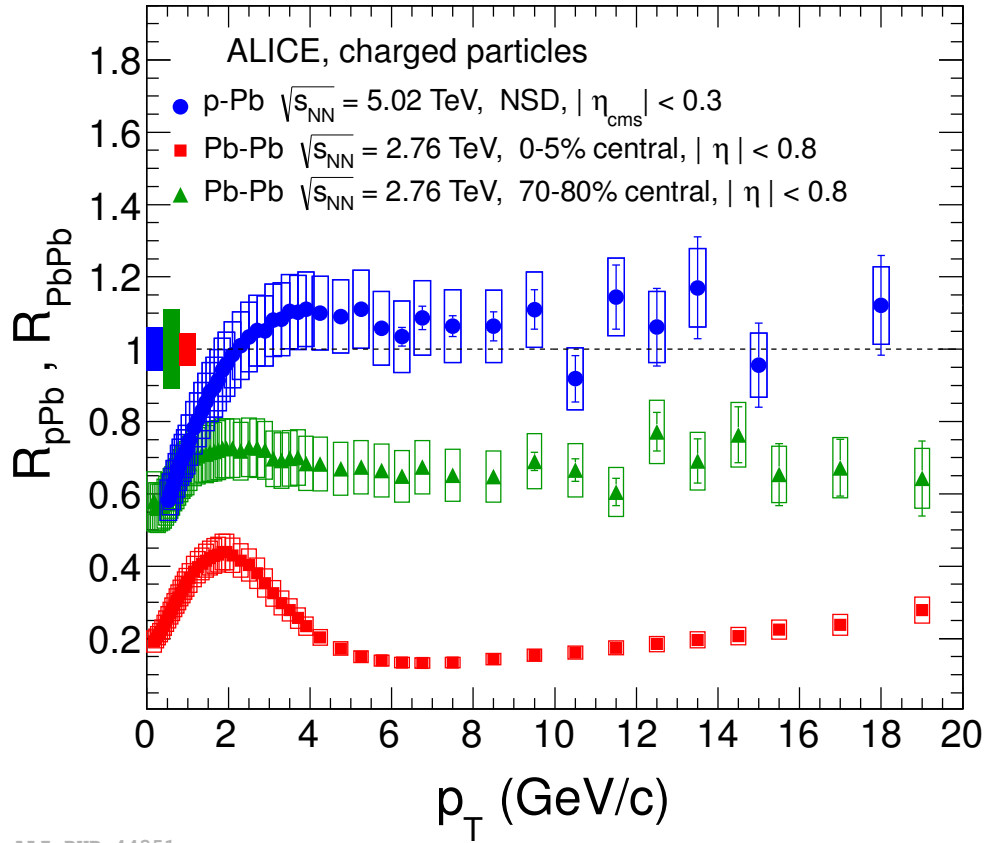
Figure 3.2: Nuclear modification factor of charged unidentified particles in p-Pb and Pb-Pb collisions at $\sqrt{s_{NN}}$ = 5.02 and 2.76 TeV respectively, measured with ALICE. Figure from [38].

In general, parton energy-loss models include two mechanisms: *collisional* energy-loss, when the hard-parton undergoes an elastic scattering on a particle of the medium and *radiative* energy-loss, when the high-p_T parton radiates a gluon induced by the medium [31]. Therefore the total energy-loss is given by sum of these two components $\Delta E^{\text{total}} = \Delta E^{\text{coll}} + \Delta E^{\text{rad}}$. These two process are illustrated in Figure 3.4 [31].

The average energy-loss in a single scattering is estimated through Equations 3.1 [31],
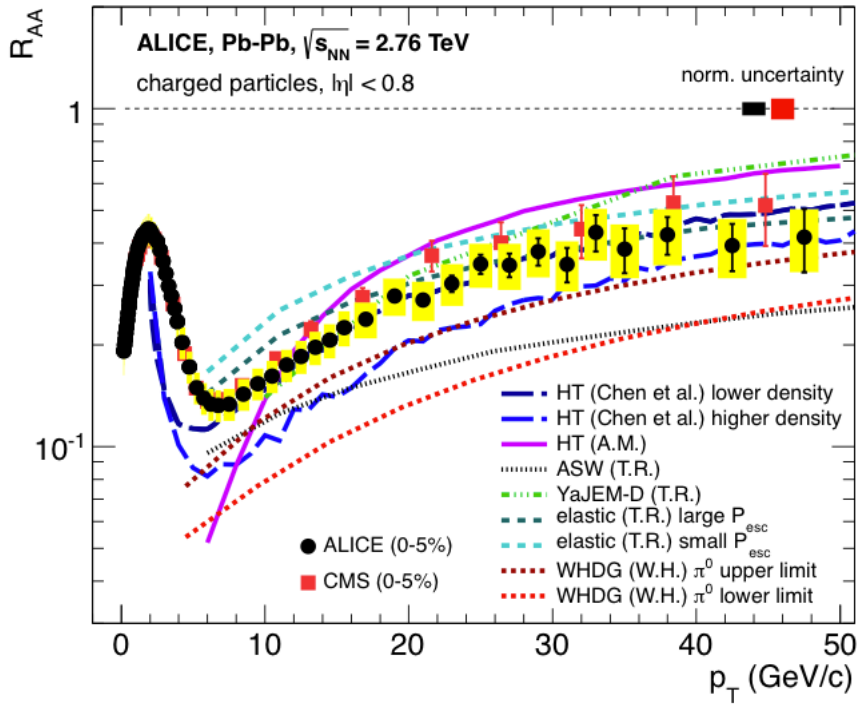
Figure 3.3: Nuclear modification factor of charged unidentified particles in Pb-Pb collisions at $\sqrt{s_{NN}} = 2.76$ TeV, measured with ALICE along with the result reported by the CMS Collaboration. The lines represent predictions from several energy loss models including mainly radiative energy loss. Figure from [39].

where q is the momentum transfered in the elastic collision, $\frac{\mathrm{d}\sigma}{\mathrm{d}q}$ is the differential cross-section for an elastic collision and $\frac{\mathrm{d}I_{\mathrm{rad}}}{\mathrm{d}\omega}$ is the gluon bremsstrahlung spectrum. Starting from the dominant contribution to the parton-parton differential cross-section and the radiation spectrum provided by DGLAP splitting functions (see [31]) lead to the expressions shown in Equation 3.2 to 3.4 for the in medium energy-loss [31]. In these equations $\hat{q} = \frac{\alpha_{\mathrm{s}} T^2}{\lambda}$ is the medium transport coefficient, a measure of the system scattering power [31]. C_{R} is the Casimir factor and it is 3 (4/3) for a gluon (quark) radiating a gluon [31], $m_{\mathrm{D}} \propto \sqrt{\alpha_{\mathrm{s}}} T^2$ is the Debye mass, a measure of the minimum momentum transfer in the medium, L is the
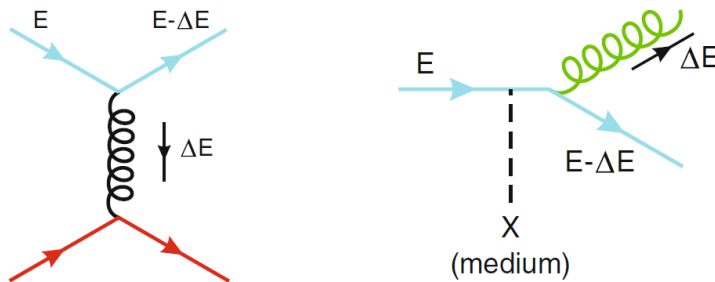
Figure 3.4: Feynman diagrams for the collisional (left panel) and radiative (right panel) energy-loss mechanisms. Figure from [31].

medium thickness and λ the mean free path [31].

$$\Delta E_{\text{coll}}^{\text{1scatt}} = \frac{1}{\sigma T} \int_{q_{\text{min}}}^{q_{\text{max}}} q \frac{\mathrm{d}\sigma}{\mathrm{d}q} \mathrm{d}q \quad ; \quad \Delta E_{\text{rad}}^{\text{1scatt}} = \int_{E_{\text{min}}}^{E_{\text{max}}} \omega \frac{\mathrm{d}I_{\text{rad}}}{\mathrm{d}\omega} \mathrm{d}\omega \tag{3.1}$$

$$\Delta E_{\text{coll}} \propto C_{\text{R}} \alpha_{\text{s}}(ET) m_{\text{D}}^2 L \log\left(\frac{ET}{m_{\text{D}}^2}\right) \tag{3.2}$$

$$\Delta E_{\text{rad}} \propto C_{\text{R}} \alpha_{\text{s}} \hat{q} L^2 \log\left(\frac{E}{L m_{\text{D}}^2}\right) \qquad (L \ll \lambda) \tag{3.3}$$

$$\Delta E_{\text{rad}} \propto C_{\text{R}} \alpha_{\text{s}} \begin{cases} \hat{q} L^2 & (\omega < \omega_{\text{c}}) \\ \hat{q} L^2 \left(\frac{E}{\hat{q} L^2}\right) & (\omega > \omega_{\text{c}}) \end{cases} \qquad (L \gg \lambda) \tag{3.4}$$

From Equations 3.2 to 3.4 it is possible to notice that, typically, the parton energy-loss law is of the form $\Delta E \propto \alpha \hat{q} L^2$ for the medium induced radiation (which is, typically the largest contribution). Therefore, as an example, the comparison between predictions from energy-loss model calculations with measurements of nuclear modification factors provides a tool to evaluate properties of the QCD matter, such as $\hat{q}$.

3.3 Jets

After the hard parton-parton scattering, one (or more) of the hard parton(s) created start to lose energy via medium-induced radiation or it can split in a quark-antiquar pair. Such a process will happen until the initial parton with large virtuality (i. e. large Q^2) reduces to a lower enough virtuality of the order $\mathcal{O}(1 \text{ GeV}^2)$ [31]. At this point, the produced particles undergoes a non-perturbative fragmentation process, in which hadrons are produced. Such a group of hadrons that is originated in the fragmentation of a single parton, forming a collimated shower is called a *jet* [31]. There are dedicated algorithms for jet reconstruction that are used in the data analysis. Introduce these algorithms is beyond the scope of this text and some information can be found in [40] and [41].

As an example of what information can be added by measuring jets compared to single particles measurements we will know reproduce a discussion made in [25]. A schematic representation of jet production in relativistic heavy-ion collisions is shown in Figure 3.5 (left panel) [25, 31]. In this Figure two high-p_{T} partons are created via an initial hard scattering and each of these partons originate a jet. One of the jets is created near the edge and it is not significantly affected by the medium. The second parton traverse a larger path in the medium, interacting and losing energy (mostly via gluon induced radiation) and, therefore, such a jet carries important information on the medium properties, such as transport coefficient $\hat{q}$, initial gluon density $\mathrm{d}N_{\text{g}}/\mathrm{d}y$ and Temperature [25, 31]. This phenomena is called *jet quenching*.
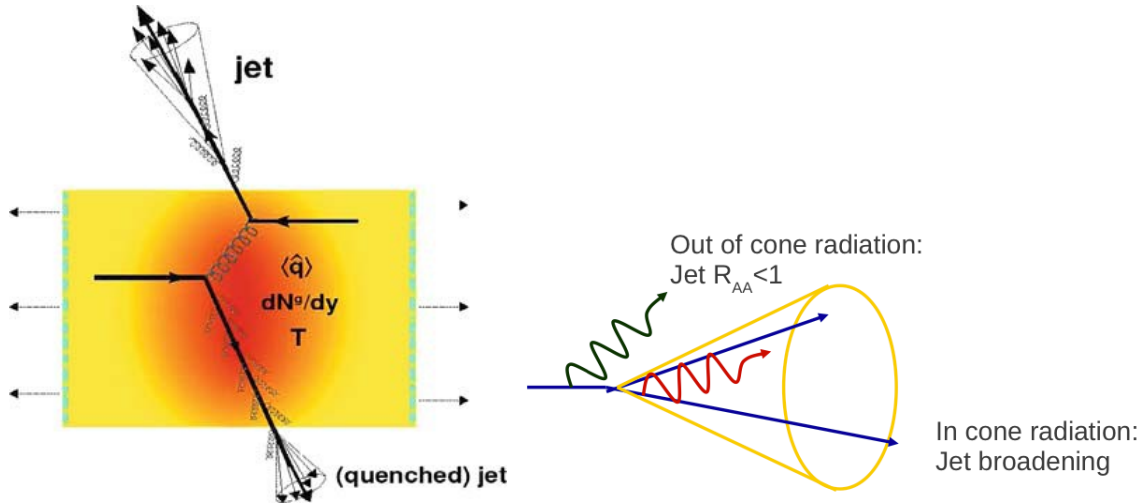
Figure 3.5: Schematic illustration of jet production and jet quenching phenomena in heavy-ion collisions. Figure from [25, 31].

On important information that can be addressed via jet measurements is whether, in the radiative energy-loss process, the gluon is emitted with large or small angles. In case of gluon emission with large angles the hadrons that are product of the fragmentation of the radiated gluon will not be counted in the jet reconstruction and the energy lost will be reflect in a nuclear modification factor smaller than unity ($R_{AA} < 1$) [25]. On the other side, in case of small angles radiation, the energy lost is recovered in the jet reconstruction, and one expects $R_{AA} \approx 1$ or, at least, a nuclear modification factor higher than that for single particles [25].
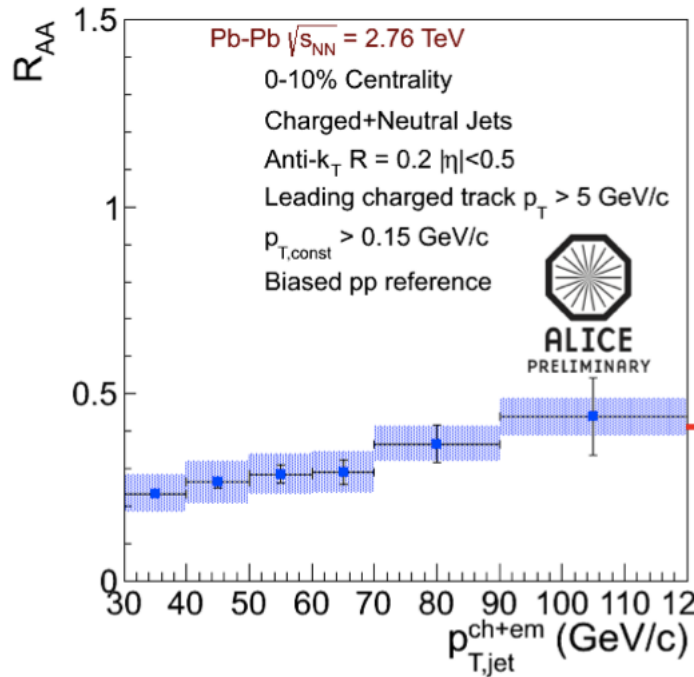
Figure 3.6: Nuclear modification factor of jets in Pb-Pb collisions at $\sqrt{s_{NN}} = 2.76$ TeV. Figure from [42].
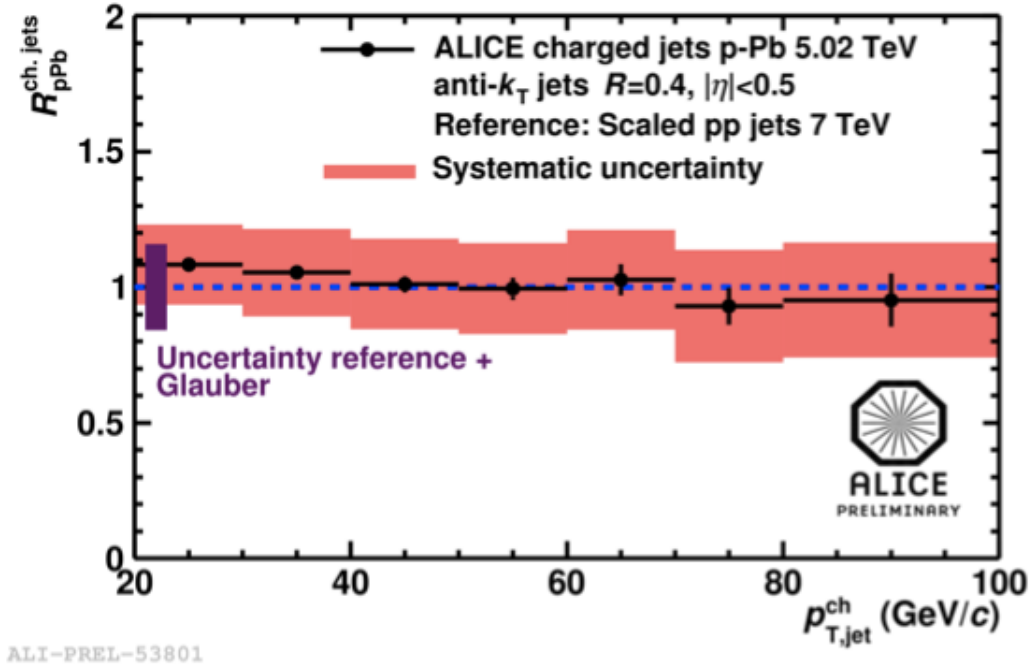
Figure 3.7: Nuclear modification factor of jets in p-Pb collisions at $\sqrt{s_{NN}}$ = 5.02 TeV. Figure from [43].

In Figure 3.6 the nuclear modification factor for jets, measured in Pb-Pb collisions at $\sqrt{s_{NN}}$ = 2.76 TeV with the ALICE detector, is shown [42]. The measured R_{AA} is consistent with that of single particles (after taking into account the fragmentation), supporting a large-angle gluon-radiation in the medium [25]. Furthermore, in Figure 3.7 one can see the results for the case of p-Pb collisions at $\sqrt{s_{NN}}$ = 5.02 TeV [43]. In p-Pb collisions the measured R_{p-Pb} is consistent with binary scaling. Therefore, the jet suppression observed in Pb-Pb collisions is an effect of the QCD medium in the final-state rather than an initial-state effect.

In the next Chapter we will discuss the effect of jets in the structure of the two-particle angular distribution, which was one of the strongest indications that a dense and dissipative medium is formed in heavy-ion collisions at high energies.

3.4 Heavy flavours

Heavy-flavours, i. e. charm and beauty quarks, are also produced in process with large momentum transfer. The lowest momentum transfer in a heavy-quark production is Q_{min} = $2m_Q \approx 2.4 \ (\approx 8.5)$ GeV/c for a c$\bar{c}$ (b$\bar{b}$) pair production. Therefore, heavy-flavours are also classified as hard probes and carries the features discussed at the beginning of this Chapter.

As argued in [46], one advantage of heavy compared to light-flavours (up, down and strange quarks) is that the latter can be obtained from several sources: valence quarks of the colliding nuclei, initial hard scattering, thermo-production in the medium and so on. Therefore, the information carried by light-flavour hadrons are ambiguous. On the other

side, heavy quarks are dominantly produced in initial hard scattering process, while other sources are very unlike.

Another advantage is the large masses involved provides a very convenient test for parton energy-loss model calculations, since these models shows a typical mass dependence, as we will discuss in the following Sections.

3.4.1   Heavy-flavour production

As aforementioned, heavy-flavour production can be calculated through the pQCD framework. The differential cross-section can be write as an expansion in powers of α_s of the form expressed in Equation 3.5 [15, 44, 45], where $\mu_{F,R}$ are typical scales of the underlying process and it is typically taken as $\mu_F = \mu_R = m_Q = \sqrt{m_Q^2 + p_T^2}$, the transverse mass of the heavy quark [44, 45].

$$\frac{d\sigma}{dp_T^2} = \alpha_s^2(\mu_F) \sum_{k=0}^{\infty} C_k(m_Q)\alpha_s^k(\mu_F) \sum_{l=0}^{k} c_{kl}\log^l\left(\frac{\mu_R}{m_Q}\right) \tag{3.5}$$

Since $\alpha_s < 1$ for heavy-flavour, a first reliable approximation for the production cross-section can obtained at leading order (LO) $\mathcal{O}(\alpha_s^2)$ and next-to-leading order (NLO) $\mathcal{O}(\alpha_s^3)$ terms, as shown in Equation 3.6 [44, 45, 46].

$$\text{NLO:} \qquad A(m_Q)\alpha_s^2 + B(m_Q)\alpha_s^3 \tag{3.6}$$

Figure 3.8 illustrates the main heavy-flavour production mechanisms at LO and NLO. At LO the contributions are from par creation via (a) gluon-gluon fusion and (b) $q - \bar{q}$ annihilation. At NLO the process are classified by the number of heavy-quarks in the final state of the hard scattering. The process are (c) flavour excitation, when a heavy quark of the incoming beam suffer a scattering with a parton of the second beam and (d) gluon splitting, when no heavy-flavour is involved in the hard scattering. The process represented in Figure 3.8 (e) is classified as gluon splitting but of flavour excitation character [44, 46].

The NLO approach yields reliable results for low and intermediary p_T i. e. for p_T of the order of the quark mass or smaller. In regimes where $p_T \gg m_Q$ the quantity $\log\frac{\mu}{m}$ is significant in the expansion and corrections from leading-log (LL) and next-to-leading log (NLL) terms, shown in Equation 3.7, are needed [44, 45].

$$\text{NLL:} \qquad \alpha_s^2 \sum_{i=0}^{\infty} a_i\left(\alpha_s\log\left(\frac{\mu_R}{m_Q}\right)\right)^i + \alpha_s^3 \sum_{i=0}^{\infty} b_i\left(\alpha_s\log\left(\frac{\mu_R}{m_Q}\right)\right)^i \tag{3.7}$$

This correction is implemented in the fixed-order next-to-leading-log (FONLL) model, described in [44, 45]. There are also other improved NLO models, which tries to account for the large log terms at high-p_T, such as the GM-VFN (general-mass variable-flavour-number) model described in [47]. In these models, the degrees of freedom of one of the partons cre-
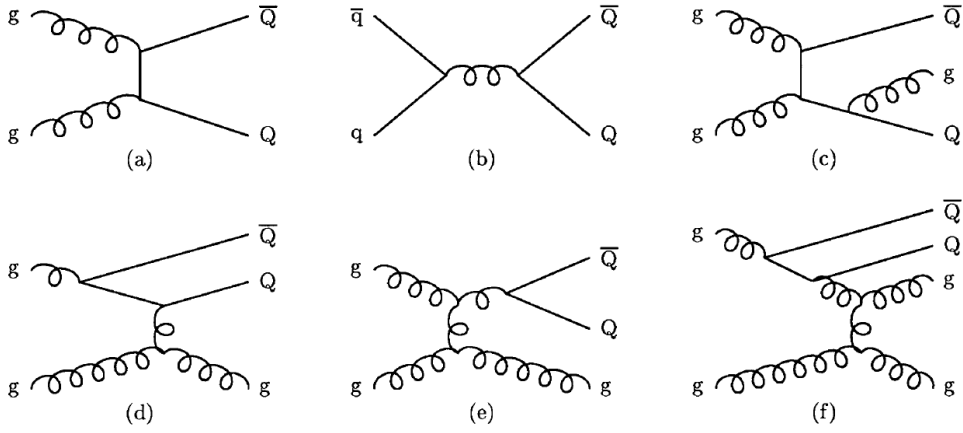
Figure 3.8: Heavy-flavour production mechanisms at LO and NLO pQCD. Figure from [46].

ated in the hard scattering is integrated over. Therefore these models can not be used for correlation studies between the quark and the anti-quark pair created. For these studies one can rely on Monte Carlo simulations, which includes the LO terms and NLO is accounted for in the so-called Parton Shower (PS) approach [46] implemented, for instance, in the PYTHIA program [48, 49]. The k_{T}-factorization model (see e. g. [50]) also provides a tool for studies of heavy-flavour correlations, accounting for the large logarithmic terms at high-p_{T}.

In these models the large contribution to the theoretical uncertainties are the quark masses, the μ process scale and, in case of a hadronic collision, the parton distribution function [44, 45].

3.4.2 Heavy-flavour energy loss: mass dependence and dead-cone effect

The collisional energy-loss of heavy-quarks in the medium gain a mass dependence, compared to Equations 3.2 [31]. The formula for heavy quarks is given in Equation 3.8 [31], where M is the heavy-quark mass.

$$-\left(\frac{\mathrm{d}E_{\mathrm{coll}}}{\mathrm{d}l}\right)_Q = -\left(\frac{\mathrm{d}E_{\mathrm{coll}}}{\mathrm{d}l}\right)_q - \frac{2}{9}C_{\mathrm{R}}\pi T^2 \alpha_{\mathrm{s}}(M^2)\alpha_{\mathrm{s}}(ET)\log\left(\frac{ET}{M^2}\right) \tag{3.8}$$

In the case of radiative energy-loss there is also a difference between heavy and light-flavours. Due to kinematics constraints, gluon emission is suppressed for angles smaller than $\theta_0 = M/E$. The cone defined by $\theta < \theta_0$ is then called dead cone. At large angles, i. e. $\theta \gg \theta_0$, the radiation spectrum does not depends on the ration M/E and, therefore, the radiative energy-loss should be identical to that of light-flavours [15, 31].

Due to the dead-cone effect, heavy quarks are expected to lose more energy than light quarks or gluons and the behavior expressed in Equation 3.9 is expected [15, 31]. Equivalently, in terms of the nuclear modification factor, light quarks are expected to be more suppressed than heavy quarks.

$$\Delta E_{\mathrm{g}} > \Delta E_{\mathrm{u,d,s}} > \Delta E_c > \Delta E_b \Longrightarrow R_{\mathrm{AA}}^{\mathrm{g}} < R_{\mathrm{AA}}^{\mathrm{u,d,s}} < R_{\mathrm{AA}}^{c} < R_{\mathrm{AA}}^{b} \tag{3.9}$$

3.4.3   Electrons from heavy-flavour hadron decays

Open heavy-flavour can be experimentally studied via several approaches: (a) reconstruction of D mesons via their hadronic decays [51, 52], (b) measurements of electrons (positrons) from heavy-flavour hadron decays, (c) requirement on the particle-displacement to the secondary vertex and (d) measurements of heavy-flavour decay muons. The second is the strategy exploited in the present work and a detailed explanation about heavy-flavour signal extraction will be discussed in Chapter 6. Indeed, measurements of heavy-flavour decay electrons can be used to test pQCD calculations and energy-loss models that has been discussed in this Chapter. Theoretically, heavy-flavour decay electrons are treated by a convolution of the partonic cross-section estimated via pQCD calculation with the energy loss model (in the case of heavy-ion collision), a fragmentation function (accounting for the hadronization of charm and beauty in D and B mesons) and a semi-leptonic decay. This is schematically drawn in Figure 3.9 and expressed in Equation 3.10 [53].
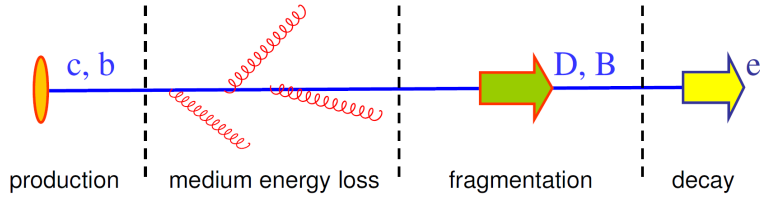
Figure 3.9: Illustration of how electrons from heavy-flavour hadron decays are obtained. Figure from [53].

$$E\frac{\mathrm{d}^3\sigma(e)}{\mathrm{d}p^3} = E_i \frac{\mathrm{d}^3\sigma(e)}{\mathrm{d}p_i^3} \otimes P(E_i \rightarrow E_f) \otimes D_{Q \rightarrow H_Q} \otimes f(H_Q \rightarrow e) \tag{3.10}$$

In Figure 3.10 the p_{T}-differential cross section of heavy-flavour decay electrons, measured in pp collisions at $\sqrt{s} = 2.76$ TeV is shown [54]. The results are compared to three set of pQCD calculations [45, 47, 50]. This result shows that, indeed the pQCD calculation models describes the data reasonably well, within theoretical and experimental uncertainties.

As mentioned earlier, in order to test the energy loss models it is interesting to measure the nuclear modification factor. Figure 3.11 shows the nuclear modification factor for heavy-flavour decay electrons reported by the STAR collaboration along with several parton energy-loss models [31]. It is visible that the measured suppression is much stronger than that predicted by the parton-energy loss models and, in fact, the measured nuclear modification factor is comparable to that obtained in the light-flavour sector.

Several explanations were proposed to account for this unexpected result for heavy-flavour
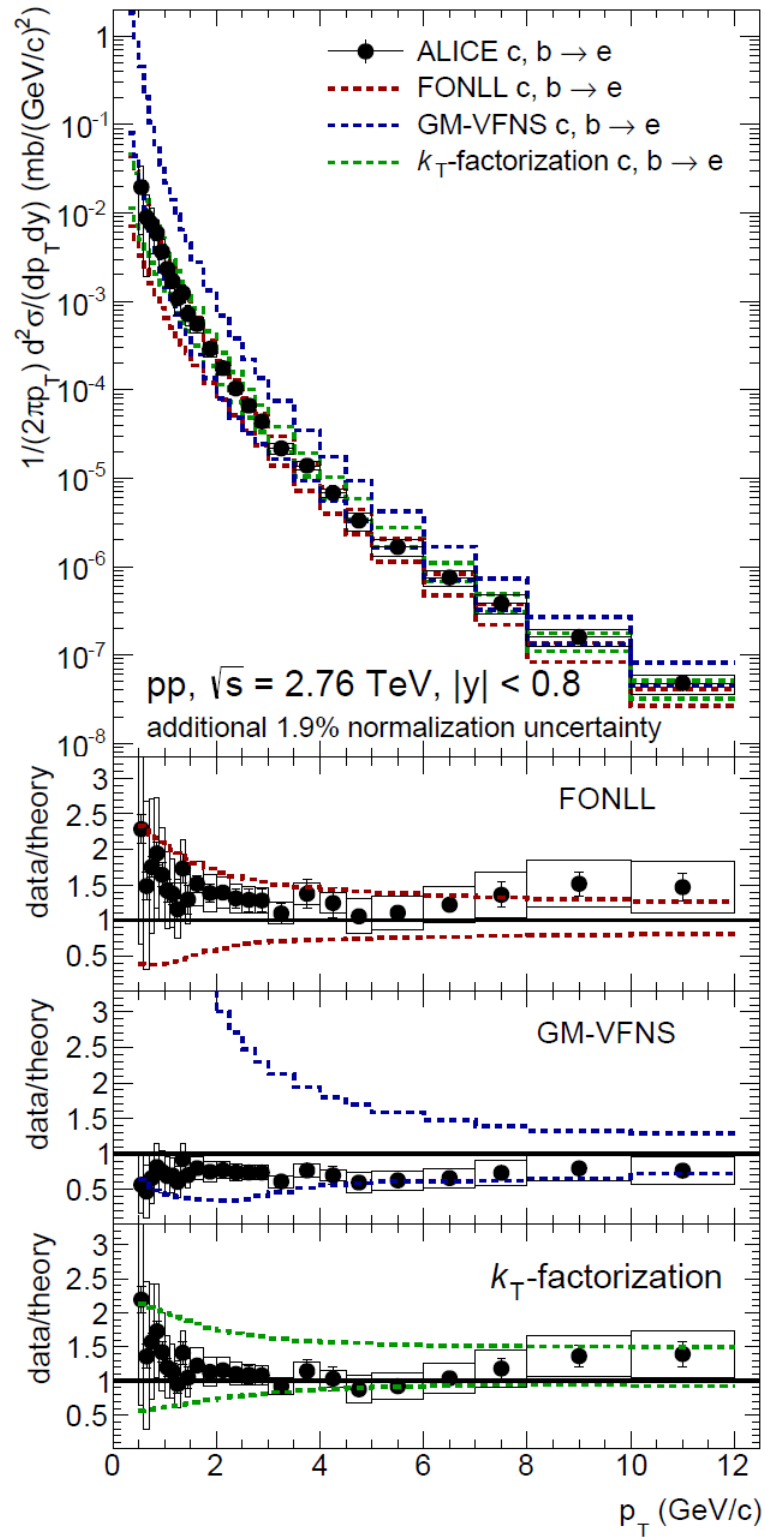
Figure 3.10: Production cross-section of electrons from heavy-flavour hadron decays in pp colli-sions at $\sqrt{s}$ = 2.76 TeV [54], compared to three set of pQCD calculations [45, 47, 50]. Figure from [54].

decay electrons. A first alternative was assume that charm quarks were the most relevant contribution, but that was not support by the data (see Chapters 4 and 7). One alternative
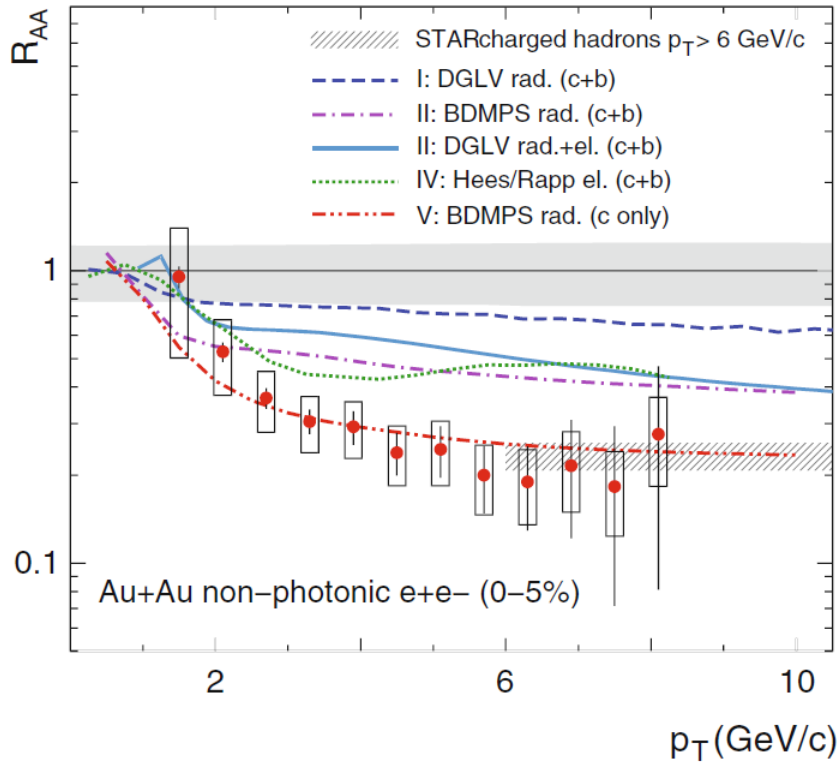
Figure 3.11: Nuclear modification factor of electrons from heavy-flavour hadron decays, as a function of p_T, in Au-Au collisions at $\sqrt{s_{NN}} = 200$ GeV, reported by the STAR Collaboration. Predictions from several in medium energy loss models, which includes radiative and collisional energy loss, are shown as lines in the Figure. Figure from [55].

that was proposed argued that elastic energy-loss are not negligible but would be as important as the gluon radiation mechanism for heavy-quark suppression and the result, as discussed e. g. in [53], where a model accounting for both, collisional and radiative mechanisms are used along with a realistic medium size and gluon density.

LHC results of the R_{AA} for heavy-flavour decay electrons, reported by the ALICE Collaboration, are shown in the left panel of Figure 3.12. A strong suppression of the electron yield is also observed in Pb-Pb relative to pp collisions at the LHC energies, endorsing that charm and beauty quarks lose energy in the medium created in Pb-Pb collisions. Furthermore, on the right side of Figure 3.12 a positive v_2 coefficient is shown for heavy-flavour decay electrons at $p_T < 4$ GeV/c. These result suggest that heavy-quarks, mainly charm, might participate of the collective expansion of the medium created in the collision. The results (R_{AA} and v_2) are described by models represented as lines in the Figure. These models includes heavy-quark energy-loss in an extended medium created in the final state of the collision [56, 57, 58, 53]. It is visible in these comparisons that a given model can not describe R_{AA} and v_2 with a good precisions. Such simultaneous description is very important to understand the properties of the QGP.

The nuclear modification factor of heavy-flavour decay electrons was also measured in
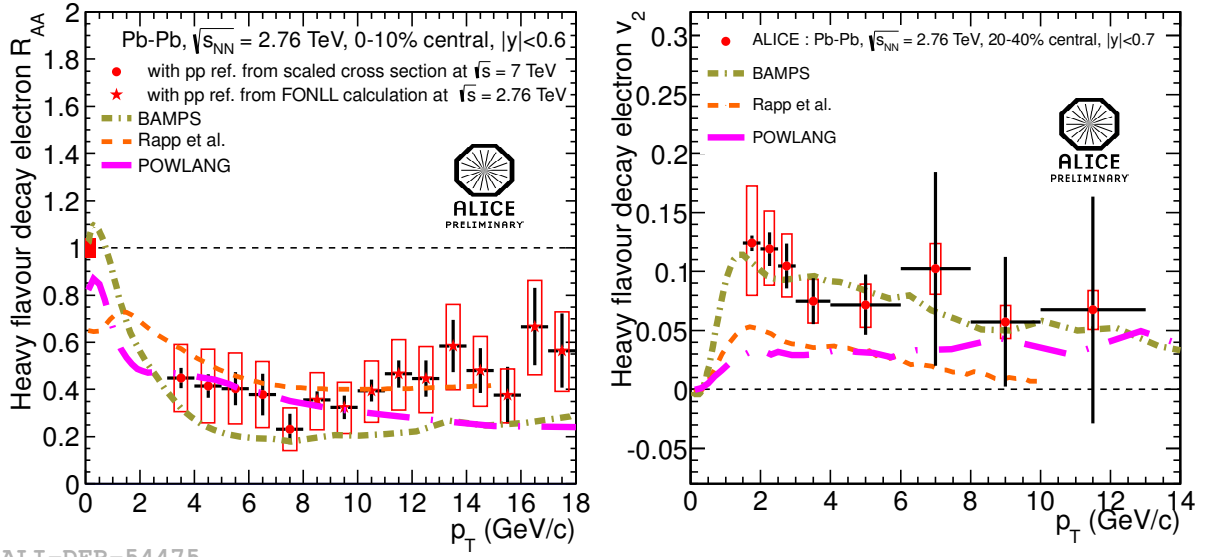
Figure 3.12: Nuclear modification factor and elliptic flow coefficient of electrons from heavy-flavour hadron decays, as a function of p_T, measured in Pb-Pb collisions at $\sqrt{s_{NN}} = 2.76$ TeV, with ALICE [55]. The experimental results are displayed along with several models, represented by lines, which includes parton energy-loss in an extended QGP phase in the final state [56, 57, 58]. Figure from [55].
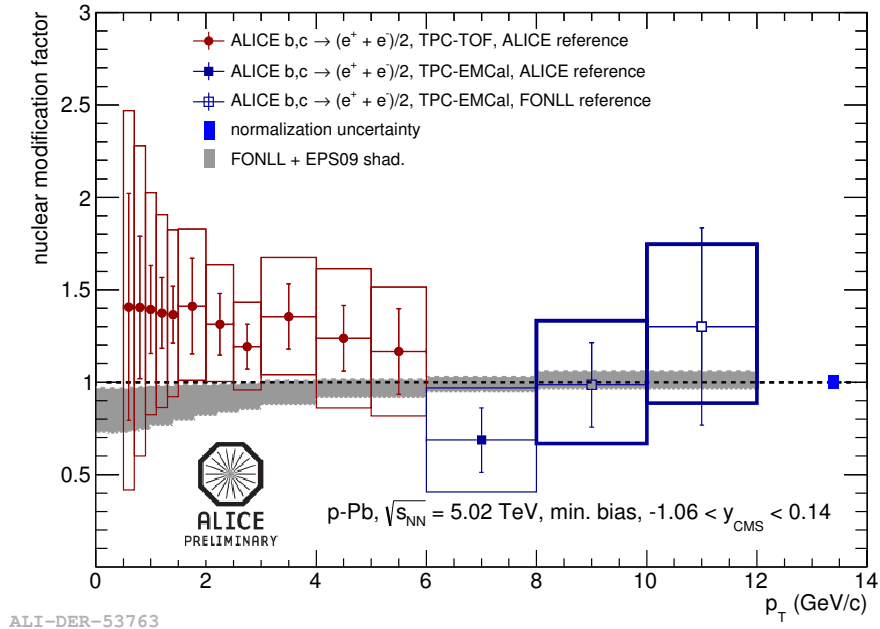
Figure 3.13: Nuclear modification factor of electrons from heavy-flavour hadron decays, as a function of p_T in p-Pb collisions at $\sqrt{s_{NN}} = 5.02$ TeV, measured with ALICE. Figure from [59].

p-Pb collisions at $\sqrt{s_{NN}} = 5.02$ TeV and the result is consistent with unity within uncertainties as can be seen in Figure 3.13 [59]. This also suggests that the measured yield suppression in heavy-ion collisions is due to energy-loss of heavy-quarks in the QCD matter rather than any

CNM effect in the initial state. These results are also consistent with shadowing modified nuclear PDF in the initial state [36].

Chapter 4

Two-particle angular correlation

4.1 Introduction and definition

Another convenient observable in relativistic heavy-ion collisions is the two-particle angular distribution. In this Chapter it will be demonstrated that the correlation between particles after freeze-out reflects the structure of jets and the back-to-back $q - \bar{q}$ pair production in the initial hard scattering. Collective effects, discussed in Chapter 2, generate a modulation in the correlation structure with magnitude given by the Fourier coefficients. Furthermore, the angular correlation distribution can be used to study heavy-flavour production in pp collisions (see Section 4.3). Particularly, the technique of angular correlations was used in the scope of the thesis to study charm and beauty production at the LHC. The analysis details are discussed in Chapter 7.

The correlation function is the distribution of the difference in azimuth $\Delta\varphi$ and in pseudorapidity $\Delta\eta$ between a trigger and an associated particle, which are often requested to be in some range of transversal momentum, i. e. $C = C(\Delta\varphi, \Delta\eta; p_\mathrm{T}^t, p_\mathrm{T}^a)$. The distribution is defined in Equation 4.1, where N_pairs is the number of pairs found in a given $\Delta\varphi$ and $\Delta\eta$ interval, with widths $\delta\Delta\varphi$ and $\delta\Delta\eta$ respectively. In practice, these widths is defined by the size of the bins of the histogram that is filled. The distribution is also normalized by the number of trigger particles N_trig and, therefore, C represents the average number of associated *per-trigger particle* as a function of transverse momentum $p_\mathrm{T}^{t,a}$ (Equation 4.1).

$$C(\Delta\varphi, \Delta\eta; p_\mathrm{T}^t, p_\mathrm{T}^a) = \frac{1}{N_\mathrm{trig}} \frac{N_\mathrm{pairs}(\Delta\varphi, \Delta\eta; p_\mathrm{T}^t, p_\mathrm{T}^a)}{\delta(\Delta\varphi)\delta(\Delta\eta)} \quad \longrightarrow \quad \frac{1}{N_\mathrm{trig}} \frac{\mathrm{d}^2 N_\mathrm{h}(\Delta\varphi, \Delta\eta; p_\mathrm{T}^t, p_\mathrm{T}^a)}{\mathrm{d}(\Delta\varphi)\mathrm{d}(\Delta\eta)} \quad (4.1)$$

It is also common to study the projection of the correlation function on azimuth $\Delta\varphi$, as defined in Equation 4.2.

$$C(\Delta\varphi; \delta\Delta\eta, p_\mathrm{T}^t, p_\mathrm{T}^a) = \frac{1}{N_\mathrm{trig}} \frac{\mathrm{d}N_\mathrm{pairs}(\Delta\varphi; \delta\Delta\eta, p_\mathrm{T}^t, p_\mathrm{T}^a)}{\mathrm{d}(\Delta\varphi)} \quad (4.2)$$

4.2   Jet quenching at RHIC

As a first example, we will examine one of the first results on two-particle correlations (2PC), from the STAR Collaboration, that is shown in Figure 4.1 [32]. In this case, both the trigger and associated particle are unidentified charged tracks and they are defined in a way such that the p_T of the trigger is always larger than that for the associated particle. Therefore, in association with a jet shower, the trigger particle can be thought as the jet leading particle, i. e. the particle which carries the largest fraction of the original parton momentum (or jet momentum), and therefore its direction is not substantially modified compared to the original quark.

In absence of other strong effects, like collectivity, the evaluated correlation function is expected to have the aspect of the continuous black line in Figure 4.1, which are the result from pp collisions at $\sqrt{s} = 200$ GeV. The two strong peaks that appears from the pp data, around $\Delta\varphi = 0$ and $\Delta\varphi = \pi$, can be understood in the following way: In the initial hard scattering typically two hard partons are created in the final state of the scattering and each of them originates a jet. The correlation between hadrons that are originated in the fragmentation of the same quark is the source of the correlation peak found around $\Delta\varphi = 0$, which is often called the near-side correlation. The peak at $\Delta\varphi \approx \pi$ is due to the correlation of a particle with those from the jet originated from the second parton created in the scattering, i. e. this reflects the correlation between the two jets created in the event. This is the so-called away-side (or back-to-back) correlation [31, 25, 60].
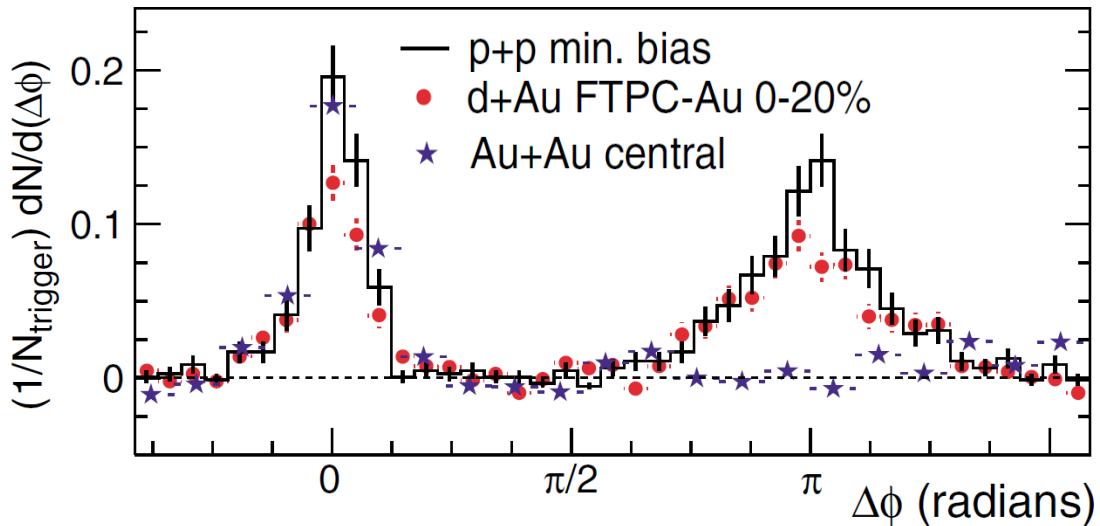
Figure 4.1: Two-particle angular correlation, between unidentified hadrons, in pp, d-Au and Au-Au collisions at $\sqrt{s_{NN}} = 200$ GeV, reported by the STAR Collaboration. Figure from [32].

The red circles correspond to the result from high-multiplicity (0-20%) d-Au collisions, where a very similar structure is observed, compared to the pp case, except for a small sup-

pression a in both the near and away-side correlation peak. The remarkable result appears in the result from Au-Au collision, in which the away-side correlation peak completely disappears. Since, such an away-side vanish is not observed in d-Au collisions, this effect is taken as due to the medium that is created in Au-Au collisions. The interpretation is that one of the partons created in the initial hard-scattering faces enough scattering in the medium and, therefore, the jet associated to this parton lose their identity, i. e. the jet is **absorbed** by the medium [31, 25, 32].

Jet quenching was one of the first and strongest indications of the creation of a QGP phase at RHIC, together with the elliptic flow discussed in Chapter 2 and the energy-loss of high-p_T particles introduced in Chapter 3.

4.3 Beauty production at RHIC

The correlation distribution in the near-side can also be used to estimate the relative contribution of beauty (and charm) to the total heavy-flavour decay electron yield, by looking at correlations between heavy-flavour decay electrons and hadrons. This technique is based on the fact that the shape of the correlation distribution in the near-side peak is strongly affected by the decay kinematics of the charm and beauty mesons and that, its width is larger for beauty decay electrons than for charm decay electrons. Therefore, the shape of the angular distribution from Monte Carlo simulations can be fitted to the measured correlation peak by varying the relative beauty contribution, through Equation 4.3, where B is also a free parameter accounting for the background due to non-correlated e-h pairs and $r_b = N(b \rightarrow e) / (N(b \rightarrow e) + N(c \rightarrow e))$.

$$C^{\text{Data}}_{\text{c,b} \rightarrow \text{e}}(\Delta\varphi) = r_b \, C^{\text{PYTHIA}}_{\text{b} \rightarrow \text{e}}(\Delta\varphi) + (1 - r_b) \, C^{\text{PYTHIA}}_{\text{c} \rightarrow \text{e}}(\Delta\varphi) + B \qquad (4.3)$$

In the top panel of Figure 4.2 the measured correlation distribution is presented along with that from PYTHIA simulations for electrons from charm and beauty hadron decays and the fit, for pp collisions at $\sqrt{s} = 200$ GeV [61]. The estimated relative production of electrons from beauty to the total heavy-flavour decay electrons is shown on the bottom panel of the same Figure along with the predictions from FONLL pQCD calculations [61].

This technique is used in the present work to estimate the beauty production at the LHC energies and, therefore more details of this type of analysis will be presented in Chapter 7.

4.4 Ridge structure in the correlation distribution

As aforementioned the structure of the angular distribution is sensitive to several properties of the system created in the collision, such as parton-medium interaction mechanisms, collective expansion, decay kinematics and so on. The property that dominates the angular
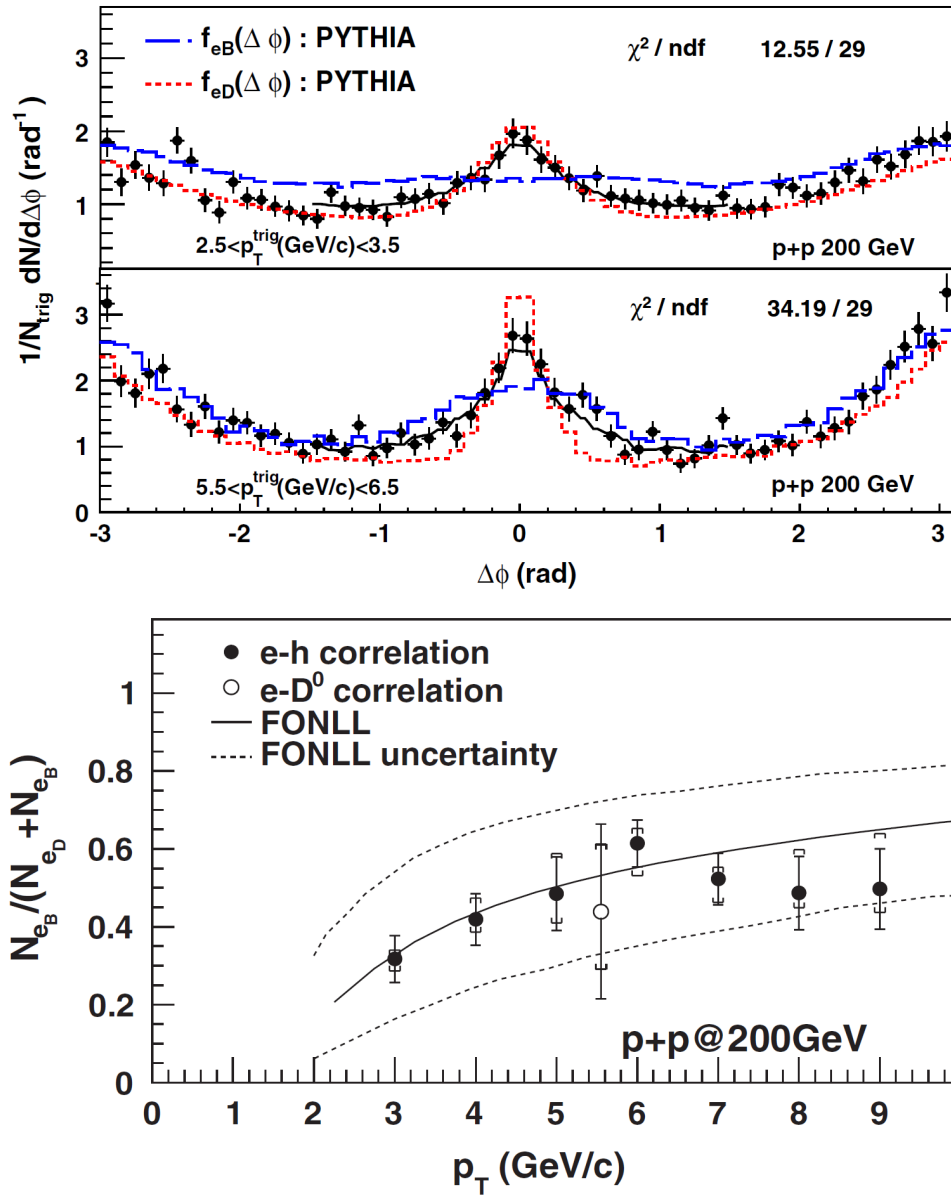
Figure 4.2: Top panel: Azimuthal correlation between heavy-flavour decay electrons and hadrons in pp collisions at $\sqrt{s_{NN}} = 200$ GeV, reported by the STAR Collaboration. The Figure shows also Monte Carlo templates for electrons from beauty and charm hadron decays and the fit performed using Equation 4.3. Bottom panel: Relative contribution of beauty hadron decays to the total heavy-flavour decay electron yield as a function of p_T, measured using the correlation technique. Figures from [61].

correlation distribution depends mainly on the kinematic region defined for the trigger and the associated particles. At low transverse momentum, collective phenomena, that are described by hydrodynamic model calculations are dominant, while for high-p_T particles jet correlations dominates the distribution structure, as argued in [60].

Particularly, if the particles that are analyzed participate in the collective expansion of the medium, the correlation function will present a modulation given by Equation 4.4 [60], where the modulation amplitude is given by the coefficients $V_{n\Delta}(p_T^t, p_T^a) = v_n^t(p_T) v_n^a(p_T)$,
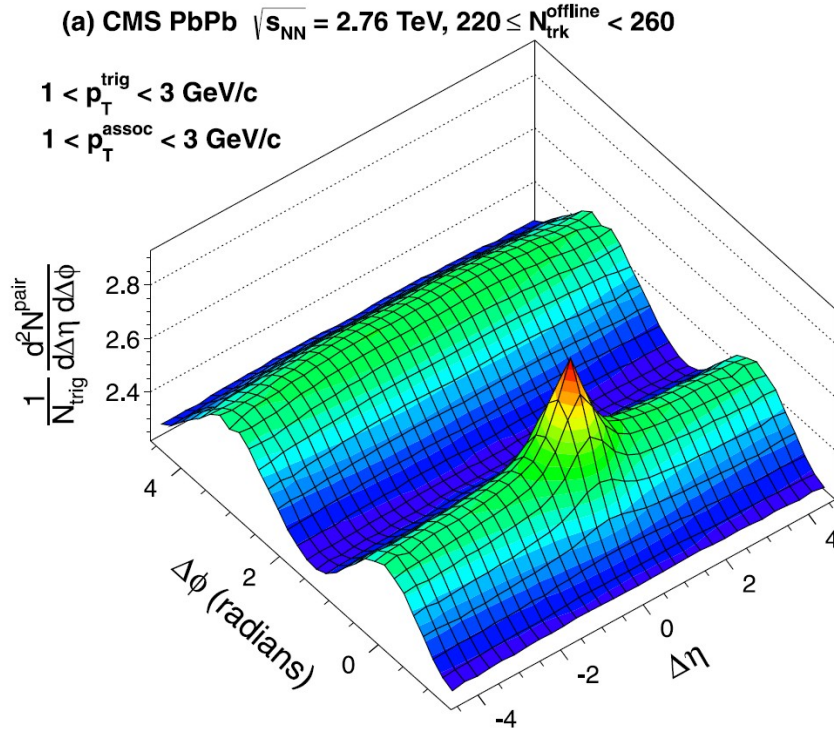
Figure 4.3: Angular correlation between two unidentified hadrons in Pb-Pb collisions at the LHC, reported by the CMS Collaboration. Figure from [62].

where ν_n is the n-th Fourier coefficient for the trigger and associated particles [60].

$$\frac{\mathrm{d}N_{\mathrm{pairs}}}{\mathrm{d}(\Delta\varphi)} = a_0 \left[1 + \sum_{n=1}^{\infty} 2V_{n\Delta}(p_{\mathrm{T}}^t, p_{\mathrm{T}}^a)\cos(n\Delta\varphi) \right] \tag{4.4}$$

Such a modulation leads to correlations of long-range in $\Delta\eta$, which appears in the 2-dimensional correlation plot as a ridge-like structure. In Figure 4.3 it is visible a double ridge structure in the two-particle correlation distribution measured in Pb-Pb collisions by the CMS Collaboration, reported in [62]. In the near-side the jet correlation peak appears on top of the ridge structure while on the away-side the two effects are mixed along the $\Delta\eta$ range.

4.5 Recent results from p-Pb collisions at the LHC

Remarkably, recent results from CMS and ALICE Collaborations has shown that such a ridge structure are present in the correlations function evaluated for high-multiplicity p-Pb collisions. The result from the CMS collaboration is shown in Figure 4.4 [62]. As discussed in the previous Chapters, pp and p-Pb analysis are used as reference/control experiment in order to disentangle initial-state effects of the Cold Nuclear Matter (such as saturation at small Bjorken-x) from those due to the presence of a deconfined QCD medium in the final state. Therefore, the result reported by the CMS Collaboration brought the doubt whether the measured positive Fourier coefficients are indeed due to the presence of a QGP phase
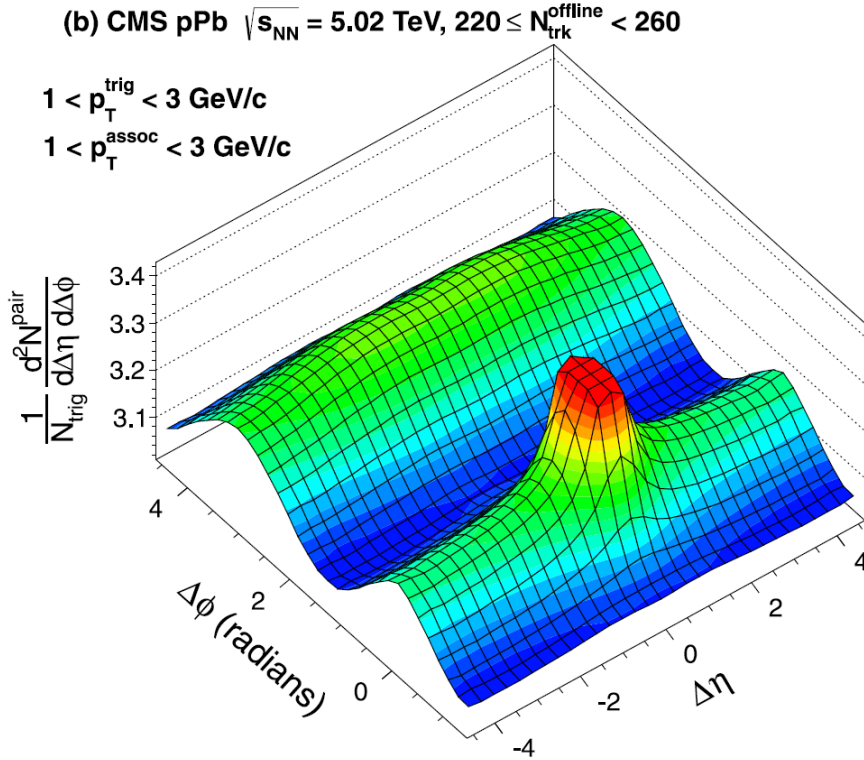
Figure 4.4: Angular correlation between two unidentified hadrons in p-Pb collisions at the LHC, reported by the CMS Collaboration. Figure from [62].

in the final state or due to modifications in the initial state. CMS also reported results that suggests correlations of long-range in pseudorapidity in pp collisions at the LHC energy [63].

A step forward in this analysis was given by the the ALICE Collaboration. ALICE proposed to disentangle the jet and ridge structures by subtracting the correlations distribution from high-multiplicity events by that evaluated in low-multiplicity. This is motivated by the fact that the correlation distribution evaluated in low-multiplicity p-Pb collisions is compatible with that from pp data. ALICE also measured the correlation distributions with identified particles. Figure 4.5 (left panel) shows the angular correlation between protons and unidentified particles after the subtraction and on the right panel the projection on $\Delta\varphi$ is displayed. The Fourier coefficients were evaluated by fitting Equation 4.4 to the measured ridge modulation in $\Delta\varphi$ [64, 65].

ALICE has done this analysis for identified particles and the evaluated Fourier coefficient, as a function of p_T is shown in Figure 4.6 [65]. The results show a mass dependence of the ν_n coefficients very similar to what has been found for Pb-Pb collisions [33, 34]. The measured ridge can be described by both hydrodynamical calculation models [66, 67, 68] that assume an extended medium in the final state and by Color Glass Condensate (CGC) model calculations [69], through which gluon saturation in the initial state is accounted for. A result from hydrodynamical models is shown in Figure 4.6 [66] and a prediction from CGC is illustrated in Figure 4.7 [69].
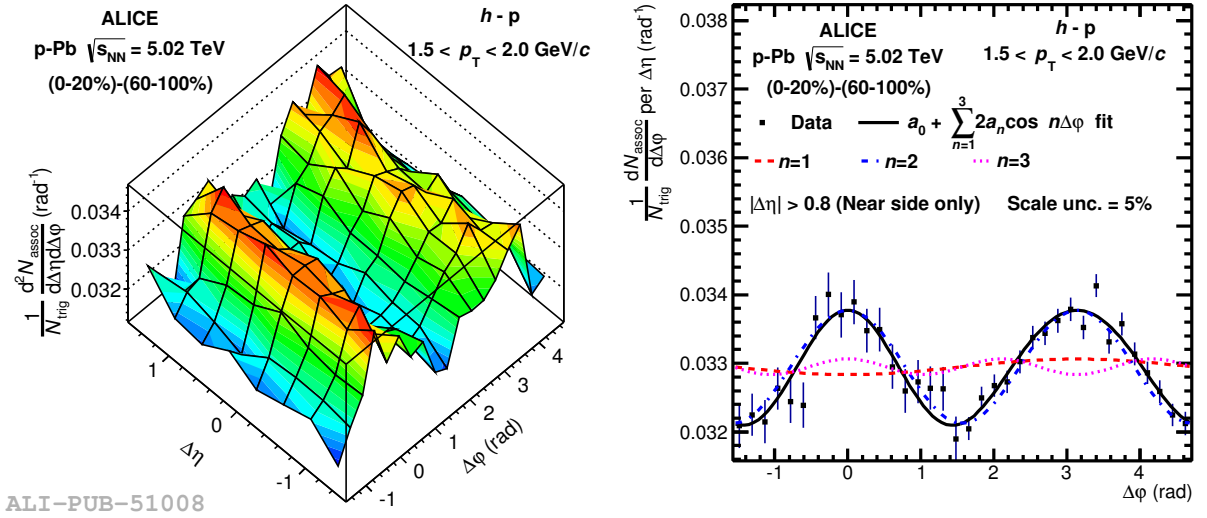
Figure 4.5: Correlations of long-range in $\Delta\eta$ for p-h angular distribution in p-Pb collisions at $\sqrt{s_{NN}} = 5.02$ TeV, measured with ALICE. Figure from [65].
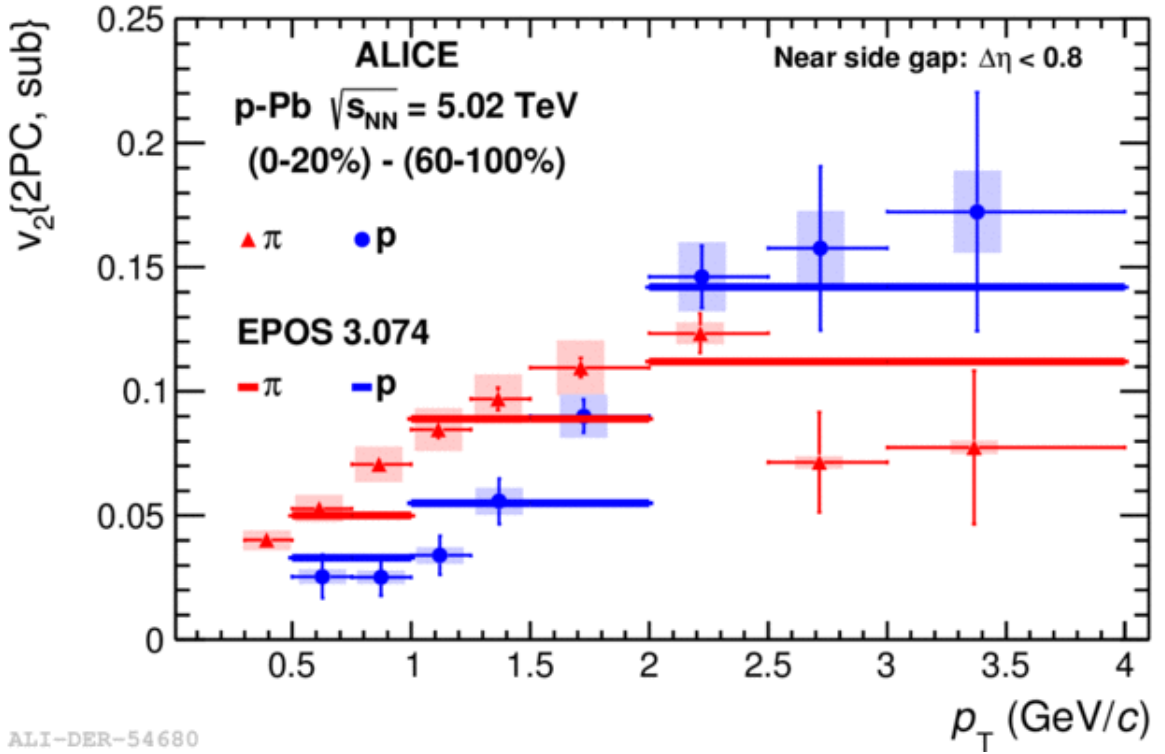
Figure 4.6: Comparison of the measured double-ridge structure in p-Pb collisions with hydrodynamical model calculations. Figure from [66].

Part of the present work is focused on the study of the two-particle correlation triggered by heavy-flavour decay electrons in p-Pb collisions. This analysis can provide further constraints for the models that describe the ridge structure for light-flavour correlations. This is the subject of Chapter 6, where the evaluation of the correlation distribution and corrections are detailed treated.
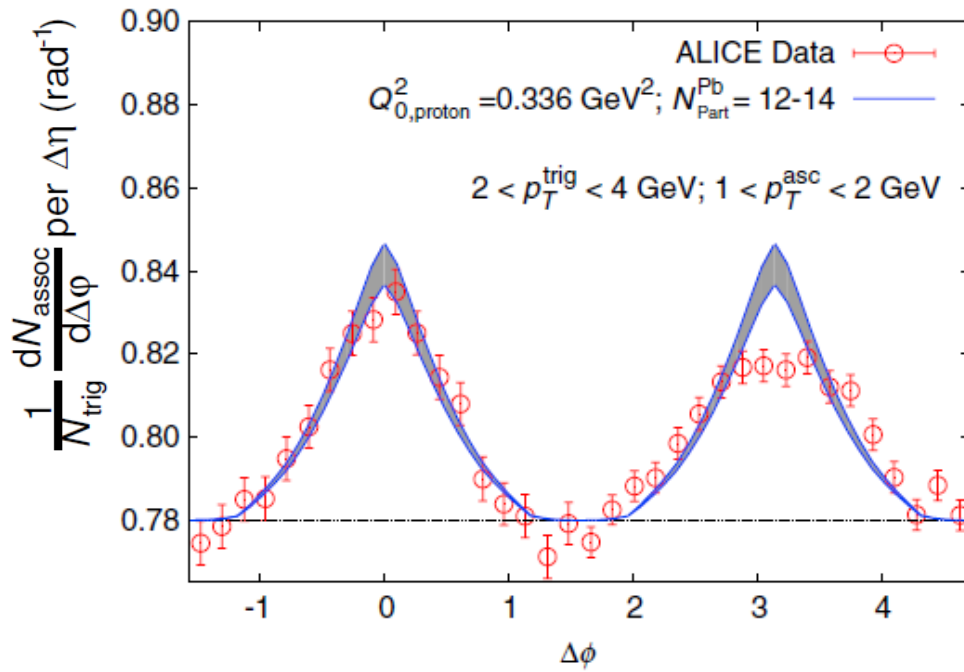
Figure 4.7: Comparison between the double-ridge reported by ALICE with predictions from color glass condensate model calculation. Figure from [69].

Chapter 5

Experimental setup and analysis framework

5.1   The CERN Large Hadron Collider

The Large Hadron Collider (LHC) is the largest hadron accelerator in the world, built near the French-Swiss border (see Figure 5.1). The LHC consist of two superconducting rings of ≈ 27 km ($R \approx 4.3$ km) through which two particle beams travel in opposite directions and collide at four specific points where the experiments are built [70]. The LHC provides pp and heavy-ion collisions at center of mass energy at the TeV scale. Table 5.1 shows what are the currently LHC available data. When reach its best performance, LHC should provide pp, p-Pb and Pb-Pb collisions at $\sqrt{s_{NN}} = 14$, 8.8 and 5.5 TeV, respectively.

Table 5.1: LHC data currently available.

Collision system	$\sqrt{s_{NN}}$ (TeV)	Year
pp	0.9	2009
pp	7	2010
Pb-Pb	2.76	2010/11
pp	2.76	2011
pp	8	2012/13
p-Pb	5.023	2012/13

The LHC is attached to a chain of accelerators at the CERN accelerator complex which provides and pre-accelerate proton and lead beams for the LHC. The complex of accelerators at CERN is schematically illustrated in Figure 5.2 [73, 74]. As an example, protons are first accelerated by the Linear Accelerator (Linac) 2, which provides proton beams at the energy of 50 MeV. After that the beam goes to the Proton Synchrotron Booster (PSB), to the Proton Synchrotron (PS) and finally to the SPS reaching the energy of 450 GeV at this last step, when the beam is finally transfered to the LHC, generating a clockwise and a anticlockwise beams, which cross each other at the experimental points aforementioned, where the

four experimental setups are built: ALICE, ATLAS, CMS and the LHCb [70].
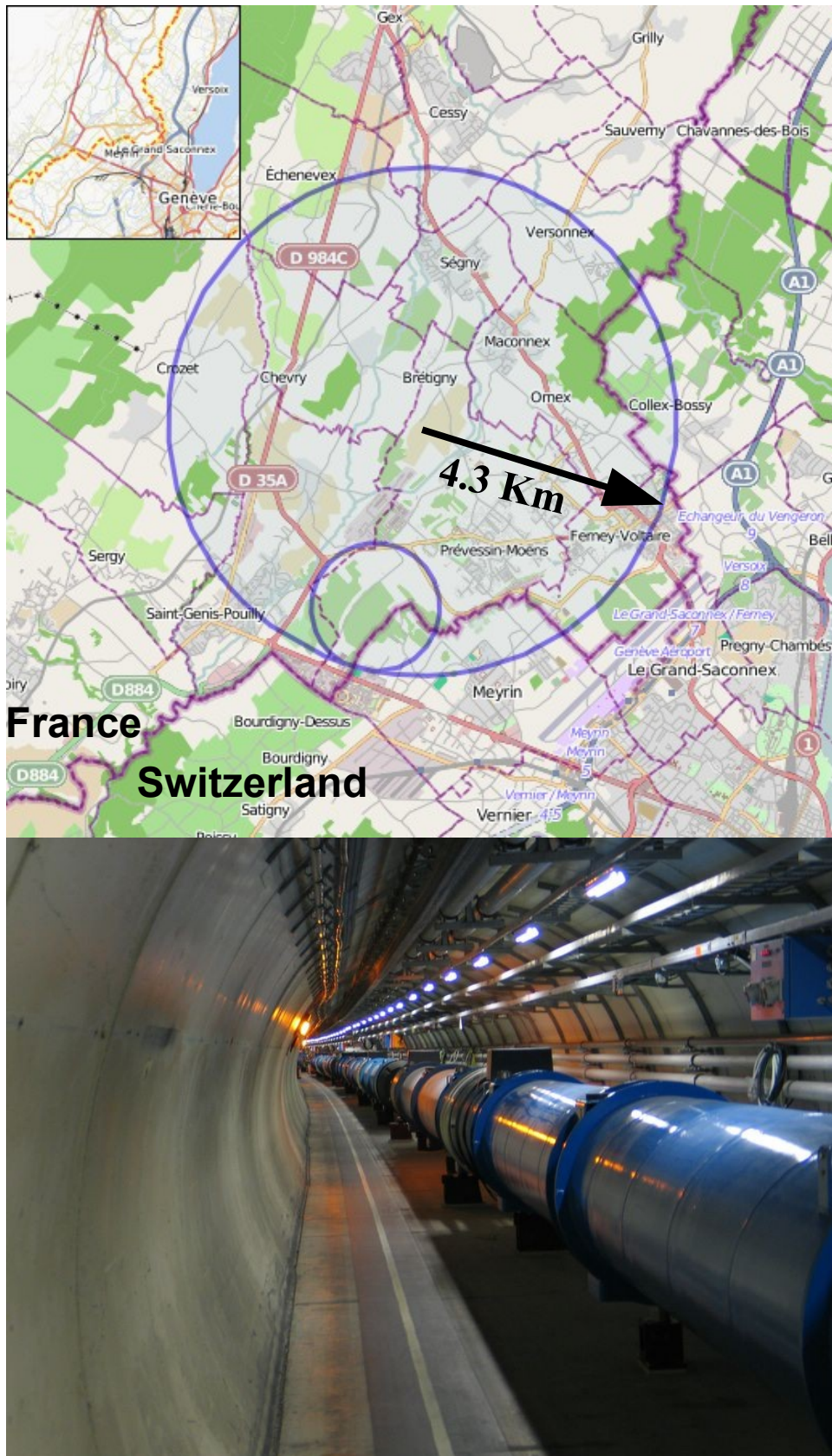
Figure 5.1: The CERN Large Hadron Collider. Figure from [71, 72].
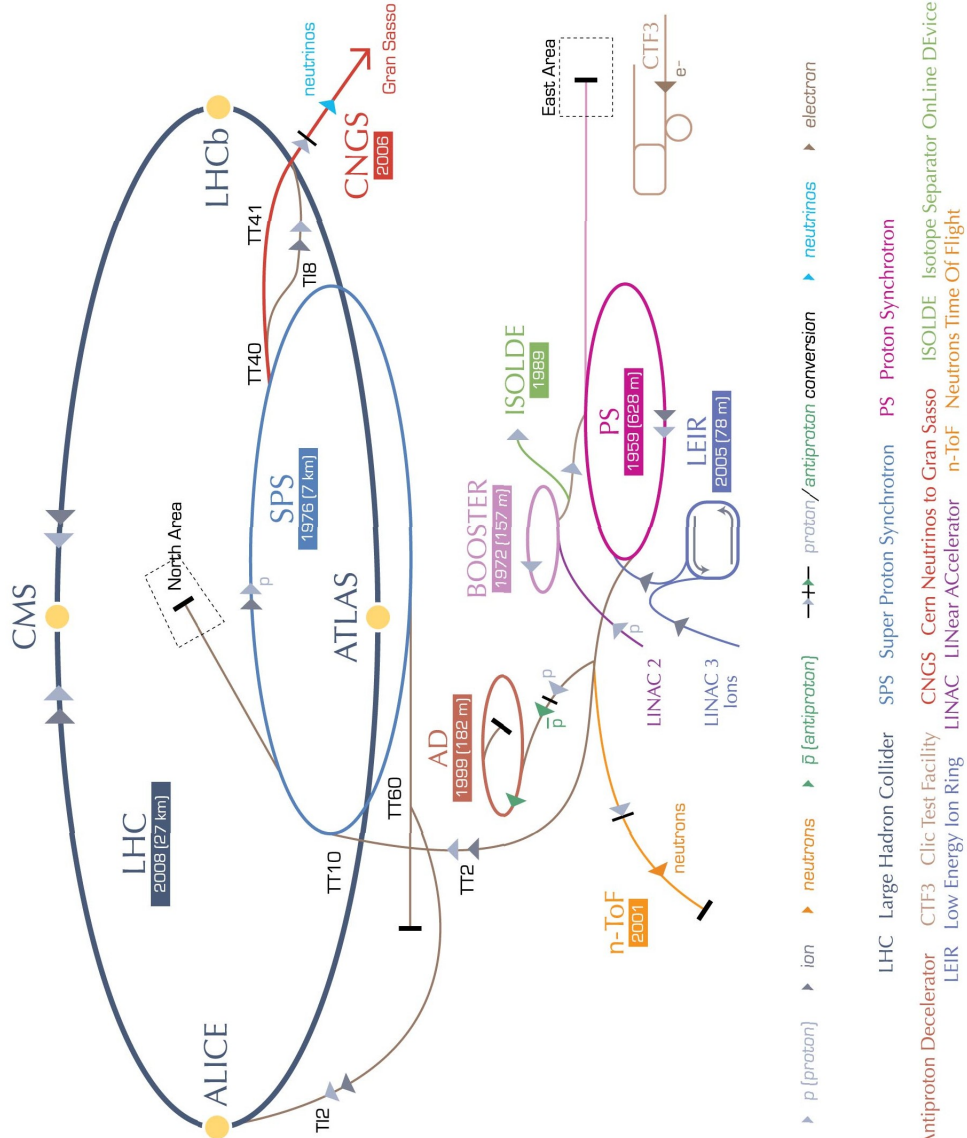
Figure 5.2: The CERN accelerator complex. Figure from [73] (see also [74]).

5.2 The ALICE experiment
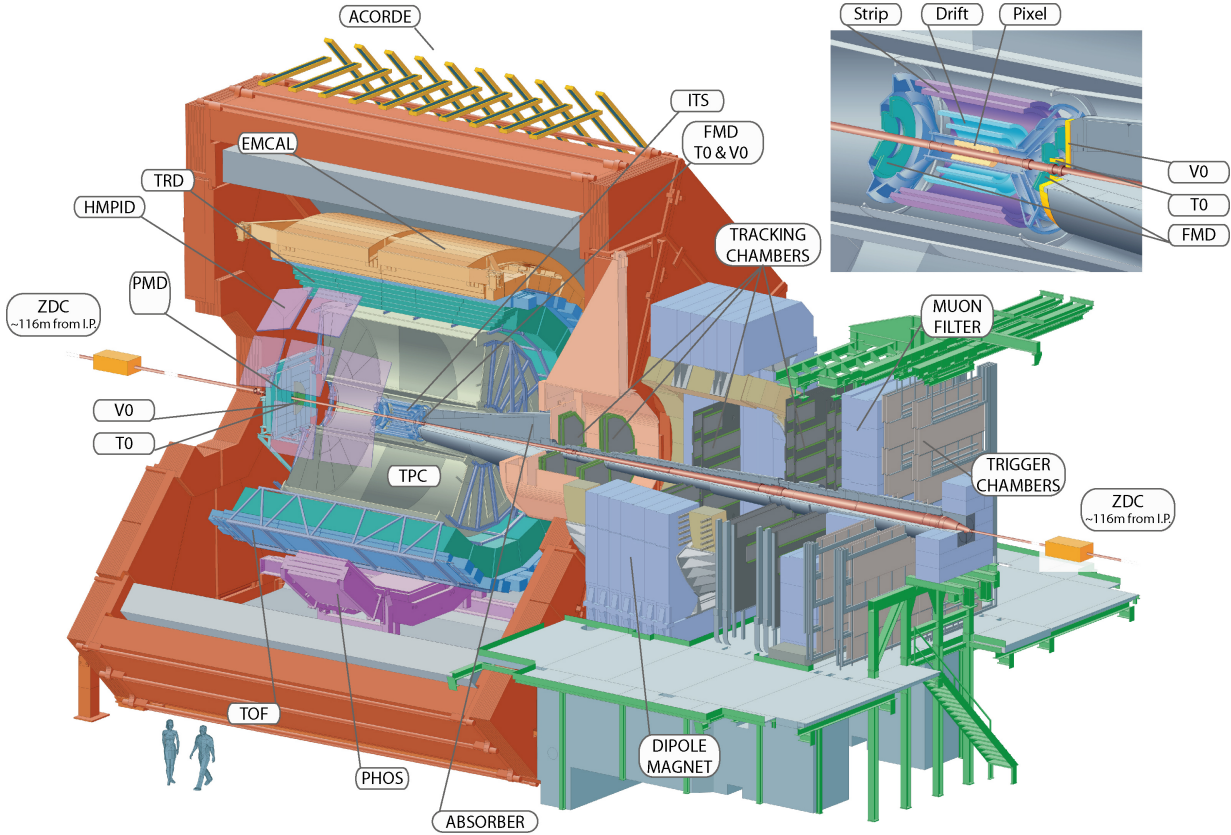
Figure 5.3: Layout of the ALICE experiment. Figure from [75].

The data analyzed in the present work were collected with ALICE (A Large Ion Collider Experiment), which is a detector setup built mainly to the study Pb-Pb collisions at the LHC [75, 76, 77]. In ALICE it is possible to reconstruct three-dimensional tracks and the interaction vertex. From the reconstructed track several properties of the measured particles can be accessed, e. g. the particle's momentum components (p_T, p_z), their azimuthal (φ) and polar angle (θ), the impact parameter relative to the collisions vertex (i. e. the displacement relative to the reaction point d_0), the distance of closest approach (DCA) to another track and so on.

The detector setup is illustrated in Figure 5.3 [75]. ALICE is divided in two parts, a central barrel covering the mid-rapidity region, defined by $|\eta| < 0.7 - 1.0$, and a muon spectrometer in the forward region ($-4.0 < \eta < -2.4$). From the innermost part of ALICE (close to the reaction point) to the outer region of the detector setup, ALICE central barrel is composed by the following subsystems: an Inner Tracking System (ITS), used for vertex and track reconstruction; a Time Projection Chamber (TPC) for tracking and particle identification; also for particle identification there are a Transition Radiation Detector (TRD), a Time Of Flight (TOF) and a High Momentum Particle Identification Detector (HMPID); two calorimeters,

the PHOton Spectrometer (PHOS) and the ElectroMagnetic Calorimeter (EMCal) are used for measurements of electrons and photons, as well as for jet reconstruction [75, 76, 77].

With the muon spectrometer J/ψ, ψ', Υ, Υ' and Υ'' are reconstructed through measurements of muons from their semi-leptonic decays as explained in [75, 76, 77].

ALICE has a cylindrical geometry with the symmetry axis coinciding with the LHC beam pipe, as illustrated in Figure 5.3 [75]. Because of this, the particle's spacial coordinates are given in terms of their azimuthal angle φ and pseudorapidity η. The latter is defined in Equation 5.1, as a function of the polar angle θ, i. e. the angle with respect to the beam axis.

$$\eta = -\ln\left(\tan\frac{\theta}{2}\right) \tag{5.1}$$

In this work, the main subsystems used were the ITS, TPC, TOF and the VZERO detectors (VZEROA and VZEROC). For these sub-detectors a few more details are provided in Subsections 5.2.1 to 5.2.4. Some of the experimental techniques, that are relevant for the present work are discussed in Subsections 5.2.5 to 5.2.7 and, the off-line framework used for data analysis is introduced in Section 5.3. However, in these Subsections only a brief description is provided for these systems. For further detail one should see [75, 76, 77].

5.2.1 Inner Tracking System (ITS)
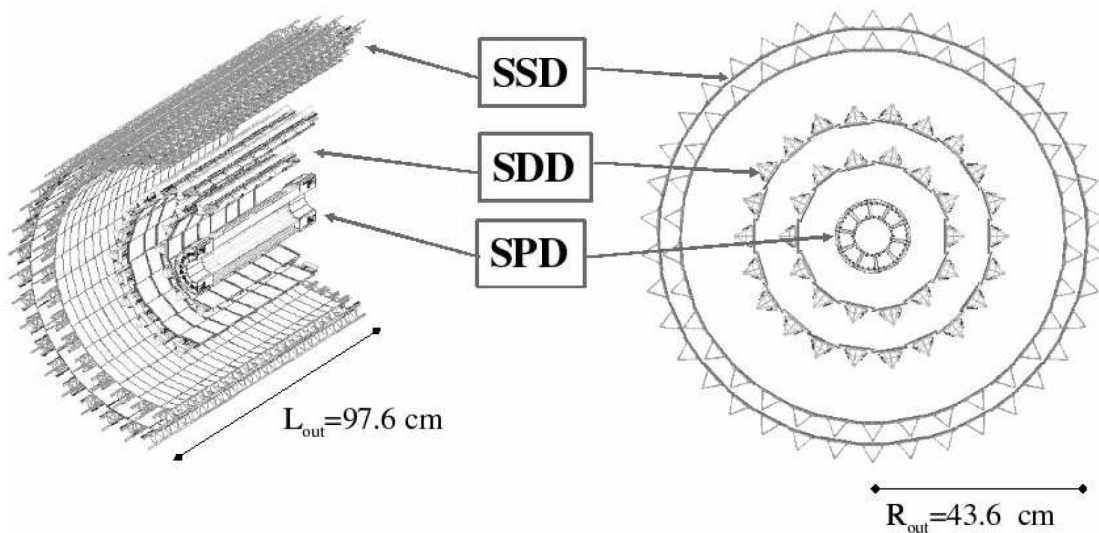
Figure 5.4: The ALICE Inner Tracking System (ITS). Figure from [75].

The Inner Tracking System (ITS) is the subsystem of the ALICE experiment closest to the interaction point, i. e. it is in the innermost part of ALICE. The detector is composed, from the inner to the outer part, by a Silicon Pixel Detector (SPD), a Silicon Drift Detector (SDD)

and the Silicon Stripped Detector (SSD), each part consisting of two cylindrical layers, covering the full azimuthal region.

The main aim of the ITS is primary vertex identification, which is performed with relatively high precision, of the order of 100μm. It also improves track reconstruction and its extrapolation to the primary vertex. This is of particular importance for analysis which exploit the displacement of tracks to the primary vertex, such as those related to the beauty and charm identification [79, 80]. Furthermore, ITS can be used for particle identification. It provides kaon/proton/pion separation at low transverse momentum, and it is used for triggers since it is a fast detector [75]. The ITS system is illustrated in Figure 5.4 [75].

5.2.2 Time Projection Chamber (TPC)
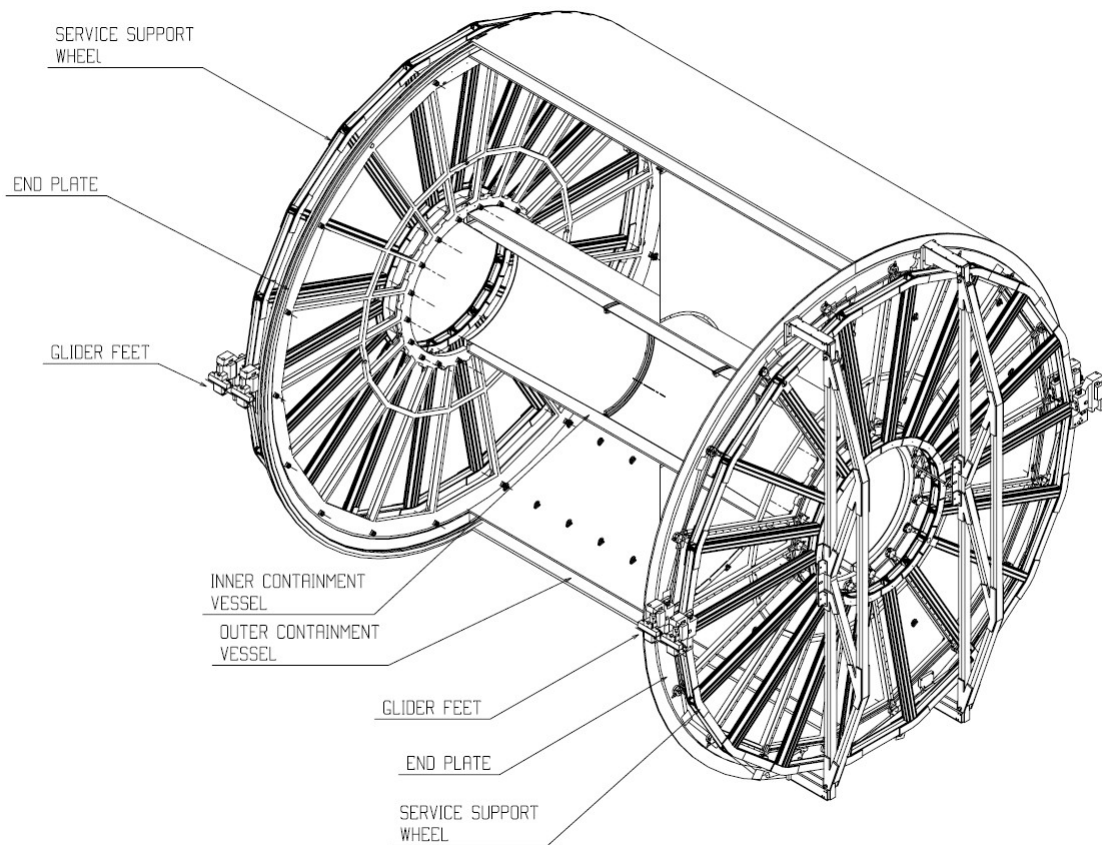
Figure 5.5: The ALICE Time Projection Chamber. Figure from [75].

The Time Projection Chamber (TPC) is also a cylindrical detector covering the full azimuth and the mid-rapidity region. The detector volume is filled with a gas mixture of Ar and CO2 and it has an electrical field in the direction parallel to the beam axis. The main tasks of the TPC is track reconstruction and particle species identification.

When a particle traverse the TPC volume it ionizes the gas and, the produced ions (and electrons) drifts to the detector walls, where the produced charge is collected. The position

where the charge is collected and the drift time is used to evaluate the position of the particle. Each information of this type is called a cluster left by the particle in the TPC. Typically a particle produces $60 - 160$ clusters in the TPC. These cluster, combined to those measured by ITS and TOF, are used find the particle's track.

The track fit is performed through the Kalman-Filter (KF) algorithm, through which the several properties of the particle are evaluated, such as its momentum $p = (p_T, p_z)$, azimuthal angle φ, pseudorapidity η and so on. In fact, these variables are free parameters of the fit implemented in the KF algorithm [75].

The energy lost by the particle in the detector material (more specifically the per-length energy-loss in the TPC gas dE/dx) depends on its mass and momentum as indicated in the Bethe-Bloch formula shown in Equation 5.2 and illustrated in Figure 5.6, where C_i are constants depending on specific detector properties. Results for the ALICE experiment and, in particular, for the case of electron identification will be discussed in Subsection 5.2.5.

$$\left\langle \frac{dE}{dx} \right\rangle = \frac{C_1}{\beta} \left\{ \log(C_2 \beta^2 \gamma^2) - \beta^2 + C_3 \right\} \tag{5.2}$$
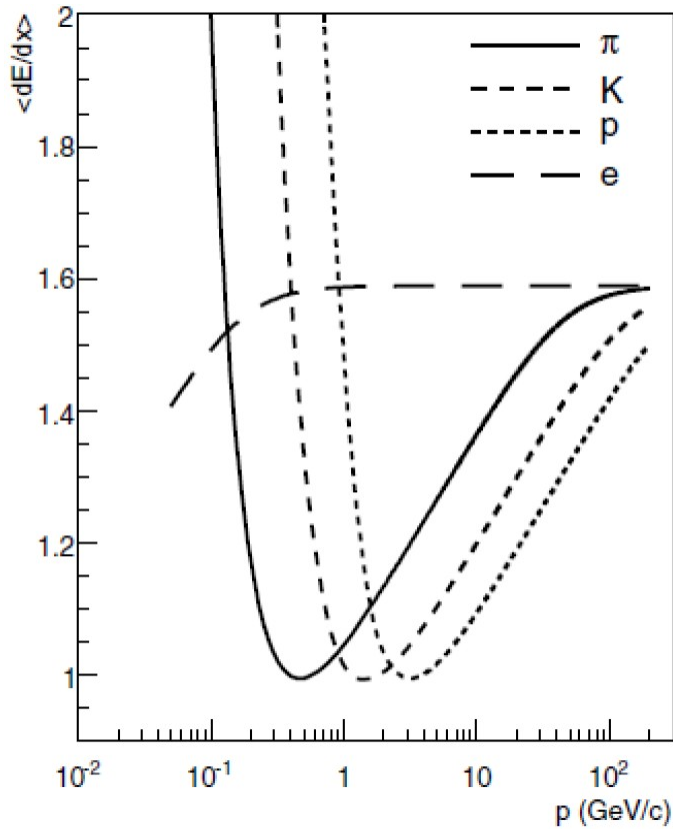
Figure 5.6: Average energy-loss (in arb. units) as a function of p_T for several particle species (Bethe-Bloch formula). Figure from [76, 77].

5.2.3　Time Of Flight (TOF)

The geometry of the TOF detector is very similar to the detectors discussed previously. Its elementary unity is a MRPC (Multi-gap Resistive-Plate Chamber) strip, which is subdivided in 96 readout pads and installed inside the gas volume, forming a module. A group of 5 modules composes a super-module covering the whole detector reach in pseudorapidity. This arrangement is illustrated in Figure 5.7 [75]. In total, TOF is composed by $\approx 10^5$ channels and, therefore the detector is well-suited for studies of high-multiplicity events, which is the case of heavy-ion collisions at the LHC energies.

The main aim of TOF is particle identification at low-p_T ($p_T < 2.5$ GeV). It provides a good separation of π/electrons from kaons and protons. Furthermore, the TOF information is combined with those from the TPC and ITS to improve track reconstruction.
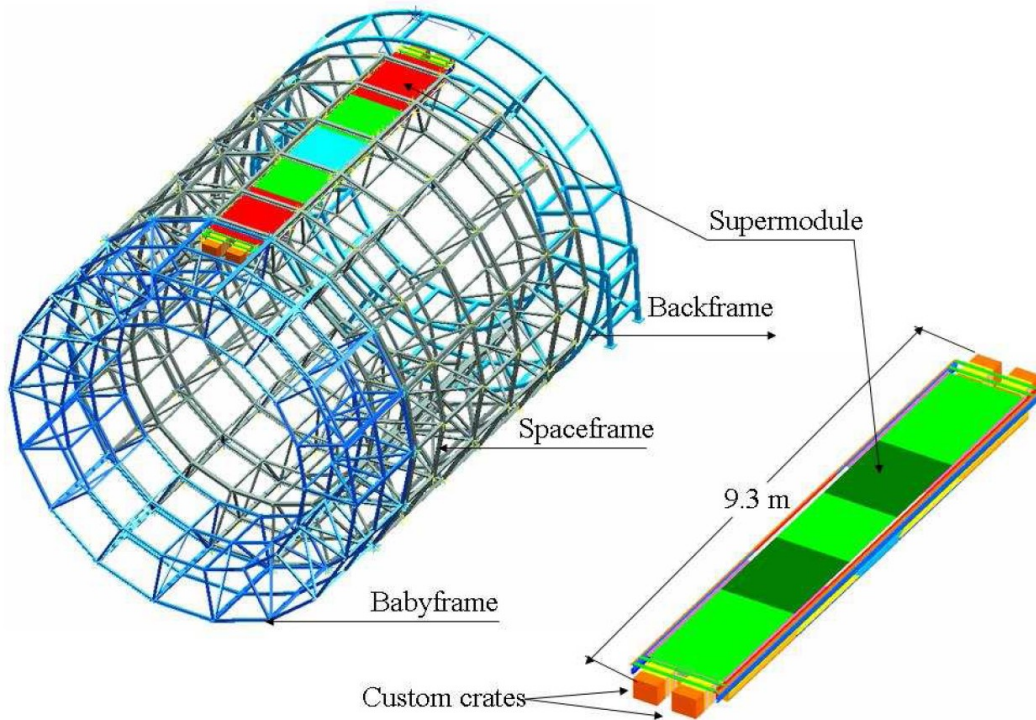
Figure 5.7: The ALICE Time Of Flight (TOF) detector. Figure from [75].

5.2.4　VZERO

The VZERO detector is composed by two scintillator counters placed on both sides (forward and backward rapidity regions) of the ALICE experiment, called V0A and V0C. These two detectors are shown in the picture of Figure 5.8 [75]. VZERO is used for event selection, i. e. it is used as trigger of several types: Minimum Bias (MB), Multiplicity (MT), Semi Central (CT1)
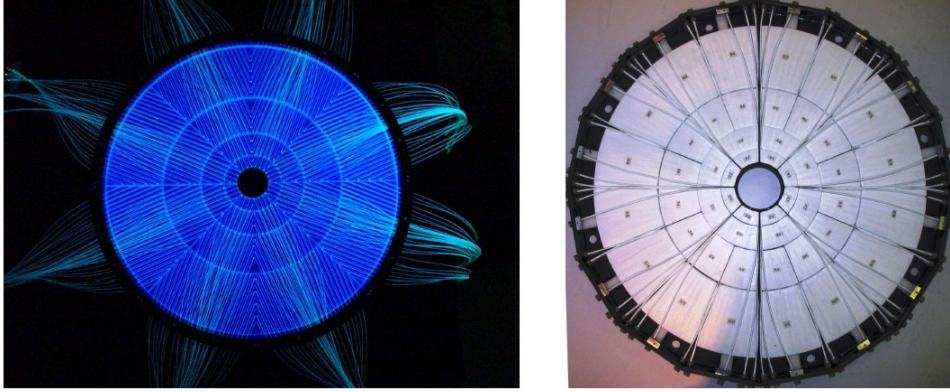
Figure 5.8: The ALICE VZERO detectors. Figure from [75].

and Central (CT2) [75]. It is also used for multiplicity (or centrality) selection. An example will be given in Subsection 5.2.7.

5.2.5 Particle identification

As aforementioned, ALICE has several techniques for particle identification (PID), from low to high transverse momentum. In Figure 5.9 it is illustrated how the PID can be performed with the TOF and the TPC detectors. In the top panel of Figure 5.9 the per-length energy-loss (dE/dx) in the TPC gas is shown as a function of momentum p for reconstructed tracks from p-Pb collisions. The dependence of dE/dx with the particle mass, which is visible in this Figure, is exploited to perform a separation between species. In the bottom panel of Figure 5.9 the Time Of Flight technique is illustrated.

Figure 5.10 shows how electron identification is performed using the TOF and TPC informations. In this Figure the so-called number of sigmas $N\sigma$, calculated assuming the electron mass, is displayed as a function of momentum p. The $N\sigma$, which is defined in Equation 5.3, is the measured dE/dx (TOF time) subtracted by the expected energy-loss (time of flight) assuming the electron mass, in numbers of standard deviation σ. In the bottom panel of Figure 5.10, the electron number of sigmas in the TPC, as a function of momentum, is shown for particles satisfying $-3 < N\sigma_{\text{TOF}} < 3$.

$$N\sigma_{\text{TPC}} = \frac{dE/dx - \langle dE/dx \rangle_{\text{e}}}{\sigma_{dE/dx}} \qquad ; \qquad N\sigma_{\text{TOF}} = \frac{\text{TOF}_{\text{time}} - \langle \text{TOF}_{\text{time}} \rangle_{\text{e}}}{\sigma_{\text{time}}} \qquad (5.3)$$

Using TOF and TPC, electron identification has a good performance in the range $1 < p_{\text{T}} < 6$ GeV/c. In the worst case, the hadron contamination in the electron sample reaches $\approx 7 - 10\%$ at the highest transverse momentum [79]. For higher p_{T} values the hadron contamination is larger using only these two detectors, but the identification is highly improved adding the EMCal E/p information [79].
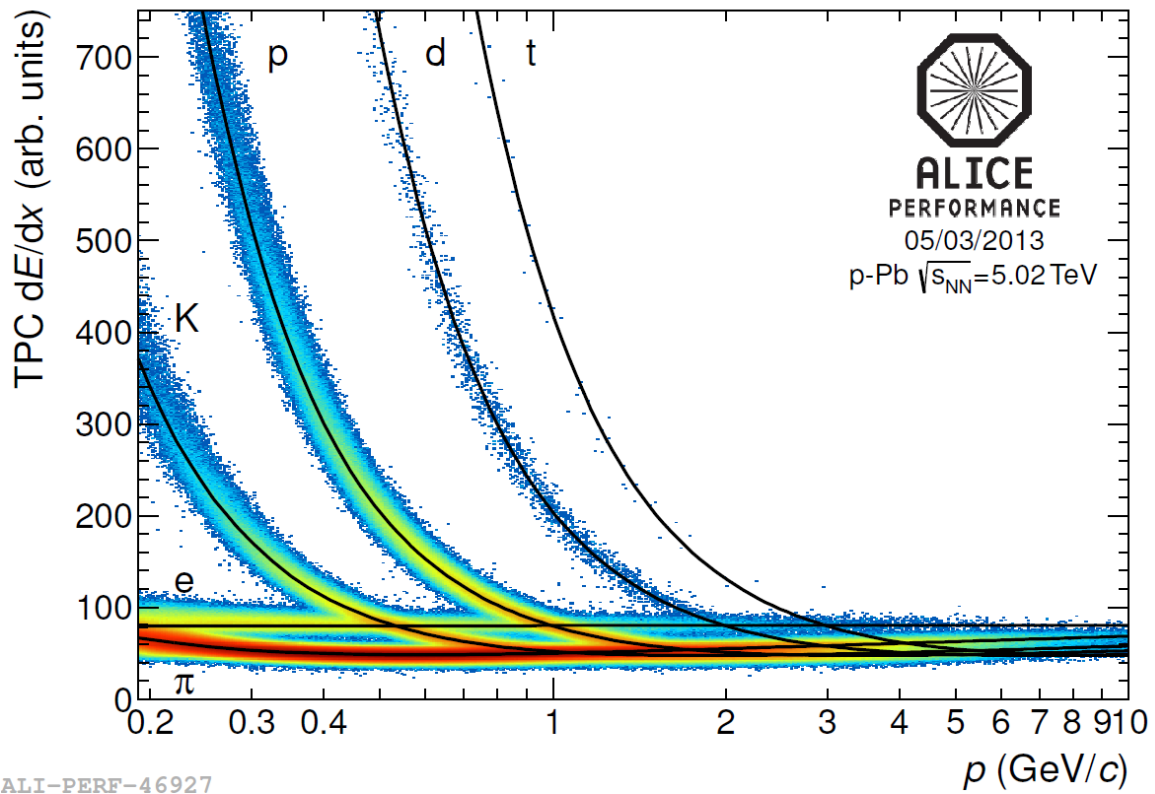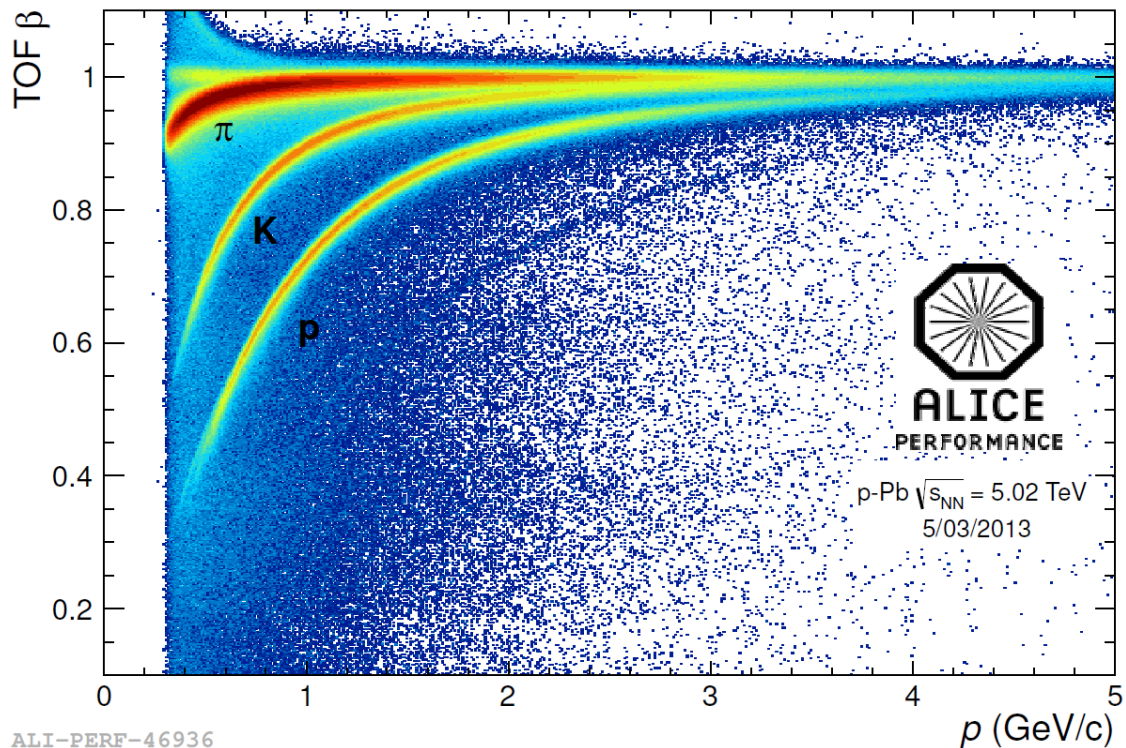
Figure 5.9: Particle identification in ALICE via measurements of the per-length energy-loss in the TPC (top panel) and the particle's time of flight information provided by TOF (bottom panel). Figures from [79, 85].

ALI-PERF-46994

ALI-PERF-46989
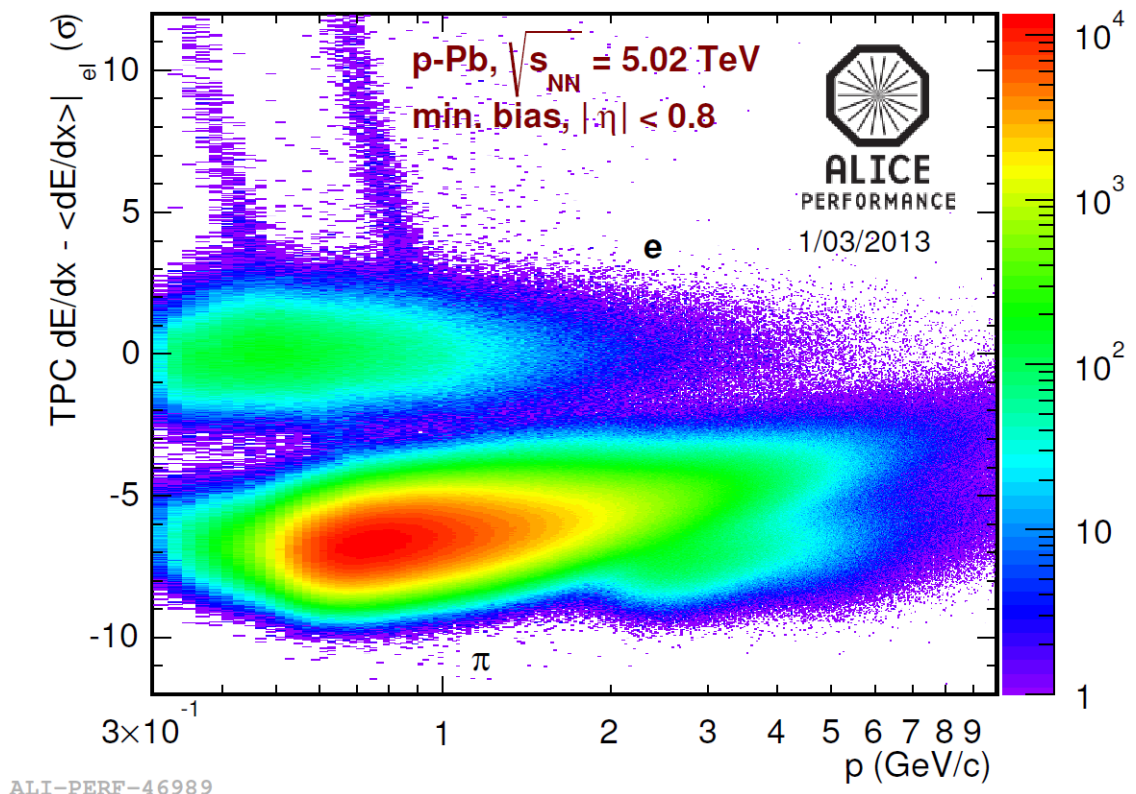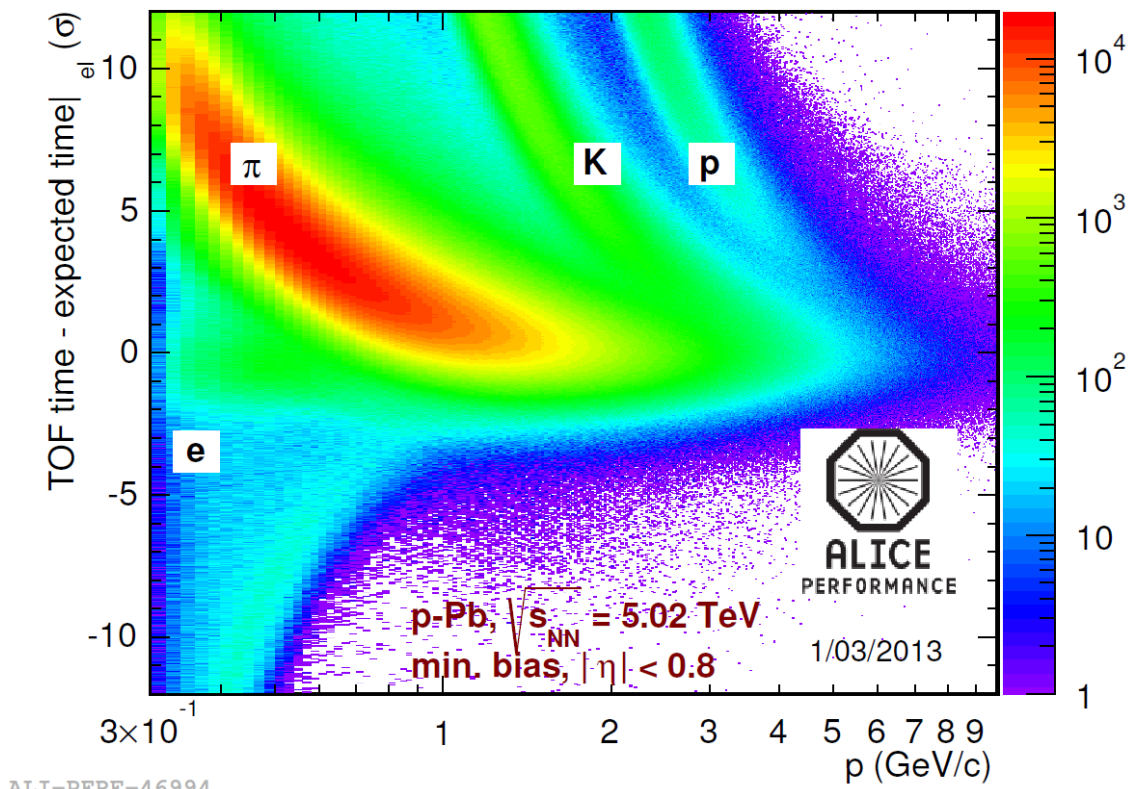
Figure 5.10: Electron identification in ALICE using the TPC and TOF combined information. Figures from [59].

5.2.6 The Minimum Bias (MB) trigger

The event record is triggered depending on a set of requirements, pre-defined accordingly on which are the phenomena of interest. In the simplest case, these requirements are chosen in order to ensure that a collisions in fact occurred, but as aforementioned additional stronger constraints can be set up to enhance a given physical process. The Minimum Bias trigger is usually a set of constraints ensuring that a collisions occurred without cause significant bias in the underlying physics.

In ALICE, Minimum Bias (MB) collisions are triggered using the VZERO detectors, located in the forward ($2.8 < \eta < 5.1$) and backward ($-3.7 < \eta < -1.7$) regions, and by the Silicon Pixel Detector (SPD), the innermost part of the Inner Tracking System (ITS) and covers the middle rapidity region, $\eta < 2.0$ and $\eta < 1.4$ for the inner and outer layer, respectively. The MB trigger requires at least one hit in either of the VZERO detectors or in the SPD, in coincidence with the presence of a LHC bunch crossing [51, 80].

5.2.7 Multiplicity class selection
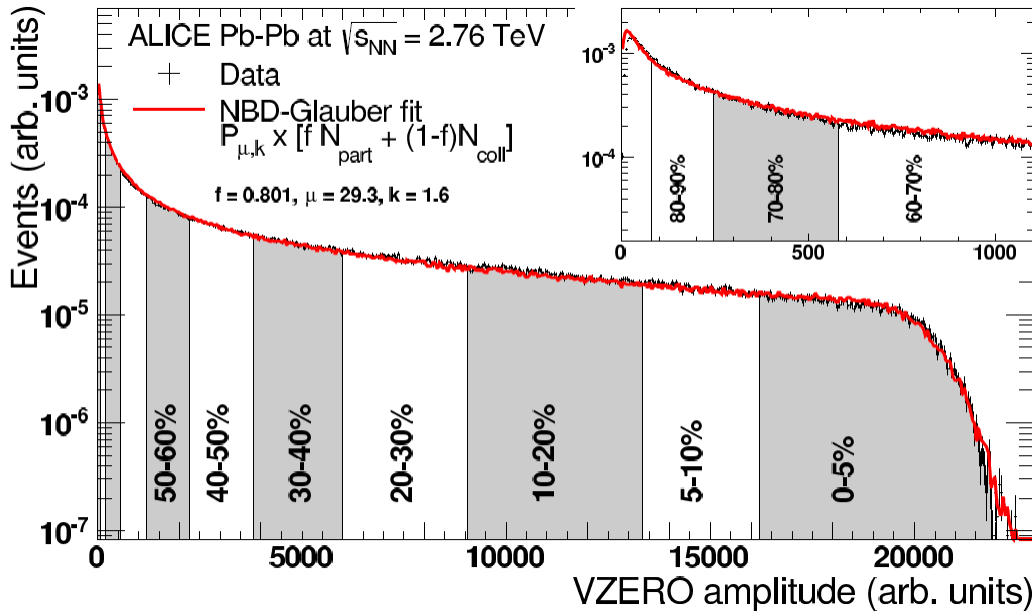
Figure 5.11: **Distribution of the event multiplicity estimated with the ALICE VZERO detector in Pb-Pb collisions at $\sqrt{s_{\mathrm{NN}}} = 2.76$ TeV. Figure from [78].**

There are few techniques to define multiplicity classes in heavy-ion (and also in pp) collisions with ALICE. VZERO can be used for this purpose as illustrated in Figure 5.11 (see [78]).

Starting from the measured multiplicity distribution, classes of multiplicity is defined in a way such that the selected subsample represent a slice $X - Y\%$ of the highest multiplicity events in the sample as represented in Figure 5.11 for $0 - 5\%$, $5 - 10\%$ and so on.

The event multiplicity can be parametrized (at least in Pb-Pb collisions), as a function of the impact parameter, on which the event multiplicity represents a given centrality class of the collision. This parametrization is done through the Glauber model [37]. As an example, a multiplicity class defined as $0 - 5\%$ indicates the 5% most central collisions or, equivalently, the 5% events with smallest impact parameter. In the same way, moderate and large percentage values indicate semi-central and peripheral collisions.

5.3   The ALIROOT framework
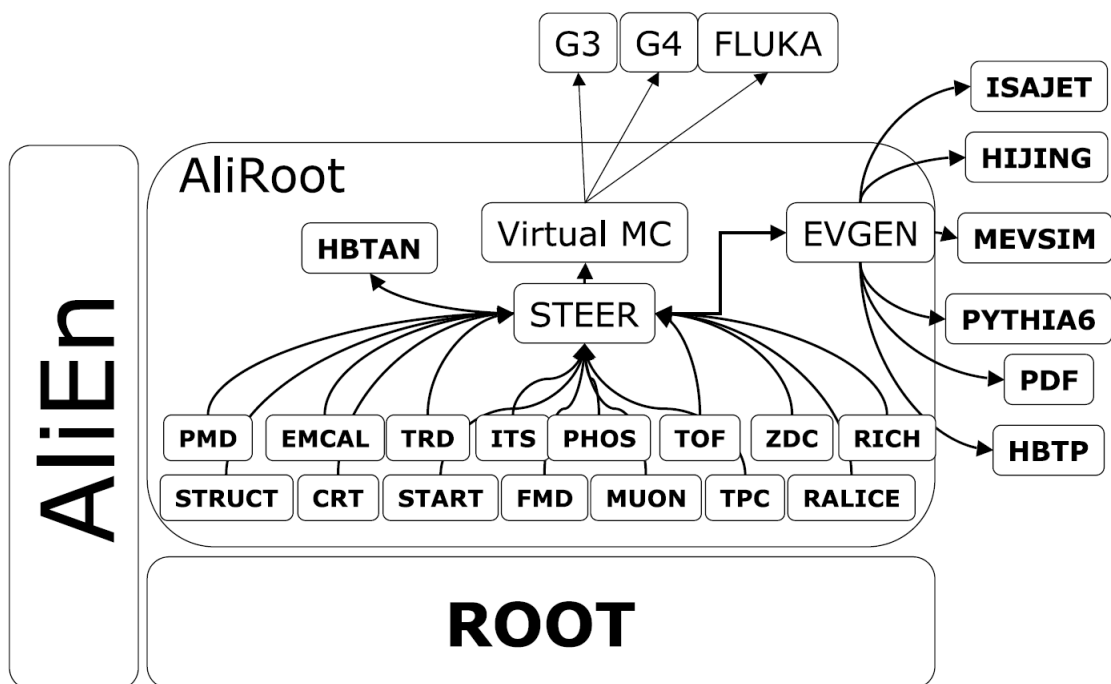
Figure 5.12: Illustration of how the ALICE analysis software (ALIROOT) is organized. Figure from [75].

The ALICE analysis software, called ALIROOT, is illustrated in Figure 5.12 [75]. ALIROOT is based on ROOT [81], a software written in $c++$ provided with several analysis tools, such as statistical packages. It has also an interface to access the grid computing (the alien) where data and Monte Carlo samples are stored.

ALIROOT provides tools for several type of tasks: detector calibration, simulations, event reconstruction, treatment of raw data and data analysis of physic purposes [75].

Furthermore, an interface for Monte Carlo event generators (e. g. PYTHIA [48, 49] and HIJING [82]) is provided by the software and the detector response can be simulated through GEANT [83] and FLUKA [84] programs. As an example, Figure 5.13 shows the geometry of the ALICE detector in an AliRoot simulation [75].

This tool is crucial to properly compare real data with Monte Carlo simulations, since in a simulations with stand-alone event generator effects due to detector resolution and efficiencies are not accounted for. Furthermore, in several analysis these effects has to be quantified in, for instance, efficiencies factors or detector non-homogeneities and, these correction factors can be calculated through the MC+GEANT combination implemented in ALIROOT. This is particularly exploited in the present work and details are provided in the next Chapter.
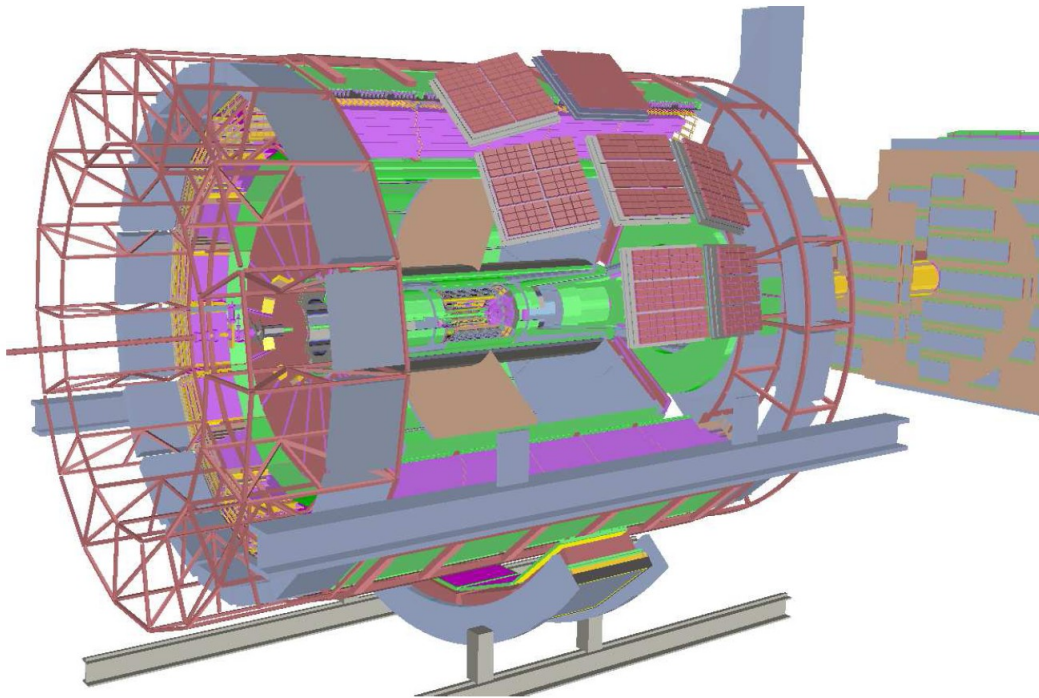
Figure 5.13: Simulation of the ALICE as implemented in ALIROOT. Figure from [75].

Chapter 6

Analysis 1: Angular correlation distribution

6.1 Analysis steps and general strategy

In the analysis described in this Chapter, the angular correlation distribution between heavy-flavour decay electrons and charged unidentified particles is evaluated in p-Pb ($\sqrt{s_{NN}} = 5.02$ TeV) and pp ($\sqrt{s} = 7$ TeV) collisions. For the case of p-Pb collisions, the correlation function was measured as a function of the event multiplicity.

The steps followed in this work are:

1. Select the events to be analyzed;

2. Define multiplicity classes and separate the selected events accordingly (for p-Pb collisions);

3. Select the tracks to be analyzed;

4. Perform the electron identification (using, in this work, TPC and TOF);

5. Identify and subtract electrons from non-heavy-flavour sources, i. e. those from gamma conversion and light meson Dalitz decays, using the invariant mass technique;

6. Calculate the correlation distribution;

7. Correct the correlation distribution accordingly:

   - Correct the distribution by the identified electron background;

   - Correct the distribution by the remaining hadron contamination in the electron sample;

   - Correct the distribution by the limited detector acceptance and non-homogeneities, using the event mixing technique;

- Correct the distribution by the tracking efficiency, fake tracks and secondary decays;

8. Evaluate the associated per-trigger particle yield as a function of multiplicity in p-Pb and for pp collision.

6.2   Data sample, Event and Track Selection

The data analyzed in this part of the work was collected in 2010 (pp, $\sqrt{s}$ = 7 TeV) and in 2013 (p-Pb, $\sqrt{s_{\mathrm{NN}}}$ = 5.02 TeV). Detailed information on the real data and Monte Carlo samples used is provided in Appendix A. In the following, the requirements for event and track selection are described.

6.2.1   Event selection

The events analyzed are required to satisfy the following criteria:

- Pass the *Minimum Bias* trigger selection.

- The primary vertex (i. e. the position of the nuclear reaction) should happens in the range $-10 < z < 10$ cm, relative to the global zero reference, the ALICE nominal center. The z coordinate refers to the direction parallel to the beam pipe.

- The number of reconstructed tracks in the event should be at least two, before consider track selection cuts.

As aforementioned for p-Pb collisions, the measured correlation distribution were studied as a function of the event multiplicity. To allow this, the selected event sample were separated in three sub-samples of three multiplicity classes: **high-multiplicity** events, that are the $0-20\%$ events with higher particle multiplicity, **intermediary-multiplicity** $(20-60\%)$ and **low-multiplicity** collisions $(60-100\%)$.

The multiplicity was defined using the signal measured with the V0A detector. The multiplicity distribution, from the V0A information is shown in Figure 6.1.

6.2.2   Track selection

After event and multiplicity selection, not all the reconstructed tracks are used in the analysis but only those satisfying the set of cuts listed below. These cuts are required in order to ensure a minimum tracking quality, reduce the number of particles from secondary decays, such as photon conversion in the detector material, and reject fake tracks. These requirements are:
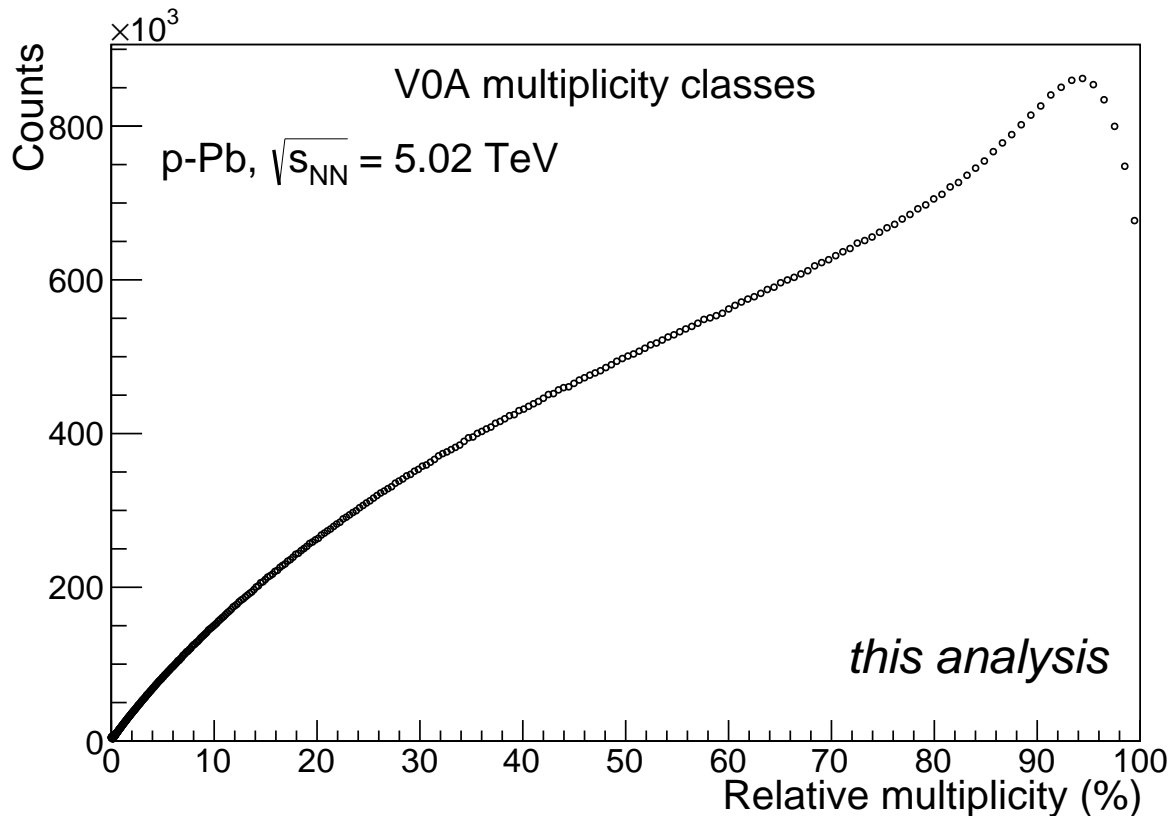
Figure 6.1: Distribution of the multiplicity percentile in p-Pb collisions at $\sqrt{s_{NN}} = 5.02$ TeV, defined using the information provided by the V0A detector [This work].

- In order to ensure a high-resolution track reconstruction and rejection of fake tracks:

    - The particle should produce at least 80 clusters in the TPC;

    - The χ^2 over the Number of TPC clusters should not be larger than 4;

    - The particle should leave 2 clusters in the ITS;

- For background reduction:

    - The particle should hit at least 1 of the SPD layers. This requirement increases the chances that the particle were produced in the collision;

    - Maximum impact parameter relative to the beam axis: 3.2 cm.

    - Maximum impact parameter relative to the transverse plane: 2.4 cm.

Due to these constraints, the tracking efficiency is reduced, i. e. the number of tracks analyzed is smaller than the total physical particles created in the reaction. The tracking efficiency for a given set of cuts can be estimated through Monte Carlo simulations using GEANT for detector response as implemented in ALIROOT (see the discussion in the previous Chapter).

The tracking efficiency estimated for the set of cuts listed above is shown in Figures 6.2 and 6.3. In the latter, the efficiency as a function of the azimuth φ (top panel) and pseudrapidity η (bottom panel) is shown and, in Figure 6.2 the result is displayed as a function of transverse momentum p_T.

In the correlation analysis the number of associated per-trigger particles is evaluated and, this number is reduced due to these track selection cuts. Therefore the correlation distribution is corrected by the numbers shown in Figures 6.2 and 6.3 in order to account for this difference, as will be mentioned later in this text. It is shown in Figure 6.3 (upper panel) that, for the pp data ($\sqrt{s} = 2.76$ TeV), the efficiency has some dependence with $\Delta\varphi$. This effect is due to hardware problem in the ITS in this particular period, and it is accounted for, in this analysis, via this efficiency correction.
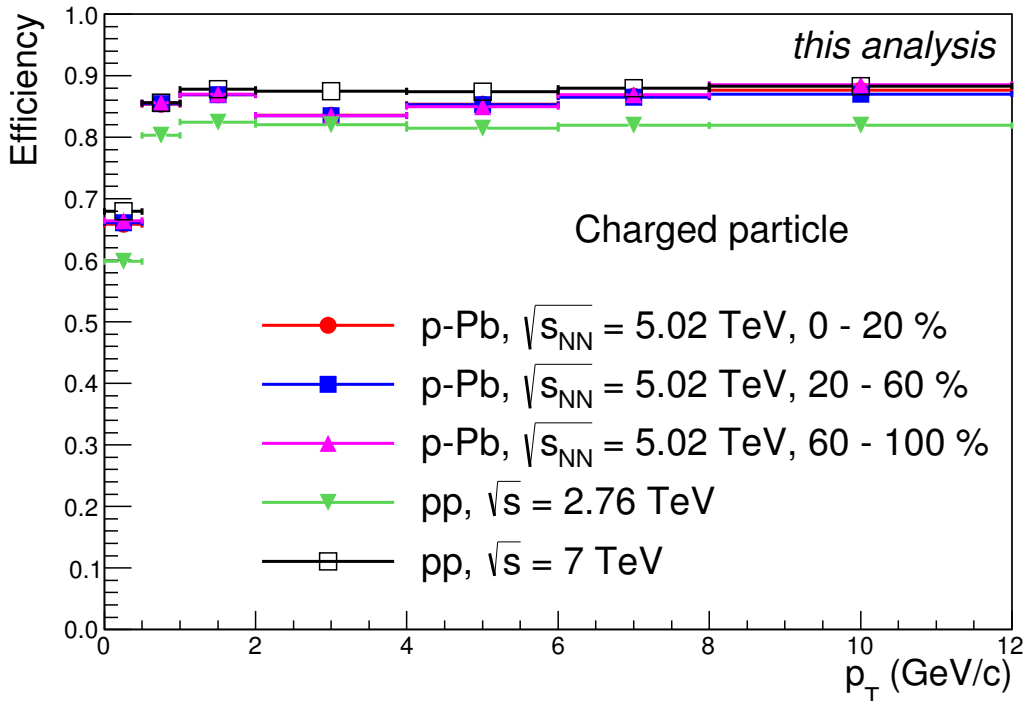
Figure 6.2: Track reconstruction efficiency for charged particles in pp ($\sqrt{s} = 2.76$ and 7 TeV) and p-Pb ($\sqrt{s_{NN}} = 5.02$ TeV) collisions, as a function of transverse momentum p_T, for the track cuts described in this Section [This work].

After the selection there are still a remaining contamination in the particle sample, composed mainly by particles from secondary decays and fake mis-reconstructed tracks. This contamination can also be estimated through Monte Carlo simulations and the results are shown in Figures 6.4 and 6.5.

In Figure 6.4 the relative contamination from secondary particles is shown as a function of p_T, for the two data samples analyzed in this work and, in Figure 6.5 the amount of remaining fake tracks are displayed. Later in this text it will be shown that these contamination affect the correlation distribution. The effect on the evaluated correlation yield is estimated
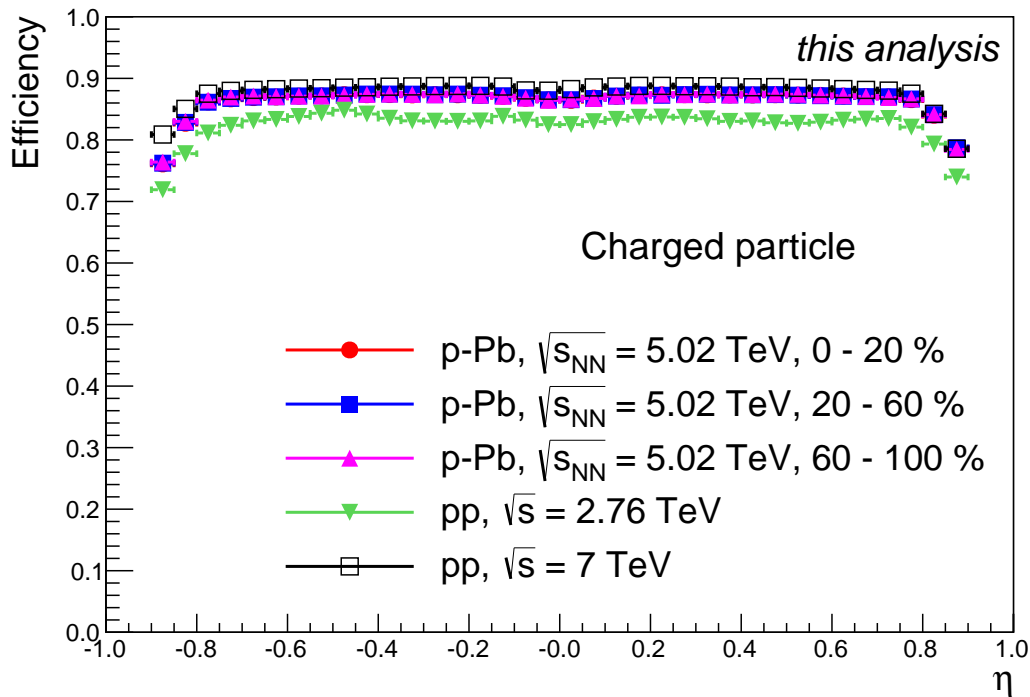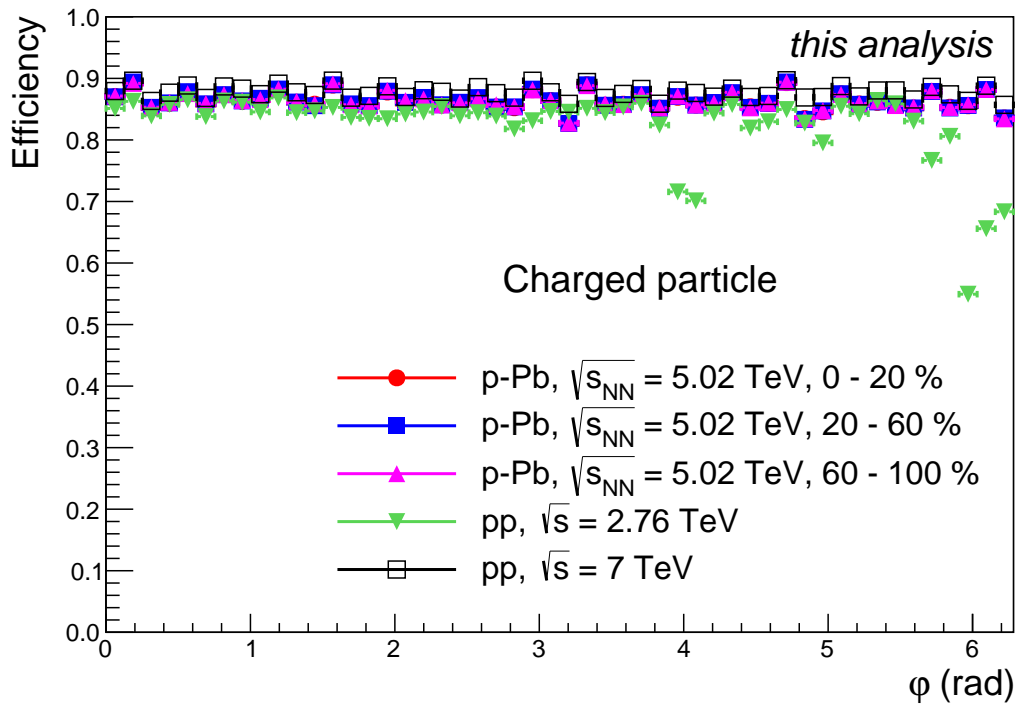
Figure 6.3: Track reconstruction efficiency for charged particles in pp ($\sqrt{s} = 2.76$ and 7 TeV) and p-Pb ($\sqrt{s_{NN}} = 5.02$ TeV) collisions, as a function of azimuth φ (top panel) and pseudorapidity η (bottom panel), for the track cuts described in this Section [This work].

and accounted for in the systematic uncertainties. Further details are provided at the end of this Chapter.
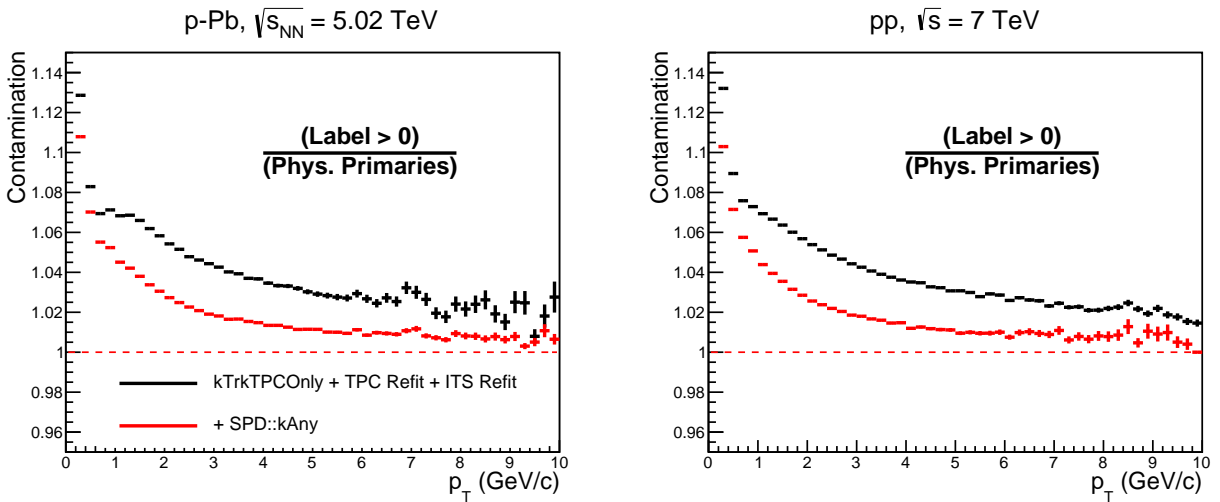
Figure 6.4: Relative amount of secondary tracks in the reconstructed particle sample, as a function of transverse momentum, obtained through Monte Carlo simulations, for p-Pb (left panel) and pp (right panel) collisions [This work].
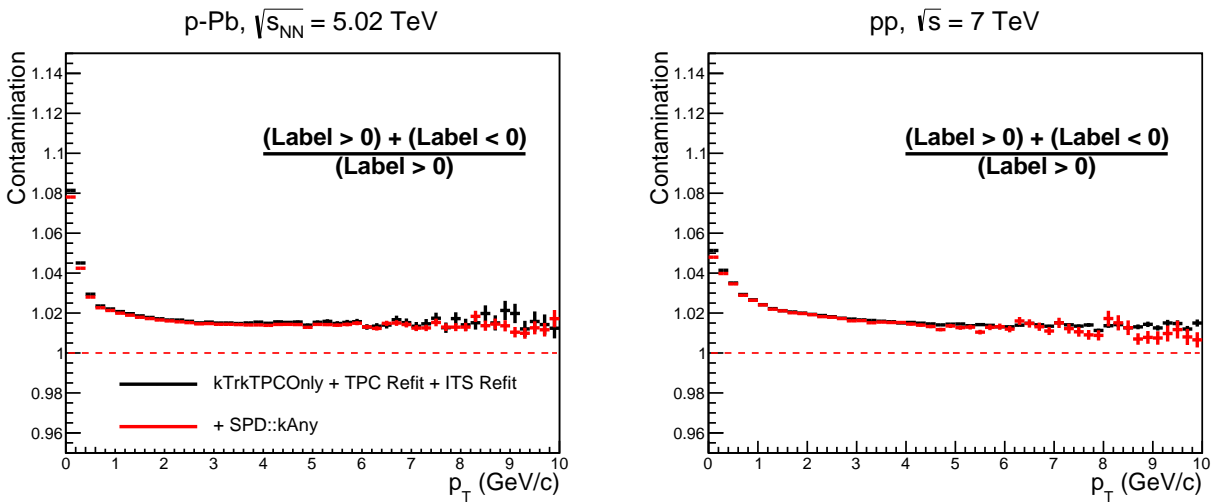
Figure 6.5: Relative amount of fake tracks in the particle sample, as a function of the transverse momentum, evaluated through Monte Carlo simulations, for p-Pb (left panel) and pp (right panel) collisions [This work].

6.3 Electron Identification

The electron identification was performed using the techniques described in the previous Chapter. In this analysis the subsystems used are the TOF and TPC detectors and the electron candidate was required to simultaneously satisfy the following cuts:

- Requirement on TOF signal: $-3 < N\sigma_{\text{TOF}} < 3$

- Requirement on TPC signal: $-0.5 < N\sigma_{\text{TPC}} < 3$

Figures 6.6 to 6.17 show the PID plots from p-Pb (for the three multiplicity classes) and

from pp data. For each Figure, the top panel shows the distribution of the electron Nσ from TPC as a function of the TOF Nσ. In these Figures the electron band is visible around the (0,0).

In the bottom panel of these Figures, the projection on the Nσ_{TPC} axis is displayed without(green filled circles) and with TOF selection (black opened circles). In the latter case, tracks are required to satisfy $-3 <$ N$\sigma_{\text{TOF}} < 3$. It is also visible in these Figures that a significant reduction of the contamination in the electron region is achieved by applying the TOF selection.

In order to quantify the electron identification in terms of the remaining hadron contamination, the Nσ_{TPC} distribution (with TOF selection) is fitted by a sum of 2 Gaussian distributions, which accounts for the electron and kaon/proton distributions respectively. The fit function has a third term to describe for the $\pi^{\pm}$ part, defined as a product of an exponential by Landau function (see Appendix C), which accounts for the asymmetry in the pion energy-loss distribution.

The fits are also shown in Figures 6.6 to 6.17. The dashed lines shows the components for each particle specie, with the magenta line representing the electrons. The blue filled area, displayed for N$\sigma_{TPC} > -0.5$, shows the hadron contamination in the selected electron sample.

The hadron contamination $\alpha(p_{\text{T}})$ is the relative amount of hadrons in the electron sample and it is evaluated via Equation 6.1. A summary of the estimated contamination, for the momentum range of this analysis and for each multiplicity class (for the p-Pb data) are summarized in Table 6.1. The contamination is negligible for low-p_{T}. The highest hadron contamination is $\approx 7.3\%$, estimated in pp collisions, for highest momentum region ($4 < p_{\text{T}}^{e} < 6$ GeV/c).

$$\alpha(p_{\text{T}}) = \frac{\left(\int_{-0.5}^{3}(\text{Gauss})\text{d}(\text{n}\sigma)\right)^{k,p} + \left(\int_{-0.5}^{3}(\text{exp})\text{x}(\text{Landau})\text{d}(\text{n}\sigma)\right)^{\pi^{\pm}}}{\left(\int_{-0.5}^{3}(\text{Gauss})\text{d}(\text{n}\sigma)\right)^{k,p} + \left(\int_{-0.5}^{3}(\text{exp})\text{x}(\text{Landau})\text{d}(\text{n}\sigma)\right)^{\pi^{\pm}} + \left(\int_{-0.5}^{3}(\text{Gauss})\text{d}(\text{n}\sigma)\right)^{e}} \tag{6.1}$$

Table 6.1: Hadron contamination in the electron sample, estimated via Equation 6.1.

Electron p_{T} / System	pp ($\sqrt{s} = 7$ TeV)	p-Pb (0-20%)	p-Pb (20-60%)	p-Pb (60-100%)
$1 < p_{\text{T}} < 2$ GeV/c	$\sim 0\%$	$\sim 0\%$	$\sim 0\%$	$\sim 0\%$
$2 < p_{\text{T}} < 4$ GeV/c	0.8%	0.1%	0.1%	0.1%
$4 < p_{\text{T}} < 6$ GeV/c	7.3%	2.8%	3.2%	3.6%

The effect of this contamination is an amount of di-hadron correlation added in the measured electron-hadron angular distribution. This is corrected, at the correlation level, by subtracting the measured correlation distribution by the di-hadron angular correlation scaled by the estimated contamination. In the following the PID graphs for every momentum range and multiplicity classes are shown.
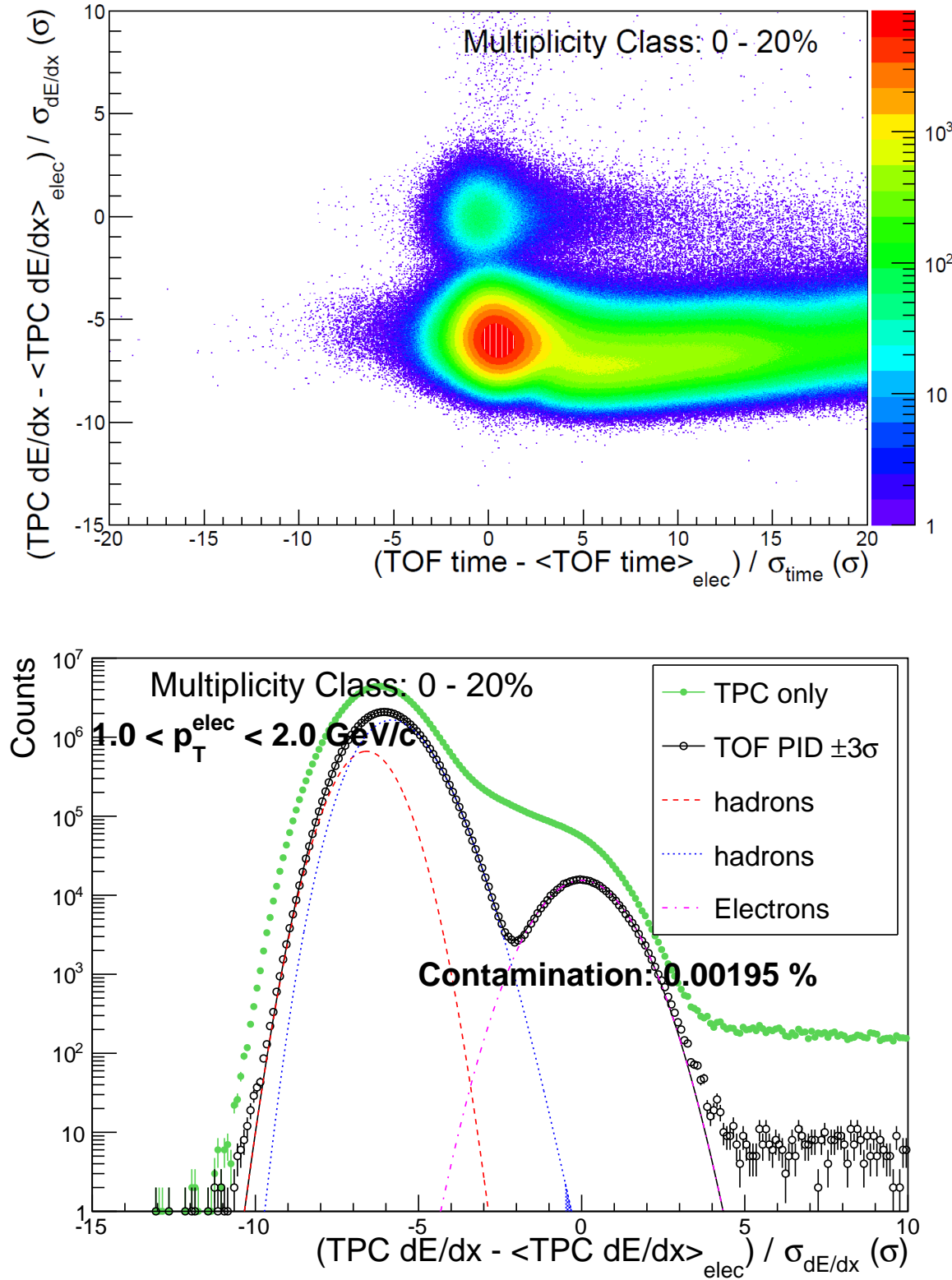
Figure 6.6: Top panel: Nσ_{TPC} **as a function of** Nσ_{TOF}. **Bottom panel:** Nσ_{TPC} **distribution for** $-3 <$ N$\sigma_{\text{TOF}} < 3\sigma$. **Results for high-multiplicity** $(0-20\%)$ **p-Pb collisions and particles within** $1 < p_T < 2$ **GeV/c. The blue filled area shows the hadron contamination in the electron sample [This work].**
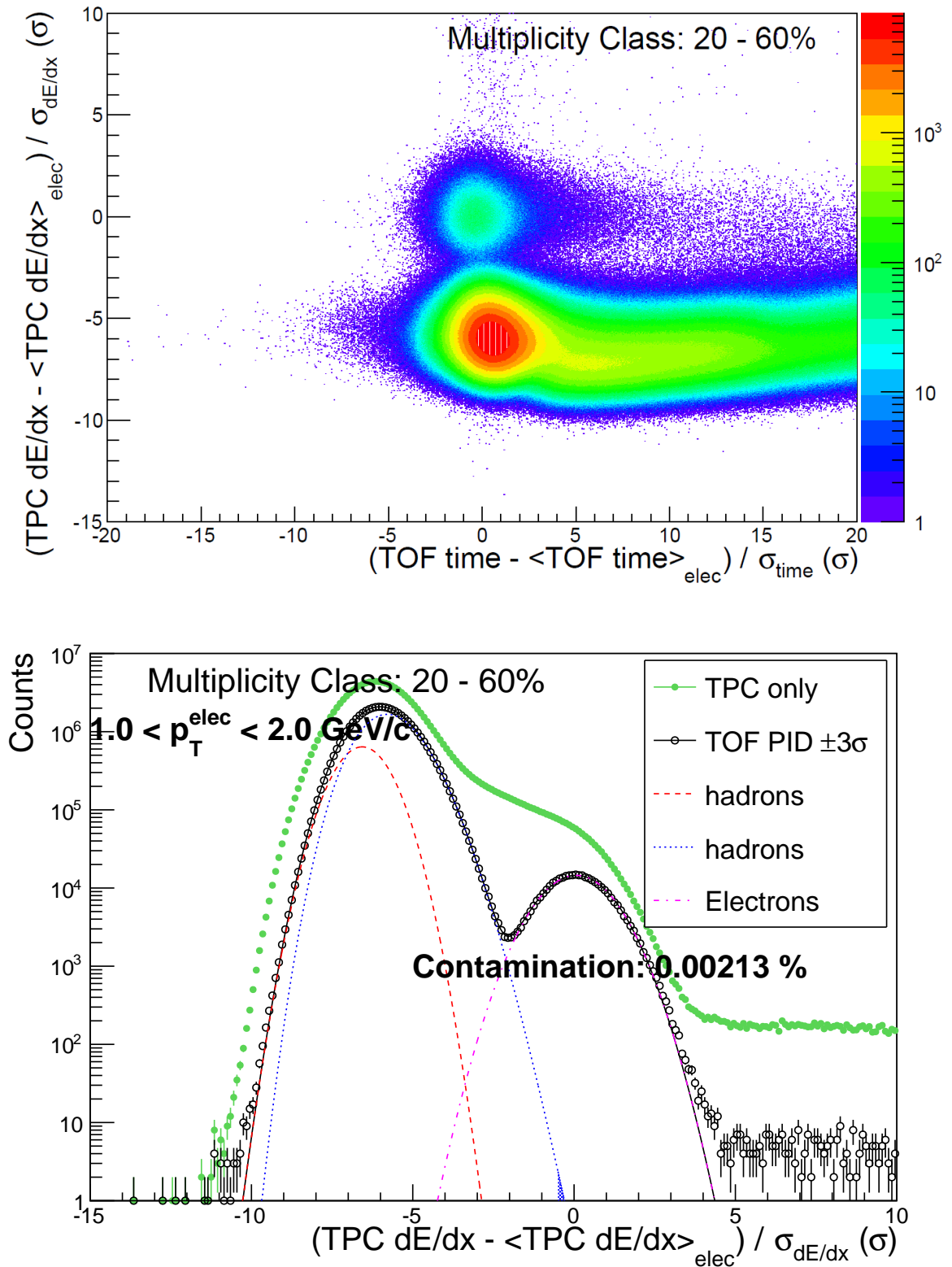
Figure 6.7: Top panel: $N\sigma_{TPC}$ **as a function of** $N\sigma_{TOF}$**. Bottom panel:** $N\sigma_{TPC}$ **distribution for** $-3 <$ $N\sigma_{TOF} < 3$**. Results for intermediary-multiplicity** $(20 - 60\%)$ **p-Pb collisions and particles within** $1 < p_T < 2$ **GeV/c. The blue filled area shows the hadron contamination in the electron sample [This work].**
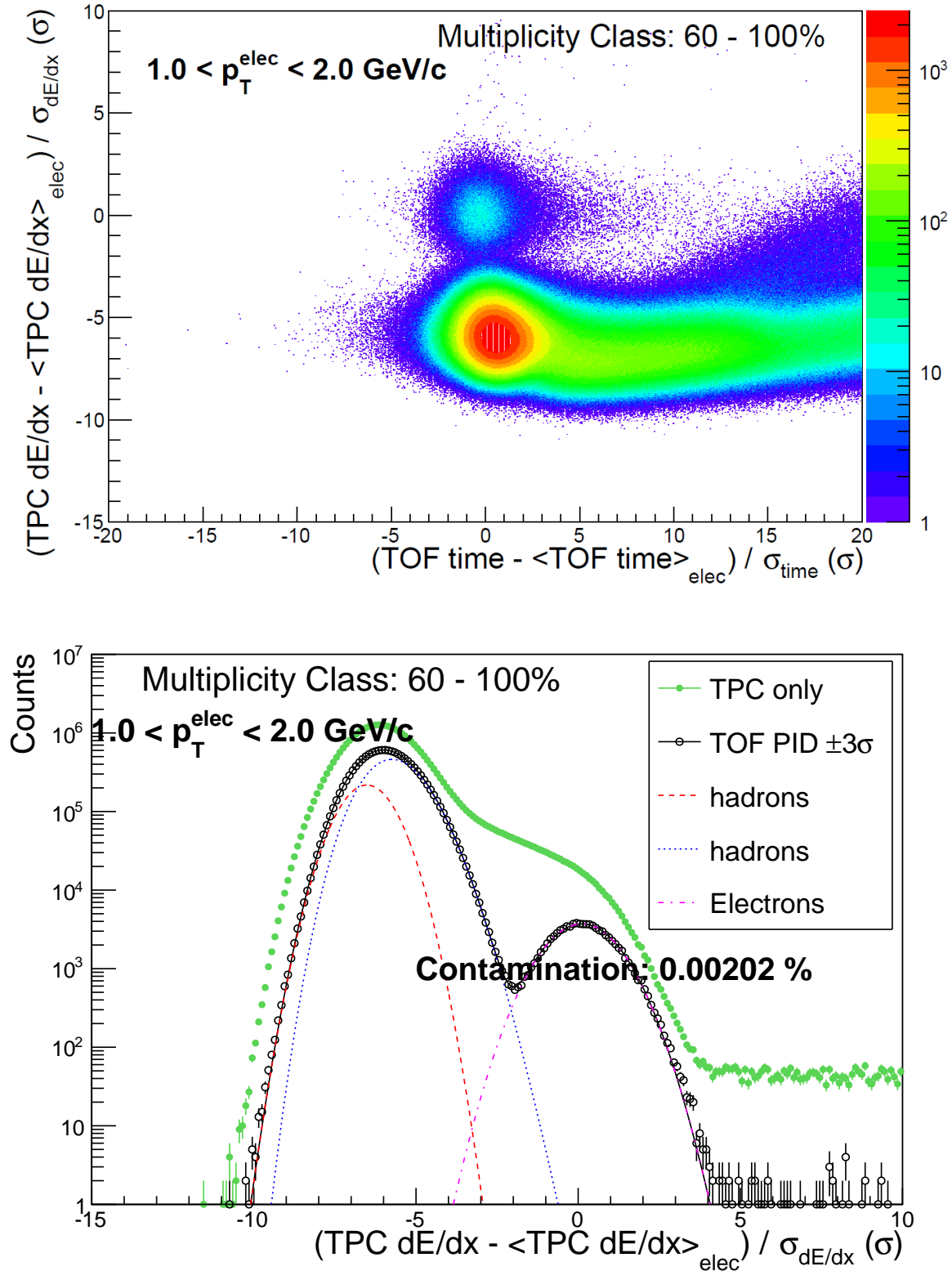
Figure 6.8: Top panel: $N\sigma_{TPC}$ **as a function of** $N\sigma_{TOF}$. **Bottom panel:** $N\sigma_{TPC}$ **distribution for** $-3 <$ $N\sigma_{TOF} < 3$. **Results for low-multiplicity** $(60 - 100\%)$ **p-Pb collisions and particles within** $1 < p_T < 2$ **GeV/c. The blue filled area shows the hadron contamination in the electron sample [This work].**
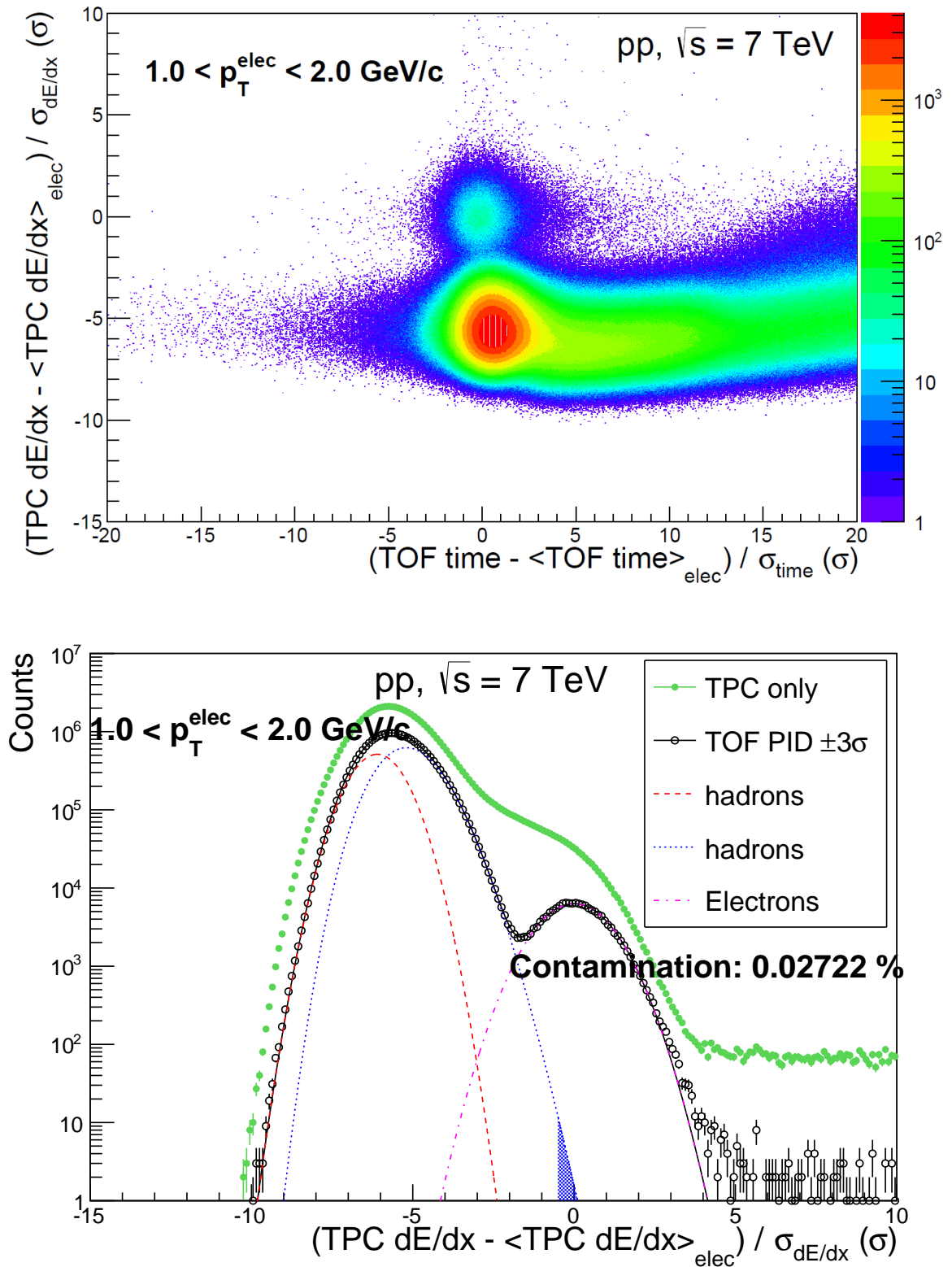
Figure 6.9: Top panel: $N\sigma_{\mathrm{TPC}}$ **as a function of** $N\sigma_{\mathrm{TOF}}$. **Bottom panel:** $N\sigma_{\mathrm{TPC}}$ **distribution for** $-3 <$ $N\sigma_{\mathrm{TOF}} < 3$. **Results for pp collisions and particles within** $1 < p_{\mathrm{T}} < 2$ **GeV/c. The blue filled area shows the hadron contamination in the electron sample [This work].**
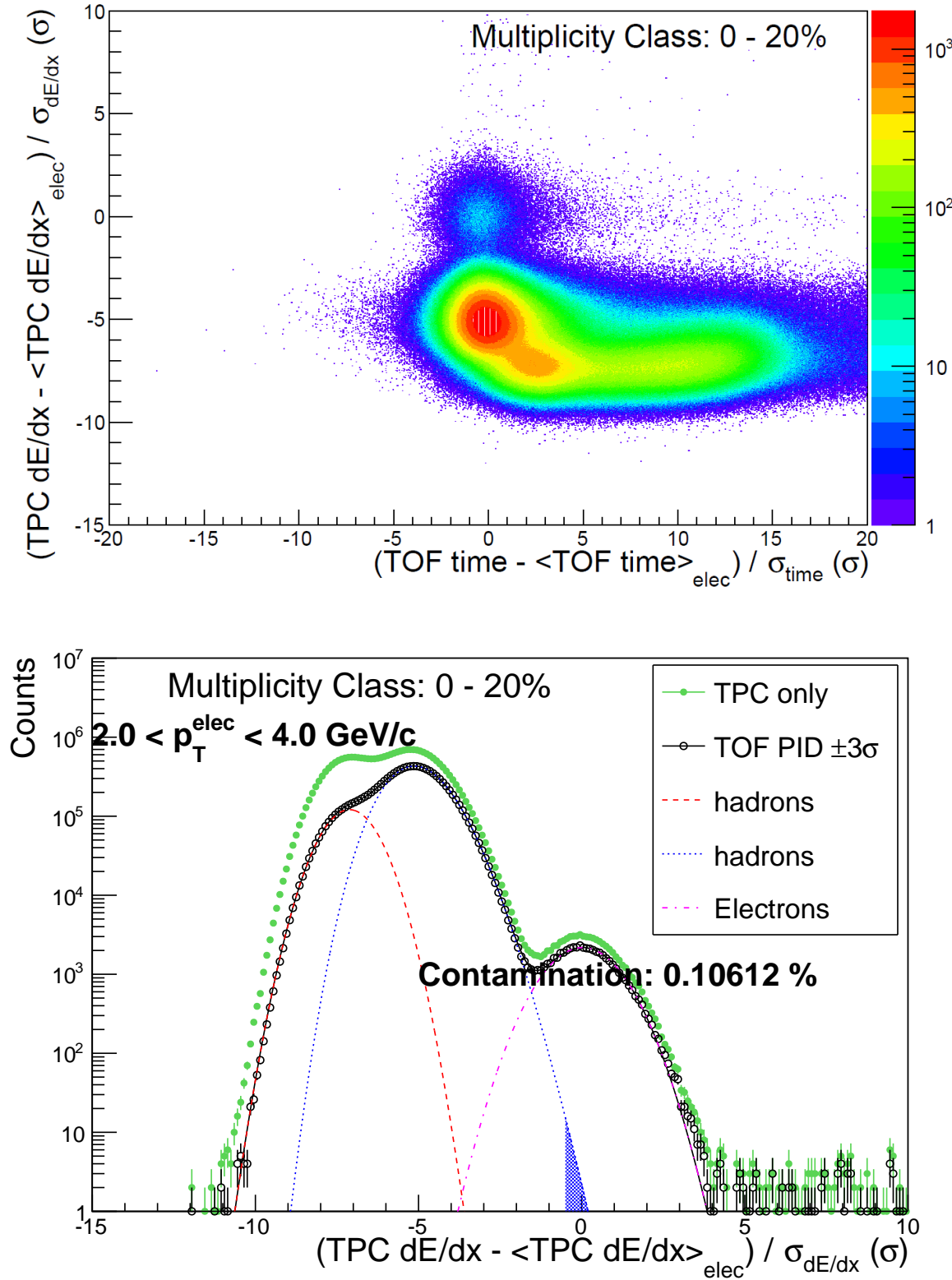
Figure 6.10: Top panel: $N\sigma_{TPC}$ **as a function of** $N\sigma_{TOF}$**. Bottom panel:** $N\sigma_{TPC}$ **distribution for** $-3 <$ $N\sigma_{TOF} < 3$**. Results for high-multiplicity** $(0 - 20\%)$ **p-Pb collisions and particles within** $2 < p_T < 4$ **GeV/**c**. The blue filled area shows the hadron contamination in the electron sample [This work].**
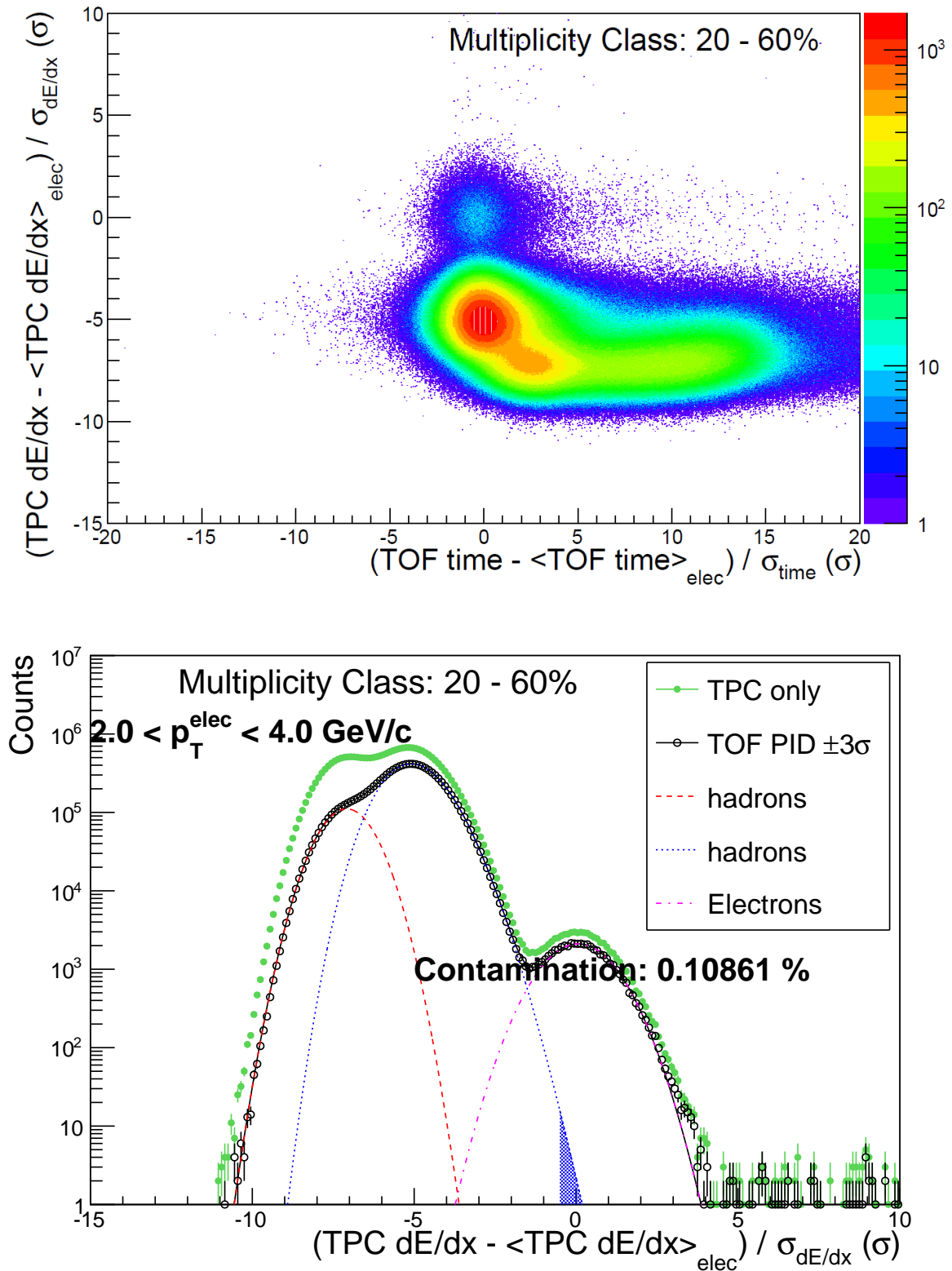
Figure 6.11: Top panel: $N\sigma_{TPC}$ **as a function of** $N\sigma_{TOF}$**. Bottom panel:** $N\sigma_{TPC}$ **distribution for** $-3 <$ $N\sigma_{TOF} < 3$**. Results for intermediary-multiplicity** $(20 - 60\%)$ **p-Pb collisions and particles within** $2 < p_T < 4$ **GeV/c. The blue filled area shows the hadron contamination in the electron sample** **[This work].**
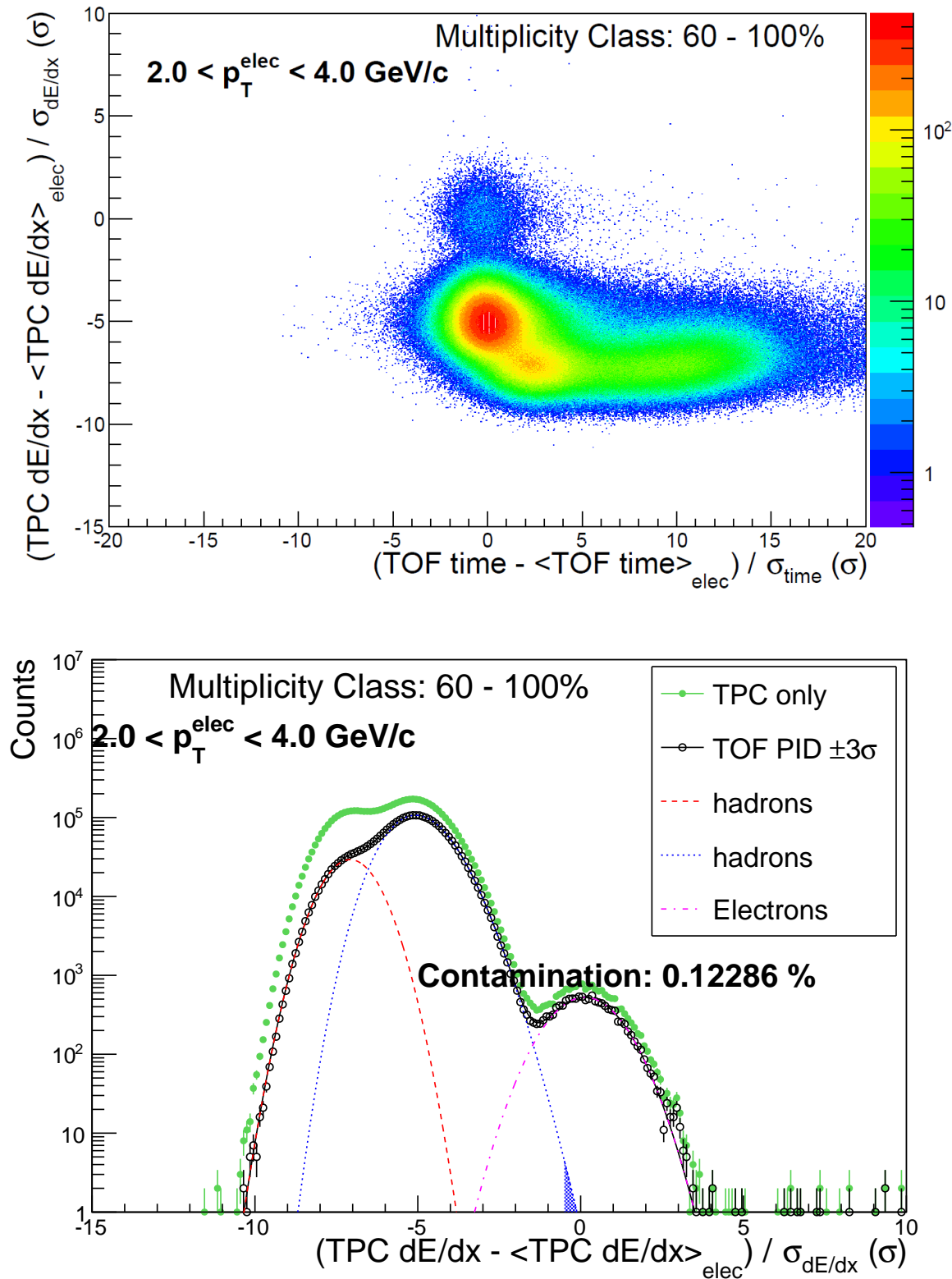
Figure 6.12: Top panel: $N\sigma_{TPC}$ **as a function of** $N\sigma_{TOF}$. **Bottom panel:** $N\sigma_{TPC}$ **distribution for** $-3 <$ $N\sigma_{TOF} < 3$. **Results for low-multiplicity** $(60 - 100\%)$ **p-Pb collisions and particles within** $2 < p_T < 4$ **GeV/c. The blue filled area shows the hadron contamination in the electron sample [This work].**
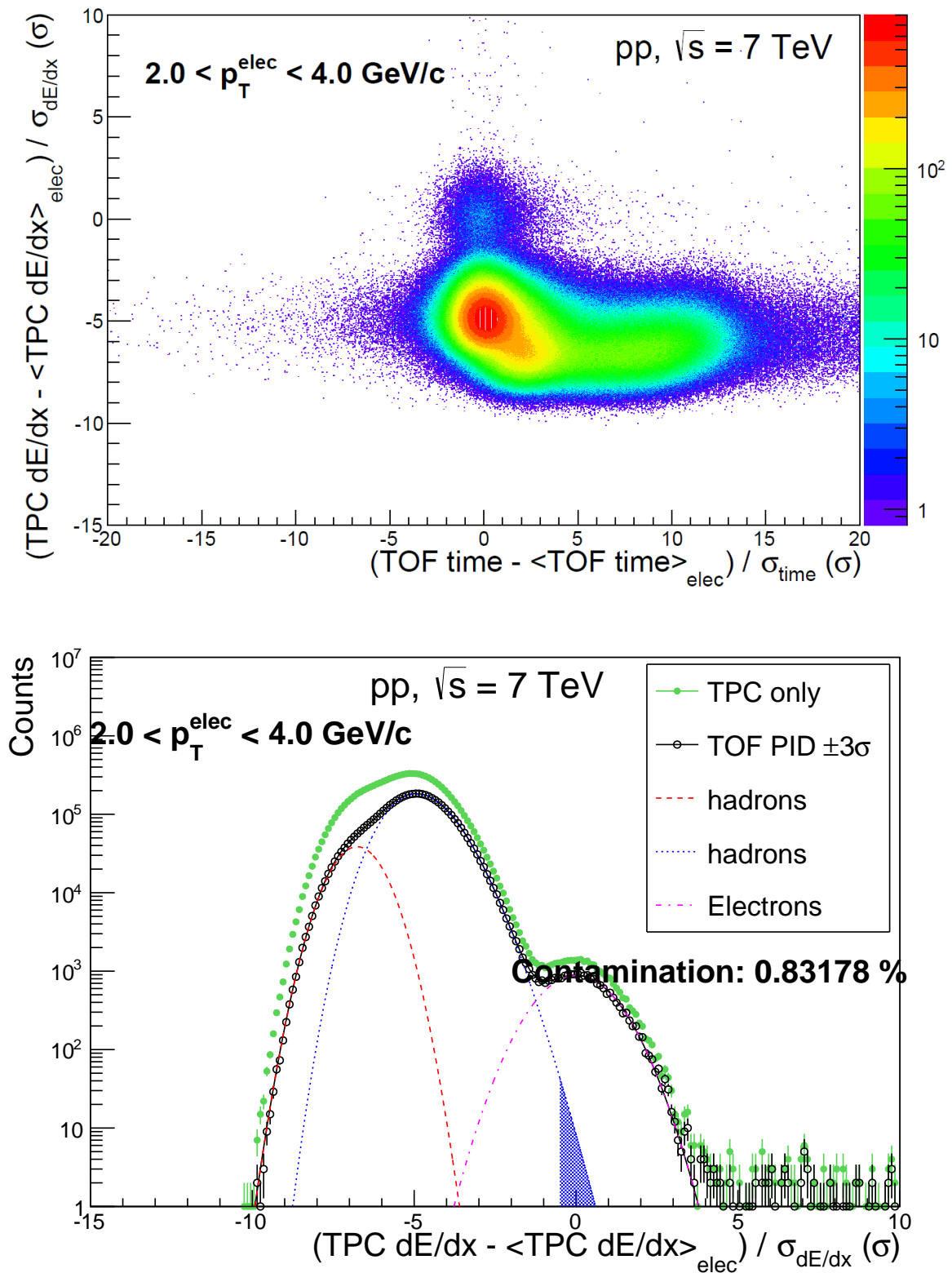
Figure 6.13: Top panel: $N\sigma_{TPC}$ **as a function of** $N\sigma_{TOF}$. **Bottom panel:** $N\sigma_{TPC}$ **distribution for** $-3 <$ $N\sigma_{TOF} < 3$. **Results for pp collisions and particles within** $2 < p_T < 4$ **GeV/**c. **The blue filled area shows the hadron contamination in the electron sample [This work].**
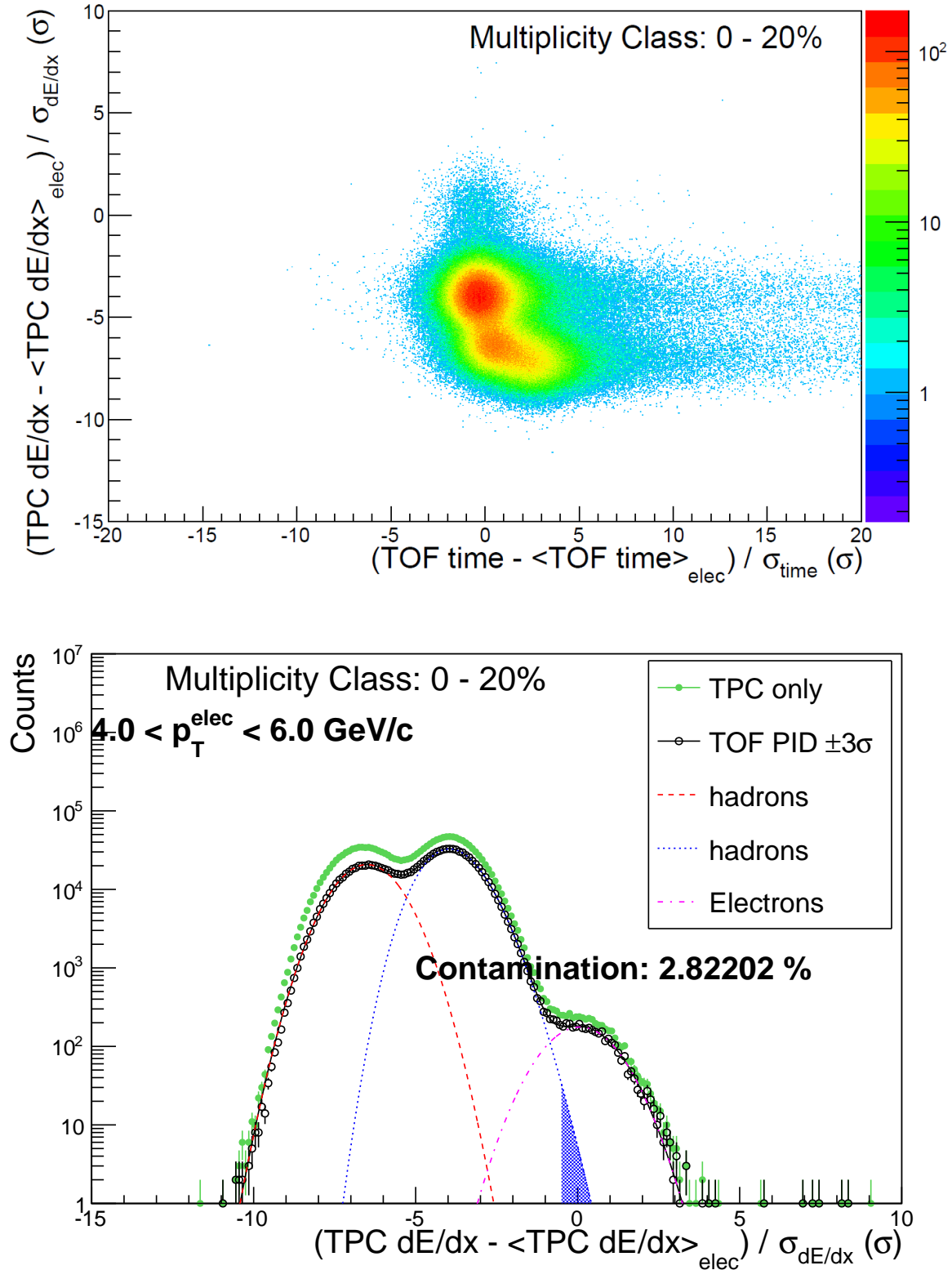
Figure 6.14: Top panel: $N\sigma_{\text{TPC}}$ **as a function of** $N\sigma_{\text{TOF}}$. **Bottom panel:** $N\sigma_{\text{TPC}}$ **distribution for** $-3 <$ $N\sigma_{\text{TOF}} < 3$. **Results for high-multiplicity** $(0 - 20\%)$ **p-Pb collisions and particles within** $4 < p_{\text{T}} < 6$ **GeV/**c. **The blue filled area shows the hadron contamination in the electron sample [This work].**
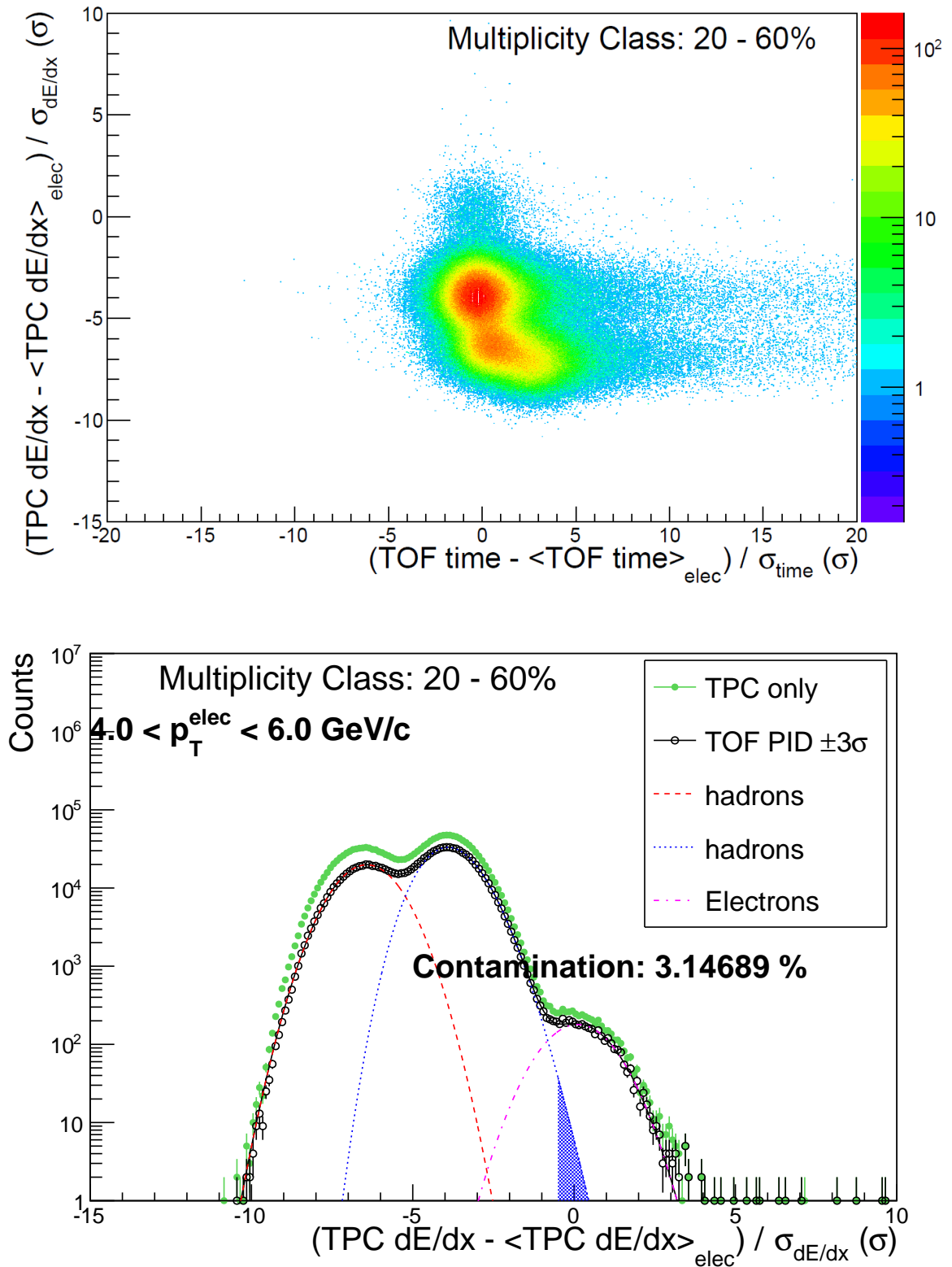
Figure 6.15: Top panel: Nσ_{TPC} **as a function of** Nσ_{TOF}. **Bottom panel:** Nσ_{TPC} **distribution for** $-3 <$ N$\sigma_{\text{TOF}} < 3$. **Results for intermediary-multiplicity** $(20 - 60\%)$ **p-Pb collisions and particles within** $4 < p_{\text{T}} < 6$ **GeV/c. The blue filled area shows the hadron contamination in the electron sample** [**This work**].
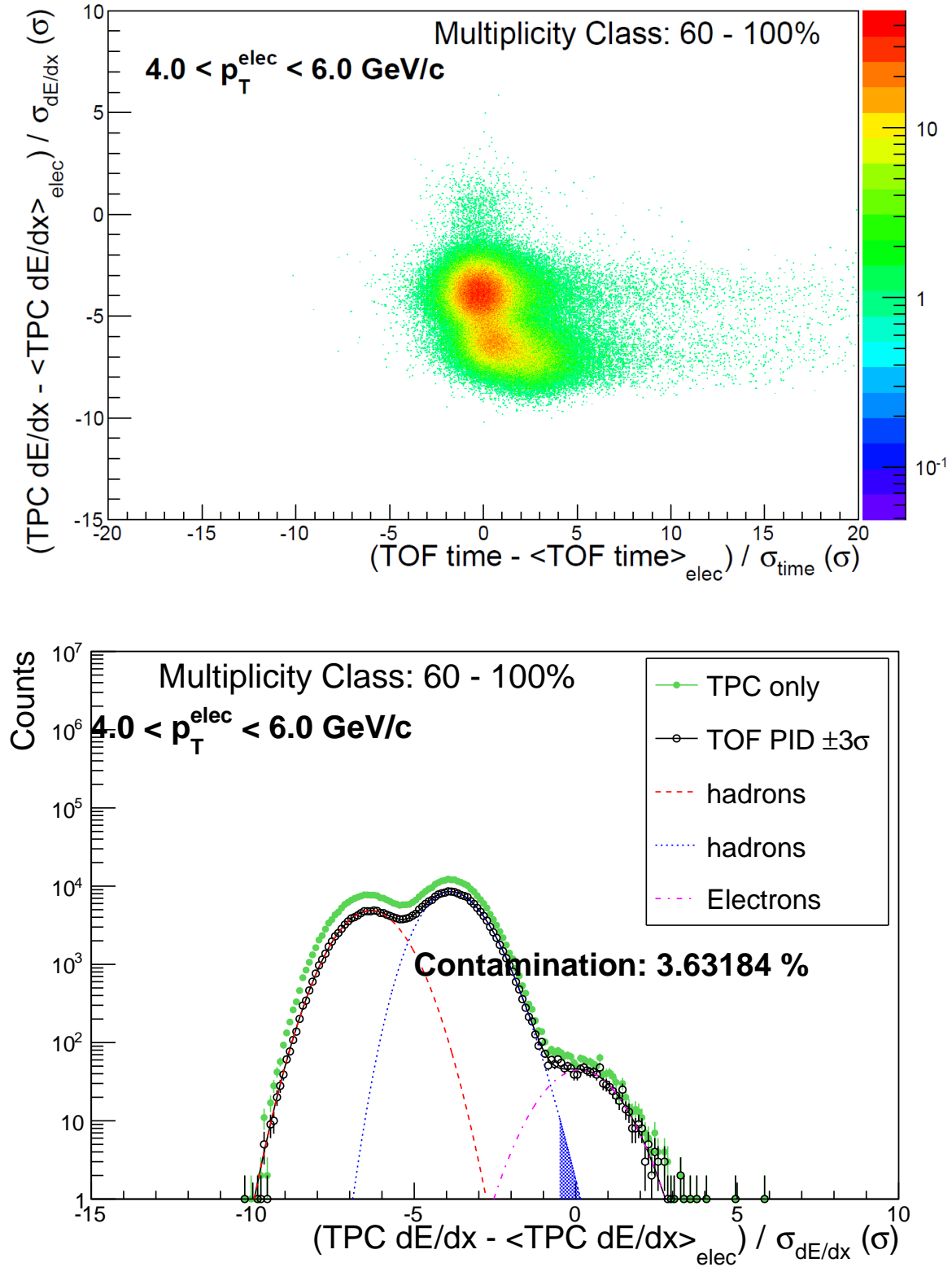
Figure 6.16: Top panel: Nσ_{TPC} **as a function of** Nσ_{TOF}. **Bottom panel:** Nσ_{TPC} **distribution for** $-3 <$ N$\sigma_{\mathrm{TOF}} < 3$. **Results for low-multiplicity** $(60-100\%)$ **p-Pb collisions and particles within** $4 < p_{\mathrm{T}} < 6$ **GeV/c. The blue filled area shows the hadron contamination in the electron sample [This work].**
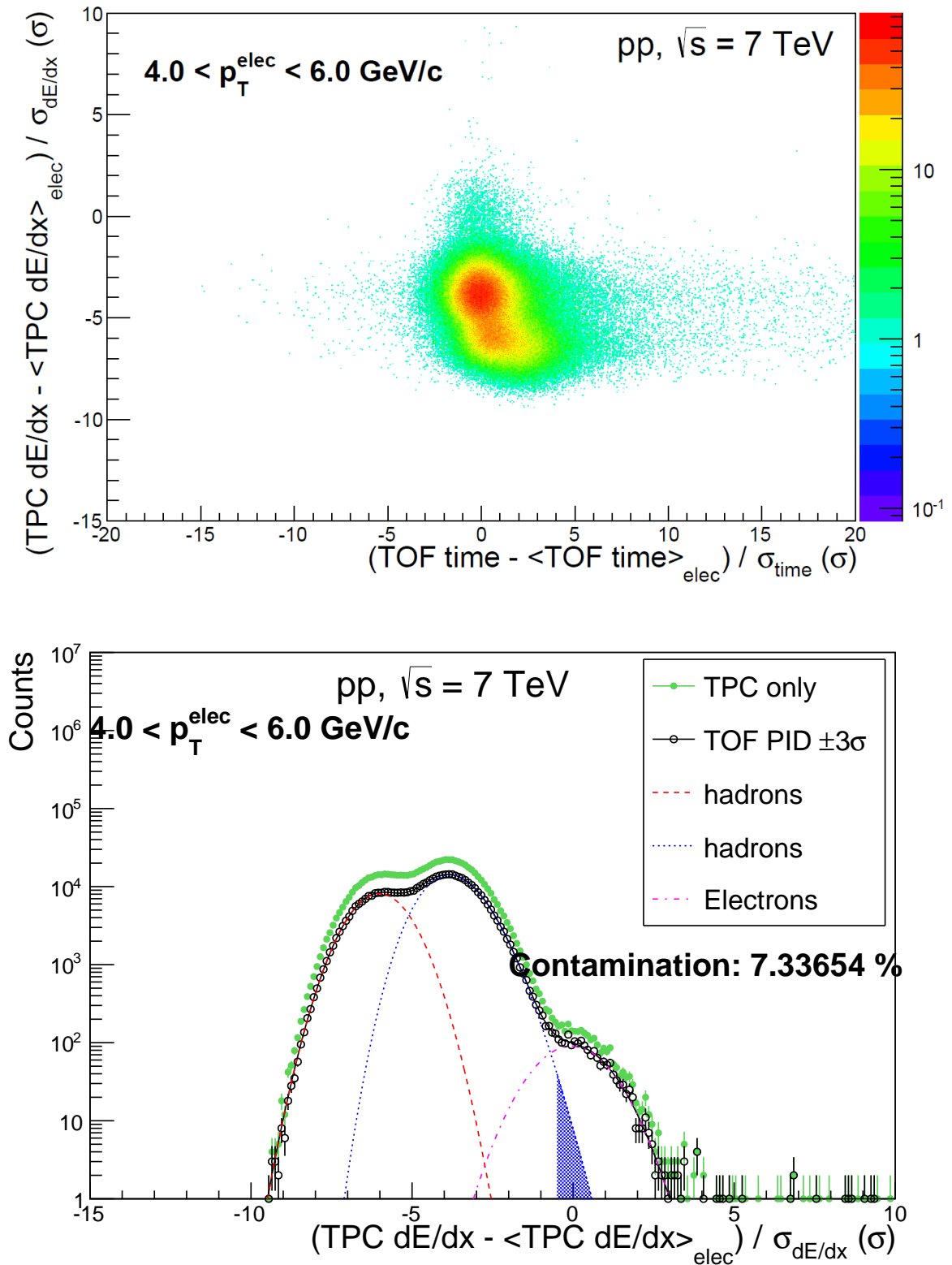
Figure 6.17: Top panel: $N\sigma_{TPC}$ **as a function of** $N\sigma_{TOF}$**. Bottom panel:** $N\sigma_{TPC}$ **distribution for** $-3 <$ $N\sigma_{TOF} < 3$**. Results for pp collisions and particles within** $4 < p_T < 6$ **GeV/c. The blue filled area shows the hadron contamination in the electron sample [This work].**

6.4 Background identification

The electron sample is composed not only by electrons from heavy-flavour hadron decays, but from other background sources. The main contributions for this background are due to photon conversions in the detector material ($\gamma + n \rightarrow e^+ + e^- + n$) and light meson Dalitz decays, e. g. $\pi^0 \rightarrow \gamma + e^+ + e^-$.

These contributions are identified using the invariant mass method (see e. g. [80, 86]). In fact, the invariant mass of electron-positron pairs ($m(e^+, e^-)$) is small for pairs coming from these two sources (photons and light mesons).

In this technique, those pairs misidentified as a background due to the combinatorial analysis, are estimated by correlation like sign pairs, i. e. the electron-electron (and positron-positron) invariant mass distribution is calculated.

Figures 6.18 to 6.21, show the invariant mass distributions for *Unlike Sign* pairs (i. e. $e^\pm e^\mp$) and *Like Sign* pairs (i. e. $e^\pm e^\pm$), with the corresponding finding efficiency displayed in the bottom panel of the figure. Background tracks are selected by cutting on a maximum pair invariant mass, taken as 100 MeV/c in this work. The same cut is requested for like sign pairs in order to evaluate the combinatorial background in the invariant mass distribution.

In the reconstruction, the electron/positron partners are requested to satisfy:

- $-3 < N\sigma_{\mathrm{TPC}} < 3$;

- $p_{\mathrm{T}} > 0$ GeV/c, i. e. by default there is no request for the p_{T} values.

Some studies were performed in order to check the stability of the background reconstruction via invariant mass. The invariant mass distribution evaluation was repeated setting different numbers for the minimum value of the associated electron momentum p_{T}^a. The values used were 0, 300, 500 and 700 MeV/c. In the bottom panel of Figures 6.18 to 6.21 the reconstruction efficiency is shown for each selection cases.

The test is performed by checking if, after efficiency correction, the estimated background yield is consistent among the selection cuts. Figures 6.22 to 6.25 shows the results of the stability test. The top panel shows the electron background yield as a function of p_{T} for each selection cut and the corresponding reconstruction efficiency, evaluated through Monte Carlo simulations. In the middle panel, the background yield after efficiency correction is shown for every case and, in the bottom panel the deviation relative to the standard selection (i. e. $p_{\mathrm{T}} > 0$ GeV/c) is displayed. The found modification reaches 10% for the lowest momentum range and is negligible for the other cases and, therefore, these tests support the invariant mass method.

In the following, the figures containing the invariant mass distributions, reconstruction efficiencies and the stability tests are presented.
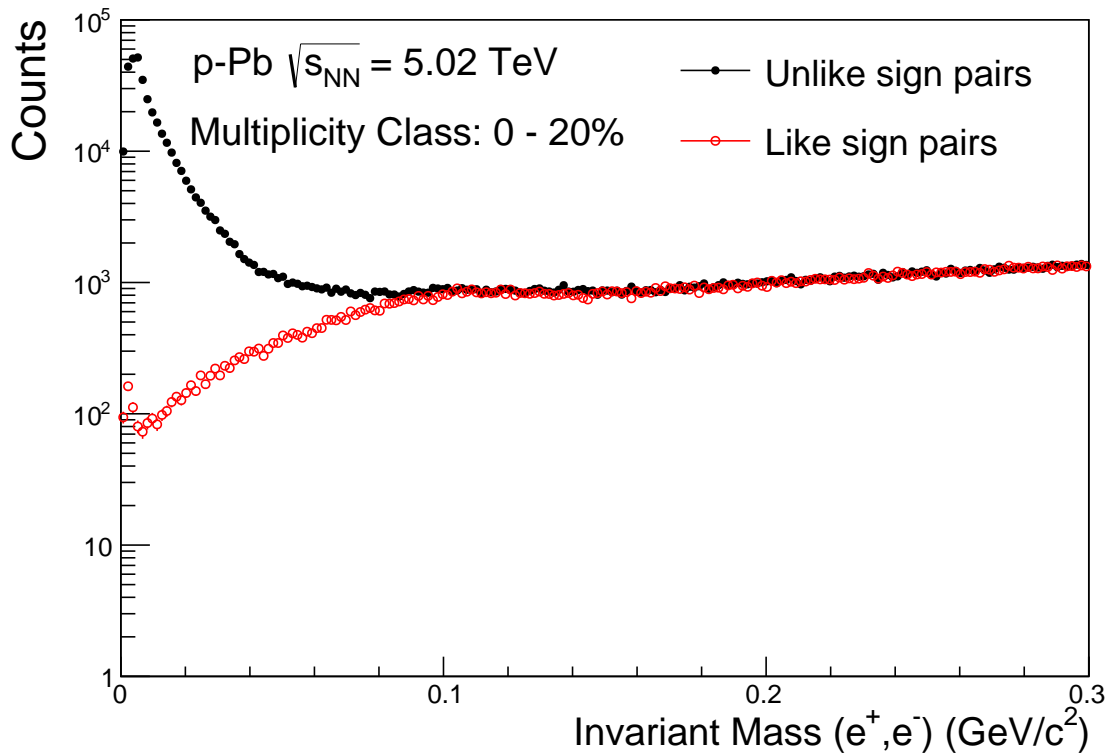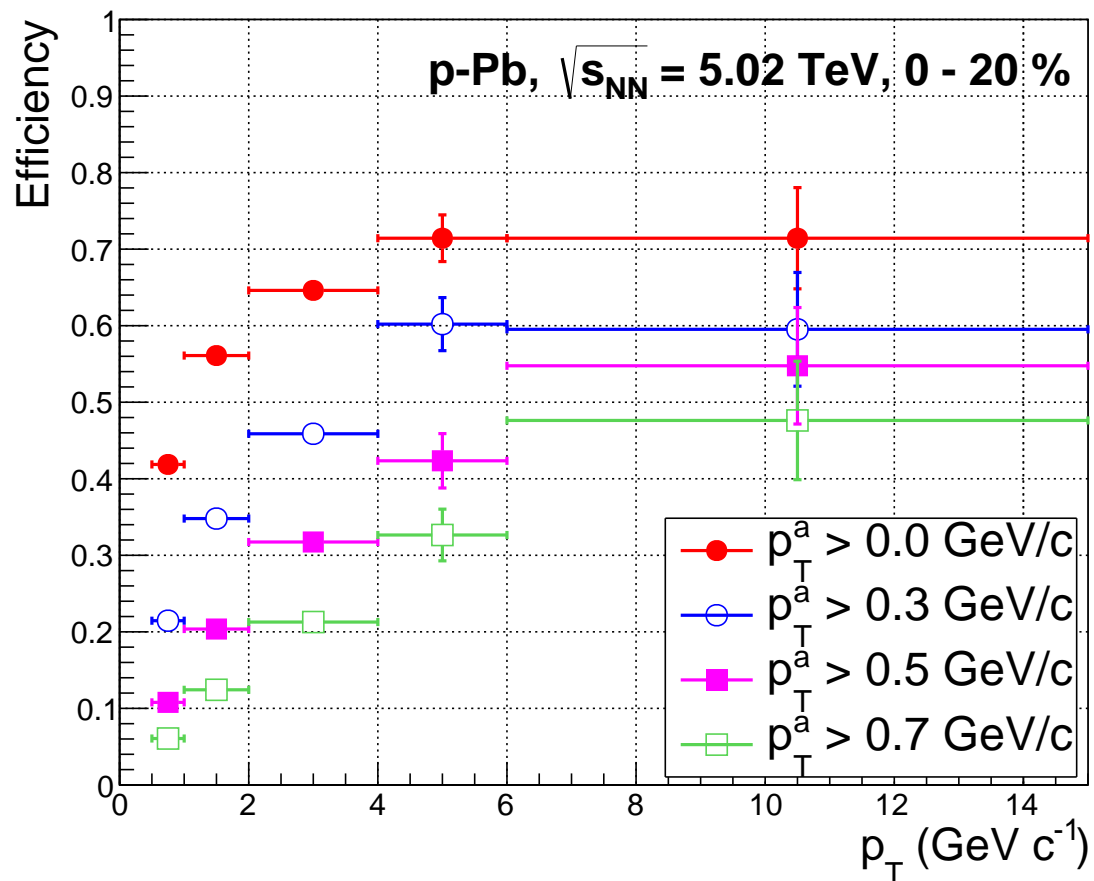
Figure 6.18: Top panel: Invariant mass distribution for unlike and like-sign pairs for $p_T^{assoc} > 0.0$ **GeV/c. Bottom panel: Background finding efficiency for** $p_T^{assoc} > 0.0$, 0.3, 0.5, 0.7 **GeV/c. Results for high-multiplicity** $(0 - 20\%)$ **p-Pb collisions [This work].**
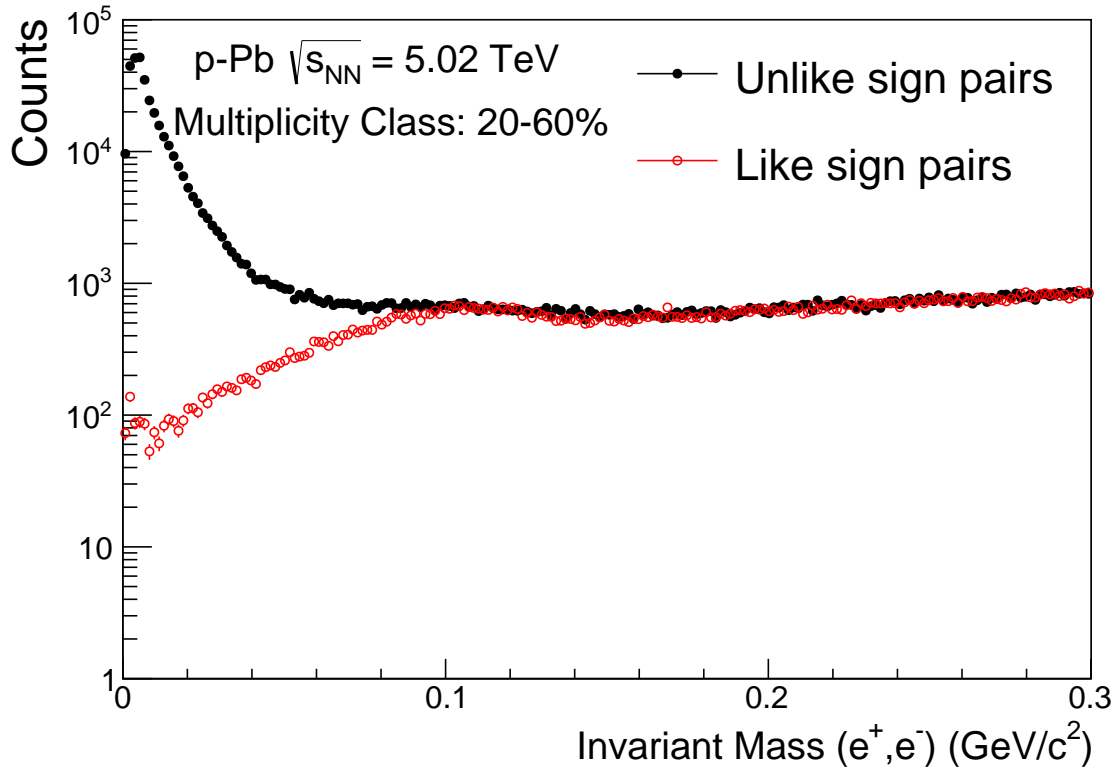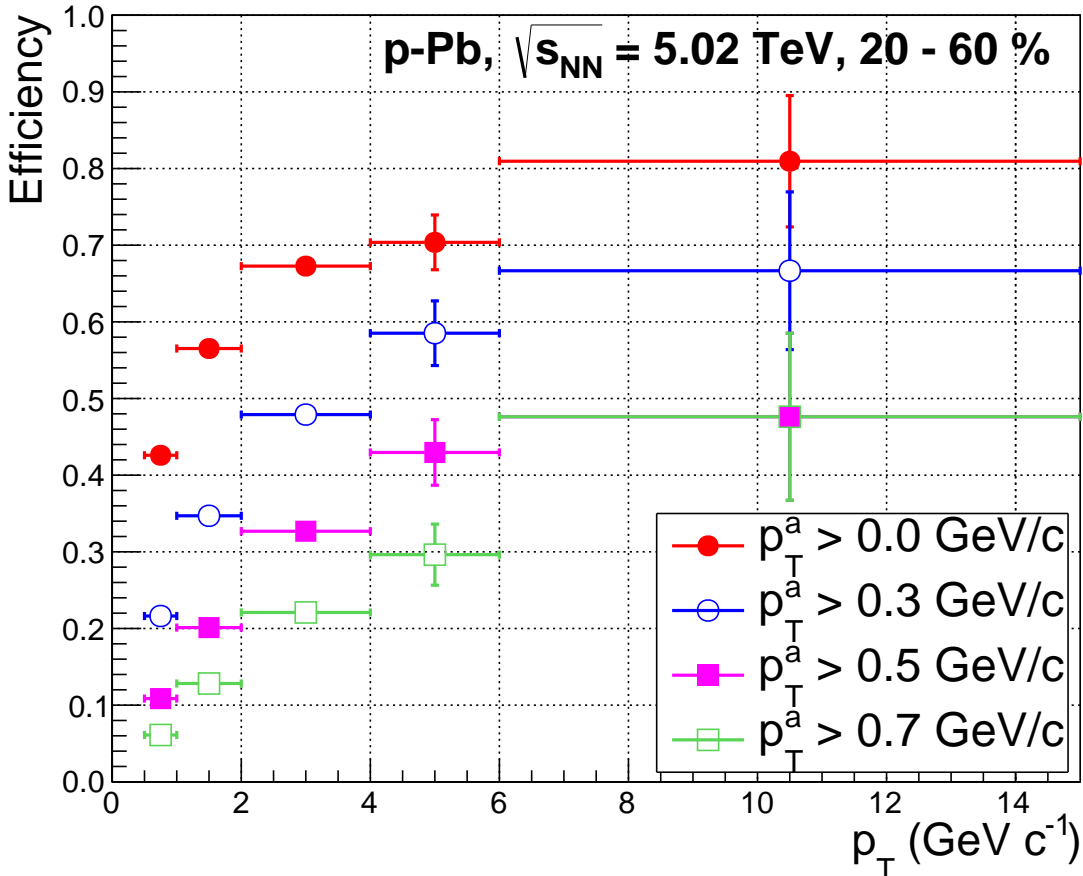
Figure 6.19: Top panel: Invariant mass distribution for unlike and like-sign pairs for $p_T^{assoc} > 0.0$ **GeV/c. Bottom panel: Background finding efficiency for** $p_T^{assoc} > 0.0, 0.3, 0.5, 0.7$ **GeV/c. Results for intermediary-multiplicity** $(20 - 60\%)$ **p-Pb collisions [This work].**
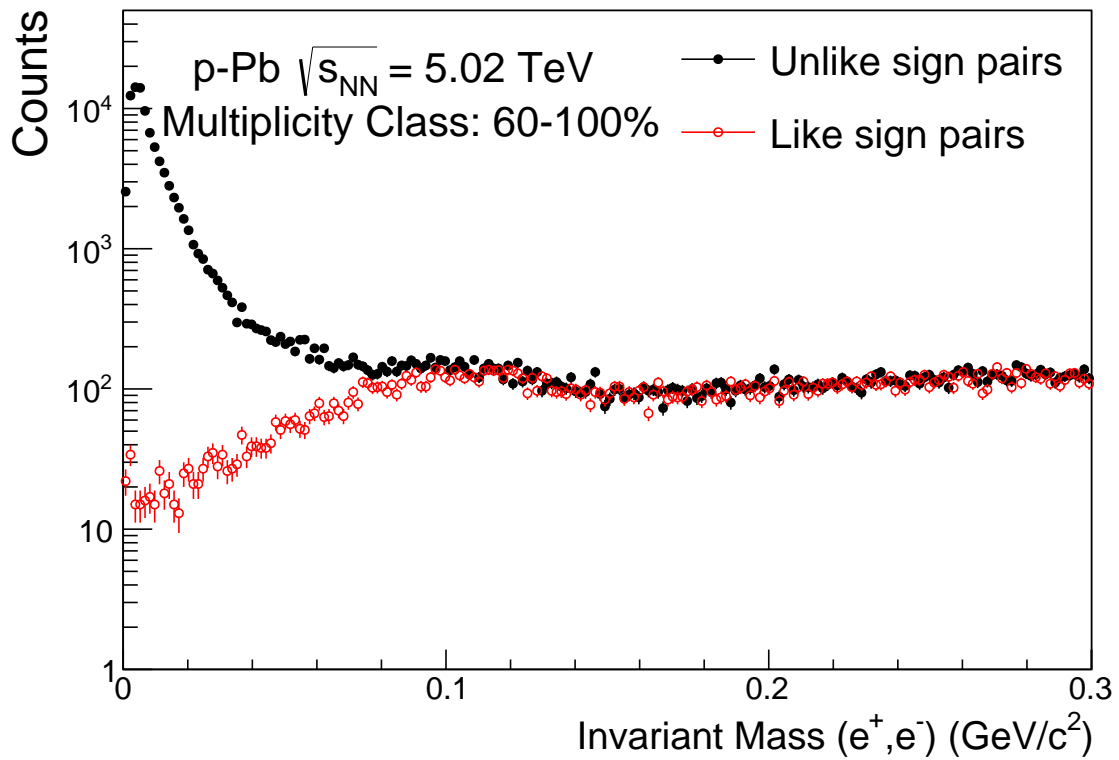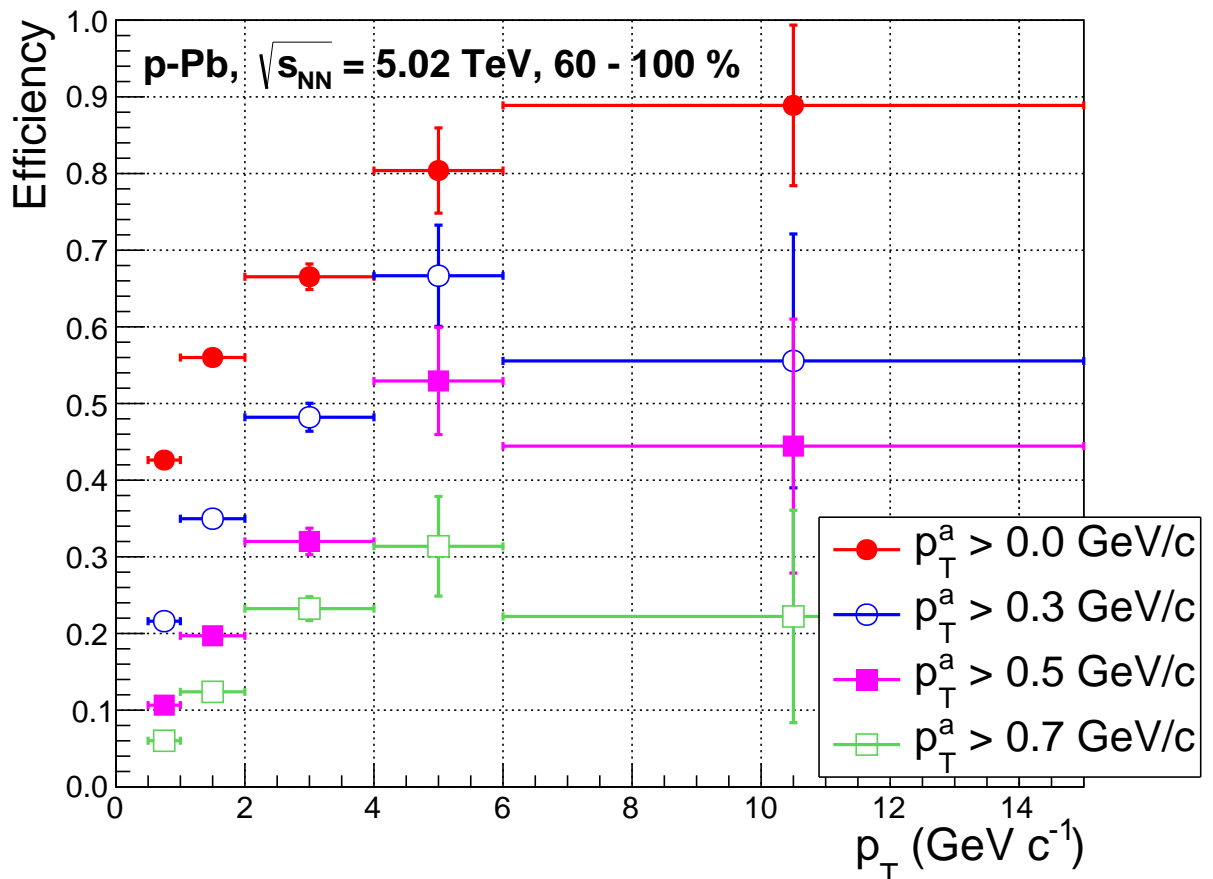
Figure 6.20: Top panel: Invariant mass distribution for unlike and like-sign pairs for $p_T^{assoc} > 0.0$ GeV/c. Bottom panel: Background finding efficiency for $p_T^{assoc} > 0.0$, 0.3, 0.5, 0.7 GeV/c. Results for low-multiplicity (60 − 100%) **p-Pb collisions [This work].**
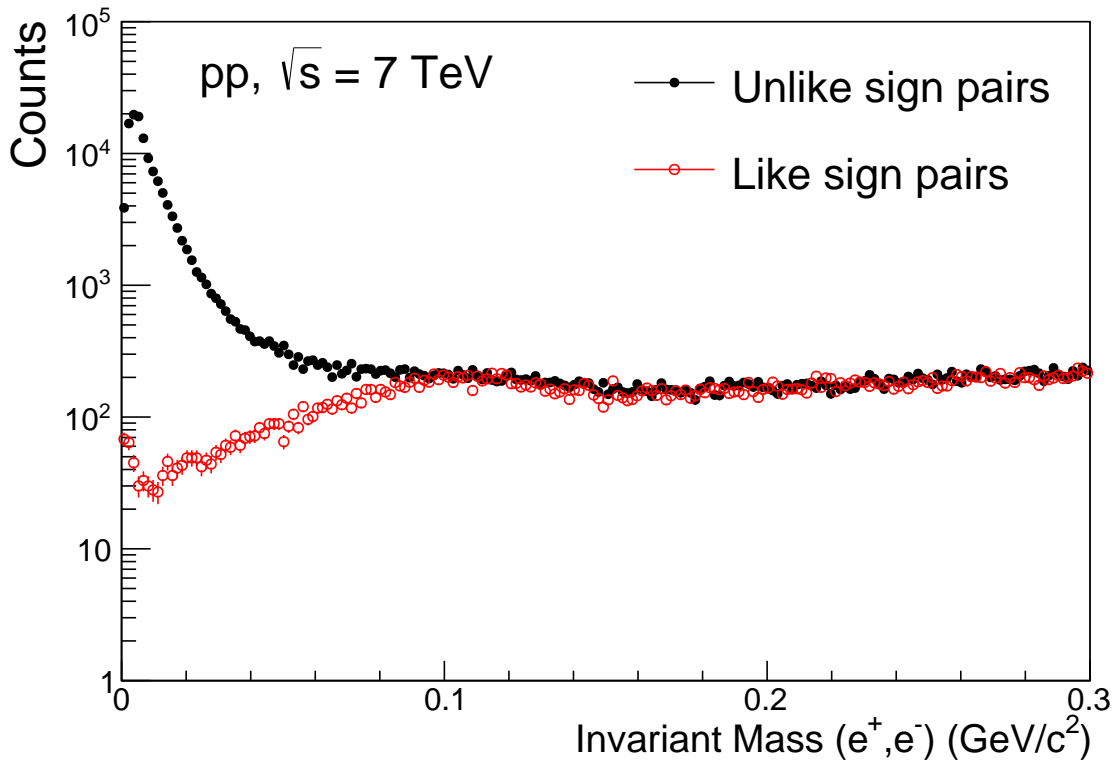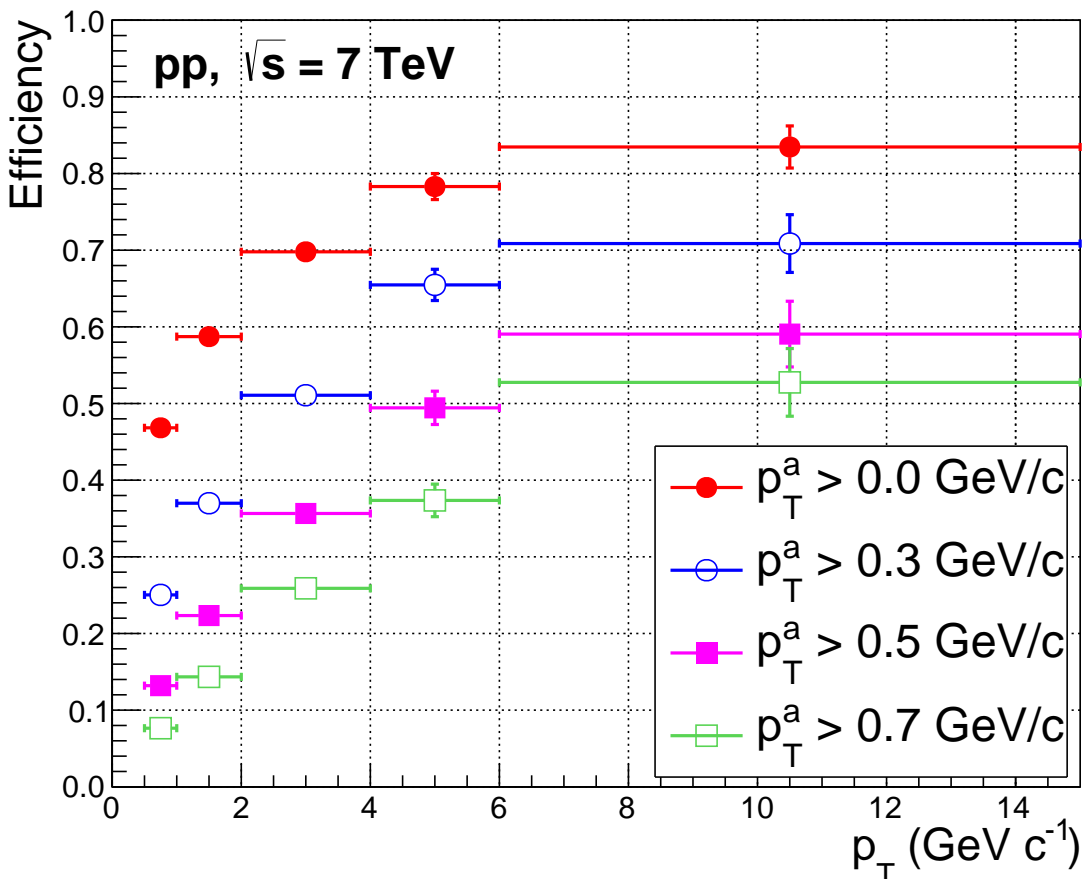
Figure 6.21: Top panel: Invariant mass distribution for unlike and like-sign pairs for $p_T^{assoc} > 0.0$ **GeV/c. Bottom panel: Background finding efficiency for** $p_T^{assoc} > 0.0$, 0.3, 0.5, 0.7 **GeV/c. Results for pp collisions [This work].**
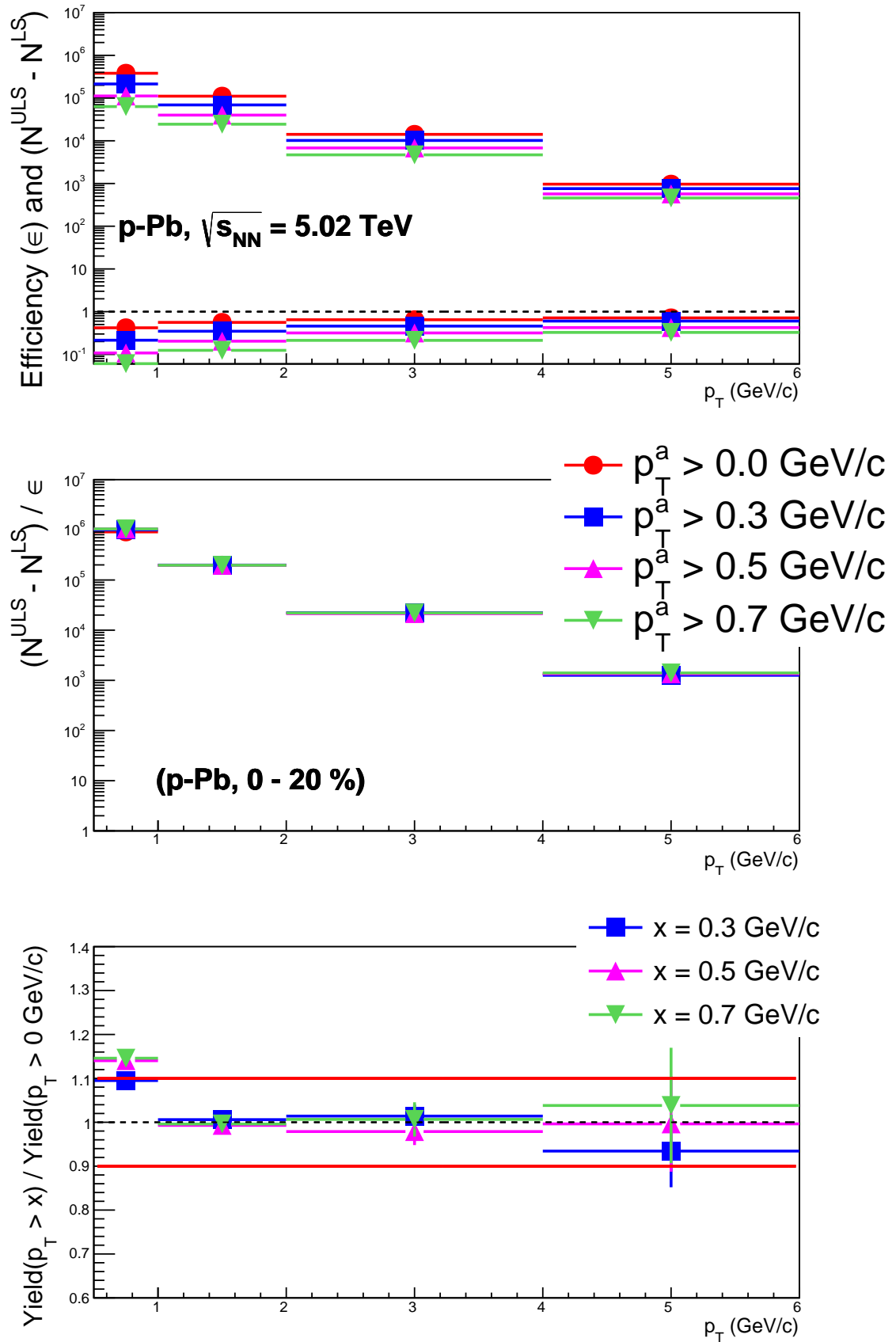
Figure 6.22: Stability test of the background reconstruction in high-multiplicity (0-20%) p-Pb collisions. The figure is explained in the text [This work].
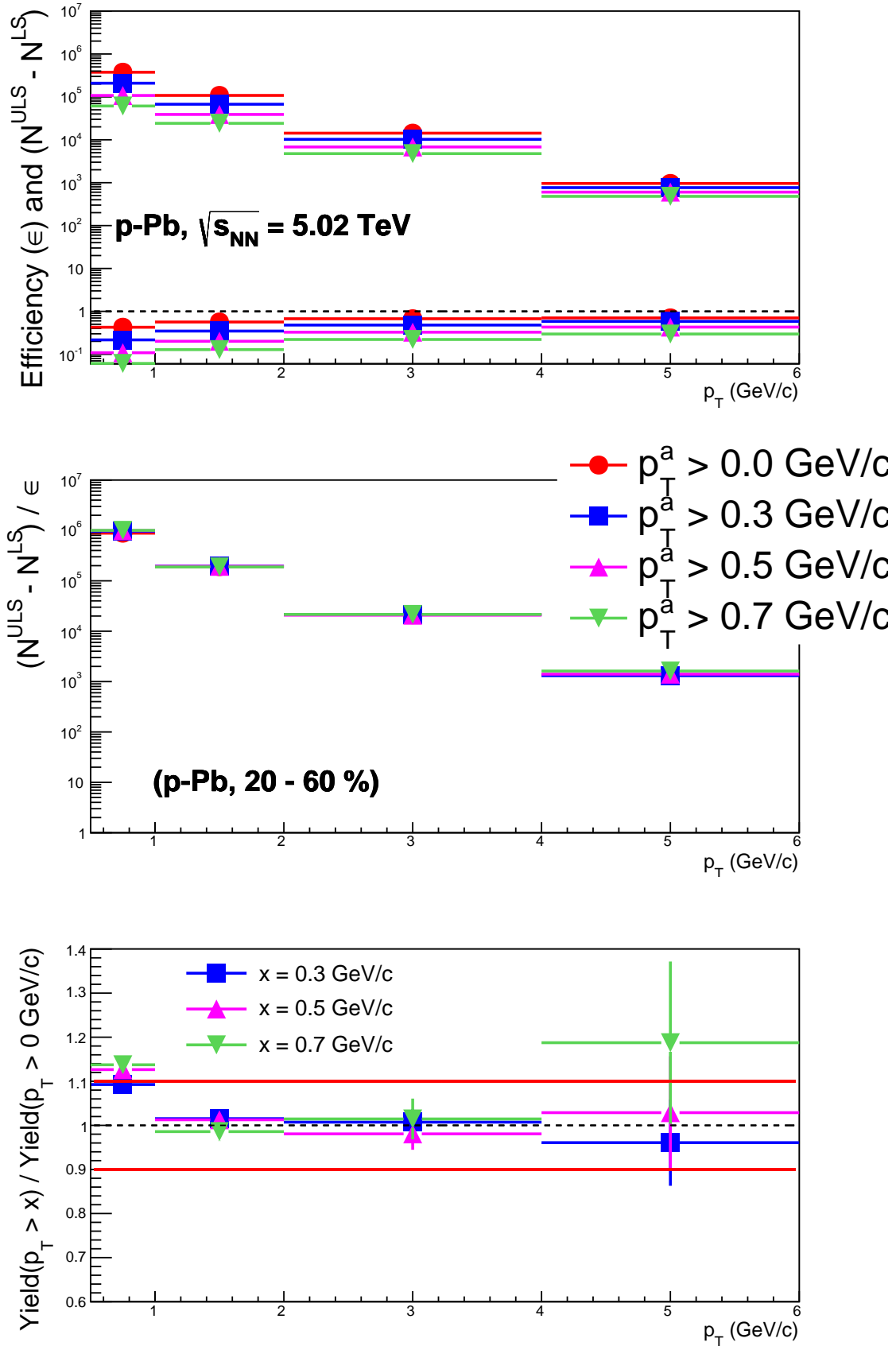
Figure 6.23: Stability test of the background reconstruction in intermediate-multiplicity (20-60%) p-Pb collisions. The figure is explained in the text [This work].
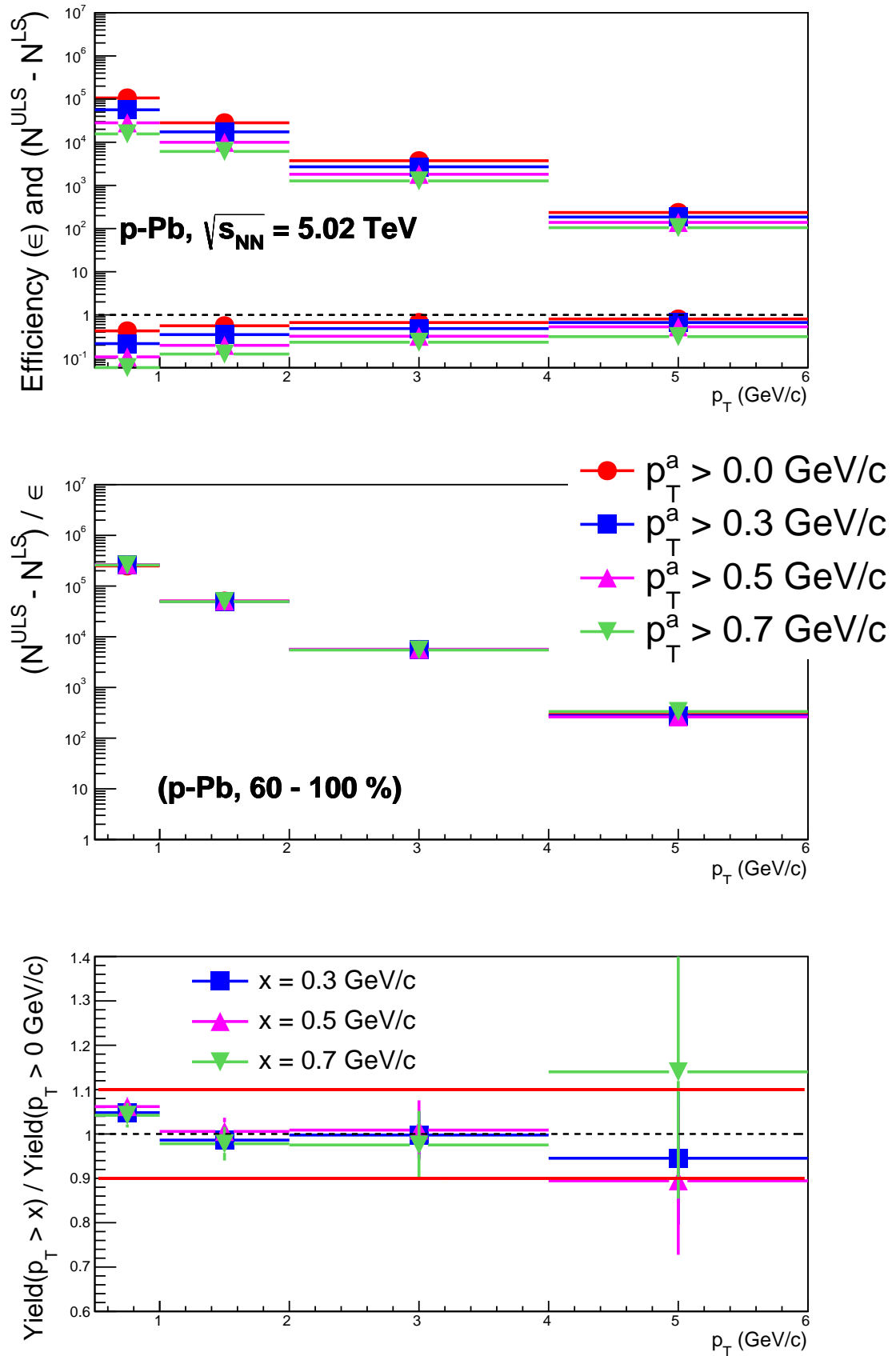
Figure 6.24: Stability test of the background reconstruction in low-multiplicity (60-100%) p-Pb collisions. The figure is explained in the text [This work].
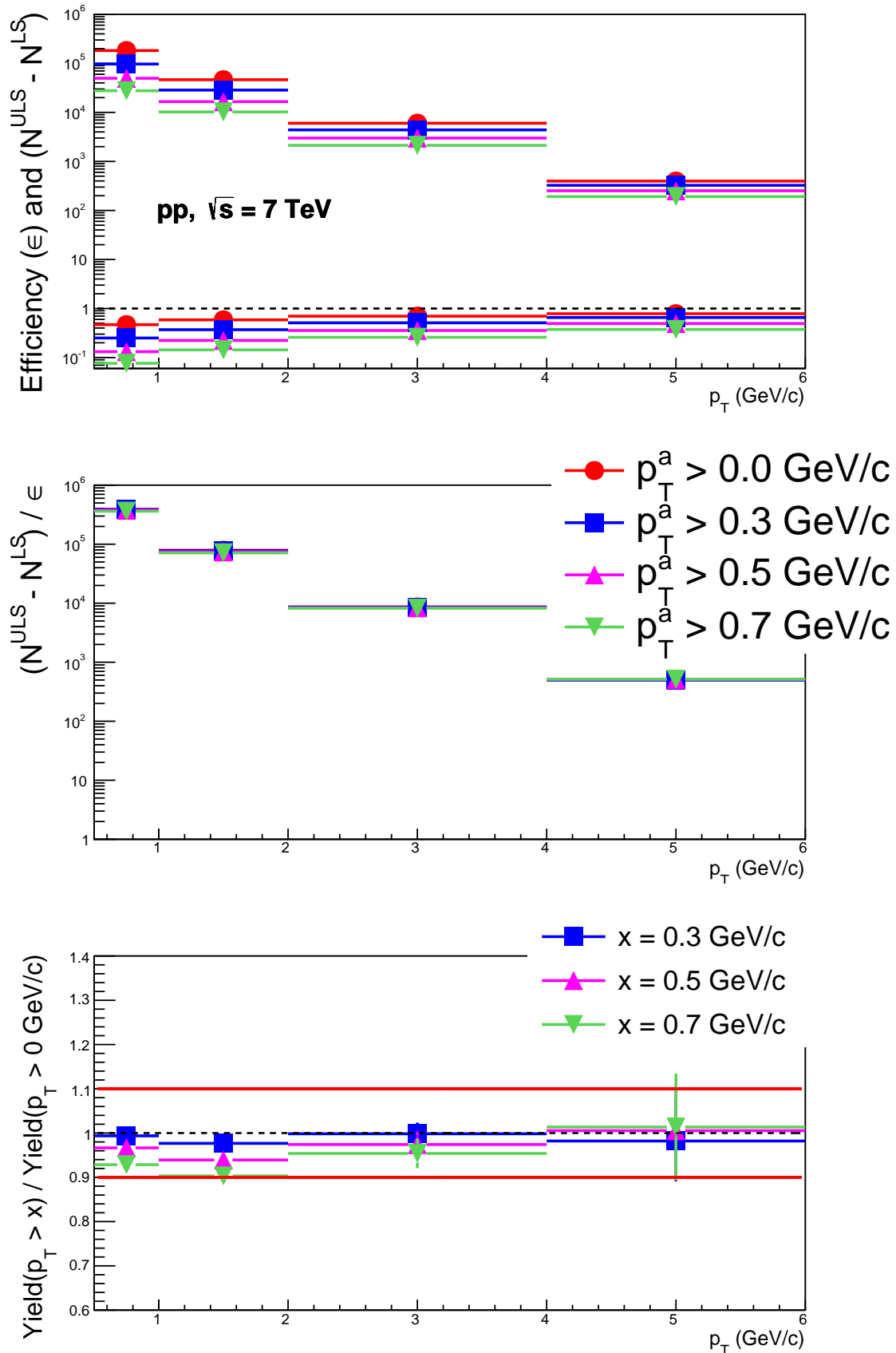
Figure 6.25: Stability test of the background reconstruction in pp collisions. The figure is explained in the text [This work].

6.4.1 Correction in the Monte Carlo input cross-section

The light meson cross-section in Monte Carlo generators can affect the reconstruction efficiency if the shape of the p_T-differential distribution is significantly different from the real distribution shape.

As an example, Figure 6.26 shows the p_T-differential cross-section of pions from a given Monte Carlo sample (black points) along with the measured distribution. The ration between MC and real data is shown on the bottom panel of the same Figure. Another example, for an alternative Monte Carlo production, for which the pion distribution differ from the first one, is shown in Figure 6.27, also with the ration between real data and simulation.

The rations shown in Figures 6.26 and 6.27 are the weights from which, the electron background distribution should be scaled, before the evaluation of the efficiency [87].

In Figure 6.28, the background reconstruction efficiency, evaluated from these two aforementioned MC samples are displayed for the cases where the weight corrections are not applied (red filled circles and back filled triangles) and after weighting correction (blue opened circles and green filled triangles). It is visible that, with correction the estimated efficiency from these two Monte Carlo samples converge to a single value, which supports the weighting correction procedure. In the calculations these corrections are considered not only for electrons from π-mesons but also for those from η-mesons and $\pi \to \gamma$ decays.
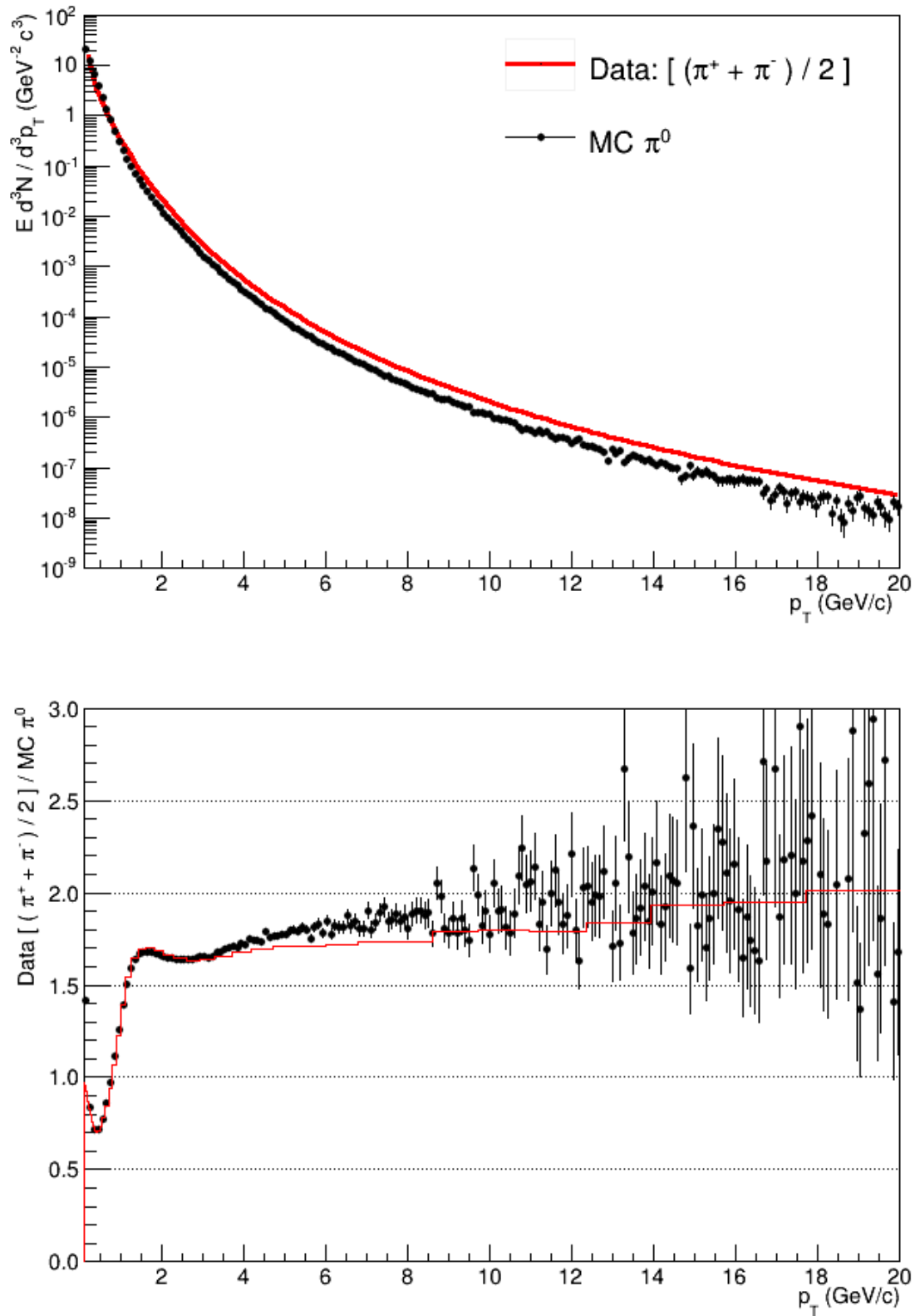
Figure 6.26: Top panel: Comparison between the p_T-differential cross-section from real data and Monte Carlo simulations in p-Pb collisions at $\sqrt{s_{NN}} = 5.02$ TeV. Bottom panel: Ration between the distributions from real data and Monte Carlo [This work]. The red line is from [87].
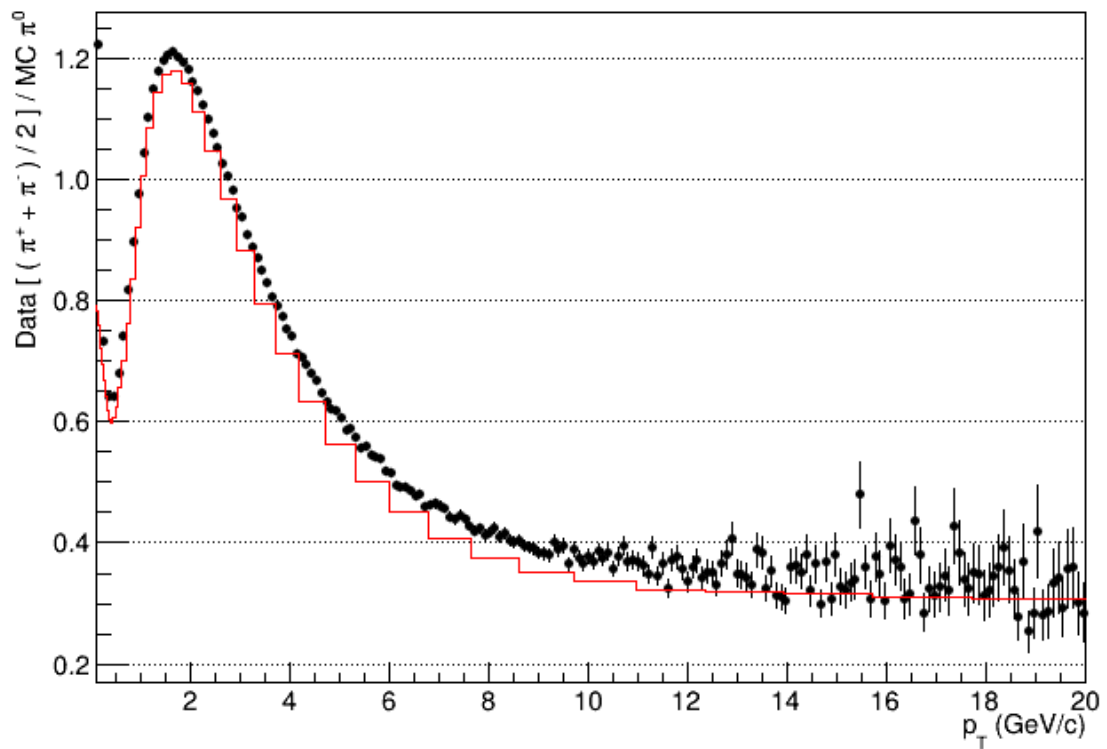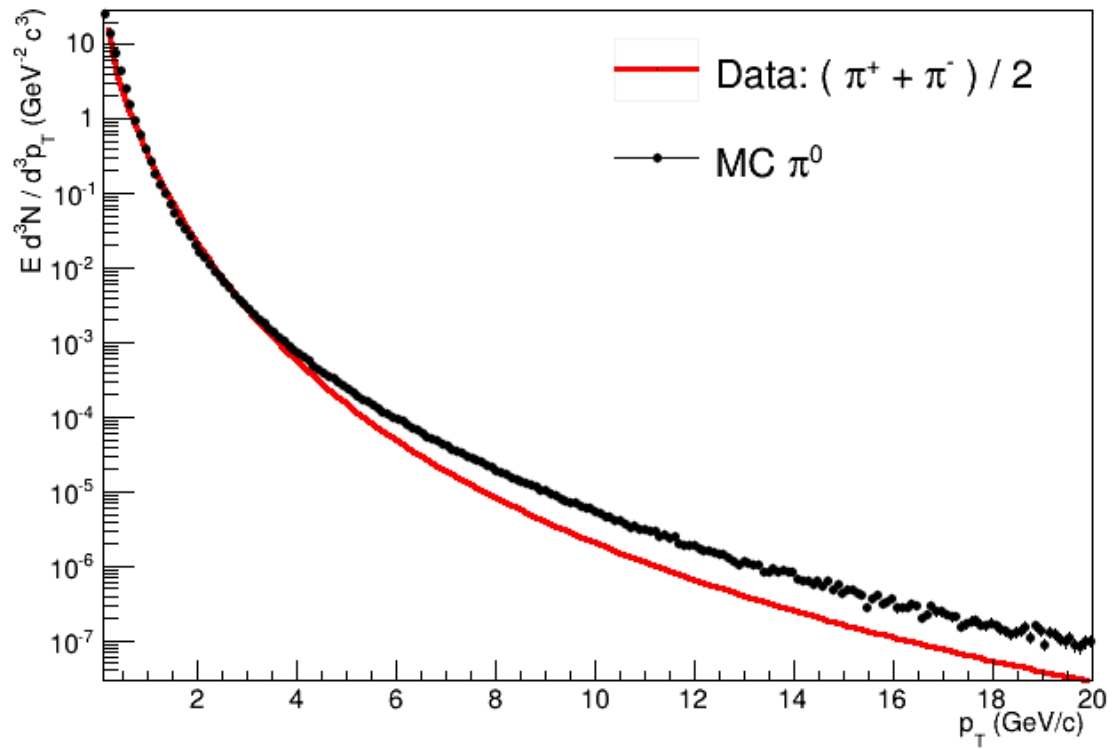
Figure 6.27: Same as in Figure 6.26 for an alternative Monte Carlo sample [This work]. The red line is from [87].
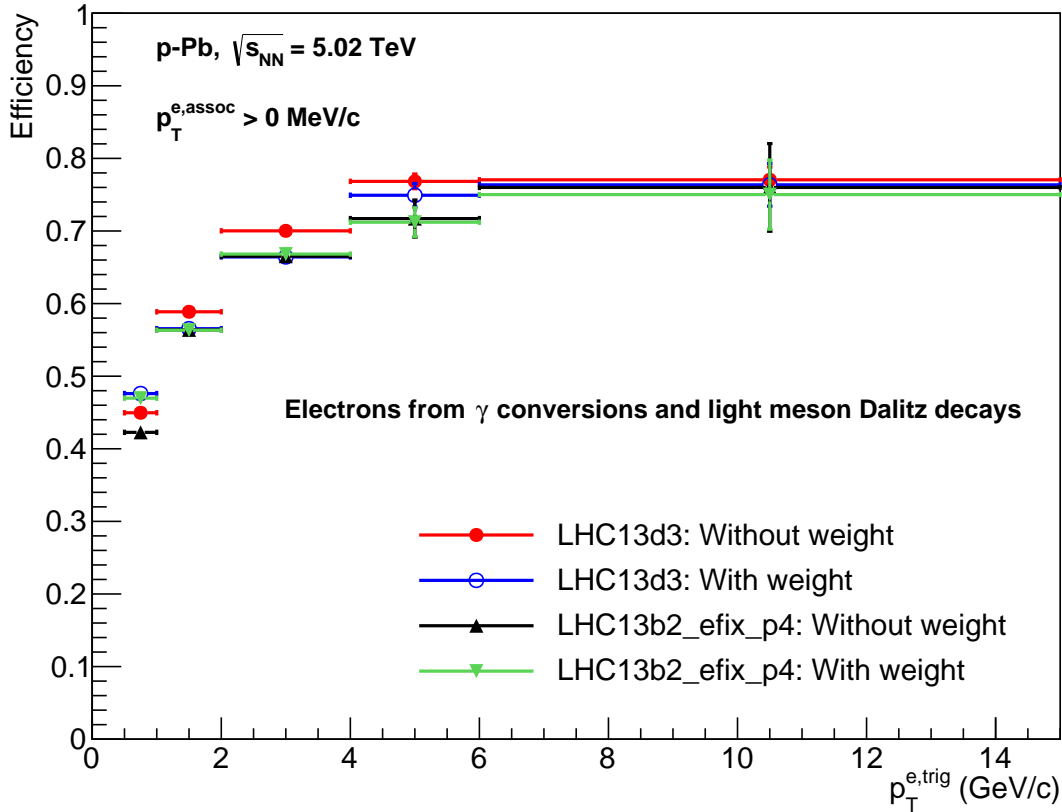
Figure 6.28: Electron background finding efficiency, as a function of p_T for two Monte Carlo samples. The results are presented for the cases where the weighting procedure is not applied (red filled circles and back filled triangles) and after the correction (blue opened circles and green filled triangles) [This work].

6.5 Correlation Function

6.5.1 Two-particle correlation function $C(\Delta\varphi, \Delta\eta; p_T^t, p_T^a)$

The two-particle correlation distribution $C(\Delta\varphi, \Delta\eta; p_T^t, p_T^a)$ is defined in Equations 6.2 to 6.4, where $S(\Delta\varphi, \Delta\eta; p_T^t, p_T^a)$ is evaluated by combining trigger-associated particle pairs from the same event and $B(\Delta\phi, \Delta\eta)$ is the mixed event correlation distribution, i. e. in B a trigger particle in one event is correlated with associated tracks from another event [64]. The latter contribution accounts for detector acceptance effects, as well as pair finding efficiency [64].

The event mixing distribution is scaled to the unity around the near side correlation peak, i. e. the normalization factor is $1/N(\Delta\phi = 0, \Delta\eta = 0)$. With it, by construction the pair-finding efficiency is 1 when the trigger and associated particle are in the same direction, i. e. if the particle are in the same direction either the two tracks are reconstructed or none of them are found.
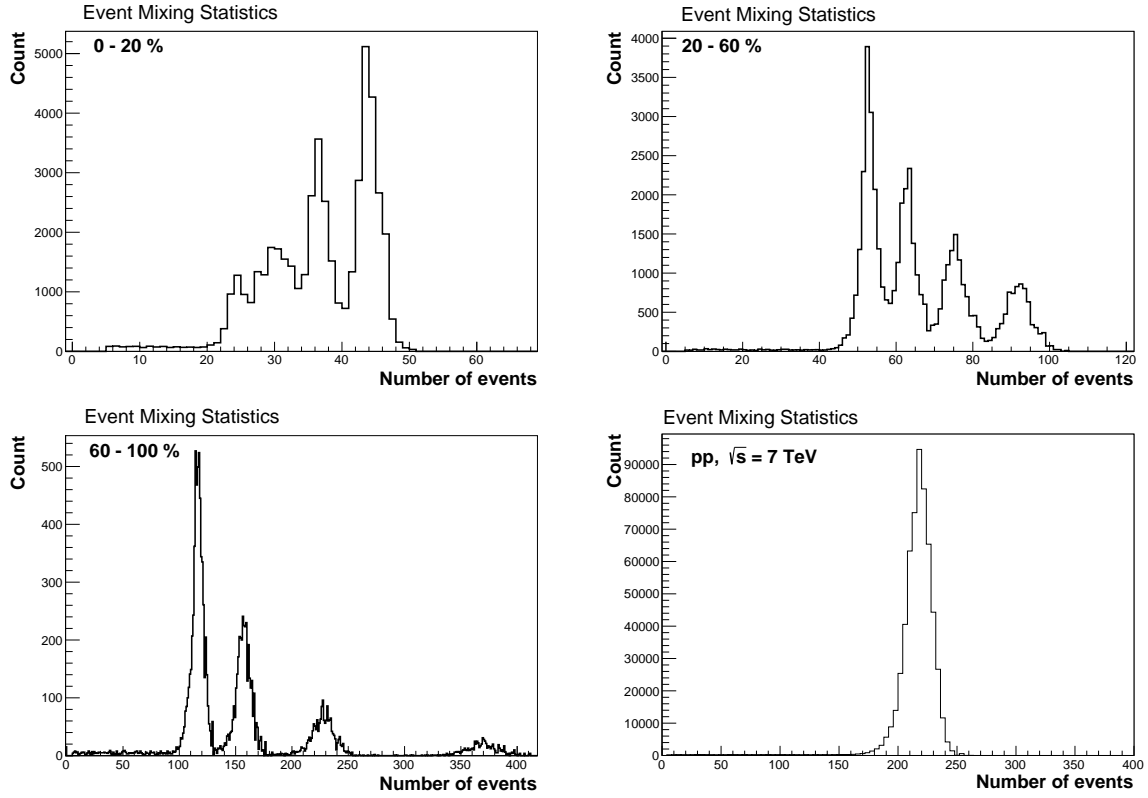
Figure 6.29: Distribution of the Number of Events with which each event was combined in the Event Mixing Analysis. Top panel: High and intermediate multiplicity classes. Bottom panel: Lowest-multiplicity class in p-Pb collisions and the distribution obtained in pp collisions [This work].

$$C(\Delta\varphi, \Delta\eta; p_T^t, p_T^a) = \frac{1}{N_{\text{trig}}} \frac{N_{\text{pairs}}(\Delta\varphi, \Delta\eta; p_T^t, p_T^a)}{\delta(\Delta\varphi)\delta(\Delta\eta)} = \frac{S(\Delta\varphi, \Delta\eta; p_T^t, p_T^a)}{B(\Delta\varphi, \Delta\eta; p_T^t, p_T^a)} \qquad (6.2)$$

$$S(\Delta\varphi, \Delta\eta; p_T^t, p_T^a) = \frac{1}{N_{\text{trig}}} \frac{N_{\text{pairs}}^{\text{Same}}(\Delta\varphi, \Delta\eta; p_T^t, p_T^a)}{\delta(\Delta\varphi)\delta(\Delta\eta)} \qquad (6.3)$$

$$B(\Delta\varphi, \Delta\eta; p_T^t, p_T^a) = \frac{1}{N(0,0)} \frac{N_{\text{pairs}}^{\text{Mixed}}(\Delta\varphi, \Delta\eta; p_T^t, p_T^a)}{\delta(\Delta\varphi)\delta(\Delta\eta)} \qquad (6.4)$$

In order to avoid a possible bias, in the event mixing technique a given particle is correlated only with particles from similar event, i. e. events within the same multiplicity class and primary vertex range. Event classes were defined in terms of multiplicity and vertex intervals. The definition of event classes are listed below:

• Multiplicity class intervals: 0, 1, 2, 3, 4, 5, 10, 20, 30, 40, 50, 60, 70, 80, 90, 100.1;

• Primary vertex intervals: -10, -7, -5, -3, -1, 1, 3, 5, 7, 10;

In the mixed event analysis, each event is combined with at least 5 other events. Figure 6.29 shows the distribution of the number of events with which each event was combined.

These distributions are presented for the three multiplicity classes considered in the p-Pb analysis and for the pp collisions.

6.5.2   Heavy-flavour decay electrons

The correlation distribution triggered by heavy-flavour decay electrons $N_{\mathrm{HFE}}(\Delta\phi, \Delta\eta)$ is built using Equation 6.5 (see also the discussion in [80, 86]), where $N^*_{\mathrm{Inc}}(\Delta\phi, \Delta\eta)$, given by Equation 6.6, is the correlation function between inclusive electrons and charged particles, corrected for the hadron contamination $(\alpha) N_{\mathrm{h-h}}(\Delta\phi, \Delta\eta)$, where α is the contamination factor defined in Equation 6.8 and obtained from the fits in the TPC Nσ distributions, discussed in Section 6.3.

$N^{\mathrm{Found}}_{\mathrm{NonHFE}}(\Delta\phi, \Delta\eta)$ corresponds to the reconstructed background, those electrons coming mostly from gamma conversion and π^0 Dalitz decays, while $\left(\frac{1}{\epsilon} - 1\right) N^{\mathrm{Found}*}_{\mathrm{NonHFE}}(\Delta\phi, \Delta\eta)$ accounts for the non-reconstructed background, where ϵ is the background finding efficiency and $N^{\mathrm{Found}*}_{\mathrm{NonHFE}}$ corresponds to the electron background ($N^{\mathrm{Found}}_{\mathrm{NonHFE}}$) after the removal of the electron (positron) partner in the correlation distribution.

This correction (the partner exclusion) is needed in order to avoid a bias in the near side peak. A true electron-positron pair contributes in the reconstructed correlation distribution but not in the non-reconstructed term. A detailed discussion on this correction can also be found in [86].

Furthermore, a correction accounting for the track reconstruction efficiency $\epsilon_{\mathrm{tracking}}$ is applied, as indicated in Equation 6.7. This is needed for a proper evaluation of the associated per-trigger particle yield, which is presented in Chapter 8.

$$N_{\mathrm{HFE}}(\Delta\phi, \Delta\eta) = N^*_{\mathrm{Inc}}(\Delta\phi, \Delta\eta) - N^{\mathrm{Found}}_{\mathrm{NonHFE}}(\Delta\phi, \Delta\eta) - \left(\frac{1}{\epsilon} - 1\right) N^{\mathrm{Found}*}_{\mathrm{NonHFE}}(\Delta\phi, \Delta\eta) \tag{6.5}$$

$$N^*_{\mathrm{Inc}}(\Delta\phi, \Delta\eta) = N_{\mathrm{Inc}}(\Delta\phi, \Delta\eta) - (\alpha) N_{\mathrm{h-h}}(\Delta\phi, \Delta\eta) \tag{6.6}$$

$$N^*_{\mathrm{HFE}}(\Delta\phi, \Delta\eta) = N_{\mathrm{HFE}}(\Delta\phi, \Delta\eta)/\epsilon_{\mathrm{tracking}} \tag{6.7}$$

$$\alpha = (N/N_{\mathrm{trig}}) x N_{\mathrm{hadron}} \tag{6.8}$$

In the following, the same-event correlation distribution ($S(\Delta\varphi, \Delta\eta; p^t_{\mathrm{T}}, p^a_{\mathrm{T}})$) and that evaluated by mixing event ($B(\Delta\varphi, \Delta\eta; p^t_{\mathrm{T}}, p^a_{\mathrm{T}})$) are shown, for the three classes of multiplicity in p-Pb collisions at $\sqrt{s_{\mathrm{NN}}} = 5.02$ TeV and for pp collisions at $\sqrt{s} = 7$ TeV.

The final (fully corrected) angular correlation function, between heavy-flavour decay electrons and charged unidentified particles $C(\Delta\varphi, \Delta\eta; p^t_{\mathrm{T}}, p^a_{\mathrm{T}}) = \frac{S(\Delta\varphi, \Delta\eta; p^t_{\mathrm{T}}, p^a_{\mathrm{T}})}{B(\Delta\varphi, \Delta\eta; p^t_{\mathrm{T}}, p^a_{\mathrm{T}})}$, in the ($\Delta\varphi, \Delta\eta$) space, will also be presented.

Same Event ($S(\Delta\varphi, \Delta\eta; p_T^t, p_T^a)$)
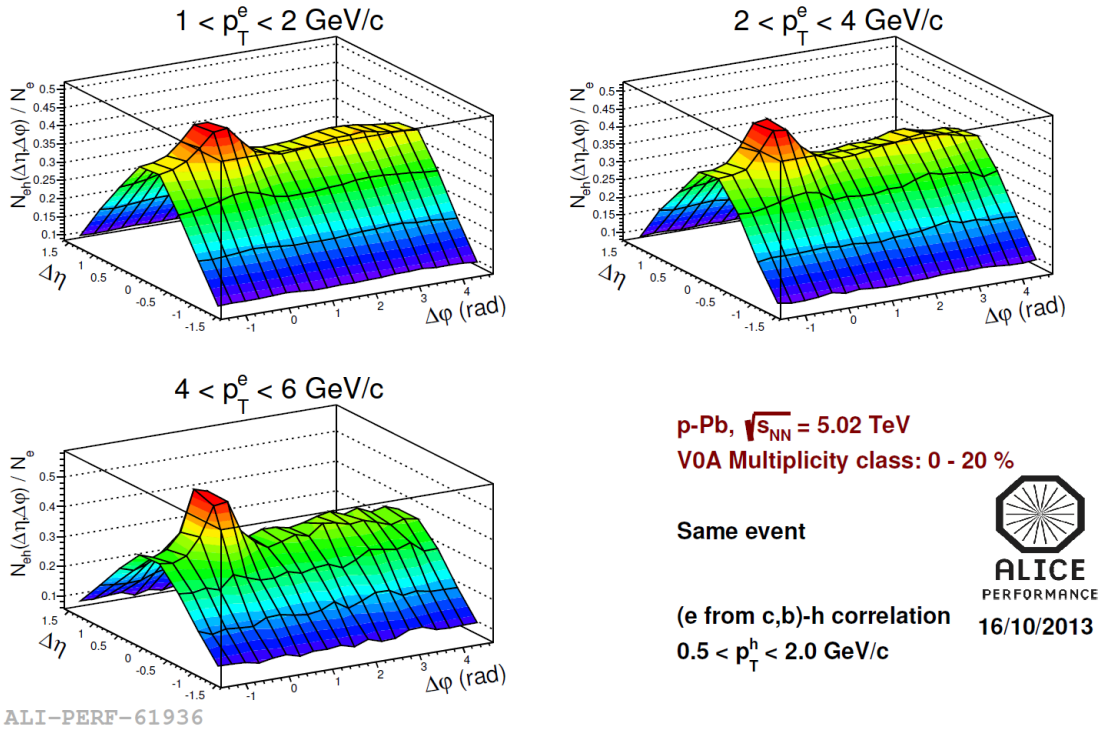
Figure 6.30: Same-event correlation, in $\Delta\varphi$ and $\Delta\eta$, between heavy-flavour decay electrons and unidentified charged particles in p-Pb collisions (0-20%) [This work].
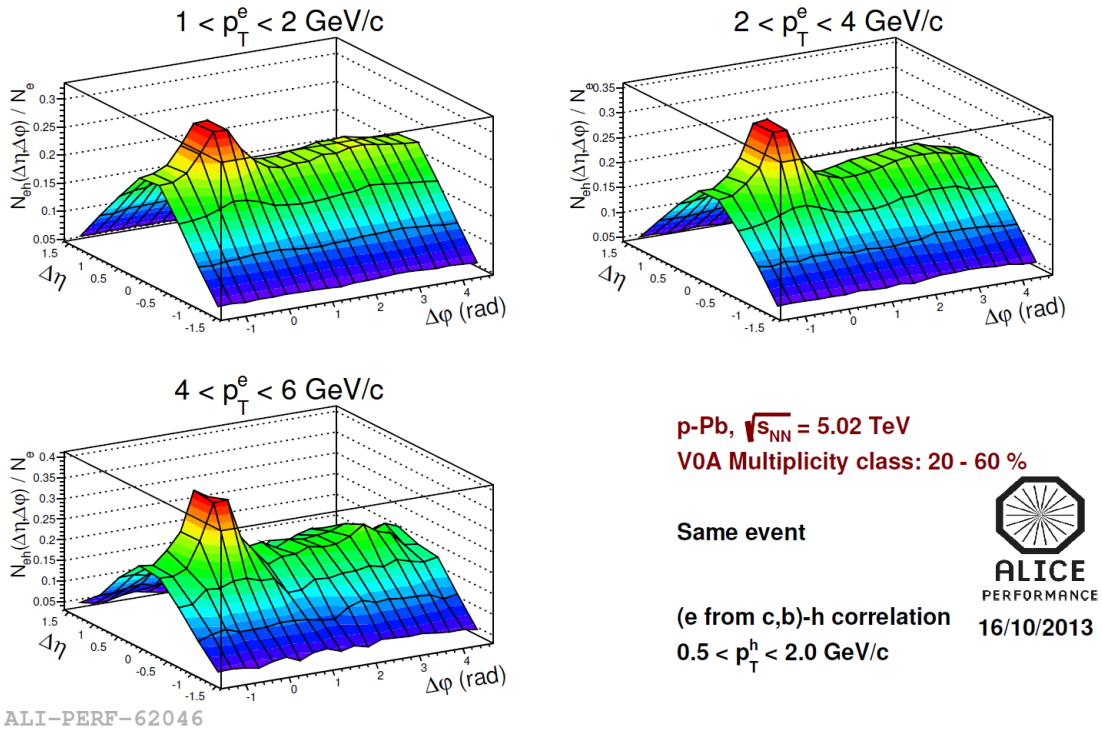
Figure 6.31: Same-event correlation, in $\Delta\varphi$ and $\Delta\eta$, between heavy-flavour decay electrons and unidentified charged particles in p-Pb collisions (20-60%) [This work].
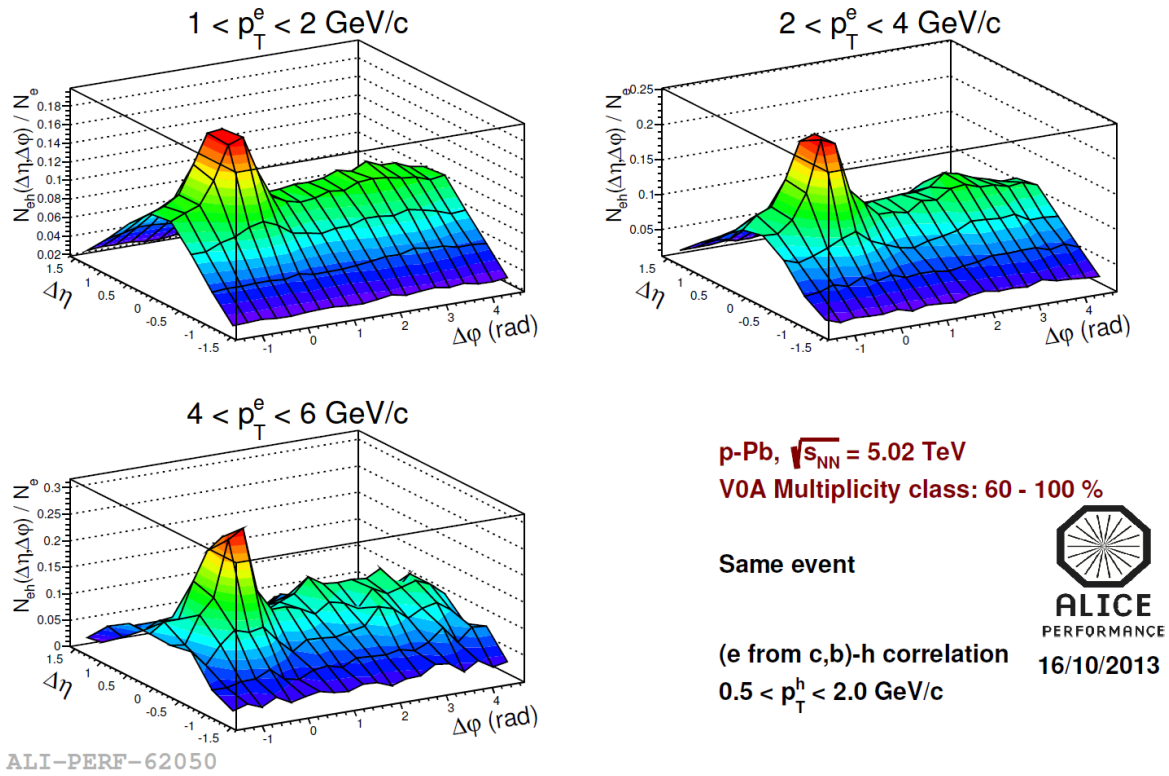
Figure 6.32: Same-event correlation, in $\Delta\varphi$ and $\Delta\eta$, between heavy-flavour decay electrons and unidentified charged particles in p-Pb collisions (60-100%) [This work].
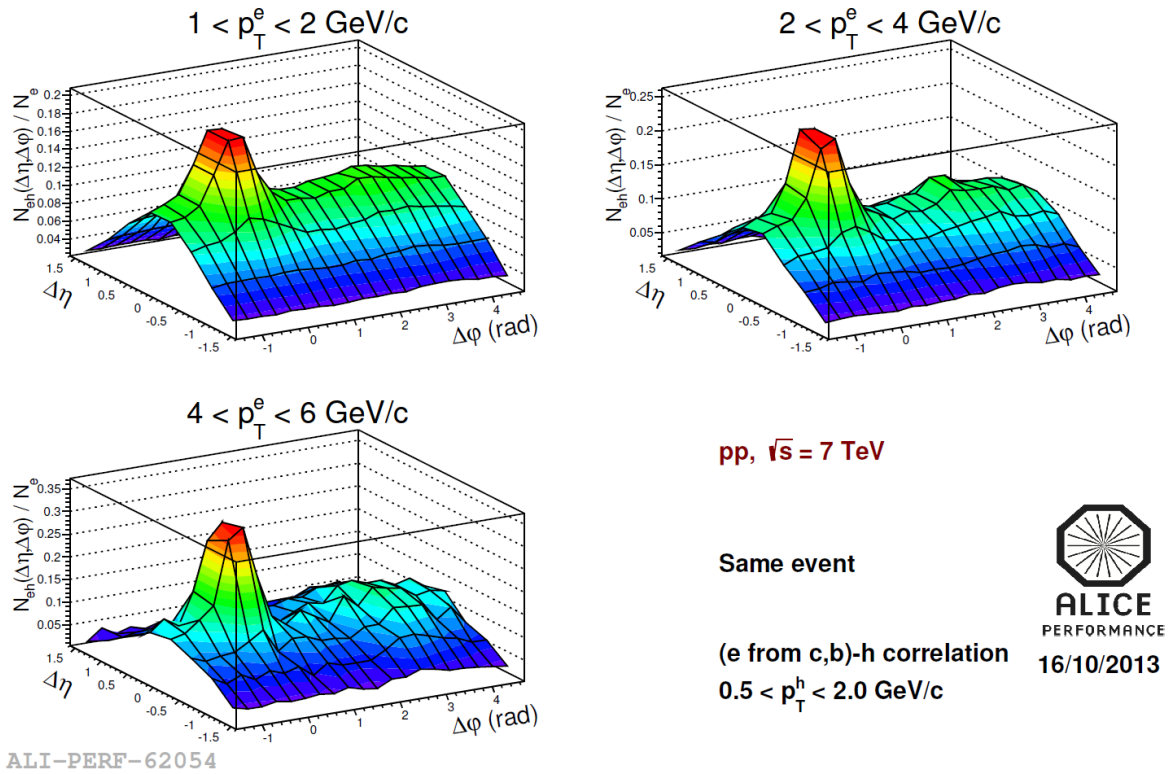
Figure 6.33: Same-event correlation, in $\Delta\varphi$ and $\Delta\eta$, between heavy-flavour decay electrons and unidentified charged particles in pp collisions [This work].

Mixed Event $(B(\Delta\varphi, \Delta\eta; p_{\mathrm{T}}^{t}, p_{\mathrm{T}}^{a}))$
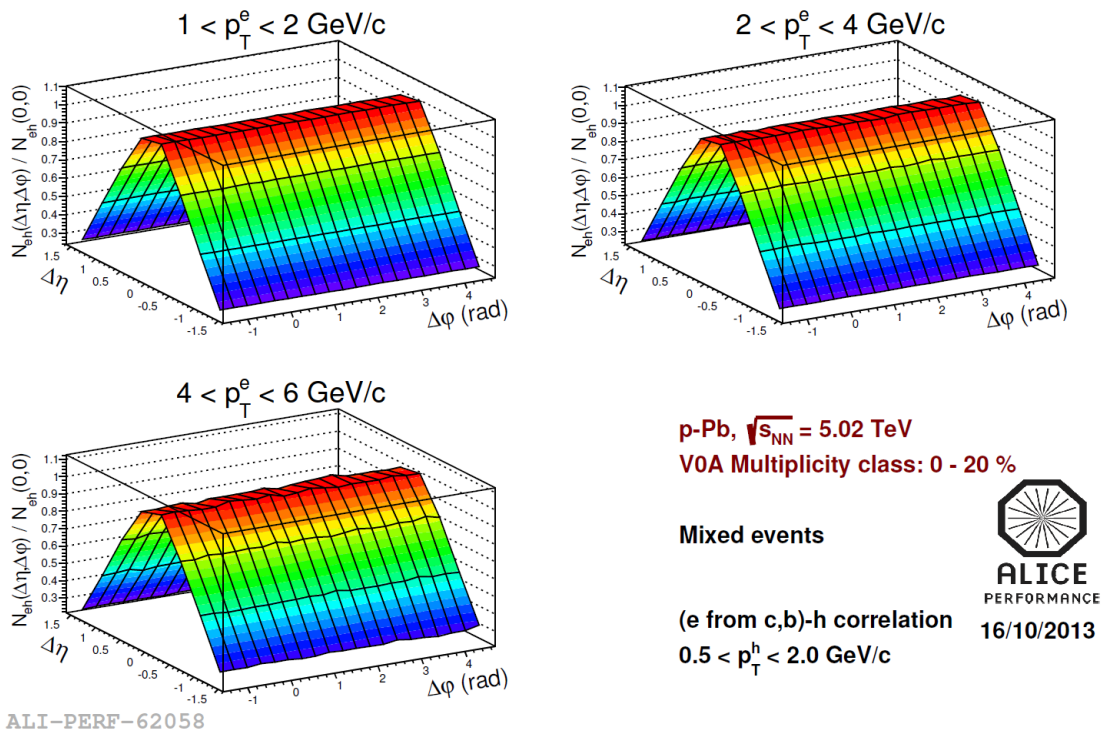
Figure 6.34: **Mixed-event correlation, in $\Delta\varphi$ and $\Delta\eta$, between heavy-flavour decay electrons and unidentified charged particles in p-Pb collisions (0-20%) [This work].**
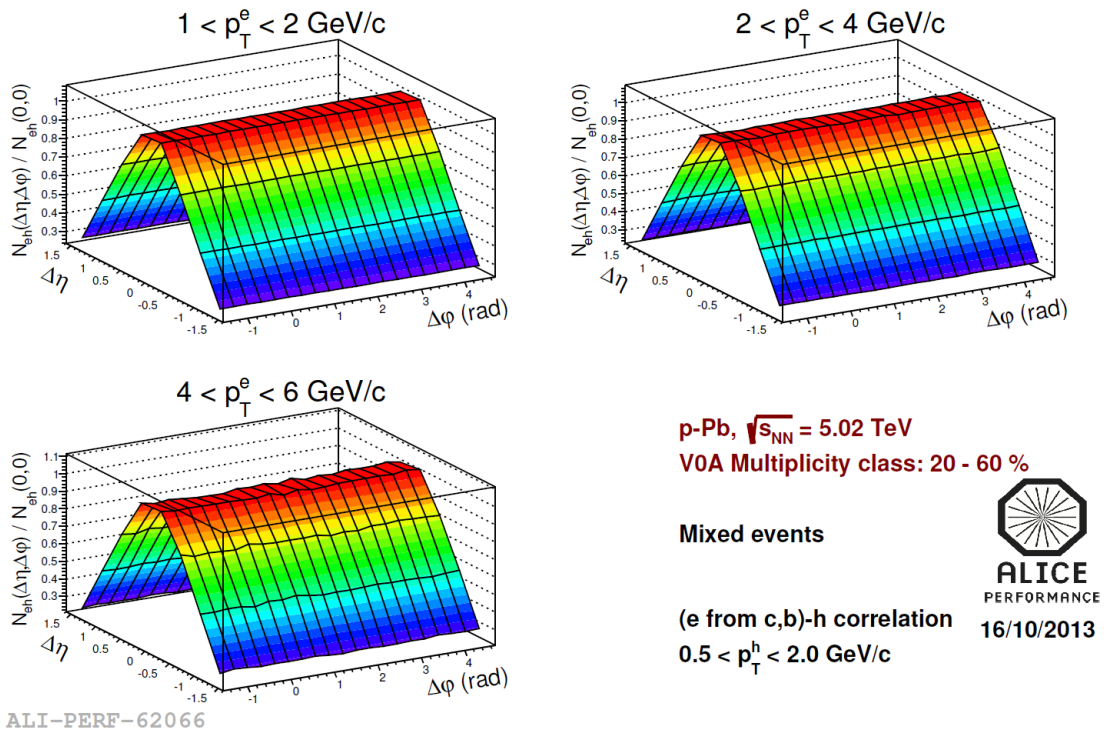
Figure 6.35: **Mixed-event correlation, in $\Delta\varphi$ and $\Delta\eta$, between heavy-flavour decay electrons and unidentified charged particles in p-Pb collisions (20-60%) [This work].**
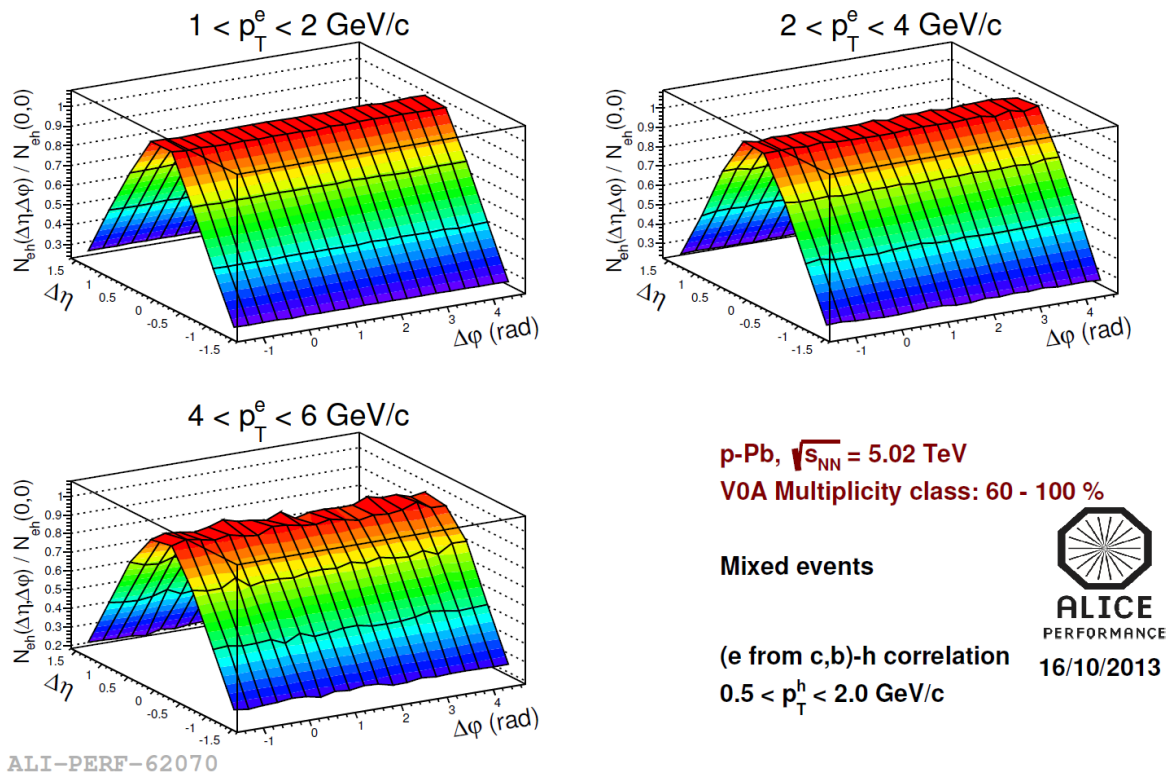
Figure 6.36: Mixed-event correlation, in $\Delta\varphi$ and $\Delta\eta$, between heavy-flavour decay electrons and unidentified charged particles in p-Pb collisions (60-100%) [This work].
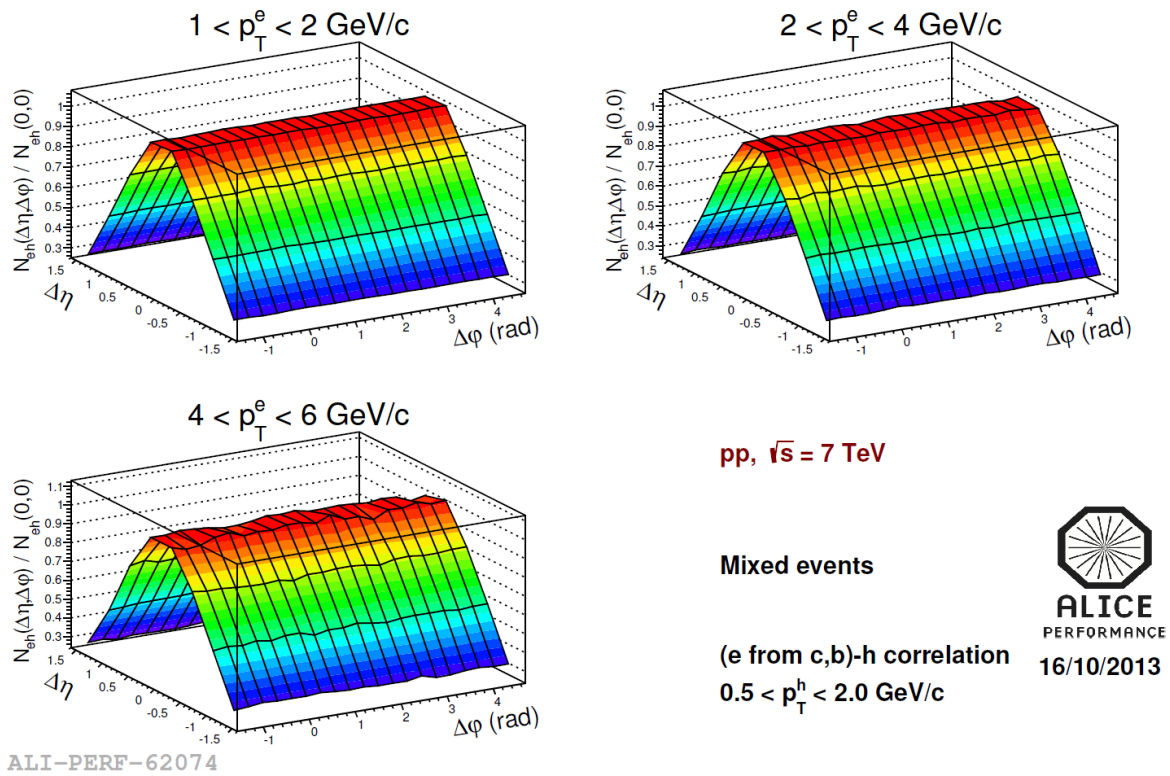
Figure 6.37: Mixed-event correlation, in $\Delta\varphi$ and $\Delta\eta$, between heavy-flavour decay electrons and unidentified charged particles in pp collisions [This work].

Correlation function $(C(\Delta\varphi, \Delta\eta; p_T^t, p_T^a))$
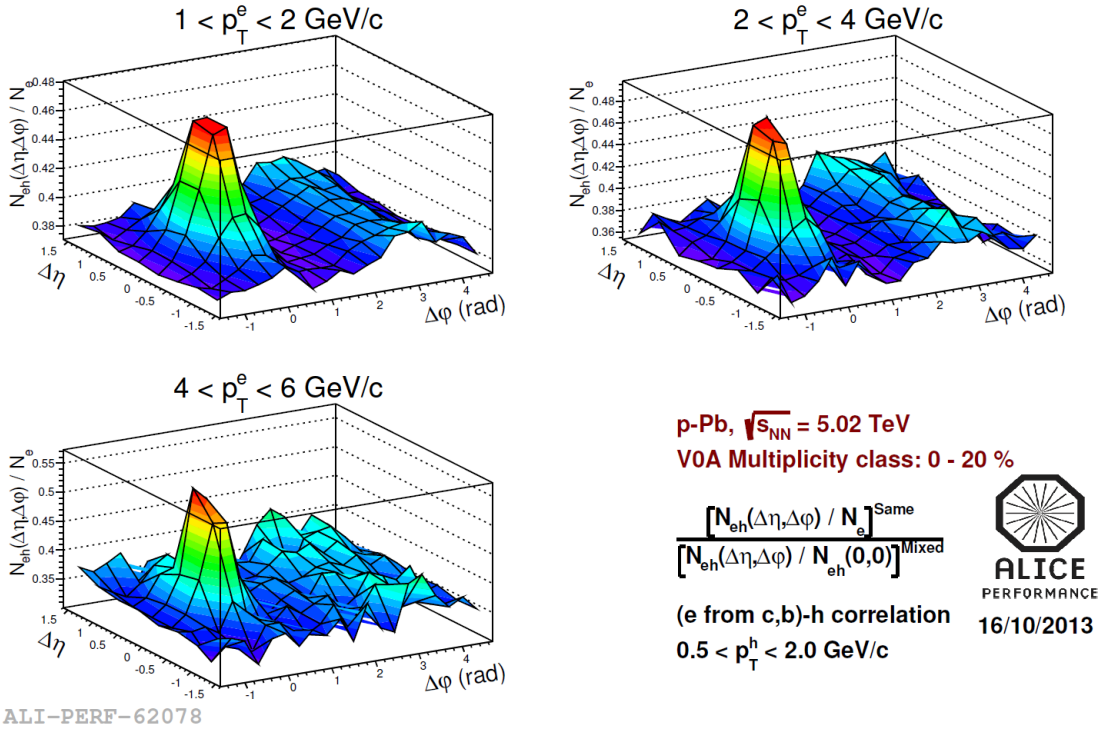
Figure 6.38: Correlation, in $\Delta\varphi$ and $\Delta\eta$, between heavy-flavour decay electrons and unidentified charged particles in p-Pb collisions (0-20%) [This work].
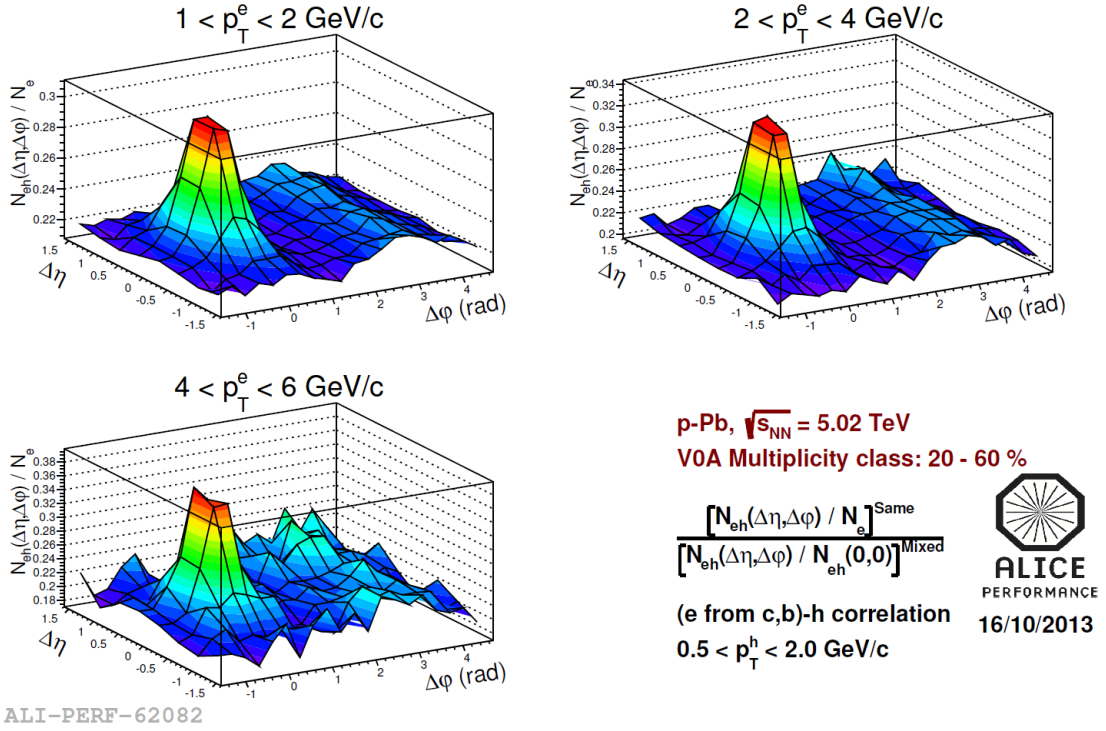
Figure 6.39: Mixed-event correlation, in $\Delta\varphi$ and $\Delta\eta$, between heavy-flavour decay electrons and unidentified charged particles in p-Pb collisions (20-60%) [This work].
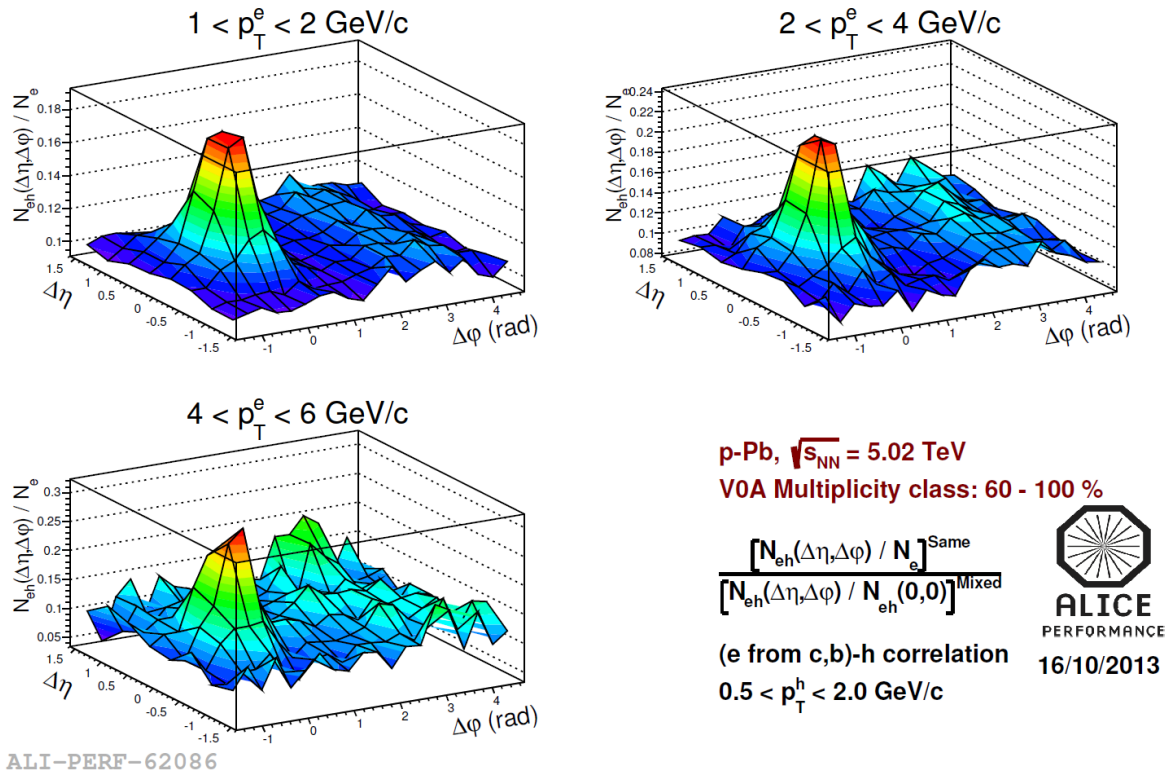
Figure 6.40: Correlation, in $\Delta\varphi$ and $\Delta\eta$, between heavy-flavour decay electrons and unidentified charged particles in p-Pb collisions (60-100%) [This work].
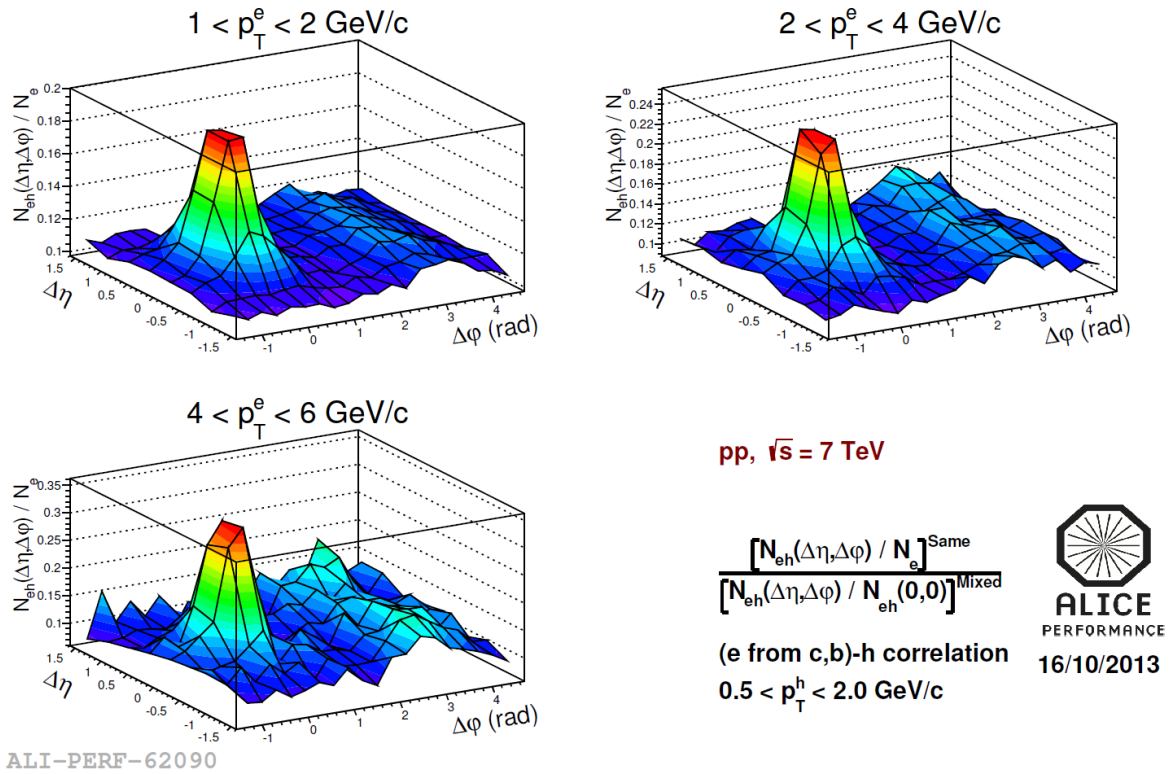
Figure 6.41: Correlation, in $\Delta\varphi$ and $\Delta\eta$, between heavy-flavour decay electrons and unidentified charged particles in pp collisions [This work].

6.5.3 Correlation distribution in azimuth and in pseudorapidity

In order to quantify the correlation distribution, the projections on azimuth and on pseudorapidity is evaluated, i. e. the angular distribution presented in Figures 6.38 to 6.41) are projected on $\Delta\varphi$ and on $\Delta\eta$ and the results are the correlation distributions $\mathrm{d}N/\mathrm{d}\Delta\varphi$ and $\mathrm{d}N/\mathrm{d}\Delta\eta$.

After the projection, these correlation functions are parametrized by Equations 6.9 and 6.10 for the $\Delta\varphi$ and $\Delta\eta$ distributions, respectively. More precisely, these Equations are fitted to the measured distributions from which, the correlation strengths are evaluated, such as the yield of associated per-trigger particle and width in the near and, in case of $\Delta\phi$, in the away-side correlation peak. In these fit functions, B is a free parameter accounting for the baseline due to uncorrelated electron-hadron pairs.

$$C(\Delta\varphi; p_{\mathrm{T}}^t, p_{\mathrm{T}}^a) = \mathrm{B} + \mathrm{Gauss}(\Delta\varphi = \pi/2) + \mathrm{Gauss}(\Delta\varphi = 3\pi/2) \tag{6.9}$$

$$C(\Delta\eta; p_{\mathrm{T}}^t, p_{\mathrm{T}}^a) = \mathrm{B} + \mathrm{Gauss}(\Delta\eta = 0) \tag{6.10}$$

Figures 6.43 to 6.47 shows the azimuthal correlation distributions for the three classes of multiplicity in p-Pb and in pp collisions. These angular correlations are shown along with the fitted two-gaussian functions (Equation 6.9) and, for the two highest-multiplicity class in the lower p_{T} interval, the fit function is added by a Fourier modulation, of which the motivation will be clear from the discussion provided in Chapter 8.

The projection of the correlation distributions on $\Delta\eta$ are presented in Figures Figures 6.49 to 6.53. The fitted functions are also displayed in these figures from where the near-side yield and width were evaluated. The main motivation of studying the projection on pseudorapidity as well as the results of this work is presented in Appendix B.

Just as a short introduction on the subject, the evaluation of v_2 from the measured azimuthal correlation distribution turned out to have some ambiguities involved, since, the flow modification to be fitted with the Fourier coefficients might include a contribution from jet yield modification on it. Looking into the $\Delta\eta$ projection is one of the proposed alternatives to disentangle collective effects from jet-yield modification in p-Pb collisions. However this work is still ongoing and the current status is presented in Appendix B.

This work has, however, focused on the $\Delta\varphi$ projection and the yield in the near and away-side was evaluated as a function of multiplicity in p-Pb collision and in pp collisions. Particularly interesting is the comparison between high and low-multiplicity events in p-Pb reactions. These results and detailed discussion is the subject of Chapter 8.

In the following, every projection plot, for the $\Delta\varphi$ projection as well as for the $\Delta\eta$ projection are presented, along with the aforementioned fit.
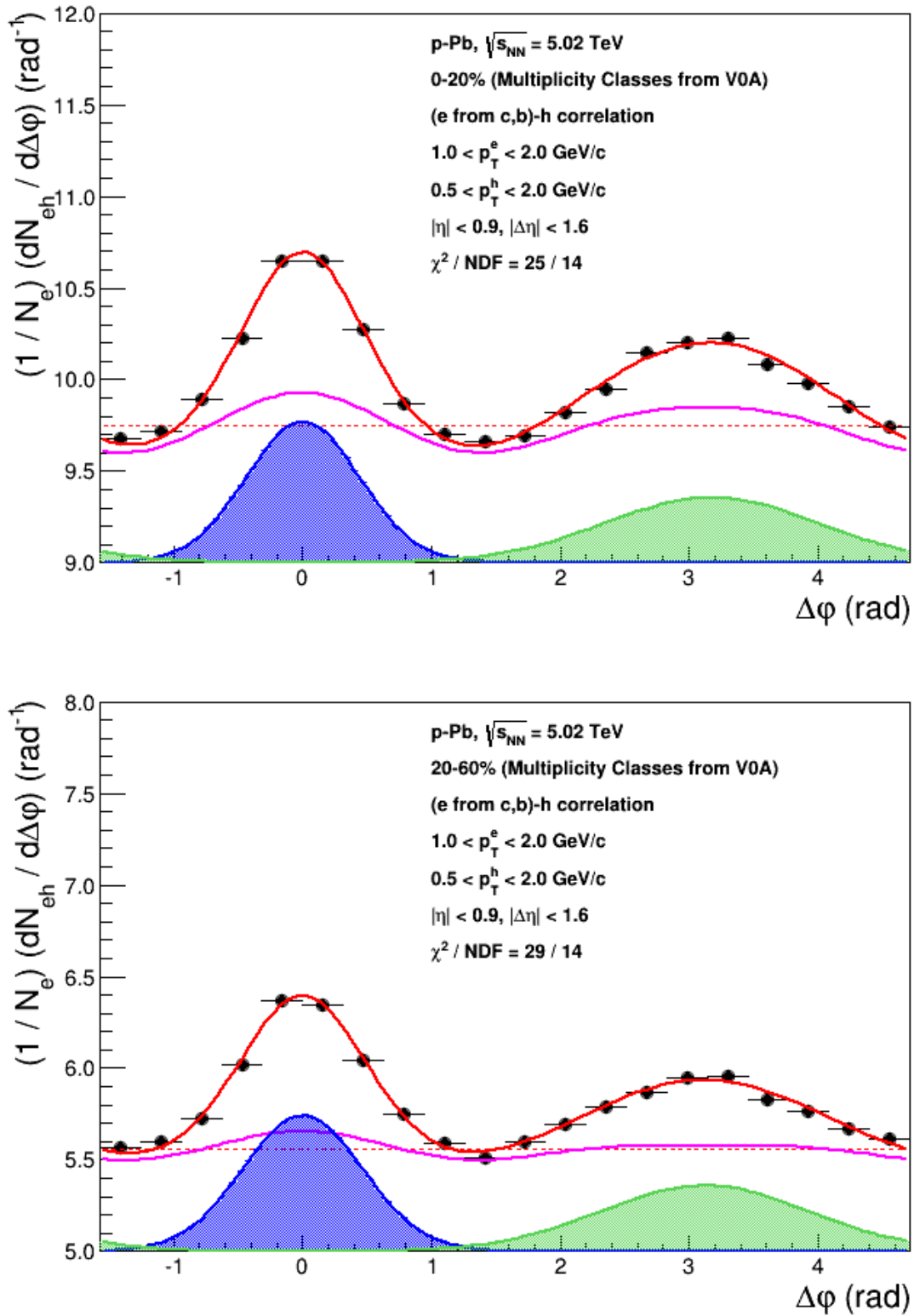
Figure 6.42: **Azimuthal correlation distribution between heavy-flavour decay electrons and charged unidentified particles in p-Pb and pp collisions for** $1 < p_T^e < 2$ **GeV/c. The results are presented for high (top panel) and intermediary-multiplicity (bottom panel) p-Pb collisions. The filled regions represent the estimated yields [This work].**
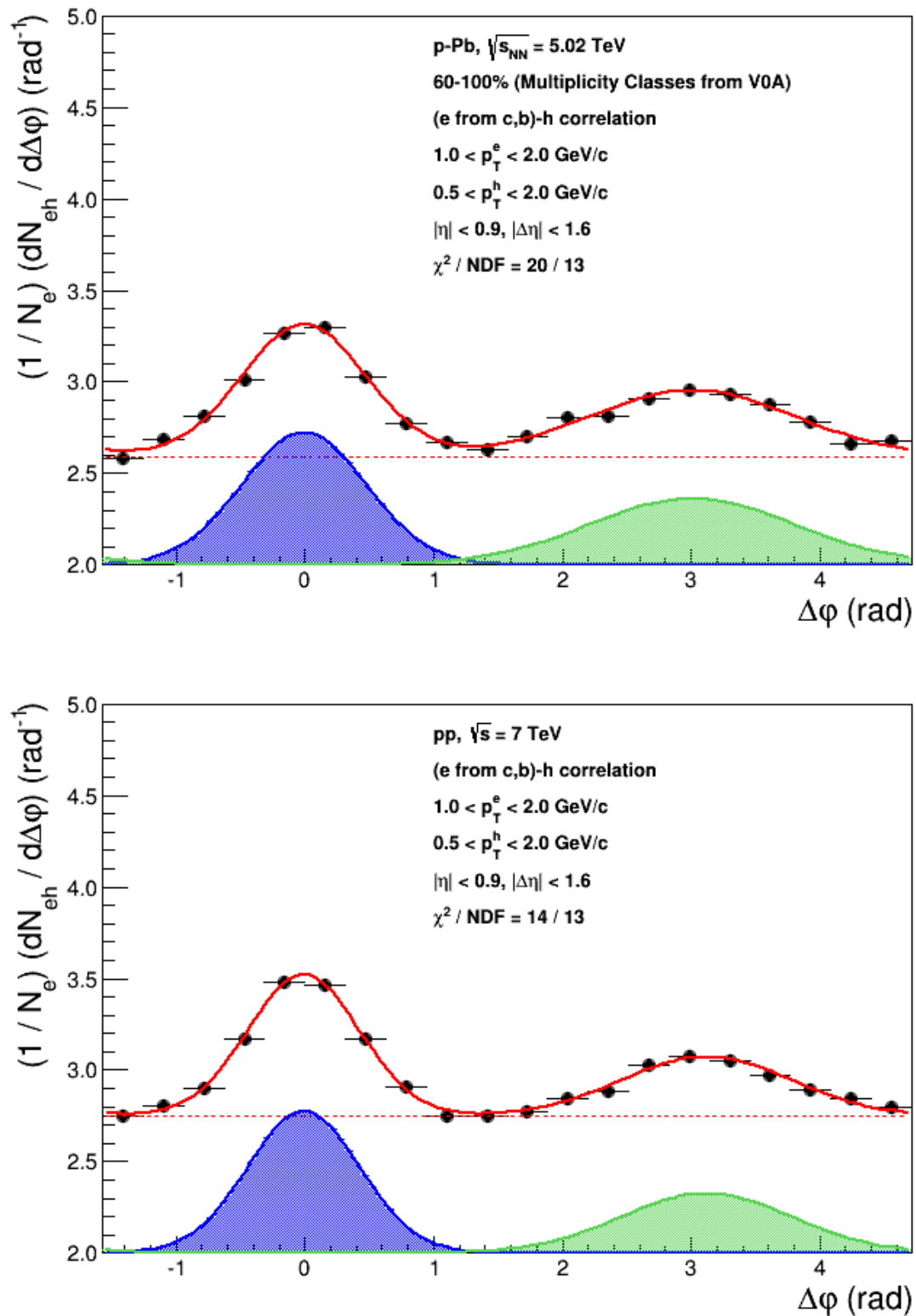
Figure 6.43: **Azimuthal correlation distribution between heavy-flavour decay electrons and charged unidentified particles in p-Pb and pp collisions for** $1 < p_T^e < 2$ **GeV/**c**. The results are presented for low-multiplicity p-Pb collisions (top panel) and for pp collisions (bottom panel).The filled regions represent the estimated yields [This work].**
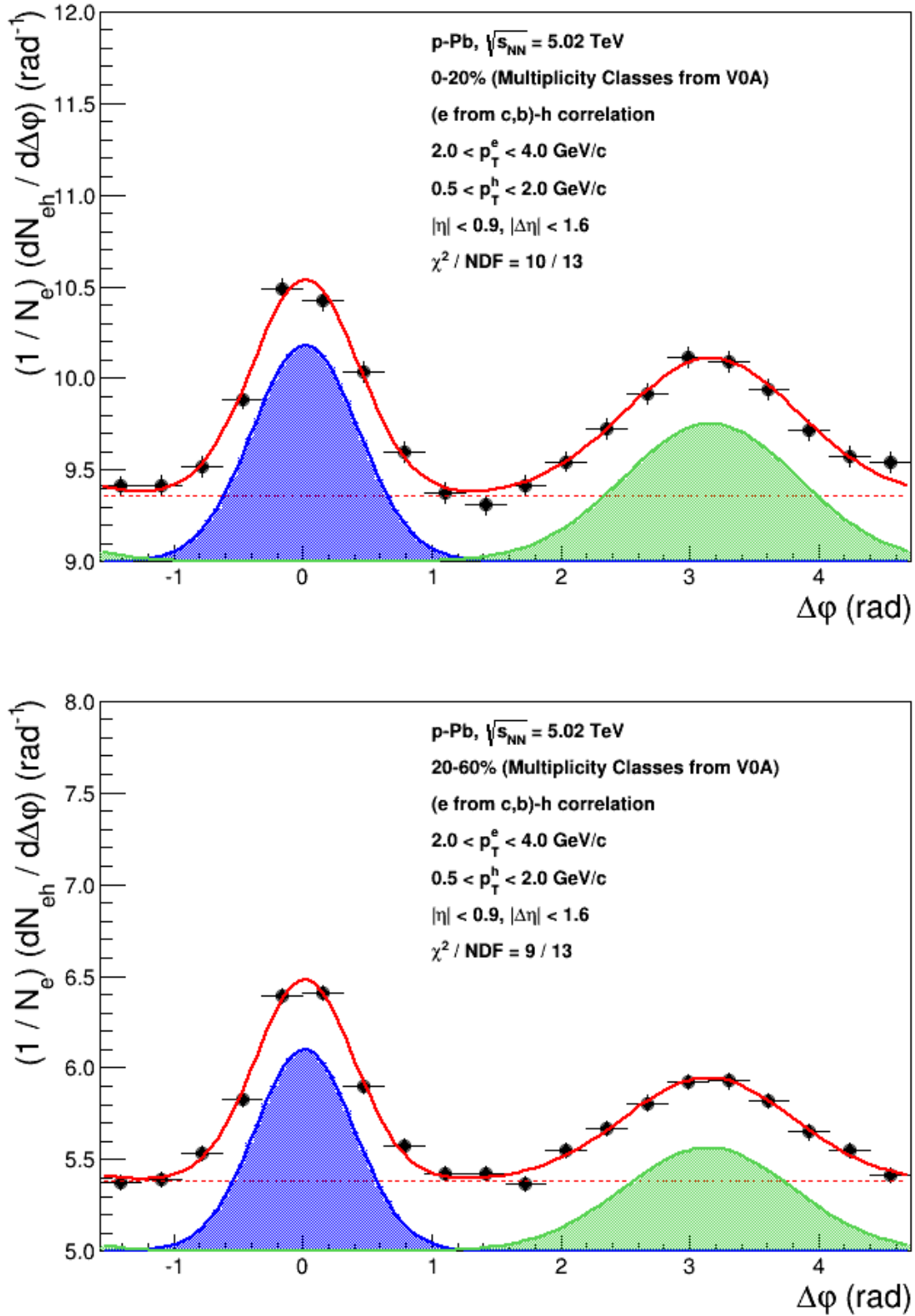
Figure 6.44: **Azimuthal correlation distribution between heavy-flavour decay electrons and charged unidentified particles in p-Pb and pp collisions for** $2 < p_T^e < 4$ **GeV/c. The results are presented for high (top panel) and intermediary-multiplicity (bottom panel) p-Pb collisions. The filled regions represent the estimated yields [This work].**
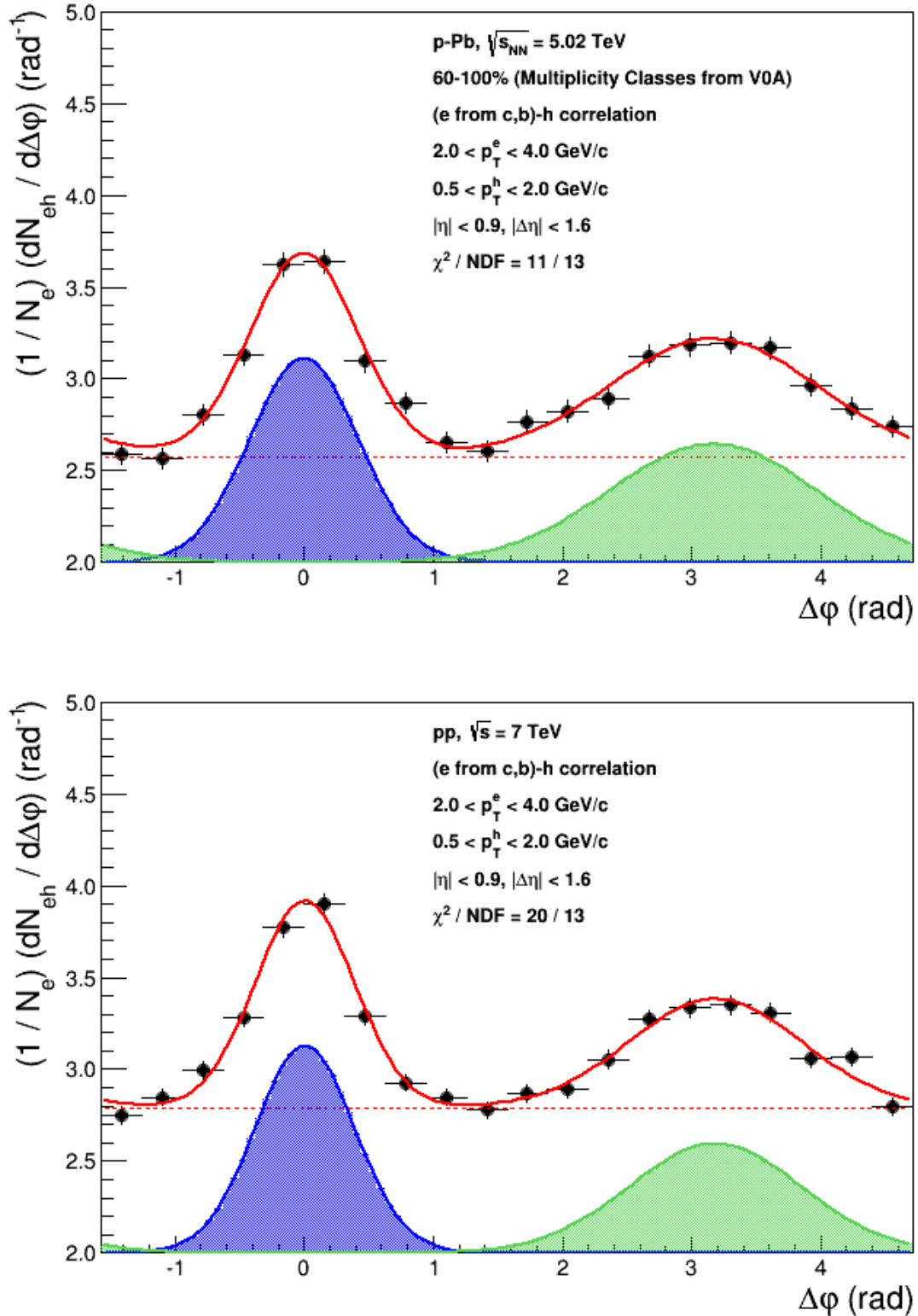
Figure 6.45: Azimuthal correlation distribution between heavy-flavour decay electrons and charged unidentified particles in p-Pb and pp collisions for $2 < p_T^e < 4$ GeV/c. The results are presented for low-multiplicity p-Pb collisions (top panel) and for pp collisions (bottom panel).The filled regions represent the estimated yields [This work].
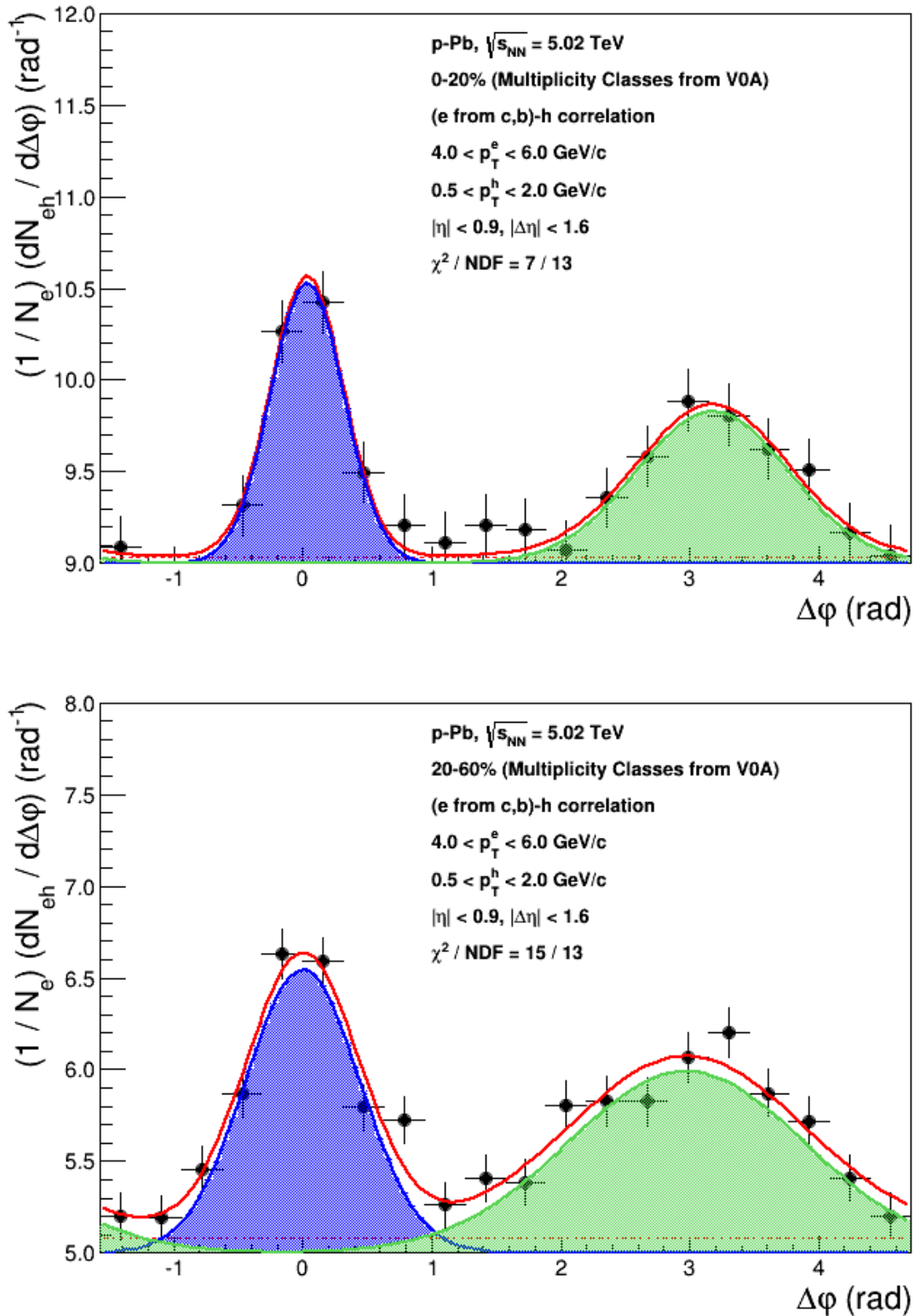
Figure 6.46: **Azimuthal correlation distribution between heavy-flavour decay electrons and charged unidentified particles in p-Pb and pp collisions for** $4 < p_T^e < 6$ **GeV/c. The results are presented for high (top panel) and intermediary-multiplicity (bottom panel) p-Pb collisions. The filled regions represent the estimated yields [This work].**
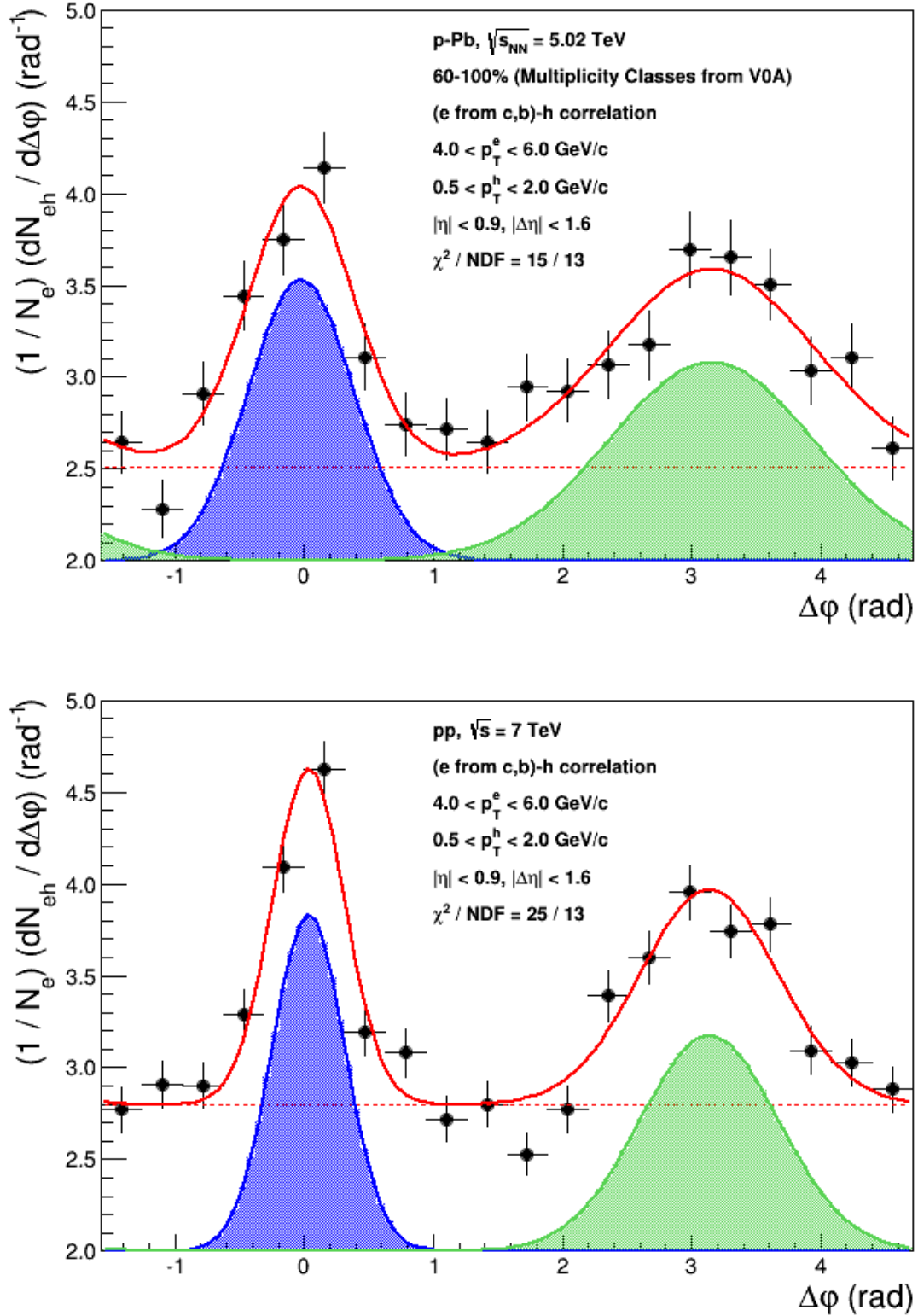
Figure 6.47: **Azimuthal correlation distribution between heavy-flavour decay electrons and charged unidentified particles in p-Pb and pp collisions for $4 < p_T^e < 6$ GeV/c. The results are presented for low-multiplicity p-Pb collisions (top panel) and for pp collisions (bottom panel).The filled regions represent the estimated yields [This work].**
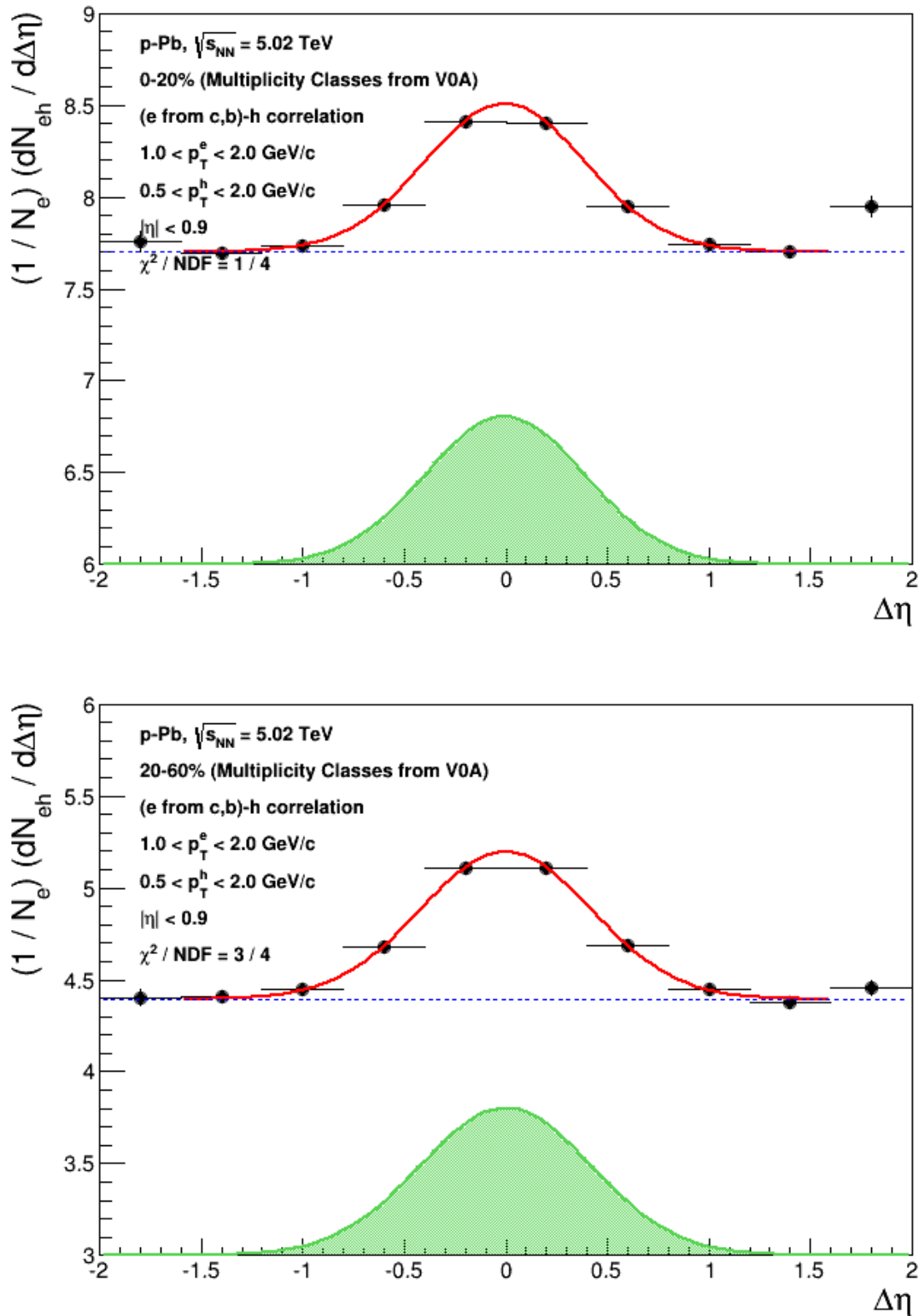
Figure 6.48: **Correlation distribution in pseudorapidity, between heavy-flavour decay electrons and charged unidentified particles in p-Pb and pp collisions for** $1 < p_T^e < 2$ **GeV/**c**. The results are presented for high (top panel) and intermediary-multiplicity (bottom panel) p-Pb collisions. The filled region represents the estimated yield [This work].**
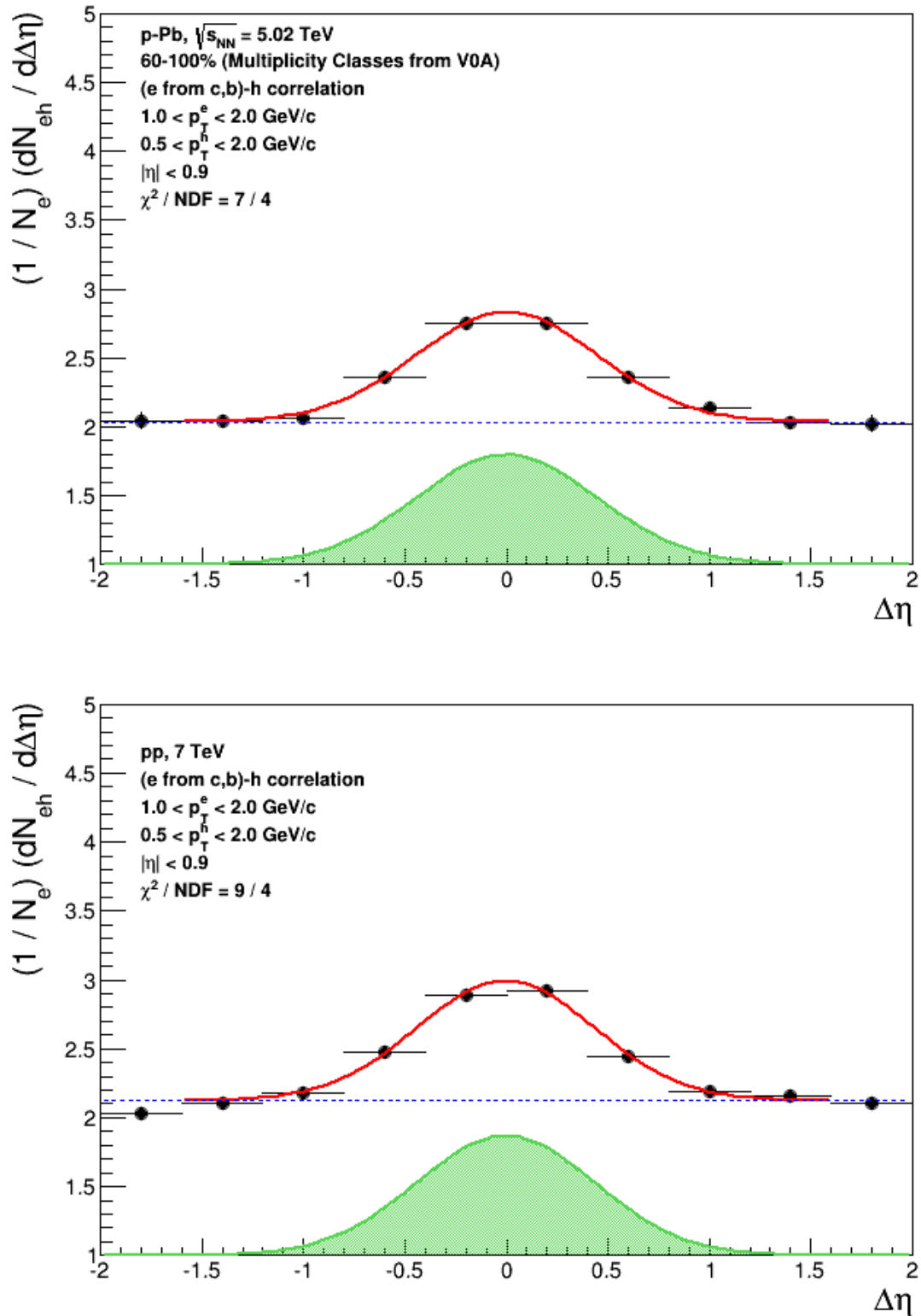
Figure 6.49: Correlation distribution in pseudorapidity, between heavy-flavour decay electrons and charged unidentified particles in p-Pb and pp collisions for $1 < p_T^e < 2$ GeV/c. The results are presented for low-multiplicity p-Pb collisions (top panel) and for pp collisions (bottom panel). The filled region represents the estimated yield [This work].
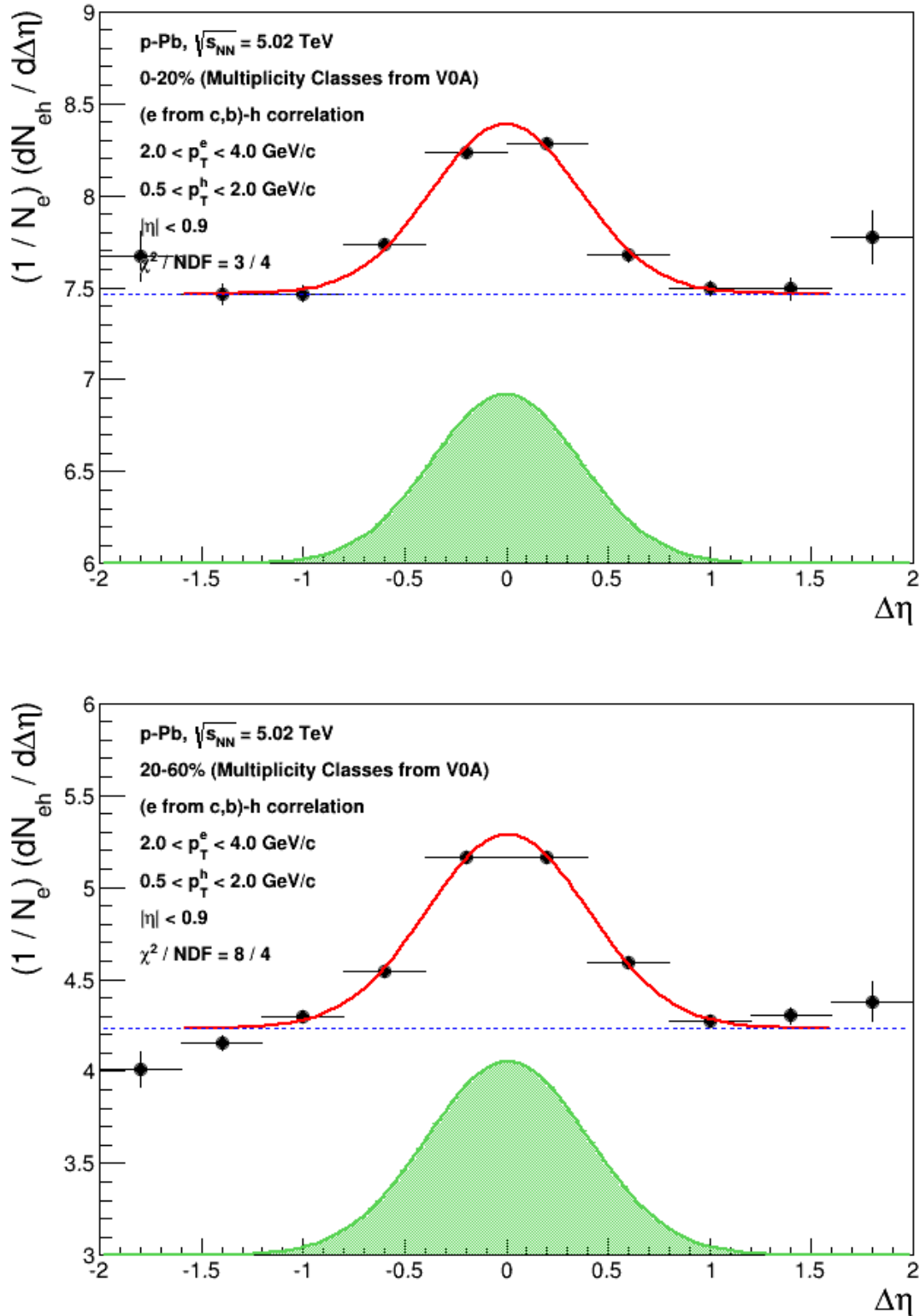
Figure 6.50: Correlation distribution in pseudorapidity, between heavy-flavour decay electrons and charged unidentified particles in p-Pb and pp collisions for $2 < p_T^e < 4$ GeV/c. The results are presented for high (top panel) and intermediary-multiplicity (bottom panel) p-Pb collisions. The filled region represents the estimated yield [This work].
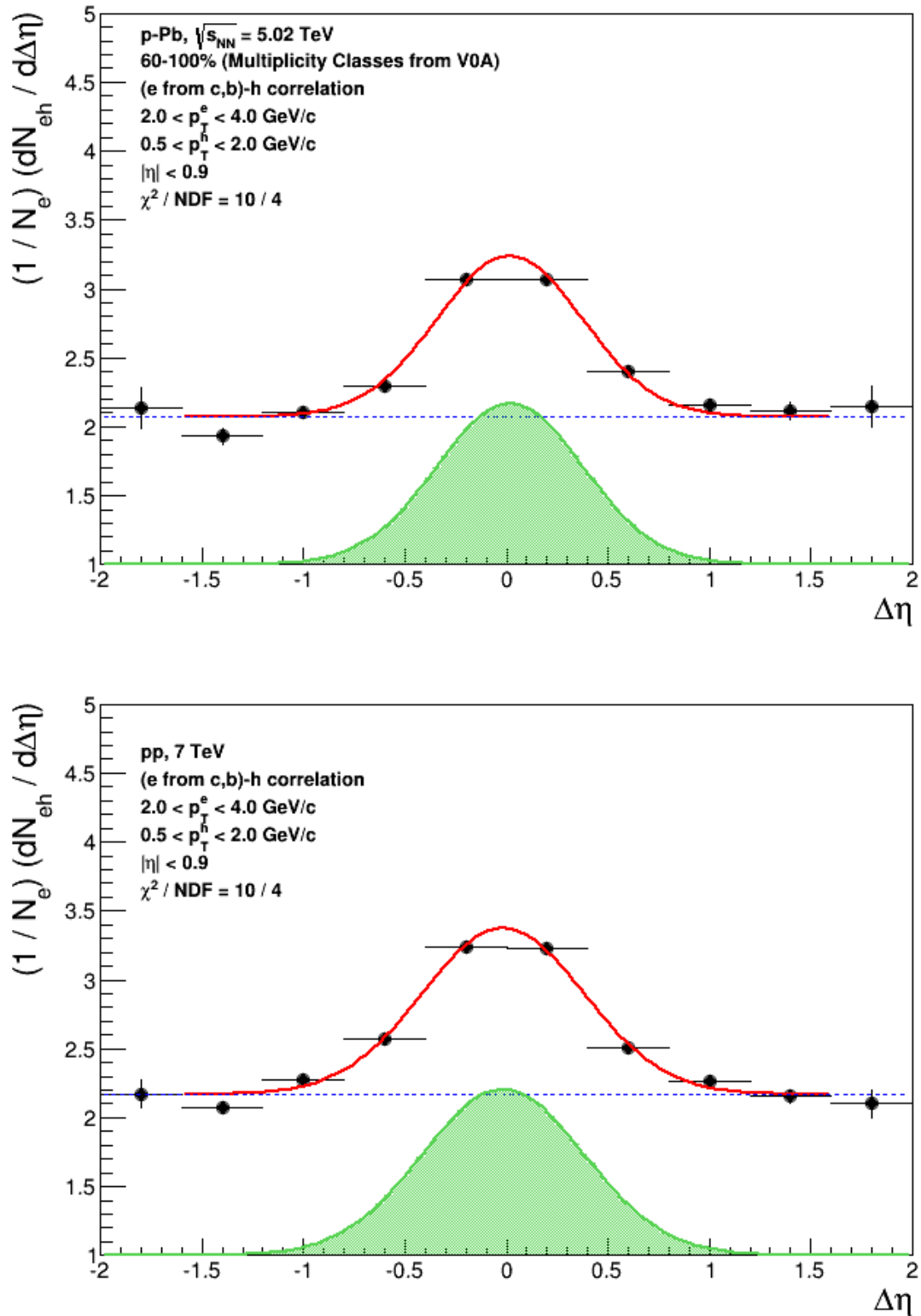
Figure 6.51: Correlation distribution in pseudorapidity, between heavy-flavour decay electrons and charged unidentified particles in p-Pb and pp collisions for $2 < p_T^e < 4$ **GeV/c. The results are presented for low-multiplicity p-Pb collisions (top panel) and for pp collisions (bottom panel).The filled region represents the estimated yield [This work].**
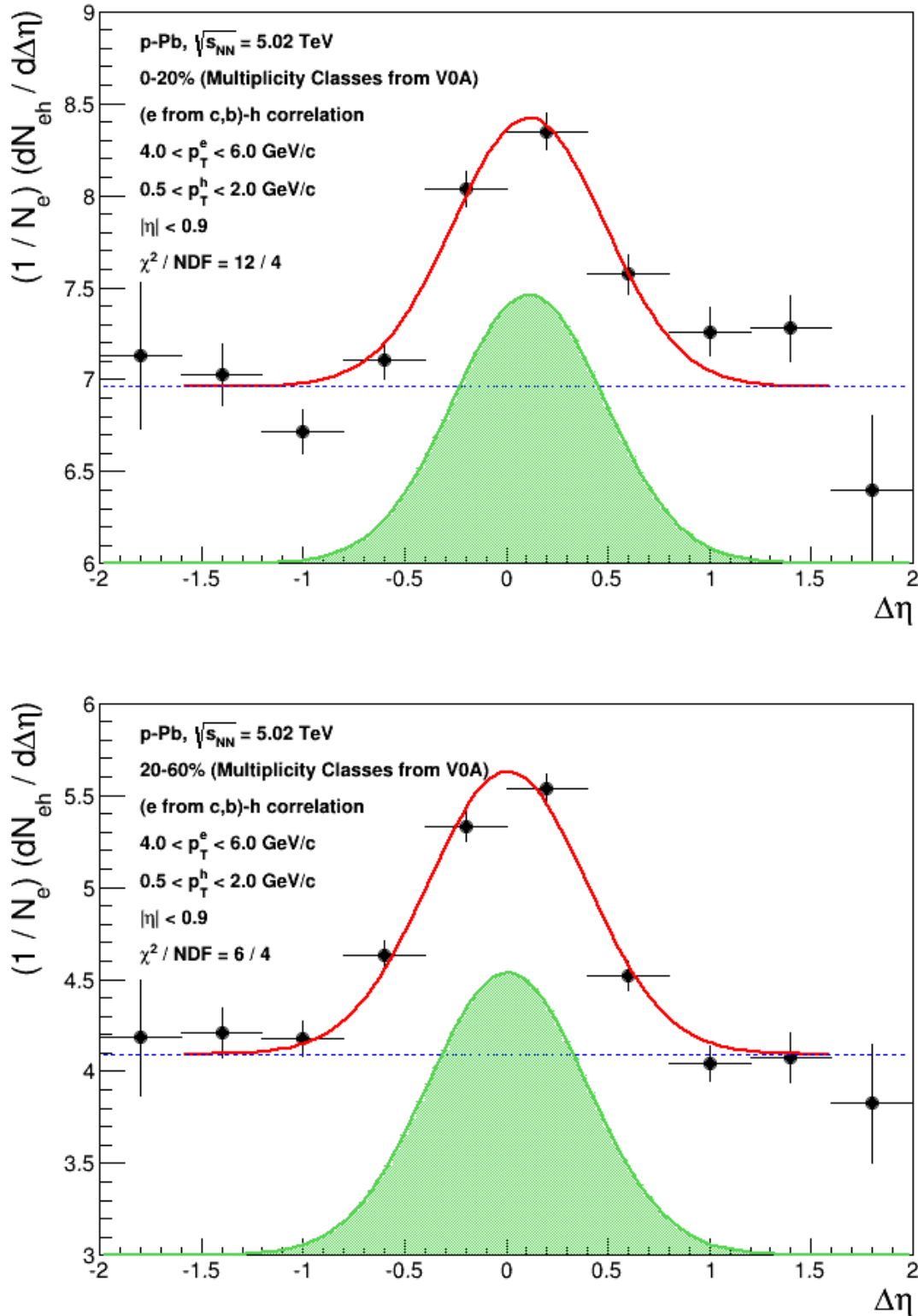
Figure 6.52: Correlation distribution in pseudorapidity, between heavy-flavour decay electrons and charged unidentified particles in p-Pb and pp collisions for $4 < p_T^e < 6$ GeV/c. The results are presented for high (top panel) and intermediary-multiplicity (bottom panel) p-Pb collisions. The filled region represents the estimated yield [This work].
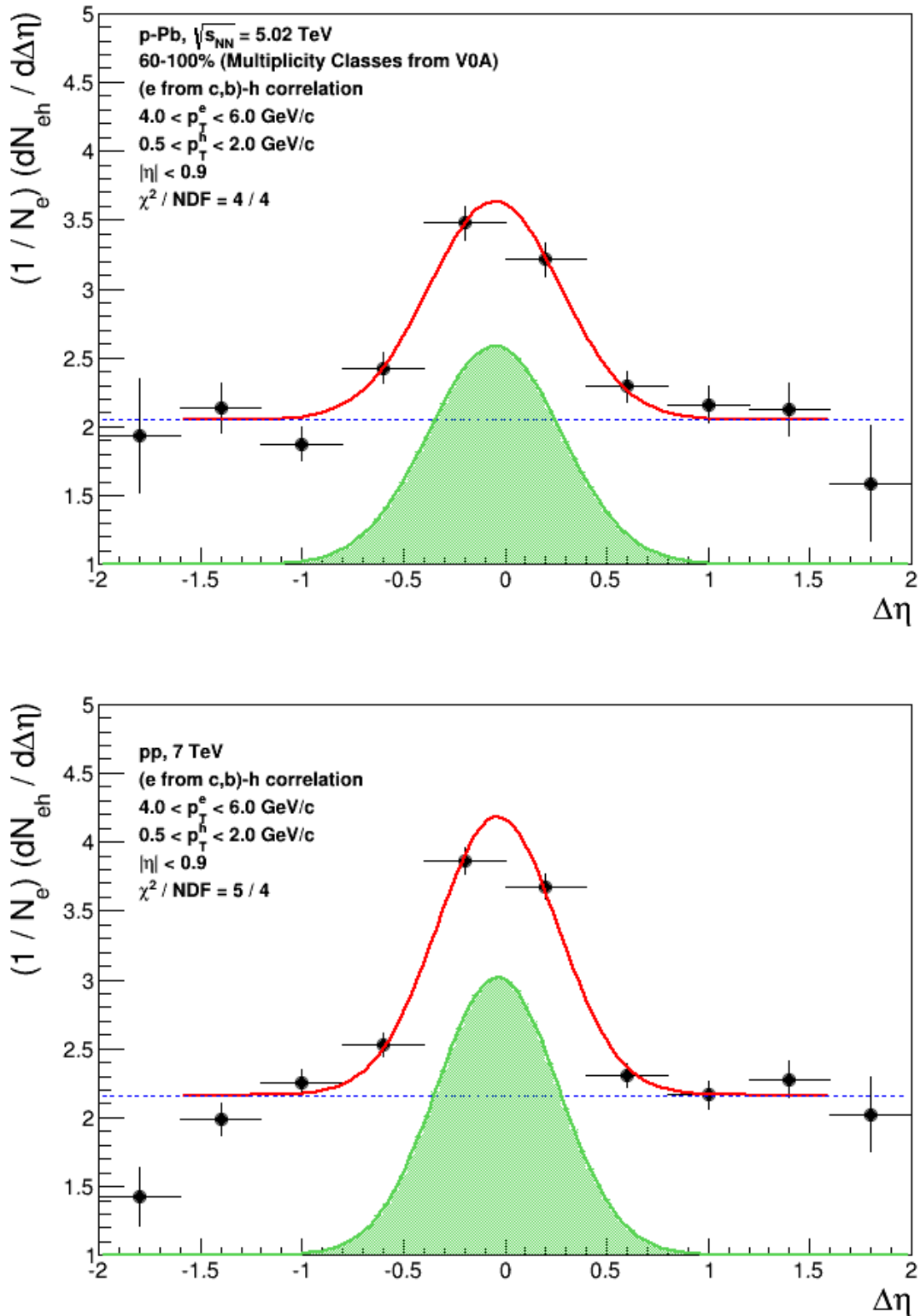
Figure 6.53: Correlation distribution in pseudorapidity, between heavy-flavour decay electrons and charged unidentified particles in p-Pb and pp collisions for $4 < p_T^e < 6$ **GeV/c. The results are presented for low-multiplicity p-Pb collisions (top panel) and for pp collisions (bottom panel).The filled region represents the estimated yield [This work].**

6.6   Systematic uncertainties

The results dependence with several parameters of the analysis were studied and, the evaluated difference, relative to the results obtained with default parameters, was assigned as systematic uncertainties of the results. These uncertainties are displayed as boxes in the final results presented in Chapter 8.

Table 6.2 summarizes what are the investigated variables that contribute to the systematic errors. This variables are mainly associated to the track selection cuts, electron identification and background reconstruction parameters. At the correlation distribution level, the yield and pedestal estimation method as well as the effect due to the remaining secondary and fake tracks contamination was investigated as well.

For each uncertainty source, its effect was investigated at several levels of the analysis, i. e. at the correlation distribution level, in the yield evaluation and on the other final variables that will be introduced in Chapter 8, such as the I_{CP} ratio.

Particularly, the effect from single particle contamination (secondary decays, conversion in the detector material and the presence of fake tracks) on the measured angular distribution, i. e. as a function of $\Delta\varphi$ was studied and and an asymmetric systematic error was found in the near-side correlation peak. This is discussed in the following Subsection.

6.6.1   Single particle contamination

The study described in this section tries to address what is the effect of fake tracks and particles from secondary decays in the near and away-side correlation peak or, to be more precise the aim is to determine by which factor the measured per-trigger yield is modified due to these contaminations.

Using Monte Carlo simulations it is possible to access the nature of the particle that is analyzed. For instance, in ALIROOT, by asking the particle label the information on whether we are dealing with a real particle (positive label) or with a fake track (negative label) is returned. One can also know if it is a primary or secondary particles. With this facility, the two-particle correlation distribution, triggered by heavy-flavour decay electrons, was evaluated with three different particle types: electron-primary, electron-secondary and electron-fake correlation distribution. The effect due to the contaminations is estimated by dividing the *contamination* correlation distribution to the total (i. e. summing all these three terms. The result is shown in Figure 6.54.

In Figure 6.54 it is visible a contamination of the order of $\approx 10 - 15\%$. However, the flat component of is removed with the pedestal subtraction and, therefore, the interest is only in the modulation that appears in the distribution due to the contamination. In fact, a modulation on the near-side is observed observed for the three bins of transverse momentum used in the present analysis, which has an amplitude of the order of 4% above the flat pedestal. Therefore an uncertainty of -4% was assigned to account for it, which appears as open boxes

in the near-side of the final correlation distributions. These results are shown in Chapter 8.

Table 6.2: Sources used in the study of the systematic uncertainties for the per-trigger yield analysis

Variable/Method	Default Choice	Alternative Choice
Tracking and PID		
Min. Num. of Clusters on TPC	80	100
		60
ITS Clusters / ITS pixel	2 / kAny	3 / kAny
		3 / kBoth
		4 / kBoth
Minimum $N\sigma$ in the TPC	-0.5	0
Background reconstruction		
Maximum Invariant Mass (Non-HFE)	100MeV/c^2	50MeV/c^2
		150MeV/c^2
Maximum Opening Angle (Non-HFE)	Not applied	0.1 rad
Minimum value of p_{T}^a	$0.0 \text{ MeV}/c$	$300 \text{ MeV}/c$
		$500 \text{ MeV}/c$
Yield evaluation		
Yield evaluation method	Gaussian Fit	Integral of the histogram
Pedestal estimation	Gaussian Fit	Average of few points
Other systematics		
Single particle contamination		
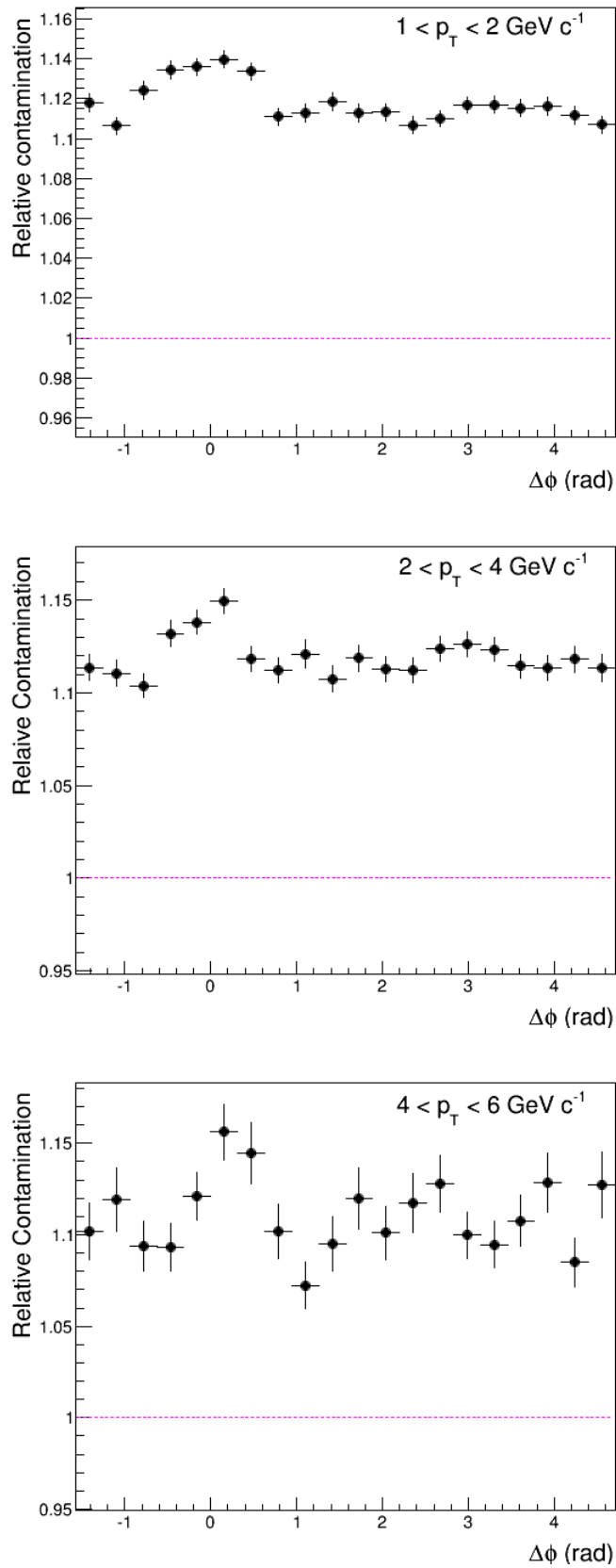
Figure 6.54: Single particle contamination (fake and secondaries) in the two particle correlation triggered by heavy-flavour decay electrons [This work].

Chapter 7

Analysis 2: Beauty production in pp collisions

7.1 Analysis steps and general strategy

The general strategy of this analysis is very similar to that described in the last Chapter, with the exception that the two last corrections are not needed and only the azimuthal correlation, i. e. the 1-dimensional angular distribution is of interest.

This analysis uses the fact that the width of the correlation distribution in the near-side is larger when triggered by electrons from beauty hadron decays, compared to the case where electrons from charm hadron decays are used to trigger the correlation distribution. It is also assumed that the difference (between the beauty and charm cases) in the near-side width is dominantly due to different decay kinematics rather than other physics aspects involved in the heavy-quark production.

Figure 7.1 shows the correlation distribution for electrons from charm and beauty hadron decays, obtained through PYTHIA simulations for pp collisions at $\sqrt{s} = 2.76$ TeV [48, 49]. Based on these assumptions, the measured correlation distribution can be fitted using these Monte Carlo templates, where the relative beauty contribution to the total heavy-flavour decay electron yield is one of the free parameters of the fit. A second parameter accounts for the baseline from uncorrelated pairs.

A similar analysis was done in STAR [86], where this method were developed and applied for the first time. In ALICE an analysis was done simultaneously to the present work, using an alternative trigger (EMCal trigger) selection and electron identification technique, in order to increase the momentum reach of the measured beauty contribution [88]. In the overlap region the two results, using MB trigger (**this analysis**) and using the EMCal trigger sample (see [88]), were combined. These results are shown in the next Chapter.
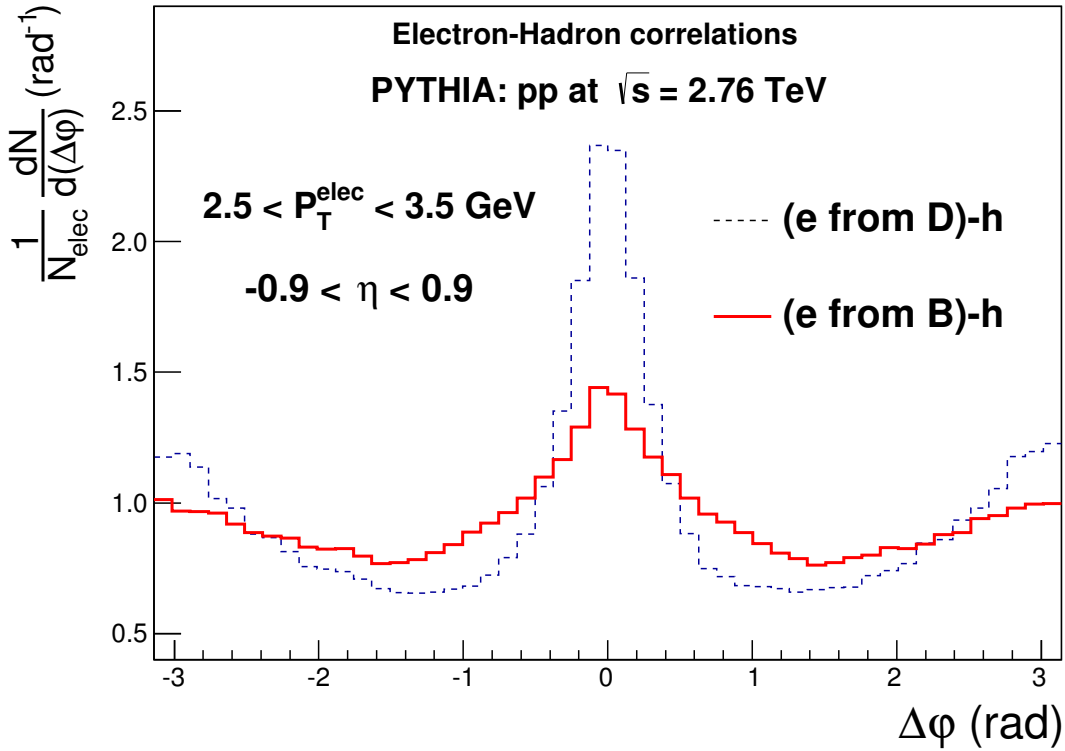
ALI−PERF−14382

Figure 7.1: Azimuthal correlation distribution between electrons from beauty (charm) hadron decays and charged particles, represented by the red continuous (blue dashed) line. These distributions were obtained from Monte Carlo simulations using the PYTHIA program [This work].

7.2   Data sample, Event and Track Selection

In this analysis, data from pp collisions at $\sqrt{s} = 2.76$ TeV, collected in 2011 with ALICE, was analyzed. Further detail on the data sample and Monte Carlo simulations used in this analysis can be found in Appendix A.

7.2.1   Event selection

The events analyzed in this work were required to satisfy:

- The Minimum Bias (MB) trigger selection;

- The primary vertex should be in the range $-10 < z < 10$ cm from the global zero reference, where z corresponds to the beam line direction;

- At least 2 tracks should be reconstructed for the event to be accepted.

7.2.2   Track selection

After the event selection, the tracks to be analyzed are chosen based on the following requests:

- Minimum Number of Clusters in the TPC: 80;

- Maximum χ^2 over the Number of TPC clusters: 4;

- Minimum Number of Clusters in the ITS: 3;

- The particle should hit at least 1 of the SPD layers.

7.3   Electron identification

Another difference of the present analysis compared to that described in the previous Chapter is that, in order to enhance the electron yield, the electron identification was performed using the TPC and TOF informations only for $p_T < 2.5$ GeV/c. For higher momentum, the identification was done using only the TPC. Therefore, since for some runs the TOF information was not properly recorded, these data is not included in the low-p_T analysis (see Appendix A).

7.3.1   Electron identification with the TPC and TOF detectors

Figure 7.2 shows the Nσ_{TOF} as a function of the transverse momentum. The electron candidate has to satisfy $-3 < $ N$\sigma_{TOF} < 3$. Figure 7.3 shows the Nσ_{TPC} as a function of the track momentum without any selection with TOF while, in Figure 7.4 this distribution is displayed only for tracks selected with TOF. In the latter case, the electron band is clearly visible around N$\sigma_{TPC} \approx 0$ and electron candidates are selected by requiring $-1 < $ N$\sigma_{TPC} < 3$, as indicated in the Figure. Figure 7.5 shows the projection on Nσ_{TPC} and the fits, in analogy to the procedure in the previous Chapter.

7.3.2   Electron identification using only the TPC information

For tracks with $p_T > 2.5$ GeV/c only the TPC information was used to select electron candidates and, as in the last case, these tracks are required to satisfy $-1 < $ N$\sigma_{TPC} < 3$. The distribution of Nσ_{TPC} are shown for the three p_T intervals of this analysis, in Figures 7.6 to 7.8.
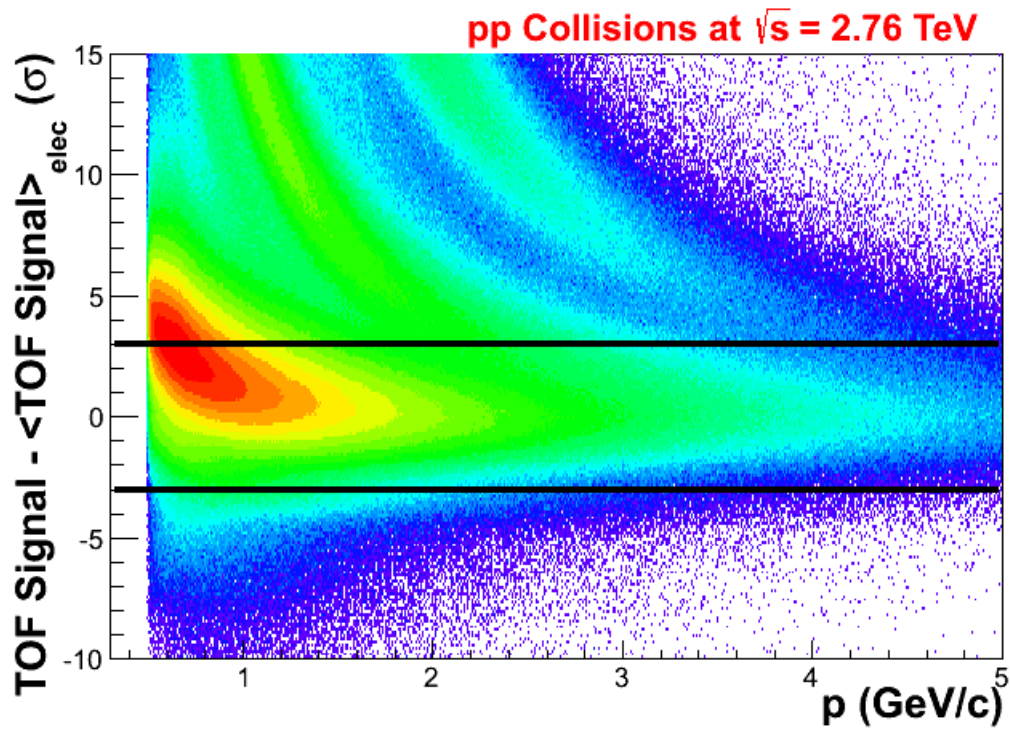
Figure 7.2: $N\sigma_{TOF}$ **as a function of momentum** p**, in pp collisions at** $\sqrt{s} = 2.76$ **TeV [This work].**
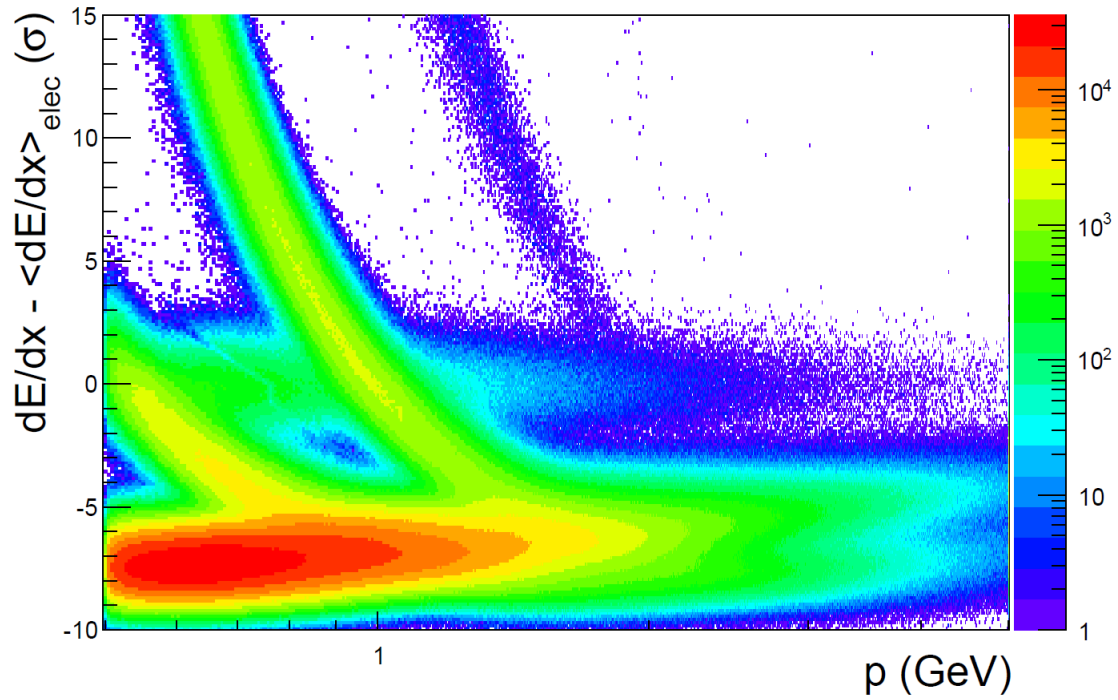
Figure 7.3: $N\sigma_{TPC}$ **as a function of momentum** p**, in pp collisions at** $\sqrt{s} = 2.76$ **TeV [This work].**
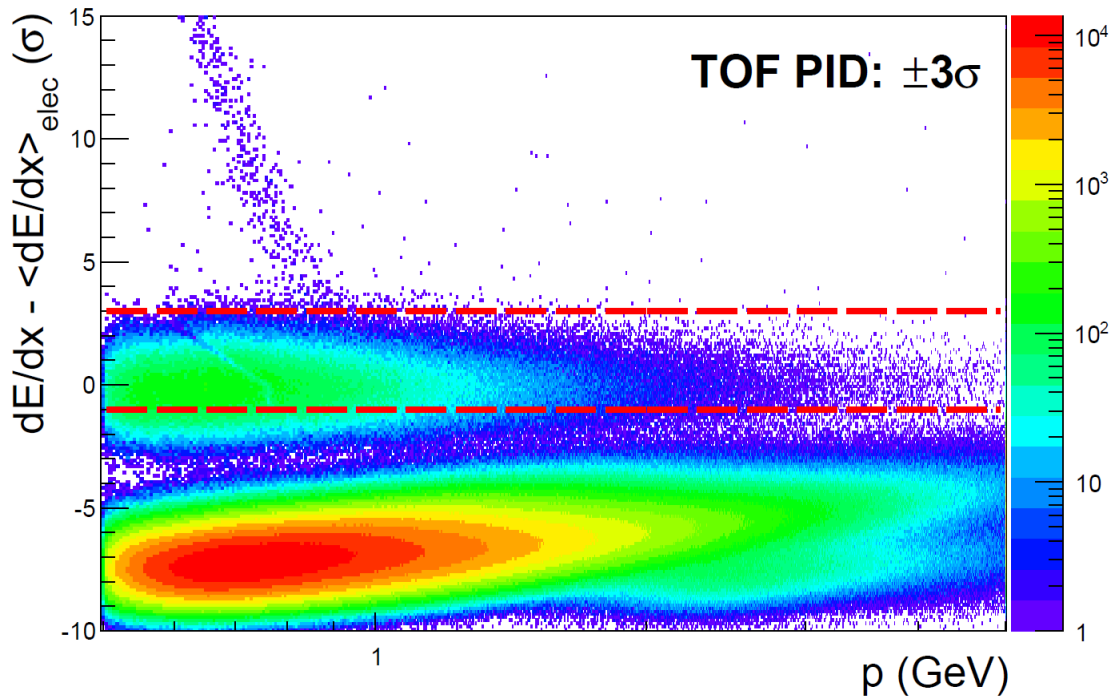
Figure 7.4: $N\sigma_{\text{TPC}}$ **as a function of momentum** p**, for particles selected using the TOF information** $(-3 < N\sigma_{\text{TOF}} < 3\sigma)$**, in pp collisions at** $\sqrt{s} = 2.76$ **TeV [This work].**
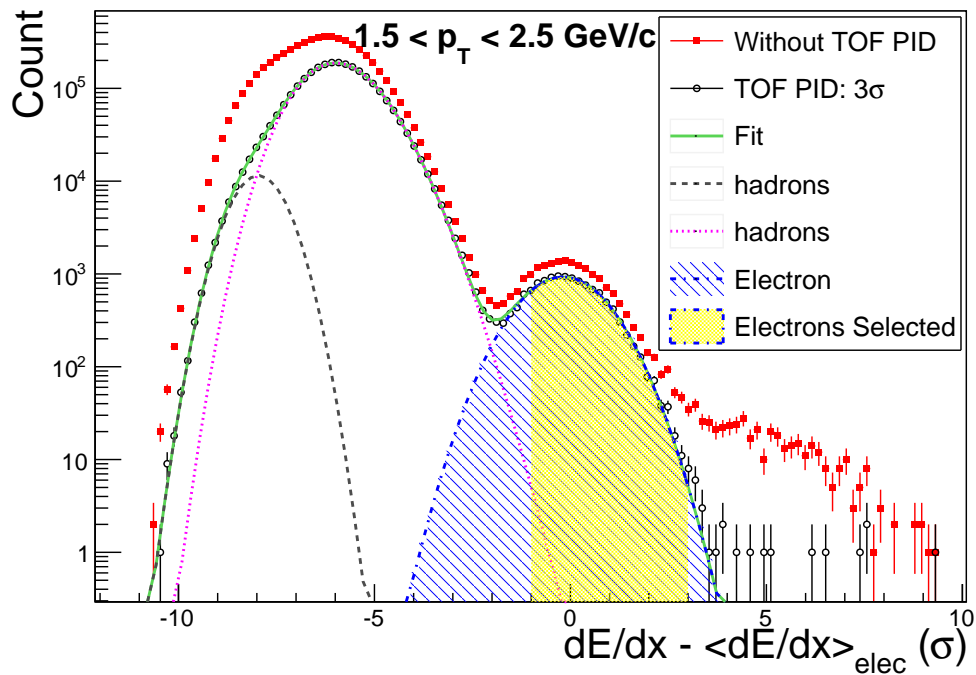
Figure 7.5: $N\sigma_{\text{TPC}}$ **distribution for** $1.5 < p_{\text{T}} < 2.5$ **GeV/**c**, in pp collisions at** $\sqrt{s} = 2.76$ **TeV [This work].**
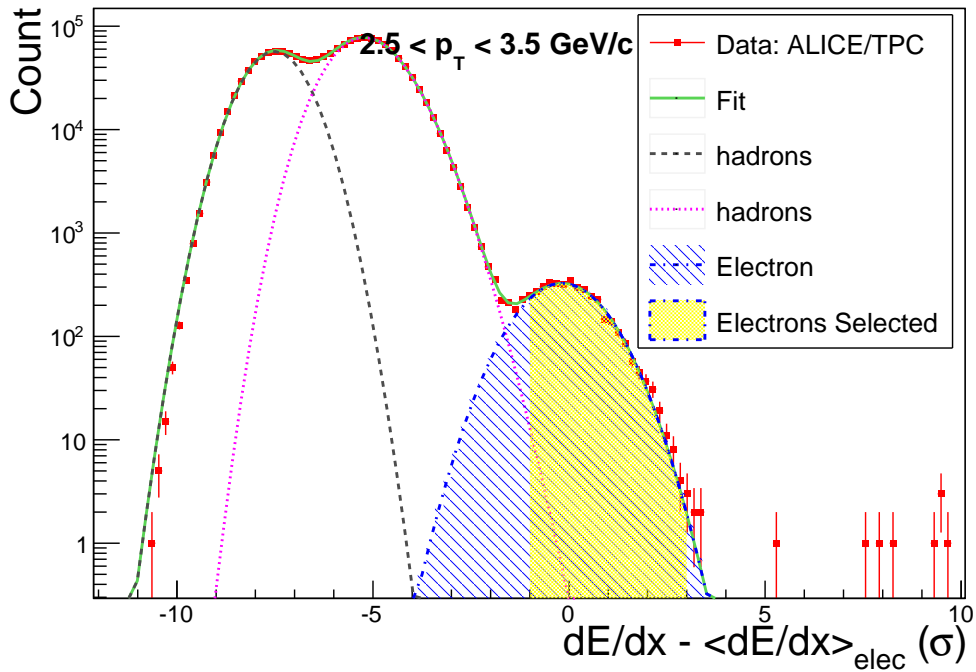
Figure 7.6: Nσ_{TPC} **distribution for** $2.5 < p_{\text{T}} < 3.5$ **GeV/**c**, in pp collisions at** $\sqrt{s} = 2.76$ **TeV [This work].**
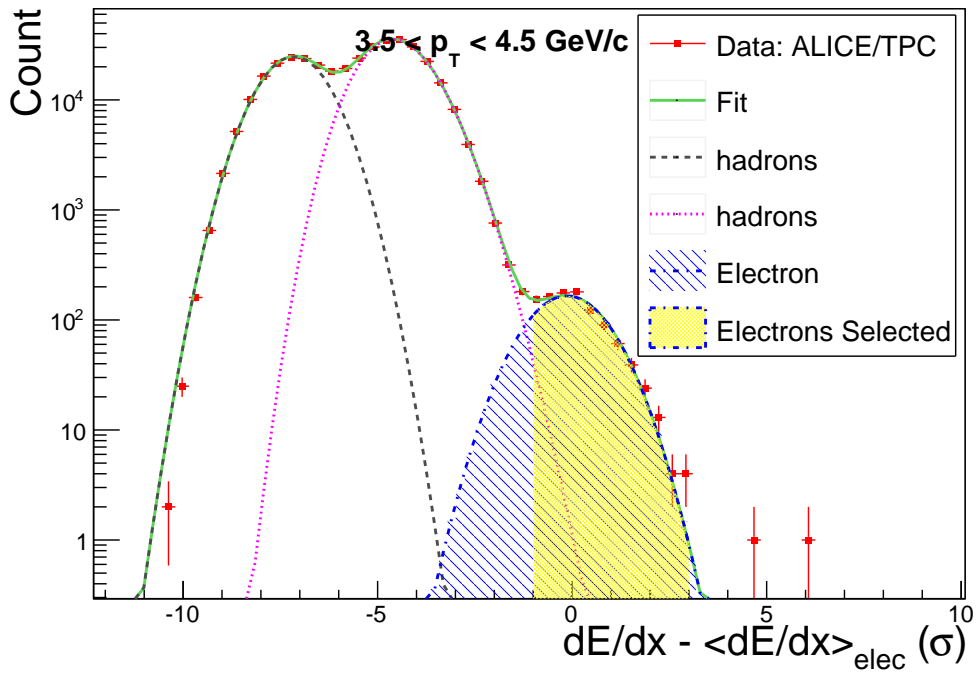
Figure 7.7: Nσ_{TPC} **distribution for** $3.5 < p_{\text{T}} < 4.5$ **GeV/**c**, in pp collisions at** $\sqrt{s} = 2.76$ **TeV [This work].**
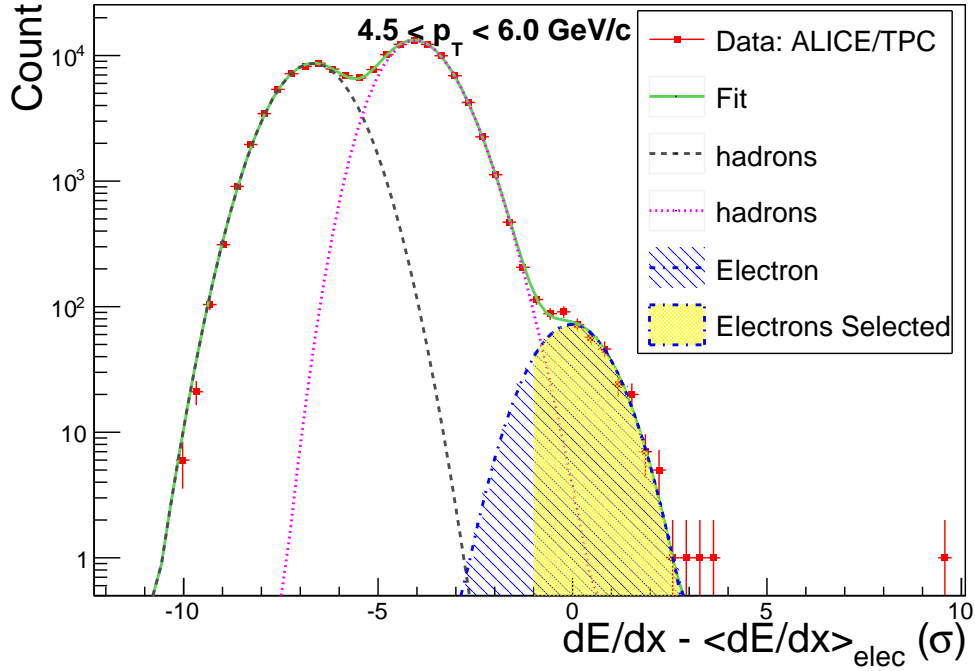
Figure 7.8: Nσ_{TPC} **distribution for** $4.5 < p_T < 6.0$ **GeV/**c**, in pp collisions at** $\sqrt{s} = 2.76$ **TeV [This work].**

7.3.3 Background identification

The treatment of the background due to electrons from non-heavy-flavour sources is very similar to that described in the previous Chapter. In the case of this analysis the electron partner is required to have $p_T > 300$ MeV/c, which reduces slightly the reconstruction efficiency via invariant mass.

The invariant mass distribution for unlike and like-sign pairs, for electrons with transverse momentum $p_T > 500$ MeV/c is shown in Figure in the top panel of Figure 7.9.

The background finding efficiency for this particular case is shown in the bottom panel of Figure 7.9, as a function of the track transverse momentum p_T. The efficiency goes from $\approx$ 20% in the lower momentum region and reaches $\approx 70\%$ for the higher transverse momentum considered in this work (i. e. 6 GeV/c).

The background is selected by requiring that the electron-positron pair should have invariant mass not larger than 100 MeV/c^2. That is applied also for like-sign pairs in order to evaluate the yield of non-background electrons mis-selected due to the combinatorial pairing.
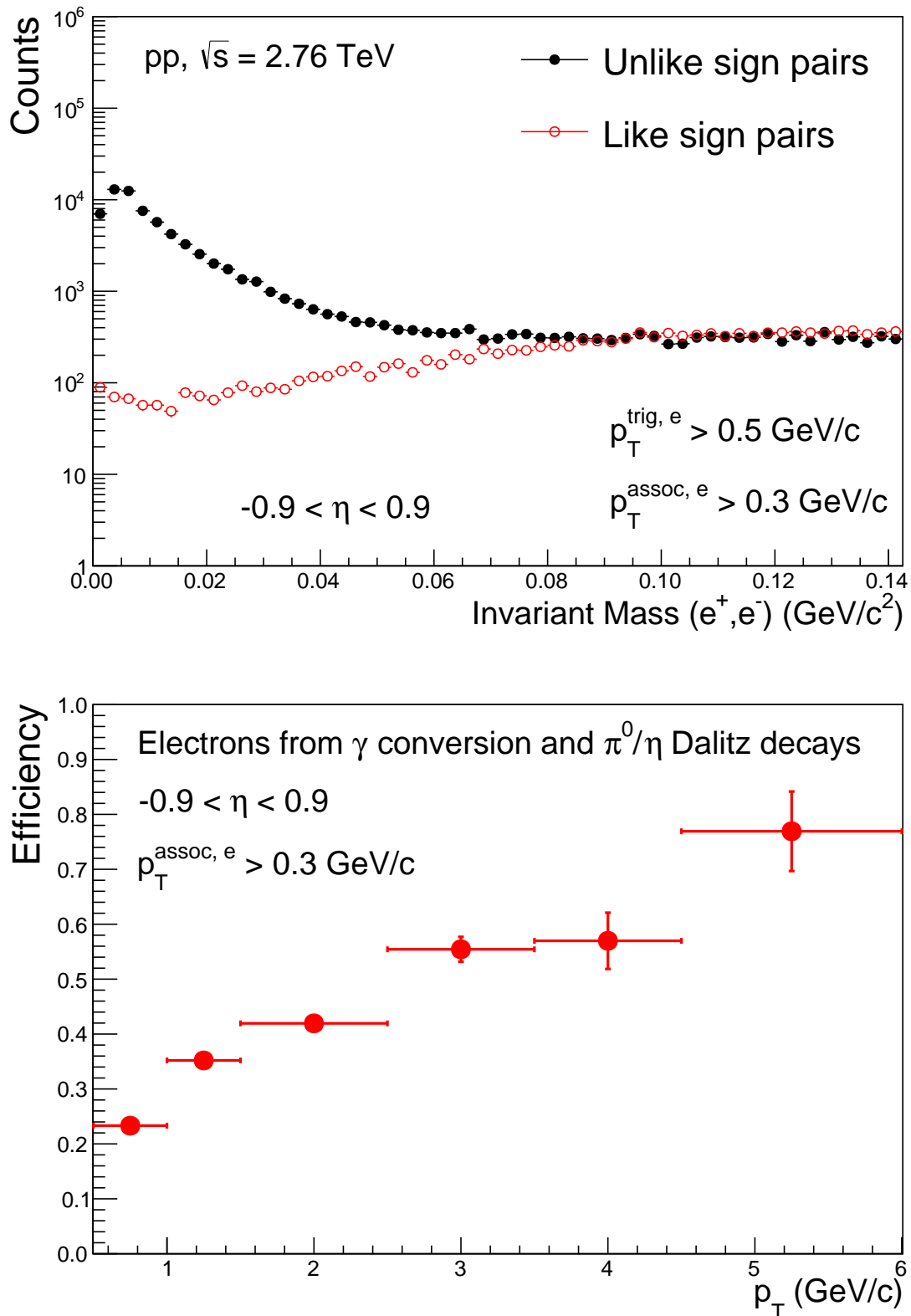
Figure 7.9: Top panel: Invariant mass distribution of electron-positron pairs, in pp collisions at $\sqrt{s} = 2.76$ **TeV. Bottom panel: Efficiency of the electron background reconstruction via invariant mass [This work].**

7.4 Beauty production

The correlation function between heavy-flavour decay electrons and charged particles is evaluated as explained in the previous Chapter. In this particular case, corrections for pair-finding and tracking efficiency are not needed. The interest is not in the near or away-side yield but in explore the different shape of the distribution for charm and beauty correlations and, since the projection of the mixed event on $\Delta\varphi$ is flat, such a correction don't affect this shape. In other words, the pair finding efficiency and non-homogeneities affects charm and beauty correlation distributions in the same way.

In order to evaluate the relative contribution of beauty-hadrons to the total heavy-flavour decay electron yield, the near-side peak was fitted using Equation 7.1, where $\left[\frac{1}{N_{\mathrm{trig}}}\frac{\mathrm{d}N_{\mathrm{e-h}}}{\mathrm{d}\Delta\varphi}\right]^{\mathrm{data}}$ represents the measured correlation distribution, $\left[\frac{1}{N_{\mathrm{trig}}}\frac{\mathrm{d}N_{\mathrm{e-h}}}{\mathrm{d}\Delta\varphi}\right]^{\mathrm{MC}}_{b\to e}$ is the angular correlation evaluated with PYTHIA for electrons from beauty hadron decays, $\left[\frac{1}{N_{\mathrm{trig}}}\frac{\mathrm{d}N_{\mathrm{e-h}}}{\mathrm{d}\Delta\varphi}\right]^{\mathrm{MC}}_{c\to e}$ is the Monte Carlo distribution for electrons from charm-hadron decays, C is a free parameter accounting for the baseline due to uncorrelated electron-hadron pairs and r_{B} is the free parameter representing the relative beauty contribution to the total yield of heavy-flavour decay electrons, i. e. $r_{\mathrm{B}} = N_{b\to e}/(N_{b\to e} + N_{c\to e})$.

$$\left[\frac{1}{N_{\mathrm{trig}}}\frac{\mathrm{d}N_{\mathrm{e-h}}}{\mathrm{d}\Delta\varphi}\right]^{\mathrm{data}} = \mathrm{C} + r_{\mathrm{B}}\left[\frac{1}{N_{\mathrm{trig}}}\frac{\mathrm{d}N_{\mathrm{e-h}}}{\mathrm{d}\Delta\varphi}\right]^{\mathrm{MC}}_{b\to e} + (1 - r_{\mathrm{B}})\left[\frac{1}{N_{\mathrm{trig}}}\frac{\mathrm{d}N_{\mathrm{e-h}}}{\mathrm{d}\Delta\varphi}\right]^{\mathrm{MC}}_{c\to e} \quad (7.1)$$

The measured correlation function, along with the Monte Carlo templates and the fit are shown in Figures 7.10 to 7.13.

In the bottom panel of Figures 7.10 to 7.13, the residual, defined in Equation 7.2 as the difference between data and fit, in numbers of σ, is shown. These results support a reasonable fit performance, since there is no strong dependence of the residual with $\Delta\varphi$ and, points displaced by more 3σ from the fit are not observed in these plots.

$$\mathrm{Residual} = \frac{\left[\frac{1}{N_{\mathrm{trig}}}\frac{\mathrm{d}N_{\mathrm{e-h}}}{\mathrm{d}\Delta\varphi}\right]^{\mathrm{data}} - \left[\frac{1}{N_{\mathrm{trig}}}\frac{\mathrm{d}N_{\mathrm{e-h}}}{\mathrm{d}\Delta\varphi}\right]^{\mathrm{Fit}}}{\sigma_{\mathrm{data}}} \quad (7.2)$$

The results of r_{B} as a function of p_{T} is shown in the next Chapter and is compared to three set of pQCD calculations.

In the following the Figures shown the measured correlation distributions along with Monte Carlo templates and the fit are shown for the four p_{T} intervals of this analysis, from 1.5 to 6.0 GeV/c.
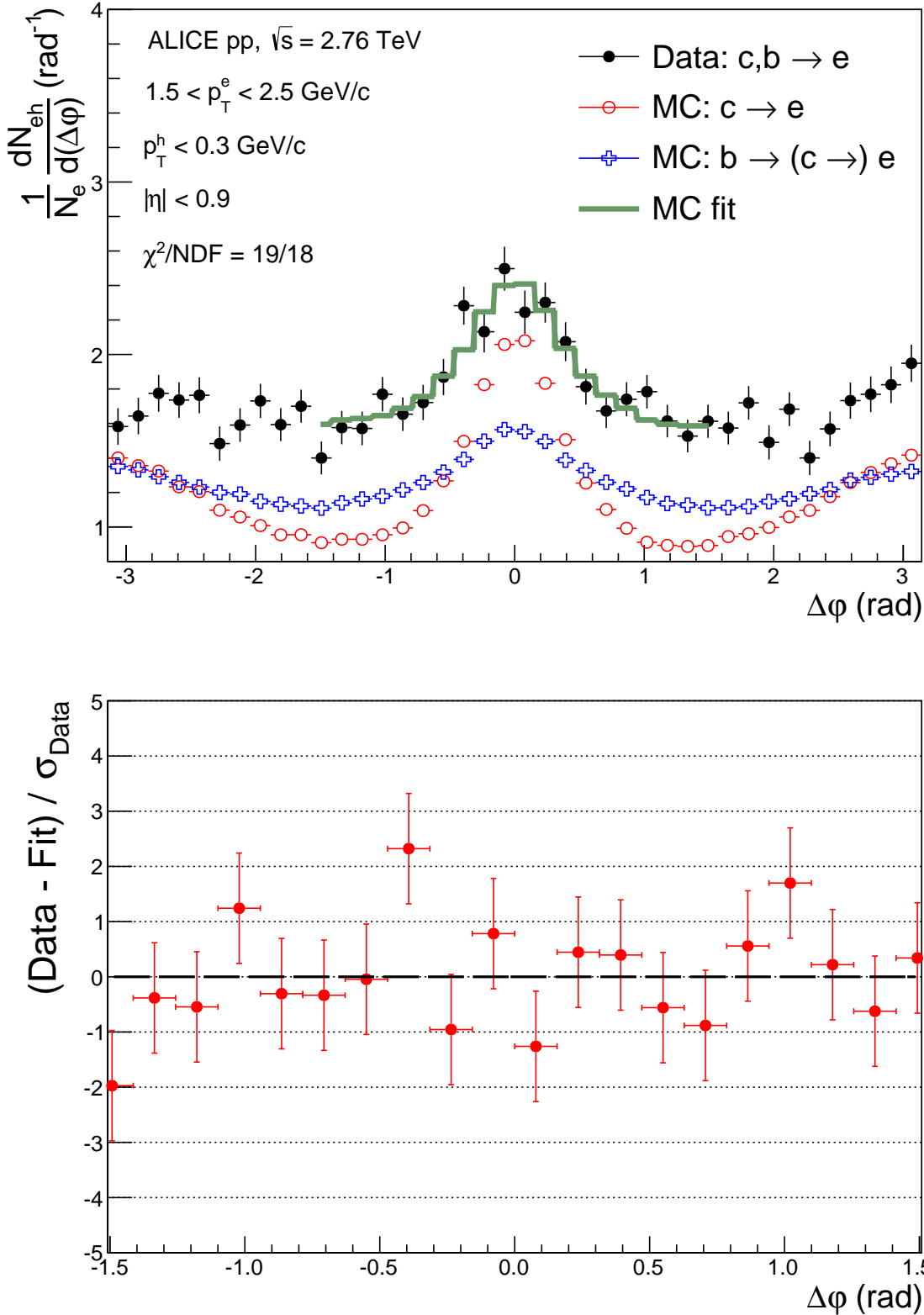
Figure 7.10: Top panel: Correlation distribution between heavy-flavour decay electrons and charged particles for $1.5 < p_{\mathrm{T}}^{e} < 2.5$ **GeV/c, from pp collisions at** $\sqrt{s} = 2.76$ **TeV and correspond-ing Monte Carlo templates for beauty and charm decay electrons. The fit from Equation 7.1 is also shown in the plot. Bottom panel: Difference between data points and the fitted function** [This work].
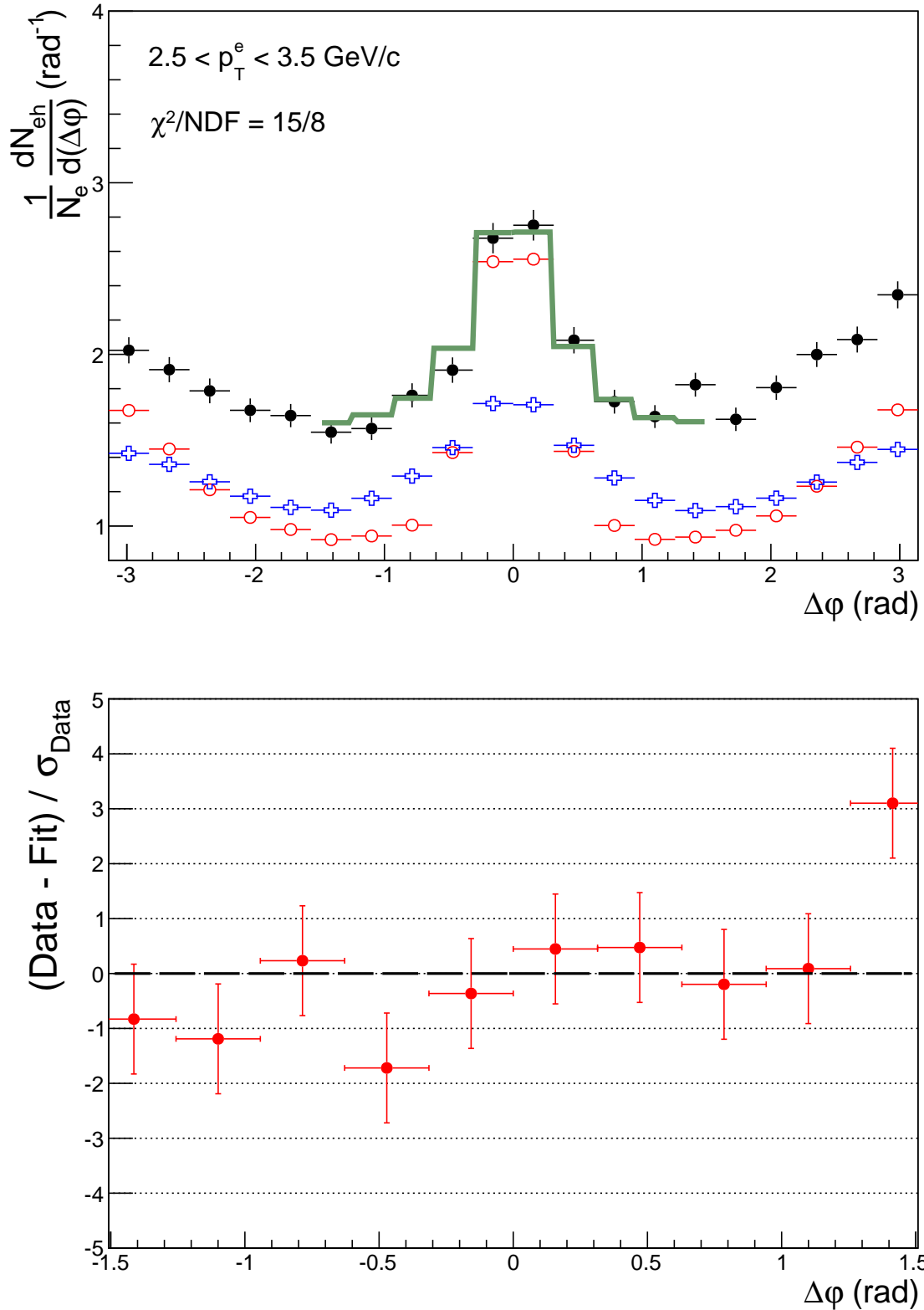
Figure 7.11: Top panel: Correlation distribution between heavy-flavour decay electrons and charged particles for $2.5 < p_T^e < 3.5$ **GeV/c, from pp collisions at** $\sqrt{s} = 2.76$ **TeV and corresponding Monte Carlo templates for beauty and charm decay electrons. The fit from Equation 7.1 is also shown in the plot. Bottom panel: Difference between data points and the fitted function [This work].**
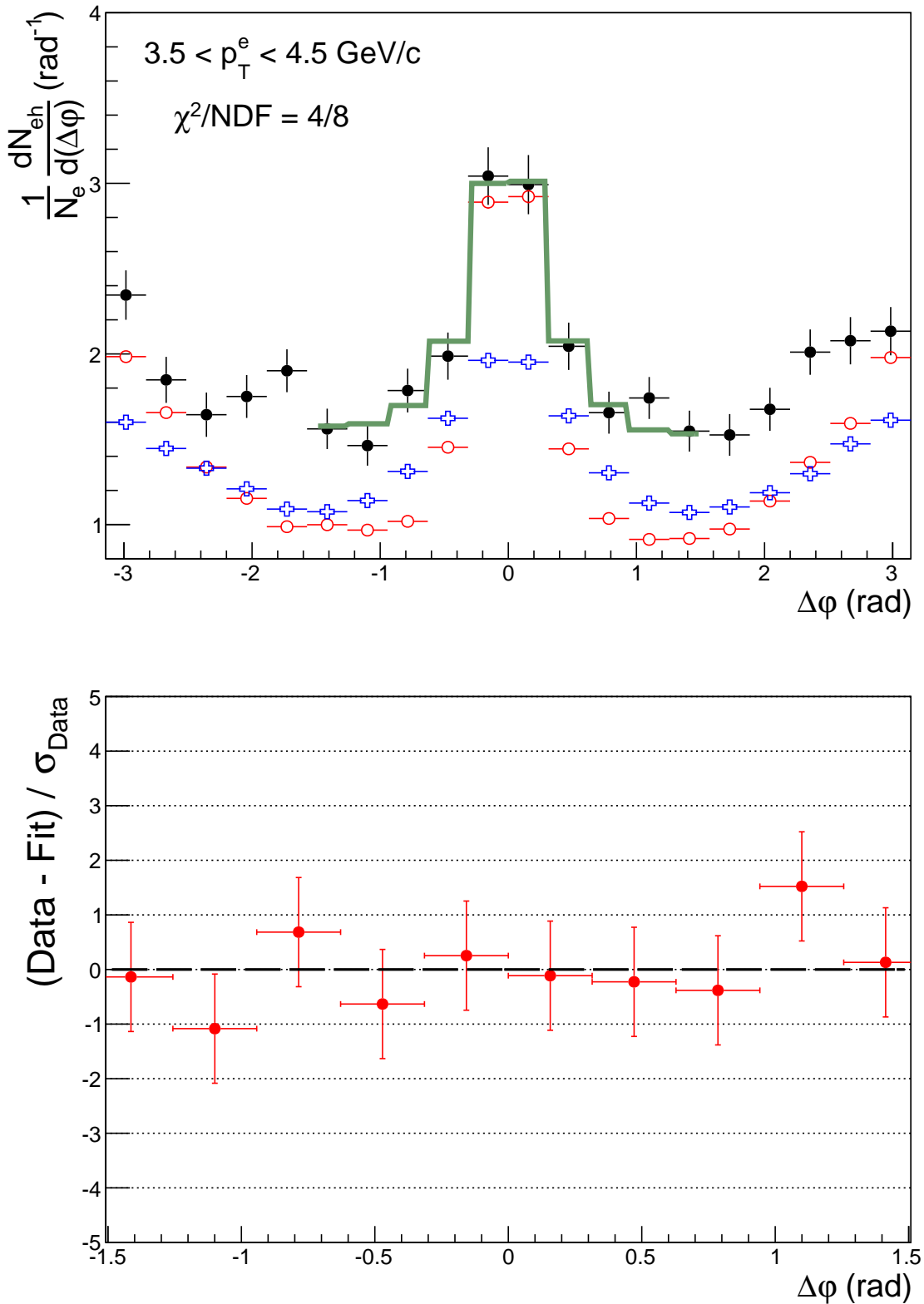
Figure 7.12: Top panel: Correlation distribution between heavy-flavour decay electrons and charged particles for $3.5 < p_T^e < 4.5$ **GeV/c, from pp collisions at** $\sqrt{s} = 2.76$ **TeV and corresponding Monte Carlo templates for beauty and charm decay electrons. The fit from Equation 7.1 is also shown in the plot. Bottom panel: Difference between data points and the fitted function [This work].**
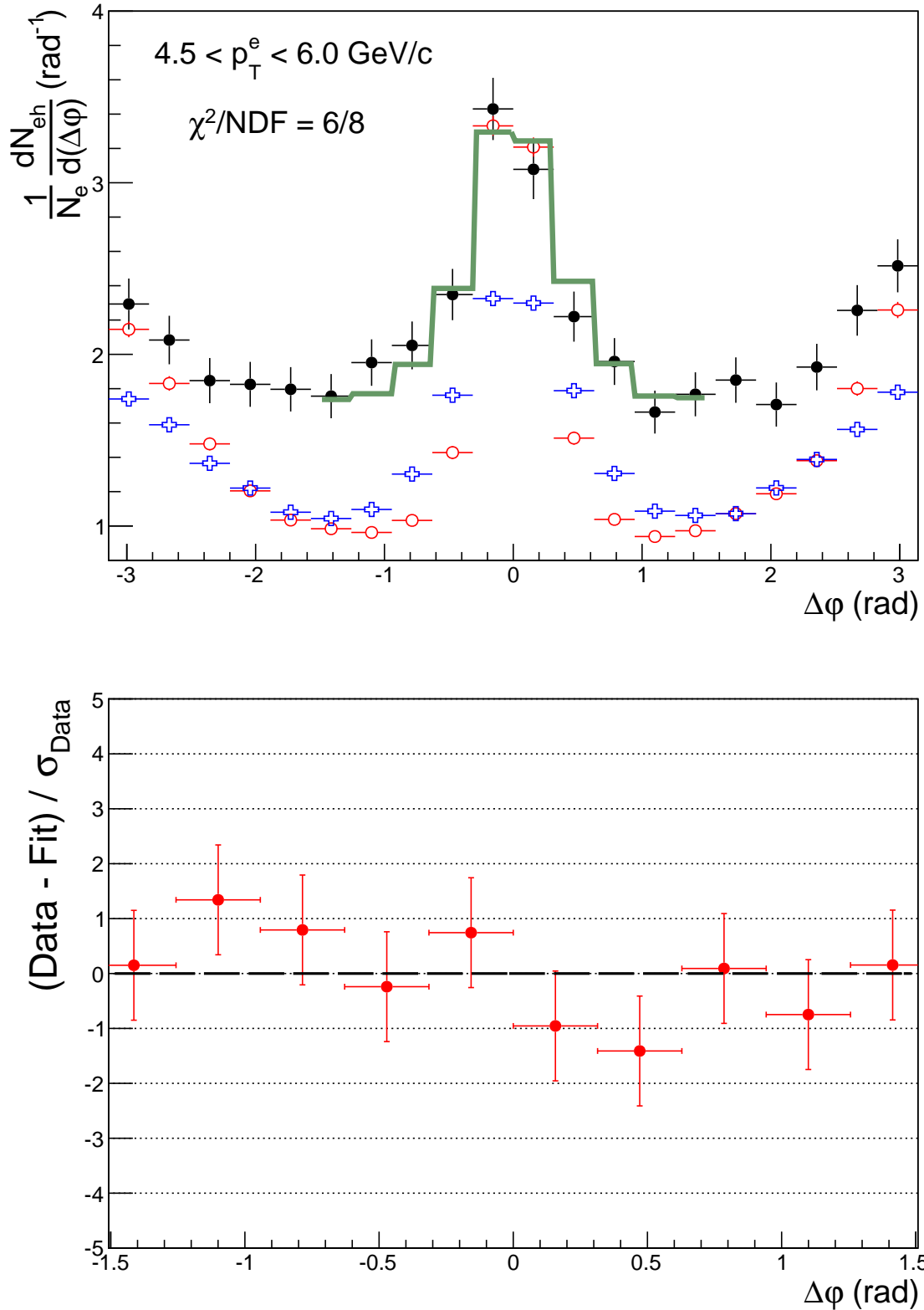
Figure 7.13: Top panel: Correlation distribution between heavy-flavour decay electrons and charged particles for $4.5 < p_T^e < 6.0$ **GeV/c, from pp collisions at $\sqrt{s} = 2.76$ TeV and corresponding Monte Carlo templates for beauty and charm decay electrons. The fit from Equation 7.1 is also shown in the plot. Bottom panel: Difference between data points and the fitted function [This work].**

7.5   Systematic uncertainties

The systematic uncertainties for the analysis described in the present Chapter is defined based on the dependence of the r_B with the parameters listed in Table 7.1.

In addition to the sources investigated in the analysis described in the previous Chapter, for the present case some of the PYTHIA parameters were studied, since the results are directly dependent on the correlation distribution obtained in the simulation. Therefore, different PYTHIA tunes as well as variations in the hard scattering process used in Monte Carlo were studied [80, 89].

Table 7.1: List of sources used to define the systematic uncertainty for the beauty production analysis

Error source
TPC Number of clusters TPC PID (Minimum $N\sigma_{TPC}$ cut)
TOF PID ($N\sigma_{TOF}$ cut)
Non-HFE reconstruction: $N\sigma_{TPC}$ cut for the associated track
Non-HFE reconstruction: Opening angle
Non-HFE reconstruction: Invariant mass
Non-HFE reconstruction: π^0 and η spectrum from simulation
Simulation: PYTHIA tune
Simulation: Hard scattering process in PYTHIA
Fit range in the $\Delta\varphi$ axis
Minimum hadron p_T

In the case of the hard scattering process the main modification in the correlation function was found to be due the amount of heavy quarks produced via the gluon splitting (GS) process. Therefore, in order to investigate a possible dependence of the results on this, the relative amount of charm and beauty created through GS was modified in PYTHIA.

In this study two extremes were considered. In the first case the amount of charm produced via GS was increased while for beauty this number was decreased and, in the second case the opposite was done. With it, the variation in the near-side width occurs in the opposite direction for electrons from charm and beauty and, therefore, the largest effect from these variations on the fit can be inferred. In both options the measured modification was found to be around $\approx 7\%$ as displayed in Table 7.2.

Table 7.2 shows also the results all the other sources. The final estimated systematic uncertainties are shown as boxes in the results presented in the next Chapter.

Table 7.2: Systematic uncertainties estimated for each source.

Source	Systematic uncertainty (%)
Clusters on TPC (lower value)	6
Clusters on TPC (higher value)	7
TPC PID	± 5 for $p_T < 3.5$ GeV/c, (+5,-20) for $p_T > 3.5$ GeV/c
TOF PID	6 for $p_T < 2.5$ GeV/c, 0 for $p_T > 3.5$ GeV/c
Invariant Mass	0.04
Opening Angle	0.03
Associated electron PID	0.1
Associated hadron Momentum	8
Fit range (lower range)	0.4
Fit range (higher range)	0.4
Light Meson spectrum	1.4
Gluon Splitting (+charm,-beauty)	7
Gluon Splitting (-charm,+beauty)	6
PYTHIA Tune	3

Chapter 8

Results

8.1 Angular correlation distribution

8.1.1 Azimuthal correlation function

Figures 8.1 to 8.2 show the azimuthal correlation function, i. e. in $\Delta\varphi$, between heavy-flavour decay electrons (trigger) and unidentified charged particles (associated), for the three multiplicity classes defined in this analysis for p-Pb collisions, and in pp collisions at $\sqrt{s} = 7$ TeV.

In these figures, the systematic uncertainty due to the single particle contamination, which was found to affect only the near-side peak, is displayed as open boxes, while that from the pedestal estimation are represented by filled boxes on the right part of the figure. Furthermore, a global normalization uncertainty, common to all the systems and event classes, is indicated by a text in the plot.

Each of the figures (8.1 to 8.2) corresponds to a particular p_T range of the trigger particle, as indicated in the caption, and the associated particle were selected in the range $0.5 < p_T < 2.0$ GeV/c for all these three cases.

In Figure 8.1 (top panel) an enhancement of the correlation distribution in the near and away-side peak is visible for high-multiplicity p-Pb collisions relative to low-multiplicity events and to pp collisions.

For higher-p_T intervals for the electrons, such enhancement are not visible and the measured azimuthal distribution are consistent among the different multiplicity classes and collision systems, as can be observed in Figures 8.1 (bottom panel) and in Figure 8.2. In the highest p_T bin, which is shown in Figure 8.2, it can also be observed that the near and away-side peak are similar to each other in terms of the per-trigger yield.

Another remark is that the correlation measured in low-multiplicity p-Pb collisions is compatible the distribution evaluated from the pp data. This is particularly visible for the first p_T interval, where modifications among the multiplicity classes are observed. This fact is used as an argument to use low-multiplicity p-Pb collisions to remove the jet-pick correlation from high-multiplicity events as will be shown later in this Chapter.

ALI-PREL-61949

ALI-PREL-61956
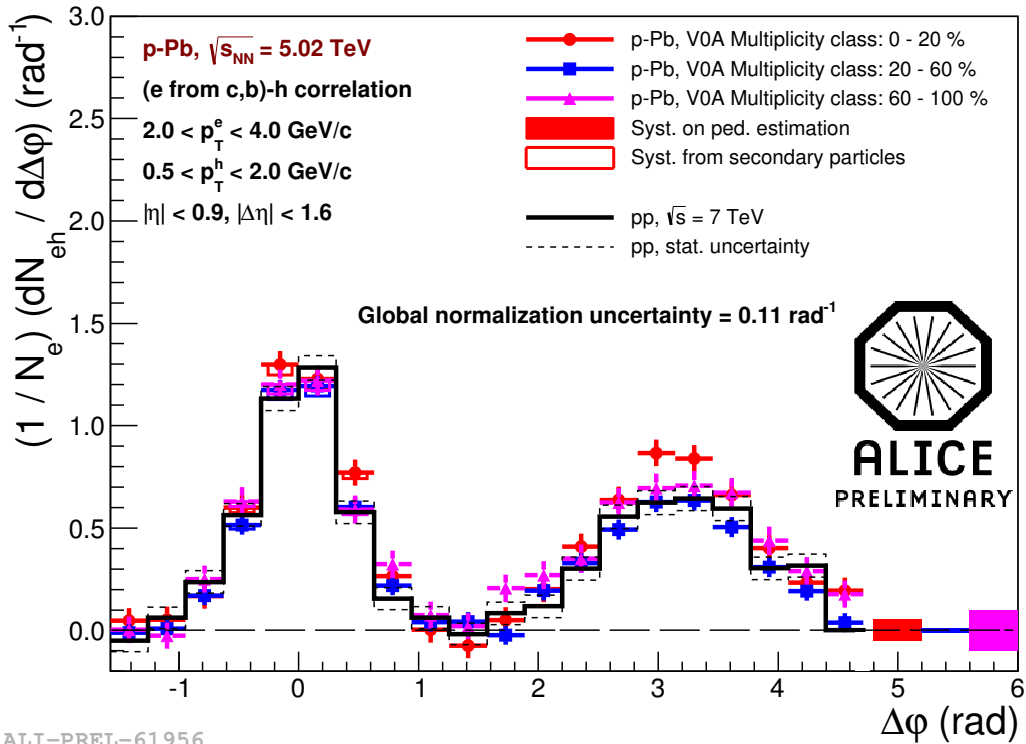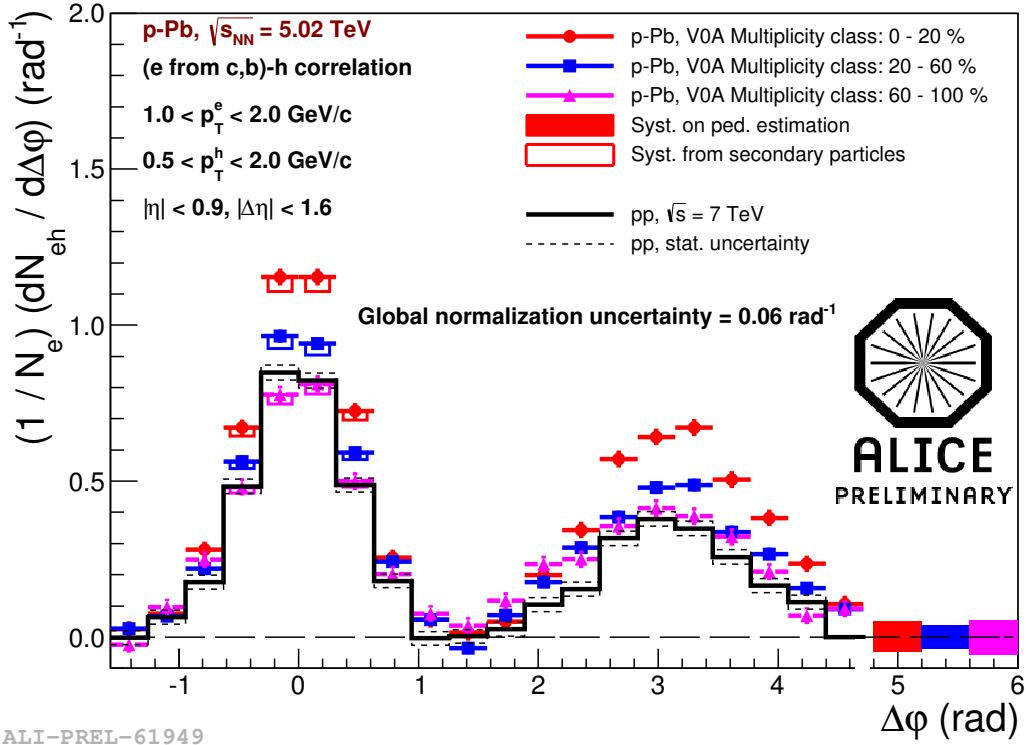
Figure 8.1: Two-particle correlation function in azimuth ($\Delta\phi$) triggered by heavy-flavour decay electrons, in high (0-20%), intermediate (20-60%) and low-multiplicity (60-100%) p-Pb and in pp collisions. The systematic errors on the pedestal estimation (filled boxes on the right side of the figure), from single particle contamination (open boxes) and a global normalization (text) are displayed as well. The trigger particle satisfies $1 < p_T < 2$ GeV/c (top panel) and $2 < p_T < 4$ GeV/c (bottom panel) [This work].
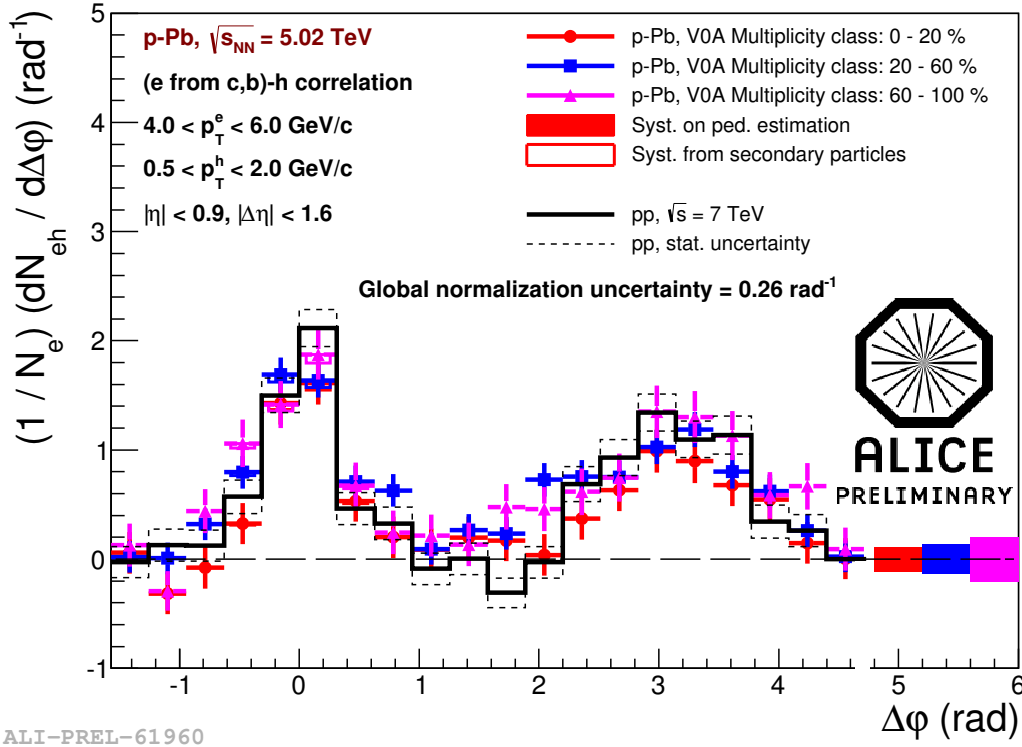
Figure 8.2: Two-particle correlation function in azimuth ($\Delta\phi$) triggered by heavy-flavour decay electrons, in high (0-20%), intermediate (20-60%) and low-multiplicity (60-100%) p-Pb and in pp collisions. The systematic errors on the pedestal estimation (filled boxes on the right side of the figure), from single particle contamination (open boxes) and a global normalization (text) are displayed as well. The trigger particle satisfies $4 < p_T < 6$ **GeV/**c **[This work].**

8.1.2 Yield in the near and away-side

The yield in the near and away-side peak is obtained by integrating the corresponding region. It is defined in Equation 8.1 and represents the number trigger-associated pairs in a given p_T and $\Delta\phi$ range relative to the number of trigger particles. Results for the yield as a function of the collision system and multiplicity class are shown in Figures 8.3 to 8.5.

$$\frac{N_{\text{eh}}(a < \Delta\phi < b)}{N_{\text{e}}} = \int\limits_a^b C(\Delta\phi; p_T^e, p_T^h) d(\Delta\phi) \tag{8.1}$$

These results endorse the suggestion of a yield modification in the near and away-side peak at low-p_T for high-multiplicity p-Pb collisions, relative to low-multiplicity events and pp reactions.

For higher momentum intervals no modification is observed as observed in the correlation distribution plots.
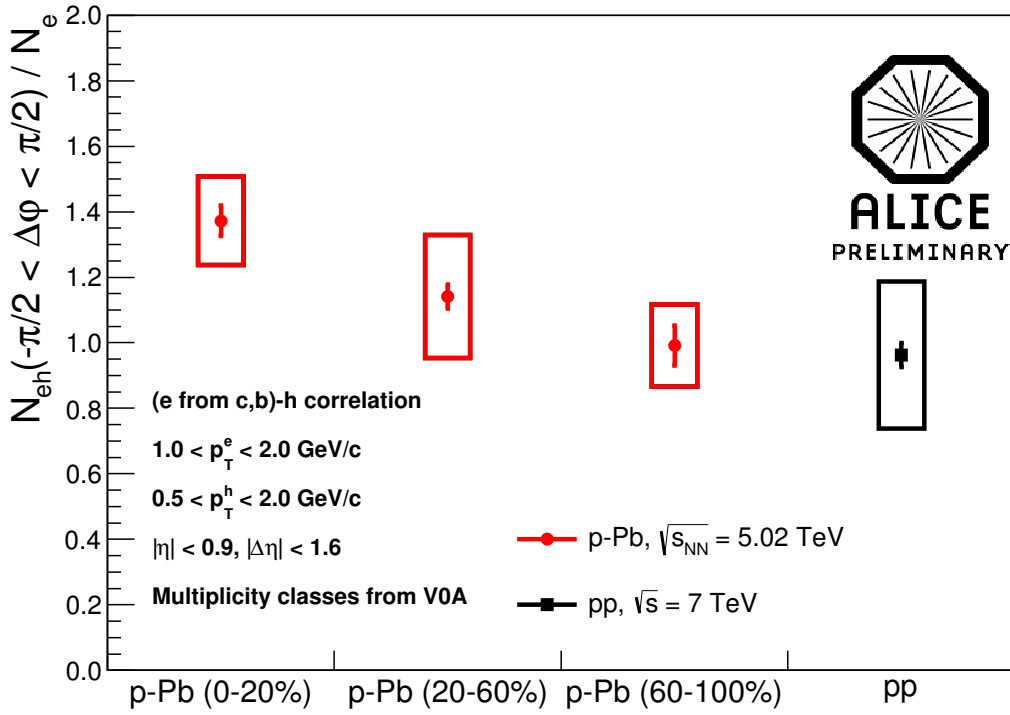
ALI−PREL−61985
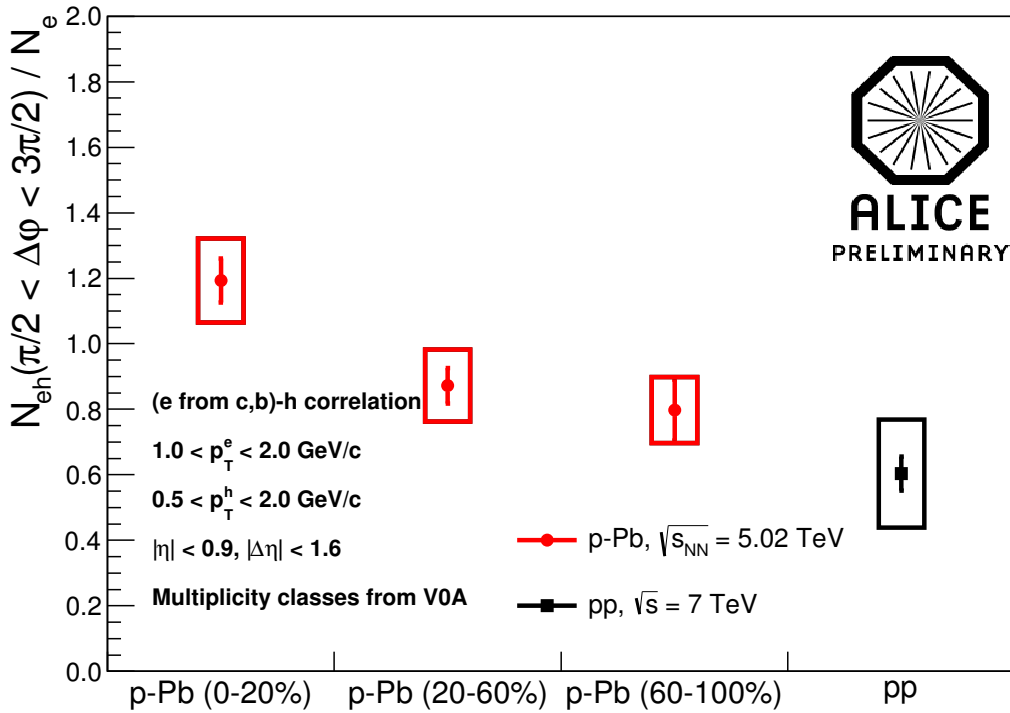
ALI−PREL−61989

Figure 8.3: Yield in the near (top panel) and away (bottom panel) side of the azimuthal correlation function between heavy-flavour decay electrons and charged unidentified particles. Results are shown for $1 < p_T < 2$ **GeV/**c **[This work].**
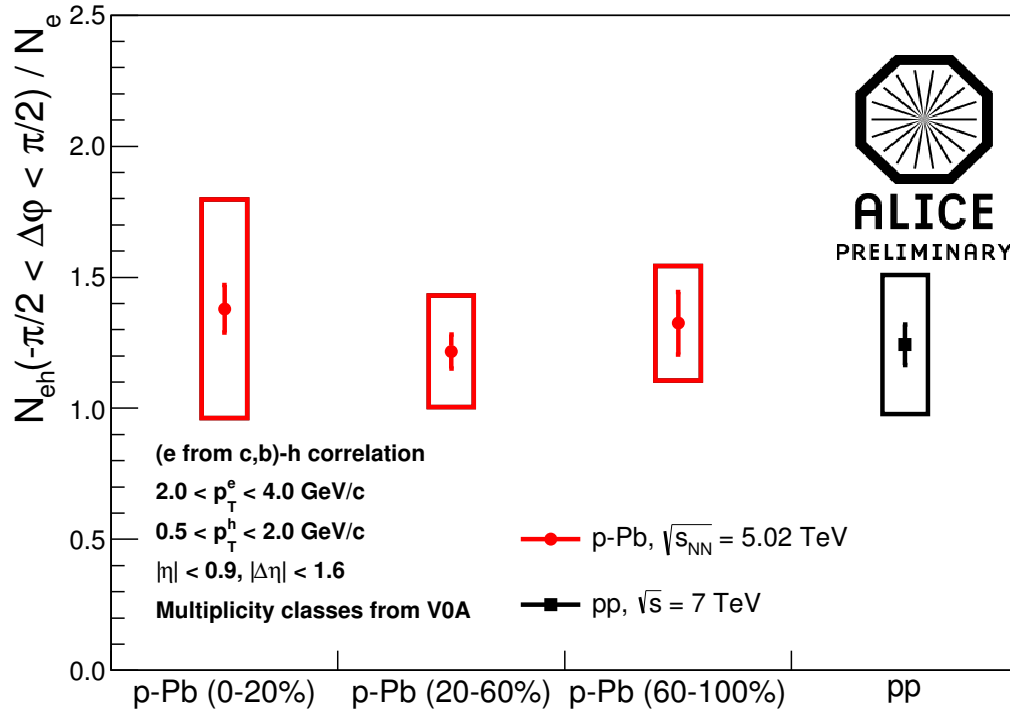
ALI-PREL-61993
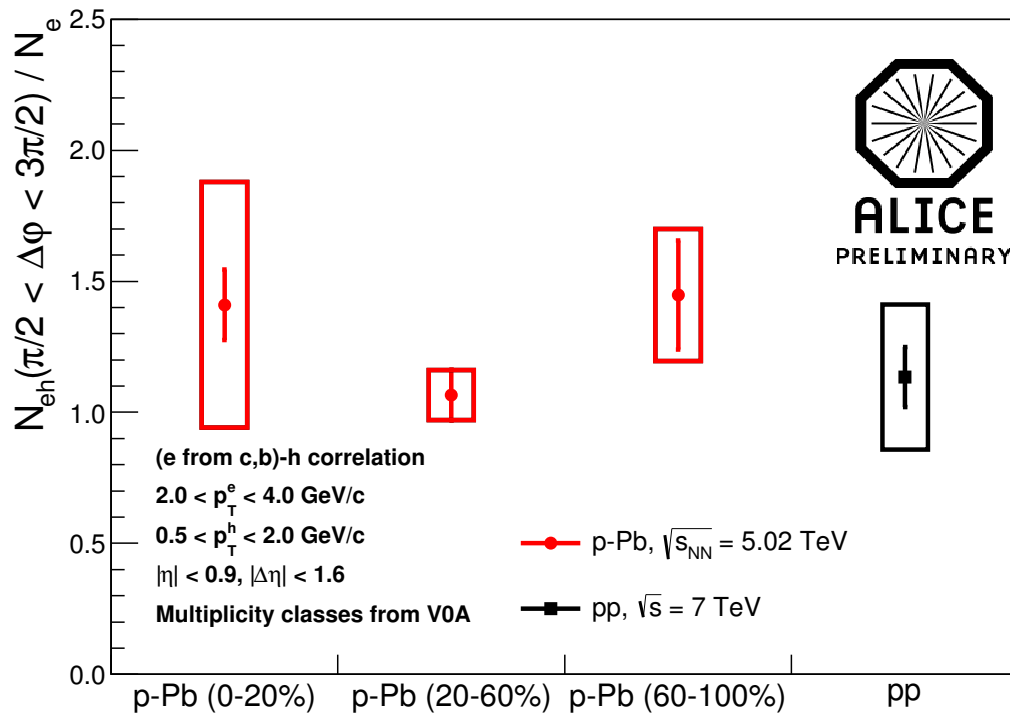
ALI-PREL-61997

Figure 8.4: Yield in the near (top panel) and away (bottom panel) side of the azimuthal correlation function between heavy-flavour decay electrons and charged unidentified particles. Results are shown for $2 < p_T < 4$ **GeV/**c **[This work].**
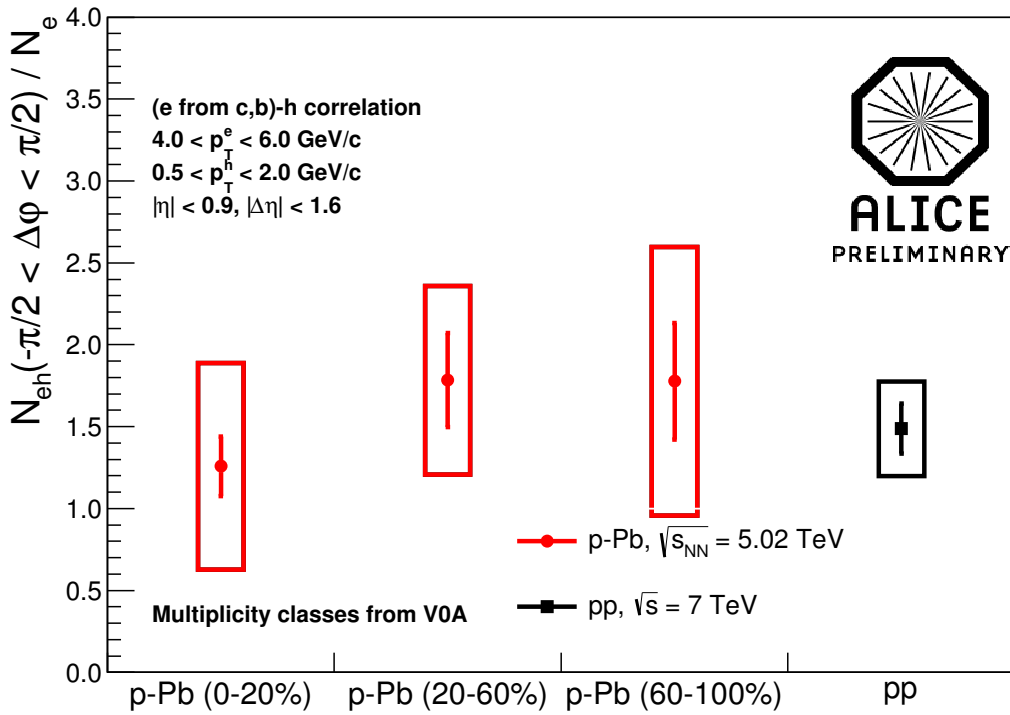
ALI-PREL-62001
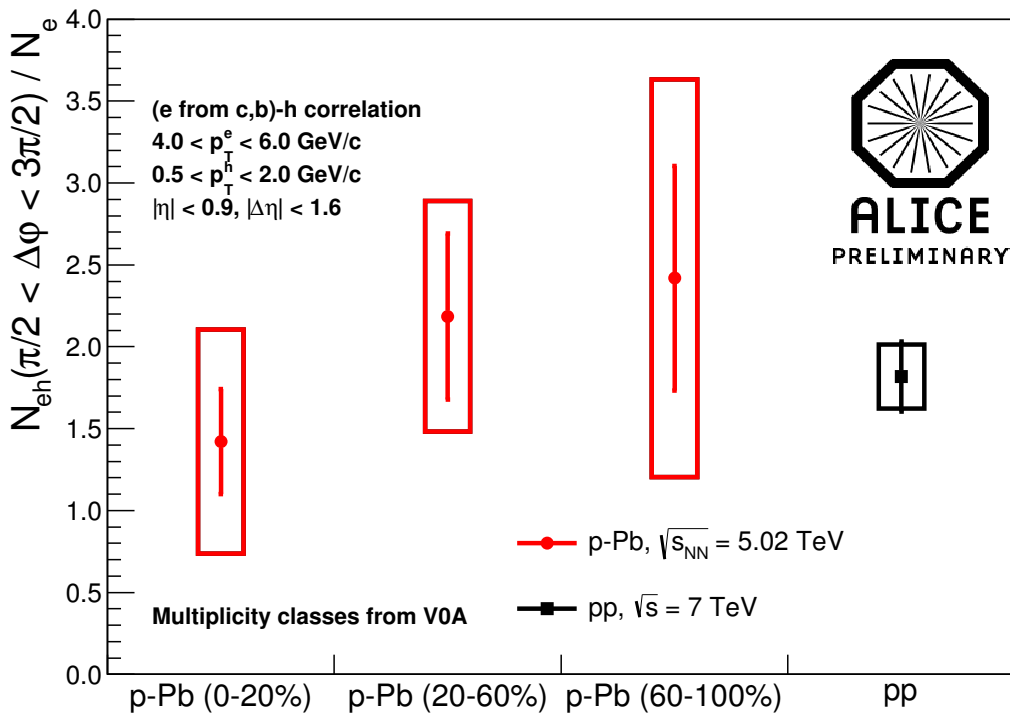
ALI-PREL-62005

Figure 8.5: Yield in the near (top panel) and away (bottom panel) side of the azimuthal correlation function between heavy-flavour decay electrons and charged unidentified particles. Results are shown for $4 < p_{\mathrm{T}} < 6$ **GeV/**c **[This work].**

8.1.3 High versus low-multiplicity p-Pb collisions

In order to understand the nature and explore the features of the observed yield enhancement in the near and away-side correlation that is visible for high-multiplicity p-Pb collisions, in the present Section a systematic comparison between results from high and low-multiplicity class in p-Pb collisions is performed. The use of low-multiplicity p-Pb collisions is motivated by the fact that the correlation distribution measured for this class of events is compatible with that evaluated from pp collisions. Therefore, the correlation distribution obtained in low-multiplicity events can be used, for instance, to remove the jet peak contribution in high-multiplicity reactions.

The first observable analyzed in this context is the ratio between the yields in high and low-multiplicity events. This ratio is often denoted by I_{CP} (central-to-peripheral ratio) and it is defined in Equation 8.2.

$$I_{CP}(p_T^e, p_T^h) = \left(\int_{-\frac{\pi}{2}}^{\frac{\pi}{2}} C(\Delta\phi; p_T^e, p_T^h) d(\Delta\phi) \right)^{0-20\%} \left[\left(\int_{-\frac{\pi}{2}}^{\frac{\pi}{2}} C(\Delta\phi; p_T^e, p_T^h) d(\Delta\phi) \right)^{60-100\%} \right]^{-1} \quad (8.2)$$

In Figure 8.6 the measured I_{CP} as a function of the electron transverse momentum is shown, for both the near and away-side correlation.

The results shown in Figure 8.6 suggest, indeed, an increase in the per-trigger yield for both, the near and away-side peak, for $1 < p_T^e < 2$ GeV/c, while the for the higher p_T bins the measured I_{CP} is consistent with unity within uncertainties.

Another very useful approach to study the observed yield modification, is to look at the subtraction of the correlation function measured in high-multiplicity events by that obtained in low-multiplicity event classes. This was done and the results are displayed in Figure 8.7 for the 2-dimensional correlation function (top panel) and the projection on the azimuthal axis (bottom panel).

In order to keep the proper baseline for the Fourier coefficients to be evaluated, the part of the pedestal that is removed in the subtraction is added back, i. e. it is necessary to ensure the only physical correlations are removed in the subtraction process.

The result shown in Figure 8.7, where a double-ridge structure is visible, suggests that the observed enhancement in the azimuthal distribution for high-multiplicity p-Pb collisions is mainly due to correlations of long-range in pseudorapidity. Furthermore the projection on $\Delta\varphi$ seems (in qualitative terms) dominated by v_2 modulation, similarly to what was observed in the measured di-hadron correlation distribution, reported by the ALICE Collaboration in [64] and [65].

However the v_2 evaluation were not performed in this work, since the evaluation method are still under investigation. A discussion about it is provided in Appendix B. In summary

it is not yet well-established how to disentangle collective effects from a possible jet-yield modification in high-multiplicity events.
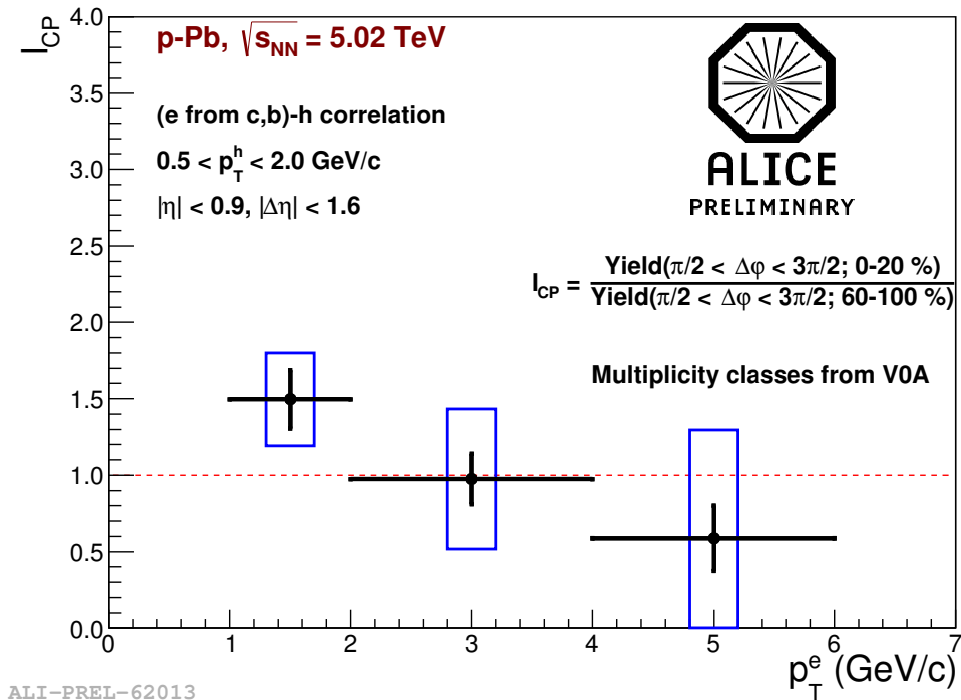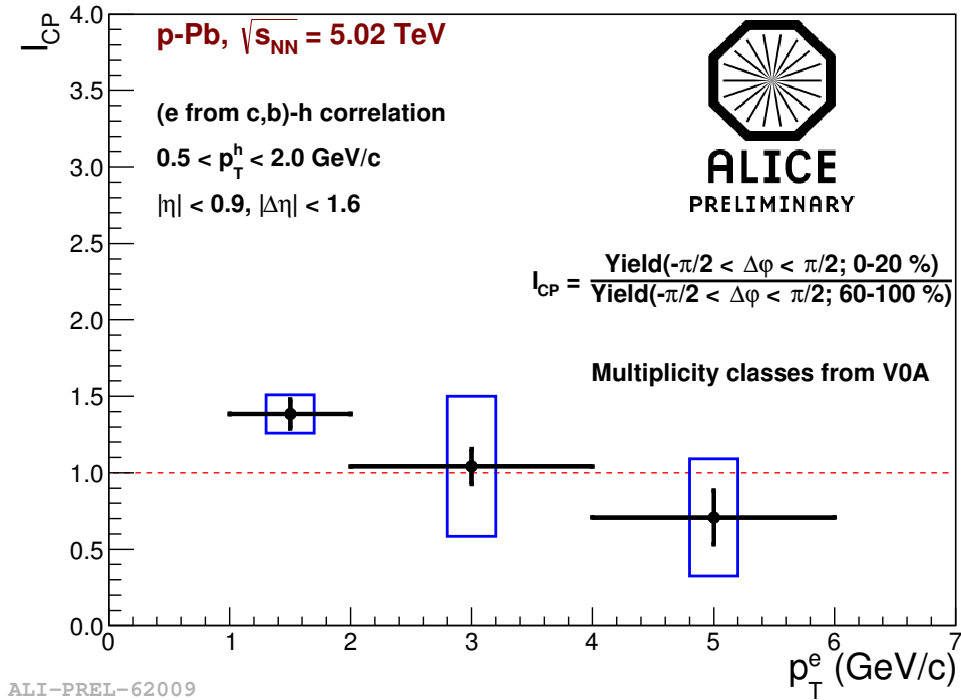
Figure 8.6: I_{CP} **as a function of the electron** p_T **for the near (top panel) and away (bottom panel) side peak [This work].**

p-Pb, $\sqrt{s_{NN}}$ = 5.02 TeV
(0-20%) - (60-100%), Multiplicity Classes from V0A
(e from c,b)-h correlation
$1.0 < p_T^e < 2.0$ GeV/c
$0.5 < p_T^h < 2.0$ GeV/c

ALICE
PRELIMINARY

ALI−PREL−62026

p-Pb, $\sqrt{s_{NN}}$ = 5.02 TeV
(e from c,b)-h correlation
(0-20%) - (60-100%), Multiplicity Classes from V0A
$1.0 < p_T^e < 2.0$ GeV/c
$0.5 < p_T^h < 2.0$ GeV/c
$|\eta| < 0.9, |\Delta\eta| < 1.6$
Global normalization uncertainty = 0.022 rad^{-1}

ALICE
PRELIMINARY

ALI−PREL−62034
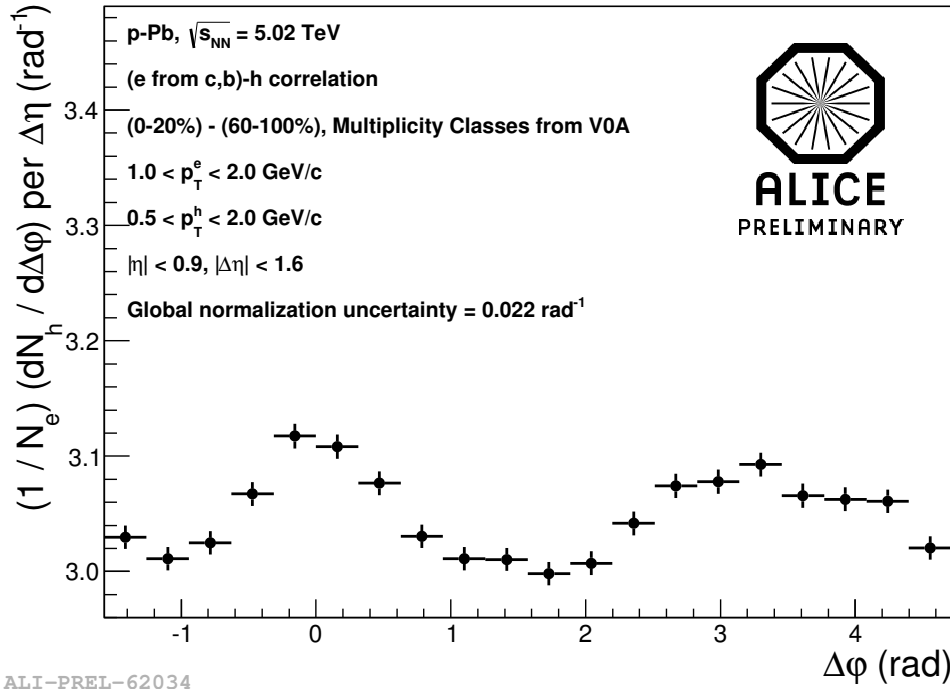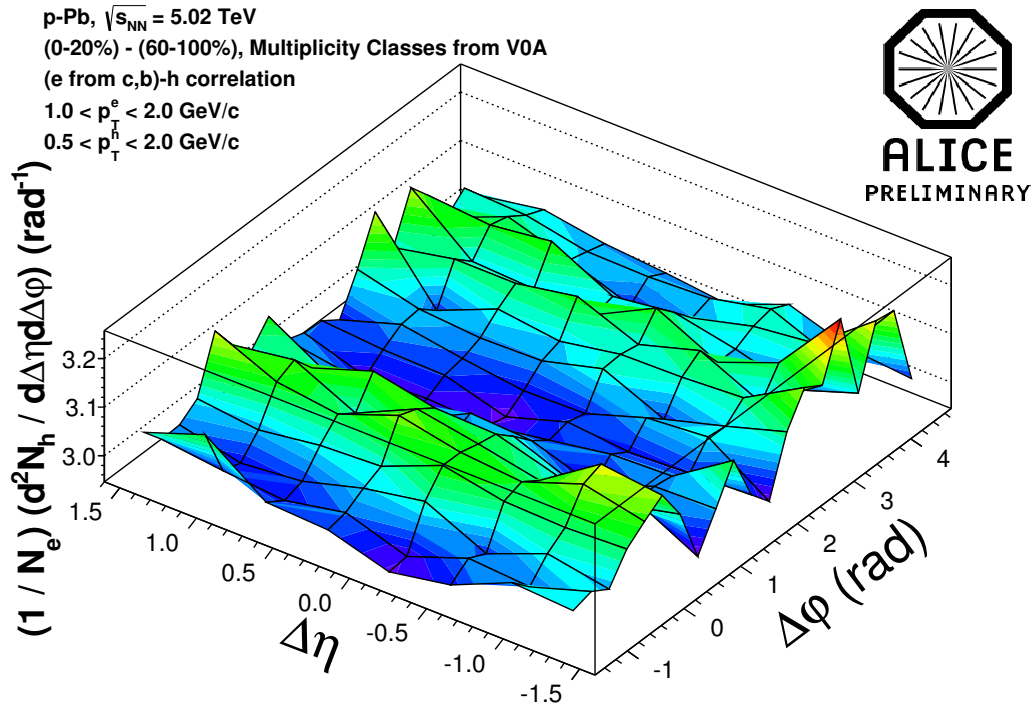
Figure 8.7: Subtraction of the correlation function obtained in high-multiplicity (0-20%) p-Pb collisions by that measured in the lowest-multiplicity (60-100%) event class defined in this analysis, for $1 < p_T^e < 2$ GeV/c [This work].

8.1.4   Comparison to Monte-Carlo Simulations

The correlation function measured in pp collisions at $\sqrt{s}$ = 7 TeV is compared to that obtained with PYTHIA perugia0 tune [89]. In the PYTHIA program, the production cross-section

of heavy quarks calculations accounts for corrections up to NLO in pQCD through the parton shower approach [46, 48, 49].

These comparisons are shown in Figure 8.8 and 8.9. The agreement between the distribution obtained using PYTHIA and the measured correlation is improved as the trigger particle p_T increases.
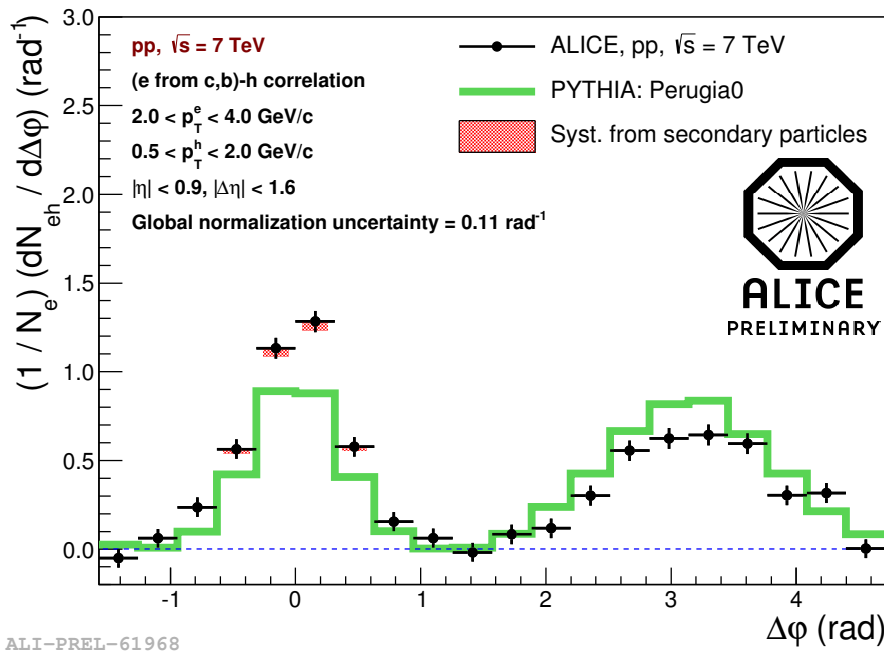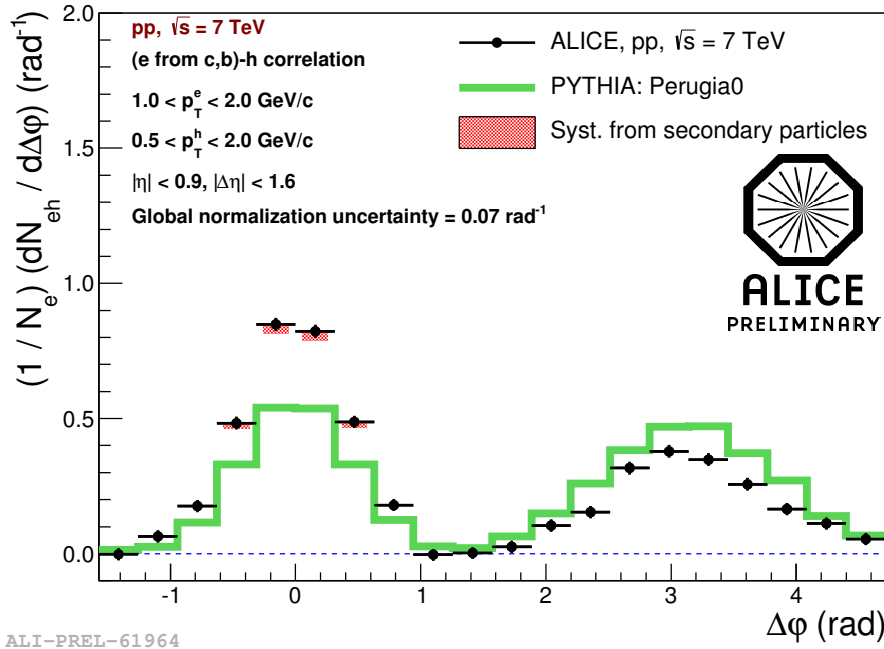
Figure 8.8: Correlation function between heavy-flavour decay electrons in pp collisions at $\sqrt{s} = 7$ TeV (black points) and from PYTHIA simulations (green line) for $1 < p_T^{trigg} < 2$ GeV/c (top panel) and for $2 < p_T^{trigg} < 4$ GeV/c (bottom panel) [This work].
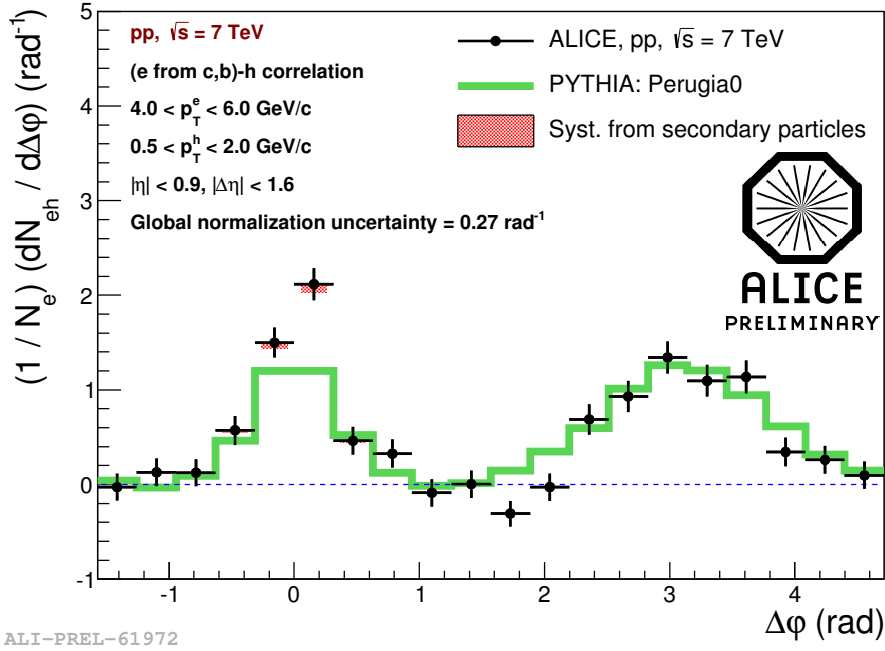
Figure 8.9: Correlation function between heavy-flavour decay electrons in pp collisions at $\sqrt{s} = 7$ TeV (black points) and from PYTHIA simulations (green line) for $4 < p_T^{\text{trigg}} < 6$ GeV/c [This work].

8.2 Beauty production

In this Section the results for the relative beauty contribution to the total yield of heavy-flavour decay electrons are presented. The black filled circles in Figure 8.10 shows the results obtained from the fits for the four bins analyzed in this work, along with five other results, represented by red filled squares, which were evaluated in another PhD thesis [88], which has used an alternative trigger and PID technique in order to increase the momentum reach of the analysis.

The three common bins that are visible in Figure 8.10 were combined using Equation 8.3.

$$r_{\text{B}} = \left[\frac{r_{\text{B}}^{\text{MB}}}{\sigma_{\text{MB}}^2} + \frac{r_{\text{B}}^{\text{EMCal}}}{\sigma_{\text{EMCal}}^2} \right] \left[\frac{1}{\sigma_{\text{MB}}^2} + \frac{1}{\sigma_{\text{EMCal}}^2} \right]^{-1} \tag{8.3}$$

The final result for the relative beauty production as a function of p_T is shown in Figure 8.11, where the three bins in the range $2.5 < p_T < 6.0$ GeV/c are the combination of the MB and EMCal analysis. In the same Figure several pQCD calculations, with their theoretical uncertainties, are shown as lines [45, 50, 90, 47, 91]. The measured beauty contribution to the heavy-flavour decay electron yield is consistent with the three set of pQCD calculations displayed in Figure 8.11, within the theoretical and experimental uncertainties. Furthermore, these results suggest that the beauty contribution to the electron yield is not negligible compared to the charm contribution for the p_T region of the present analysis.
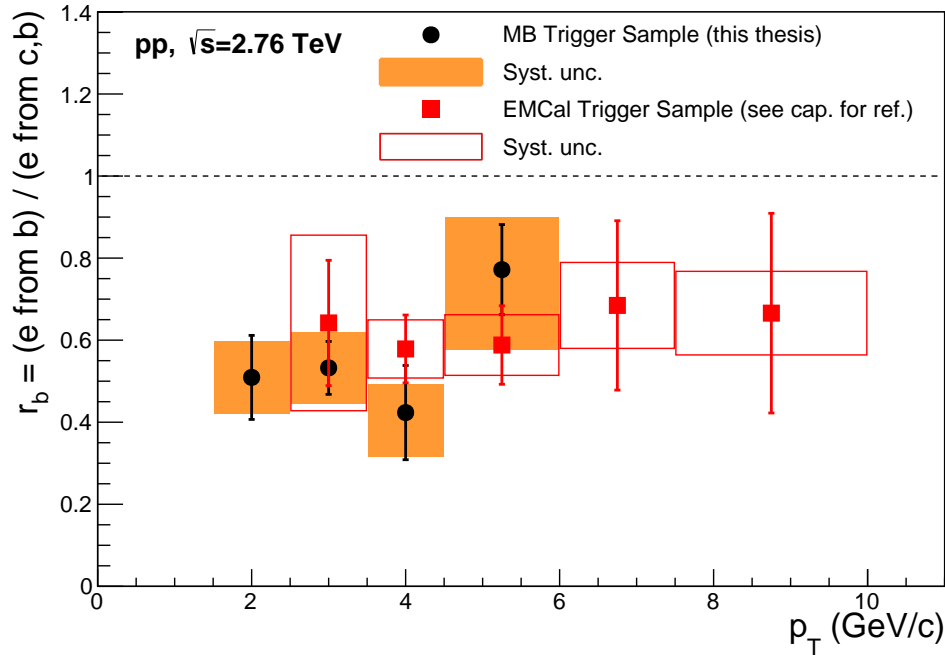
Figure 8.10: **Relative beauty contribution to the total production cross-section of heavy-flavour decay electrons, as a function of the electron p_T. Black circles belongs to the present work and were obtained from a minimum-bias trigger sample [This work]. Red squares show the results obtained in another thesis [88] which uses a EMCal trigger sample and an alternative PID technique to increase the momentum range of this measurement.**
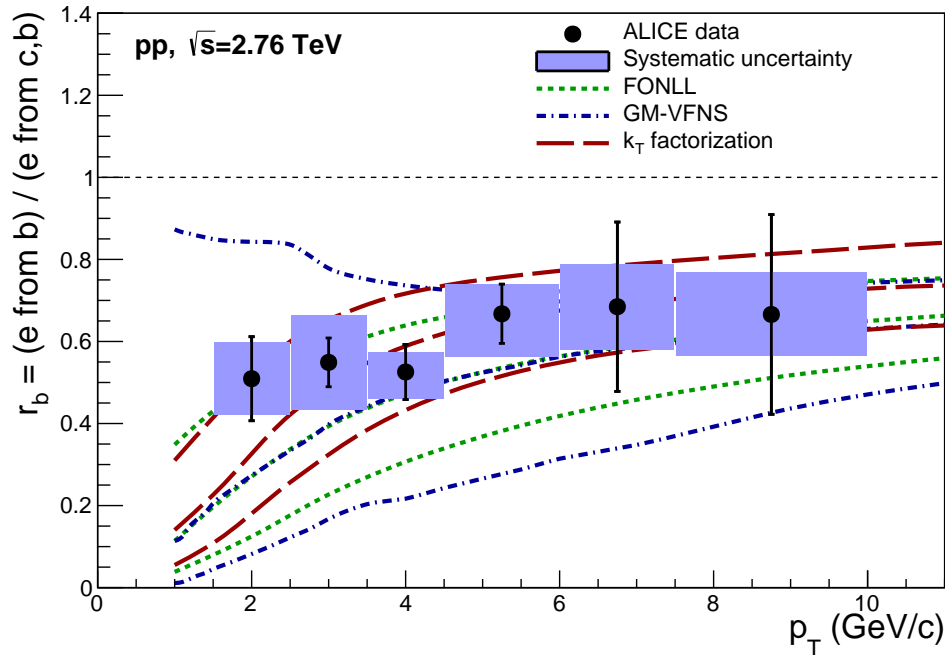
Figure 8.11: **Final result for the relative beauty contribution to the total production cross-section of heavy-flavour decay electrons, calculated as the weighted average of the results from the MB [This work] and EMCal trigger samples [88]. Several pQCD calculations are shown as well [45, 50, 90, 47, 91]. This result is published in [80].**

Chapter 9

Conclusions and outlook

9.1 Conclusions

The angular correlation distribution between electrons from heavy-flavour hadron decays and charged particles was evaluated in proton-lead collisions at $\sqrt{s_{\mathrm{NN}}} = 5.02$ TeV, at the LHC, using the ALICE detector. The correlation function was evaluated for electrons with $1 < p_{\mathrm{T}} < 6$ GeV/c, in three separated p_{T} intervals, and requiring associated charge particles with $0.5 < p_{\mathrm{T}} < 2.0$ GeV/c. In order to investigate the dependence of the correlation with the event multiplicity, three classes of multiplicity were defined.

Furthermore, the relative beauty contribution to the total heavy-flavour decay electron yield was estimated in proton-proton collisions at $\sqrt{s} = 2.76$ TeV using the correlation technique. This analysis is complementary to the work performed in [88]. For this case, electron candidates were required to have the transversal momentum within $1.5 < p_{\mathrm{T}} < 6$ GeV/c, for which the analysis was done in four intervals of p_{T}. Constraints were not required for the associated particle p_{T} selection.

The results of the present work suggests that, in high-multiplicity p-Pb collisions the associated per-trigger yield in the near ($\Delta\varphi \approx 0$) and away-side ($\Delta\varphi \approx \pi$), for the angular correlation distribution triggered by heavy-flavour decay electrons, is enhanced compared to low-multiplicity events and to pp collisions, for electrons with $1 < p_{\mathrm{T}} < 2$ GeV/c. Furthermore, this work provides also evidences that such yield modification is due to correlations of long-range in pseudorapidity, since a double-ridge structure is observed after the subtraction of the distribution measured in low-multiplicity from that evaluated in high-multiplicity p-Pb collisions.

This result is qualitatively similar to what has been observed in correlations with light-flavour hadrons. In that case, v_2 coefficients were calculated using the measured angular distribution, by fitting the Fourier coefficients to the projection of the ridge structure on $\Delta\varphi$, for $\pi^{\pm}$, K and (anti-)protons. These results, for light flavour can be described by hydrodynamic models, which assumes an extended medium in the final-state, as well as by Color-

Glass Condensate (CGC) models, through which Gluon Saturation (GS) in the initial-state is described. This thesis suggests that the responsible mechanism for the ridge-structure in the light-flavour domain might affect charm and beauty quarks as well, or more generally, the heavy-flavour sector, since the mechanism could act on hadrons rather than partons. The evaluation of the v_n coefficients as well as the jet yield in the near and away-side, is currently under discussion within the ALICE Collaboration and some information and advances on this are provided in Appendix B.

For electrons with higher transverse momentum, i. e. $2 < p_T < 4$ GeV/c and $4 < p_T < 6$ GeV/c, no modification in the correlation distribution are observed among different multiplicity classes and collision system, within the current statistical and systematic uncertainties. Nevertheless, it can be observed that near and away-side becomes similar as the electron p_T increases.

Heavy-flavour measurements in proton-proton collisions provides important tests for perturbative QCD (pQCD) calculations. The result obtained in this work for the relative beauty contribution to the heavy-flavour decay electron yield is in agreement with several pQCD calculations, within experimental and theoretical uncertainties. In the present work, this analysis was performed for the data sample of pp collisions at $\sqrt{s} = 2.76$ TeV, collected with a Minimum Bias trigger. In [88] a similar analysis using an EMCal trigger sample was performed in pp collisions at $\sqrt{s} = 2.76$ and 7 TeV.

The results of this work were presented in several international conferences (Hadron Physics 2012, Strangeness in Quark Matter 2013, Hard Probes 2013, Quark Matter 2014) and they are published in [59, 80, 92, 93]. Particularly, the beauty production analysis is published in [80].

9.2 Outlook

In ALICE, heavy-flavour correlations have been studied in Pb-Pb collisions as well, in which the correlation distribution is sensitive to parton-medium interaction. The study of the away-side correlation distribution is sensitive to the jet quenching phenomena, while the near-side it provides information about the fragmenting jet leaving the medium. A first measurement of such a correlation function in Pb-Pb collisions at the LHC energies is reported in [88] by D. Thomas (see also [55]). However, the conclusions that can be drawn from this analysis is currently statistically limited. With the next LHC runs, starting in 2015, larger data samples are expected to be taken, which should allow stronger conclusions to be stated.

Another challenge in this topic is the study of correlations where both trigger and associated particles are from heavy-flavour hadron decays, or in which one of the particles carries a heavy-flavour, in the case of D mesons. Some examples of this type of correlations are: di-electron ($e^{\pm}$-$e^{\pm}$ or $e^{\pm}$-$e^{\mp}$) correlations; electron-muon correlation; electron-D and D-D correlations. In the last two cases, the D meson are reconstructed via its hadronic decay

channels (e. g. results on D-h correlations, where this approach is applied, are reported in [94]). A common feature between these analysis is that one knows for sure that two heavy-flavour jets are being correlated. Among several motivations, these correlation distribution can be evaluated in the framework of the theoretical models significantly easier compared to the case of heavy-light flavour correlations.

Finally, measurements of charm and beauty is expected to be significantly improved, in terms of resolution, after the upgrade of the ALICE Inner Tracking System (ITS), which should occur during the second LHC long shut down in 2017/18 (see e. g. [95]). The ITS upgrade is expected to increase by a factor 3 the resolution of impact parameter measurements, which is crucial, among other thing, for measurements of D mesons via its hadronic decays as well as for the separation of electrons from charm and beauty hadron decays (see e. g. [51] and [80]).

Appendices

Appendix A

Data and Monte Carlo samples

A.1   Analysis 1: Per-trigger yield

A.1.1   Data sample 1 (p-Pb part 1)

- Data sample: LHC13b (collected in 2013)

- System: p-Pb at $\sqrt{s_{NN}} = 5.02$ TeV.

- Run list: 195344, 195390, 195351, 195389, 195391, 195478, 195479, 195480, 195481, 195482, 195483.

- Total Number of Selected Events: 18M

A.1.2   Data sample 2 (p-Pb part 2)

- Data sample: LHC13c (collected in 2013)

- System: p-Pb at $\sqrt{s_{NN}} = 5.02$ TeV.

- Run list: 195529, 195531, 195532, 195566, 195567, 195568, 195592, 195593, 195596, 195633, 195635, 195644, 195673, 195675, 195677.

- Total Number of Selected Events: 73M

A.1.3   Data sample 3 (pp, $\sqrt{s} = 7$ TeV)

- Data sample: LHC10d (collected in 2010)

- System: pp at $\sqrt{s_{NN}} = 7$ TeV.

- Run list: 125855, 125851, 125850, 125849, 125848, 125847, 125101,125100, 125097, 125085, 125023, 126097, 126090, 126008, 126007, 126004, 125844,125843, 125842, 125633,

125632, 125630, 125186, 125156, 125140, 125139, 125134, 125133, 122375, 126158, 126088, 126082, 126081, 126078, 126073, 125296, 122374.

- Total Number of Selected Events: 67M

A.1.4   Monte-Carlo Sample 1

- Sample: LHC13b2_efix_p4.

- Event generator: DPMJET.

- System: p-Pb at $\sqrt{s_{NN}} = 5.02$ TeV (LHC13b,c anchor runs).

- Run list: 195344, 195390, 195351, 195389, 195391, 195478, 195479, 195480, 195481, 195482, 195483, 195529, 195531, 195532, 195566, 195567, 195568, 195592, 195593, 195596, 195633, 195635, 195644, 195673, 195675, 195677.

- Total Number of Selected Events: 28M.

- Using GEANT for detector simulation.

A.1.5   Monte-Carlo Sample 2

- Data sample: LHC10f6a.

- Event generator: PYTHIA (tune: perugia0).

- System: pp at $\sqrt{s} = 7$ TeV (LHC10d anchor runs).

- Run list: 25855, 125851, 125850, 125849, 125848, 125847, 125101,125100, 125097, 125085, 125023, 126097, 126090, 126008, 126007, 126004, 125844,125843, 125842, 125633, 125632, 125630, 125186, 125156, 125140, 125139, 125134,125133, 122375, 126158, 126088, 126082, 126081, 126078, 126073, 125296, 122374.

- Total Number of Selected Events: 57M.

- Using GEANT for detector simulation.

A.2   Analysis 2: Beauty production

A.2.1   Data sample

- Data sample: LHC11a (collected in 2011)

- System: pp at $\sqrt{s} = 2.76$ TeV.

- Run list (TPC only analysis): 146686, 146688, 146689, 146746, 146747, 146748, 146801, 146802, 146803, 146804, 146805, 146806, 146807, 146808, 146812, 146813, 146814, 146817, 146824, 146856, 146858, 146859, 146860.

- Total Number of Events (TPC only analysis): 66.3 M

- Run list (TPC+TOF analysis): 146801, 146802, 146803, 146804, 146805, 146806, 146817, 146824.

- Total Number of Selected Events (TPC+TOF analysis): 39.6 M

A.2.2 Monte Carlo Sample 1

- Sample: LHC12e6.

- Event generator: PYTHIA (tune: perugia0).

- System: pp at $\sqrt{s} = 2.76$ TeV (LHC11a anchor runs).

- Run list: 146801, 146802, 146803, 146804, 146805, 146806, 146817, 146824.

- Description: MB sample used to study the background reconstruction efficiency.

- Using GEANT for detector simulation.

A.2.3 Monte Carlo Sample 2

- Data sample: LHC12a9.

- Event generator: PYTHIA (tune: perugia0).

- System: pp at $\sqrt{s} = 2.76$ TeV (LHC11a anchor runs).

- Run list: 146686, 146688, 146689, 146746, 146747, 146748, 146801, 146802, 146803, 146804, 146805, 146806, 146807, 146808, 146812, 146813, 146814, 146817, 146824, 146856, 146858, 146859, 146860.

- Description: Enhancement of electrons from heavy-flavour (charm and beauty) meson decay, to generated the angular distribution templates that are used to fit the measured distribution.

- Using GEANT for detector simulation.

Appendix B

Jet yield and v_2 evaluation

In this Appendix some considerations about the evaluation of the Fourier coefficients and the jet-yield will be discussed. In Figures B.1 and B.2 the subtraction method was applied and the double-ridge structure is visible for both $(0-20\%)$ and $(20-60\%)$ on the top panel of these figures. The long-range correlation in $\Delta\eta$ can be quantified, from one side, by the projection of the ridge on $\Delta\varphi$, through which the Fourier coefficients can be determined by fitting the expression defined in Equation B.1 (in this case up to the third coefficient) to the observed modulation.

$$a_0\left\{1+2V_{1\Delta}\cos(\Delta\varphi)+2V_{2\Delta}\cos(2\Delta\varphi)+2V_{3\Delta}\cos(3\Delta\varphi)\right\} \tag{B.1}$$

This fits were performed for the high and intermediary-multiplicity data and the results are shown in the bottom panel of Figures B.1 and B.2, and the results for the Fourier coefficients are displayed in Figure B.3.

However, the subtraction method is based on the assumption that the jet yield is not modified among multiplicity classes. Figure B.4 shows the yield and width in the near-side of the azimuthal correlation distribution where no strong modification is observed among multiplicity classes and relative to pp collisions. However this result is biased by the fact that the Fourier coefficients estimated through the subtraction method is removed in the yield evaluation.

In order to have an unbiased estimative, the yield was evaluated from the $\Delta\eta$ projection, since the modulation due to collective effects is expected to be flat in pseuodrapidity. The results, that are shown in Figure B.5 suggest a dependence of the near-side yield and width with the multiplicity class of the p-Pb collision and among collision systems, i. e. relative to pp collisions. Therefore, part of the modification interpreted in terms of the Fourier coefficients might be due to a jet-yield modification and broadening.

In the following the Figures of the Fourier fits and the evaluated yields and widths are presented.
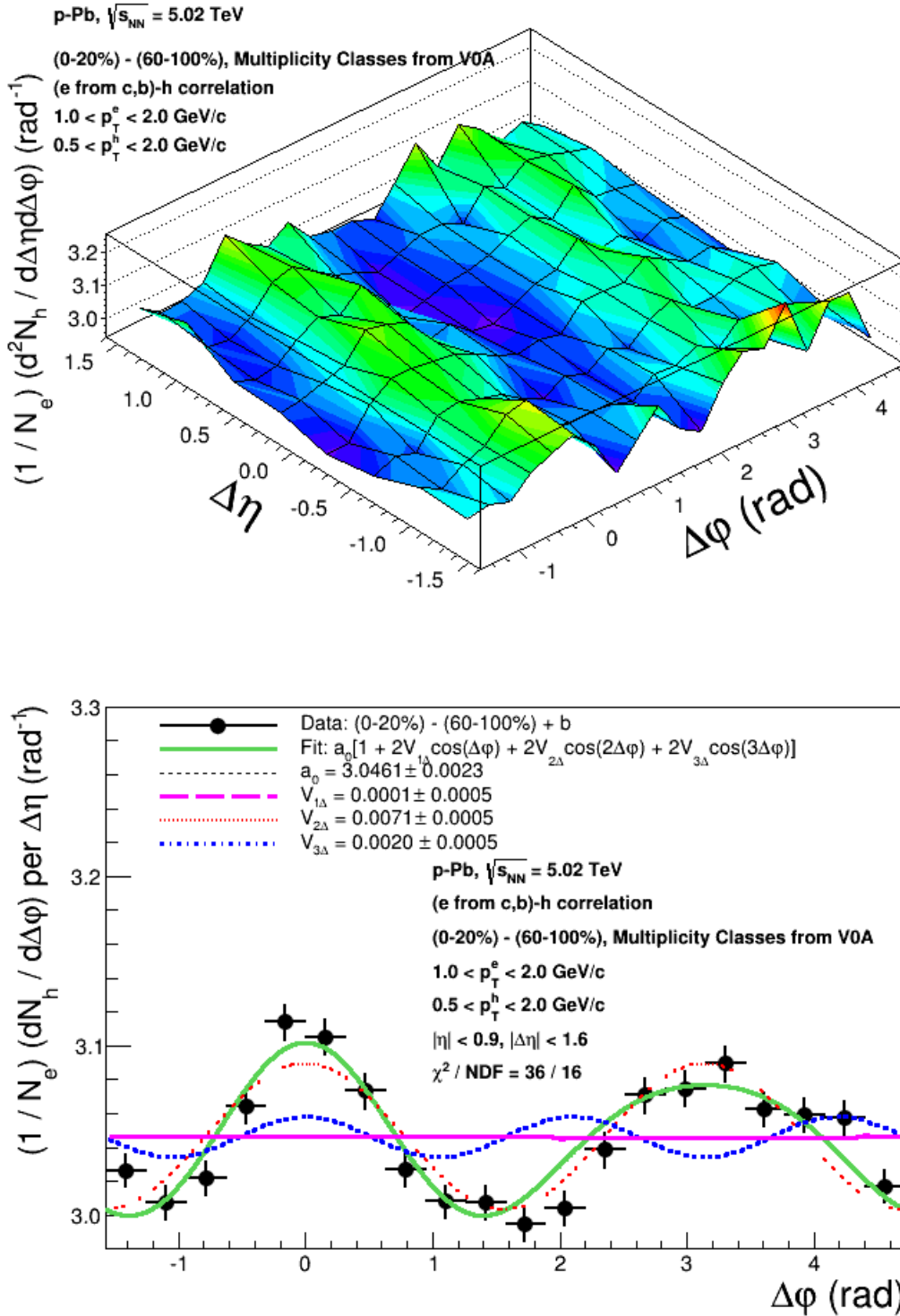
Figure B.1: Top panel: Subtraction of the correlation distributions for high-multiplicity events, (0−20%) - (60−100%), between heavy-flavour decay electrons and charged particles, in p-Pb collisions at $\sqrt{s_{NN}}$ = 5.02 TeV. Bottom panel: Projection of the double-ridge structure on $\Delta\varphi$ along with the Fourier expansion fit [This work].
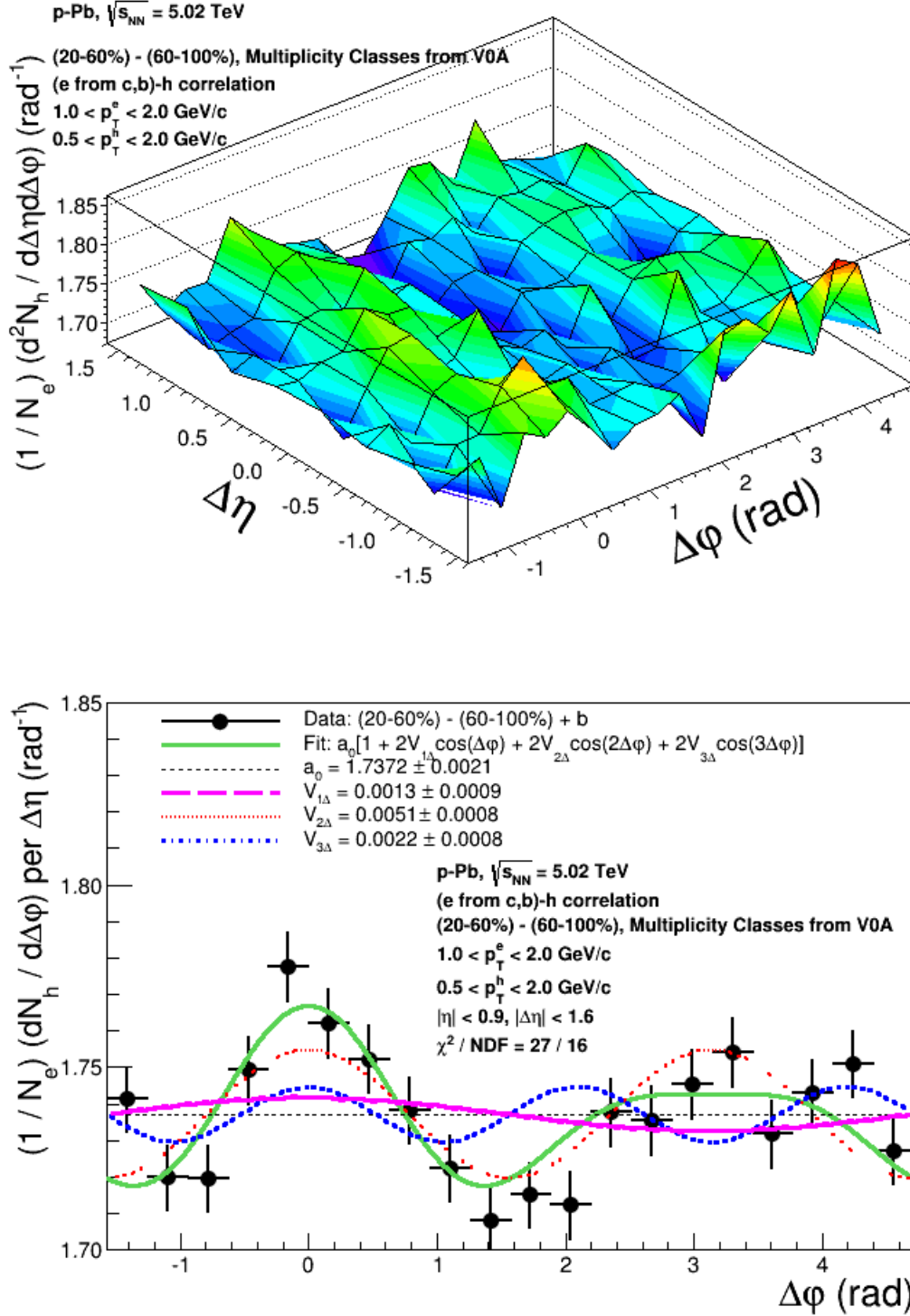
Figure B.2: Top panel: Subtraction of the correlation distributions for intermediary-multiplicity events, $(20-60\%)$ - $(60-100\%)$, between heavy-flavour decay electrons and charged particles, in p-Pb collisions at $\sqrt{s_{NN}} = 5.02$ TeV. Bottom panel: Projection of the double-ridge structure on $\Delta\varphi$ along with the Fourier expansion fit [This work].
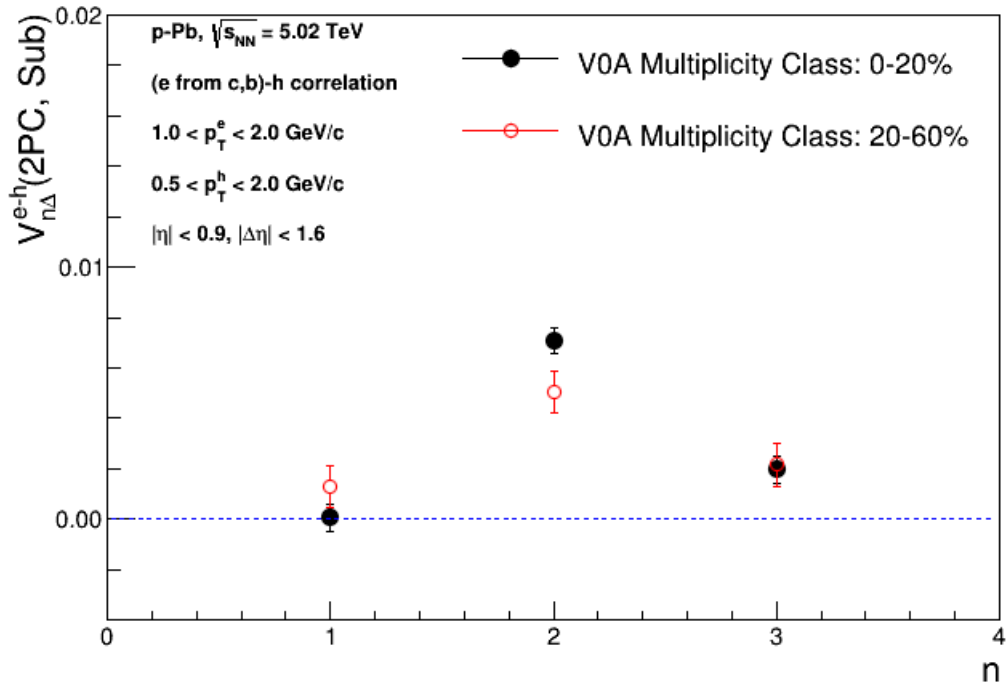
Figure B.3: Fourier coefficients $V_{1\Delta}$**,** $V_{2\Delta}$ **and** $V_{3\Delta}$**, evaluated from the correlation distribution triggered by heavy-flavour decay electrons in p-Pb collisions at** $\sqrt{s_{\mathrm{NN}}} = 5.02$ **TeV [This work].**
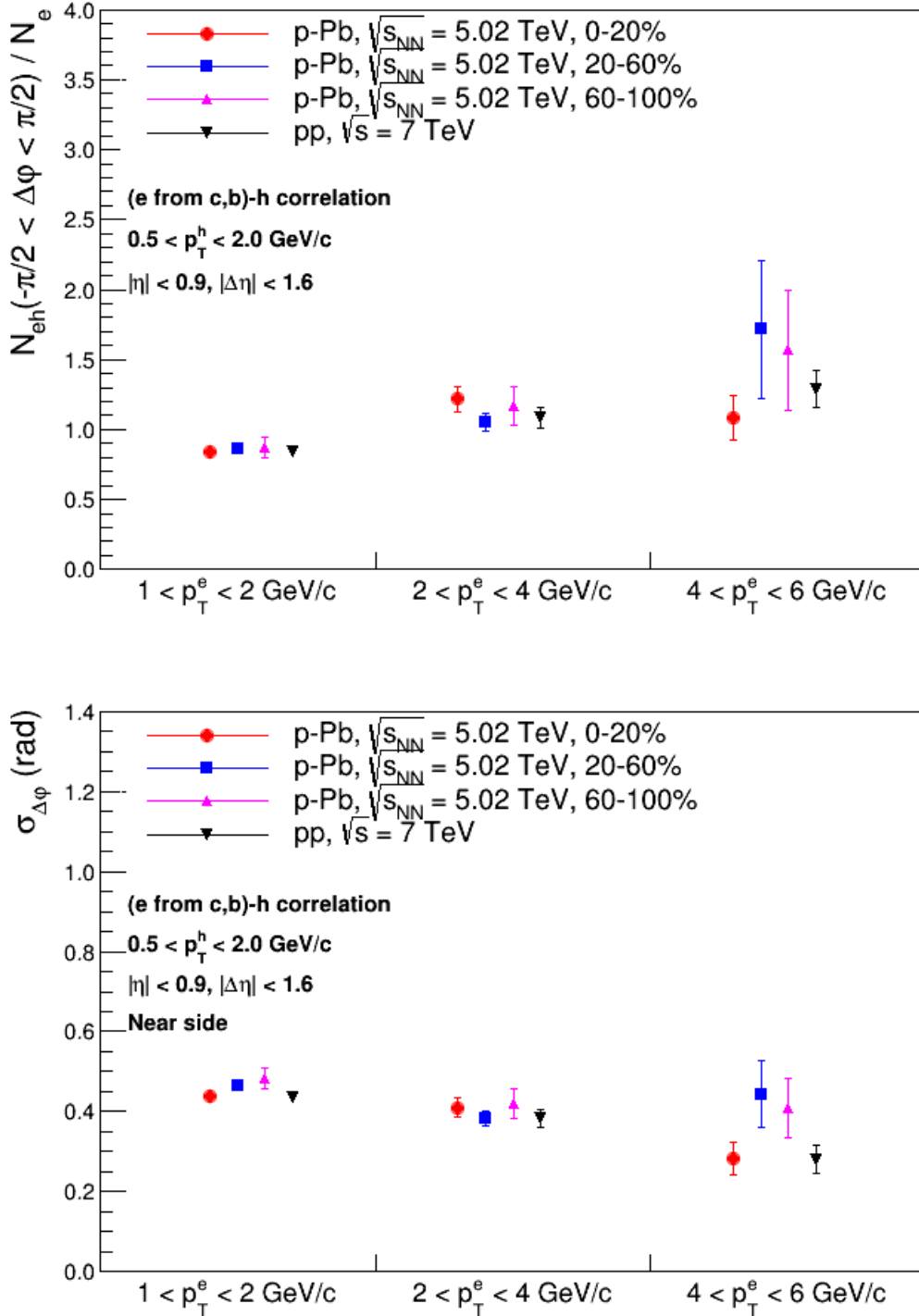
Figure B.4: Yield and width in the near and away-side correlation, between heavy-flavour decay electrons and charged particles, in p-Pb ($\sqrt{s_{NN}}$ = 5.02 TeV) and pp ($\sqrt{s}$ = 7 TeV) collisions [This work].
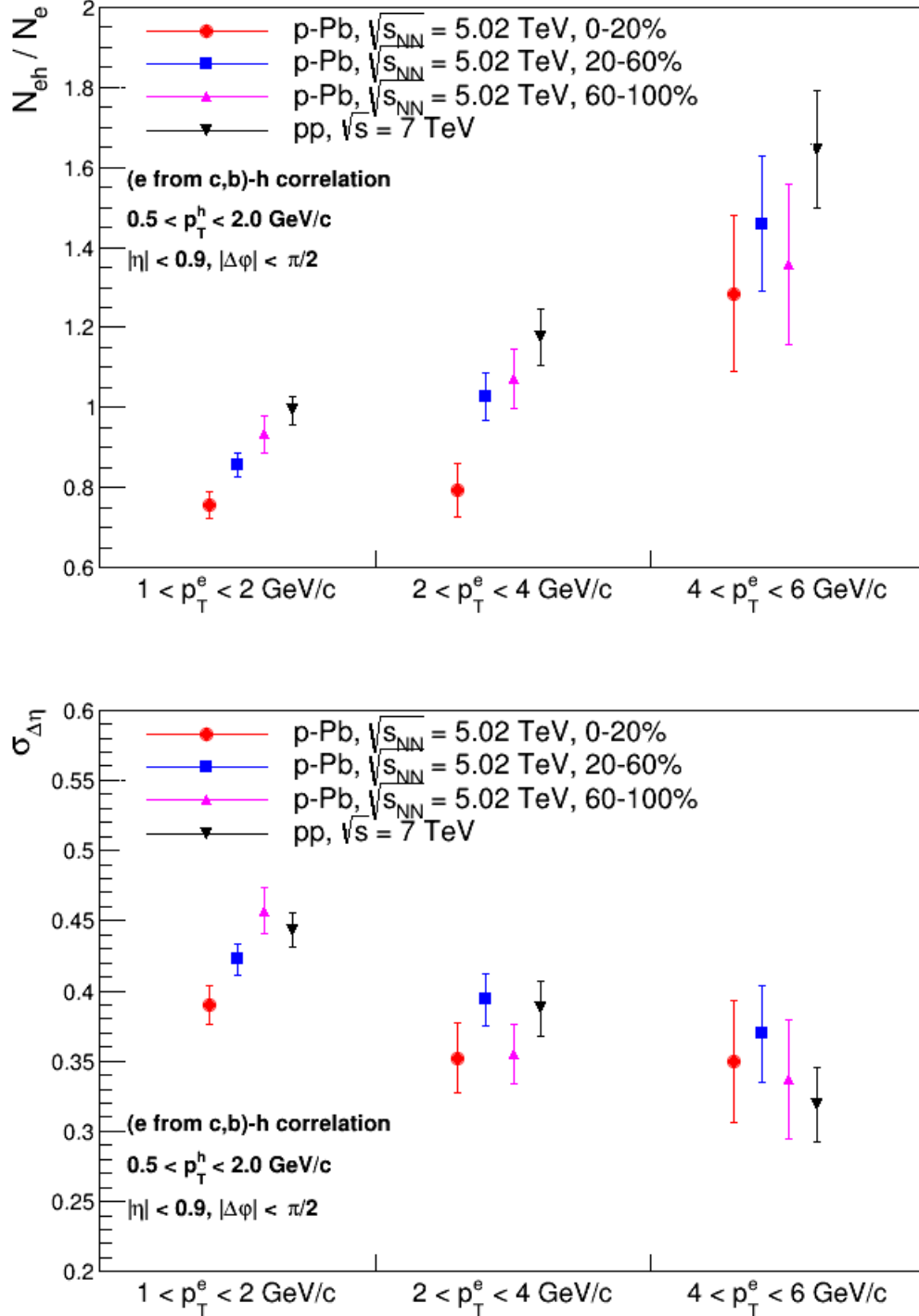
Figure B.5: Yield and width in the near-side $\Delta\eta$ correlation distribution, between heavy-flavour decay electrons and charged particles, in p-Pb ($\sqrt{s_{NN}}$ = 5.02 TeV) and pp ($\sqrt{s}$ = 7 TeV) collisions [This work].

Appendix C

Landau distribution

The Landau distribution is defined in Equation C.1, and an example of the distribution is provided in Figure C.1, where the location parameter, corresponding to approximately the most probable value, was set to 5.

In this work, the Landau distribution was used to describe the distribution of the energy loss of pions through ionization in the TPC gas (see Section 6.3).

$$L(x) = \frac{1}{\pi} \int_0^\infty e^{-t\log t - xt} \sin(\pi t) \mathrm{d}t \tag{C.1}$$
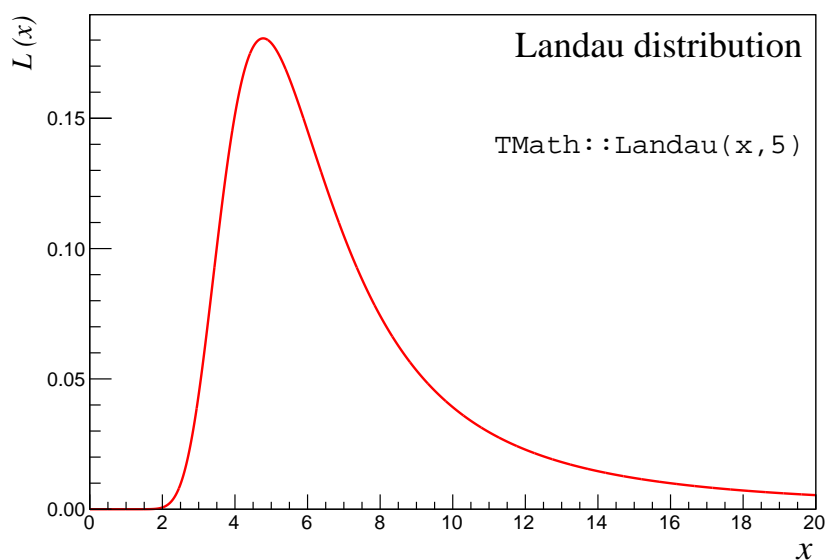
Figure C.1: Landau distribution with the location parameter at 5 (the location parameter corresponds approximately to the most probable value).

Bibliography

[1] F. Halzen and A. D. Martin, "Quarks & Leptons: An Introductory Course in Modern Particle Physics," (John Wiley & Sons, 1984).

[2] D. Griffiths, "Introduction to Elementary Particles," (John Wiley & Sons, 1987).

[3] W. Florkowski, "Phenomenology of Ultra-Relativistic Heavy-Ion Collisions," (World Scientific Publishing, 2010).

[4] http://en.wikipedia.org/wiki/Standard_Model (on April, 2014).

[5] http://www.desy.de/ gbrandt/feyn/ (on July, 2014).

[6] http://www.mit.edu/ hasell/DKH_zeus.html (on July, 2014).

[7] G.M. Prosperi, M. Raciti, C. Simolo, "Review on the running coupling constant in QCD," Progress in Particle and Nuclear Phys. 58 (2007) 387-438.

[8] R. Averbeck, "Heavy-flavor production in heavy-ion collisions and implications for the properties of hot QCD matter," Prog. in Part. and Nucl. Phys. 70 (2013) 159-209.

[9] S. B. Rüster et al., "Phase diagram of neutral quark matter: Self-consistent treatment of quark masses," Phys. Rev. D 72, 034004 (2005).

[10] M. A. Stephanov, "QCD phase diagram: an overview," arXiv:hep-lat/0701002 (2006).

[11] E. Laermann, O. Philipsen, "Lattice QCD at Finite Temperatures," Annu. Rev. Nucl. Part. Sci. 53 (2003) 163-198.

[12] A. Bazavov (HotQCD Collaboration), "The equation of state in (2+1)-flavour QCD," arXiv:1407.6387 [hep-lat] (2014).

[13] A. Chodos et al., "Baryon structure in the bag theory," Phys. Rev. D 10, 2599 (1974).

[14] A. Chodos et al., "New extended model of hadrons," Phys. Rev. D 9, 3471 (1974).

[15] A. Dainese, "Charm production and in-medium QCD energy loss in nucleus-nucleus collisions with ALICE. A performance study," arXiv:nucl-ex/0311004v2 (2003).

[16] P. Braun-Munzinger and J. Stachel, "The quest for the quark–gluon plasma," Nature 448, 302-309 (2007).

[17] S. A. Chin, "Transition to hot quark matter in relativistic heavy-ion collisions," Phys. Lett. B 78 (1978) 552-555.

[18] http://www.bnl.gov/world/ (on Sep/2014)

[19] http://home.web.cern.ch/ (on Sep/2014)

[20] http://www.bnl.gov/rhic/default.asp (on Sep/2014)

[21] http://press.web.cern.ch/press-releases/2000/02/new-state-matter-created-cern (2000).

[22] https://www.star.bnl.gov/ (on Sep/2014)

[23] http://www.phenix.bnl.gov/phenix/WWW/intro/index.html (on Sep/2014)

[24] http://home.web.cern.ch/topics/large-hadron-collider (on Sep/2014)

[25] A. Dainese, "Lectures on Heavy Ions," CERN-Fermilab HCP Summer School (2013).
Part 1/3: http://indico.cern.ch/event/226365/contribution/23/material/slides/0.pdf
Part 2/3: http://indico.cern.ch/event/226365/contribution/24/material/slides/0.pdf
Part 3/3: http://indico.cern.ch/event/226365/contribution/25/material/slides/0.pdf

[26] J. D. Bjorken, "Highly relativistic nucleus-nucleus collisions: The central rapidity region," Phys. Rev. D 27, 140 (1983).

[27] PHENIX Collaboration, http://www.phenix.bnl.gov/WWW/plots/ (on Sep/2014).

[28] S. Chatrchyan et al. (CMS Collaboration), "Measurement of the Pseudorapidity and Centrality Dependence of the Transverse Energy Density in Pb-Pb Collisions at $\sqrt{s_{\text{NN}}} =$ 2.76," Phys. Rev. Lett. 109, 152303 (2012).

[29] M. Wilde (ALICE Collaboration), "Measurement of Direct Photons in pp and Pb-Pb Collisions with ALICE," Nucl. Phys. A 904-905 (2013) 573.

[30] Leonardo Milano (ALICE Collaboration), " Identified charged hadron production in Pb–Pb collisions at the LHC with the ALICE Experiment," Nucl. Phys. A 904–905 (2013) 531.

[31] S. Sarkar, et al., "The Physics of the Quark-Gluon Plasma," Lecture notes in physics 785 (2010).

[32] STAR Collaboration, "Experimental and theoretical challenges in the search for the quark–gluon plasma: The STAR Collaboration's critical assessment of the evidence from RHIC collisions," Nucl. Phys. A 757 (2005) 102-183.

[33] B. Abelev, et al. (ALICE Collaboration), "Anisotropic flow of charged hadrons, pions and (anti-)protons measured at high transverse momentum in Pb-Pb collisions at $\sqrt{s_{NN}} = 2.76$ TeV," arXiv:1205.5761 [nucl-ex] (2012).

[34] Y. Zhou (ALICE Collaboration), "Anisotropic flow of identified particles in Pb–Pb collisions at $\sqrt{s_{NN}} = 2.76$ TeV with the ALICE detector," arXiv:1309.3237 [nucl-ex] (2013).

[35] J. L. Abacete, et. al., "CGC predictions for p+Pb collisions at the LHC," Nucl. Phys. A 897 (2013) 1-27.

[36] K.J. Eskola, et al., "EPS09 — A new generation of NLO and LO nuclear parton distribution functions," JHEP 04 (2009) 065.

[37] M. L. Miller, et al., "Glauber Modeling in High Energy Nuclear Collisions," Ann. Rev. of Nuclear and Particle Science Vol. 57, 205-243 (2007).

[38] B. Abelev, et al. (ALICE Collaboration), "Transverse Momentum Distribution and Nuclear Modification Factor of Charged Particles in p–Pb Collisions at $\sqrt{s_{NN}} = 5.02$ TeV," Phys. Rev. Lett. 110, 082302 (2013).

[39] B. Abelev, et al. (ALICE Collaboration), "Centrality dependence of charged particle production at large transverse momentum in Pb–Pb collisions at $\sqrt{s_{NN}} = 2.76$ TeV," Phys. Lett. B 720 (2013) 52-62.

[40] G. O. V. de Barros, "Proposta de Novos Observáveis Para Jatos Reconstruídos em Colisões Entre Íons Pesados Relativísticos," PhD thesis, University of São Paulo, Brazil (2013).

[41] M. Verweij, "Modelling and measurement of jet quenching in relativistic heavy-ion collisions at the LHC," PhD thesis, Utrecht University, the Netherlands (2013).

[42] R. Reed (ALICE Collaboration), "Full Jet Reconstruction in 2.76 TeV pp and Pb-Pb collisions in the ALICE experiment," arXiv:1304.5945 [nucl-ex] (2013).

[43] R. Haake (ALICE Collaboration), "Charged Jets in Minimum Bias p-Pb Collisions at $\sqrt{s_{NN}} = 5.02$ TeV with ALICE," arXiv:1310.3612v1 [nucl-ex] (2013).

[44] M. Cacciari, et al., "The p_T spectrum in heavy-flavour hadroproduction," JHEP 05 (1998) 007.

[45] M. Cacciari, et al., "Theoretical predictions for charm and bottom production at the LHC," JHEP 1210 (2012) 137.

[46] E. Norrbin, T. Sjöstrand, "Production and Hadronization of Heavy Quarks," Eur. Phys. J. C 17, 137-161 (2000).

[47] P. Bolzoni, G. Kramer, "Inclusive lepton production from heavy-hadron decay in pp collisions at the LHC," Nucl. Phys. B 872 (2013) 253–264.

[48] T. Sjöstrand, et al., "PYTHIA 6.4 physics and manual," JHEP 05 (2006) 026.

[49] T. Sjöstrand, et al., "A brief introduction to PYTHIA 8.1," Comput. Phys. Comm. 178 (2008) 852-867.

[50] R. Maciula, et al., "Open charm production at the LHC - kt-factorization approach," Phys.Rev. D87 (9) (2013) 094022.

[51] B. Abelev, et al. (ALICE Collaboration), "Measurement of charm production at central rapidity in proton proton collisions at $\sqrt{s_{NN}} = 2.76$," JHEP 1207 (2012) 191.

[52] B. Abelev, et al. (ALICE Collaboration), "D meson elliptic flow in non-central Pb-Pb collisions at $\sqrt{s_{NN}} = 2.76$ TeV," Phys. Rev. Let. 111, 102301 (2013).

[53] Magdalena Djordjevic, "An overview of heavy quark energy loss puzzle at RHIC," J. Phys. G: Nucl. Part. Phys. 32 S333 (2006).

[54] B. Abelev, et al. (ALICE Collaboration), "Measurement of electrons from semileptonic heavy-flavor hadron decays in pp collisions at $\sqrt{s} = 2.76$ TeV," arXiv:1405.4117 [nucl-ex] (2014).

[55] D. Thomas (ALICE Collaboration), "Measurement of electrons from heavy-flavour decays in Pb-Pb collisions at $\sqrt{s_{NN}} = 2.76$ TeV with ALICE," arXiv:1312.1489 [hep-ex] (2013).

[56] J. Uphoff, O. Fochler, Z. Xu, C. Greiner, "Open heavy flavor in Pb+Pb collisions at $\sqrt{s_{NN}} = 2.76$ TeV within a transport model," Phys. Lett. B 717 (2012), p. 430-435.

[57] M. He, R. J. Fries, R. Rapp, "Non-perturbative Heavy-Flavor Transport at RHIC and LHC," arXiv:1208.0256 [nucl-th].

[58] M. Monteno et al., "Heavy-flavor dynamics in nucleus-nucleus collisions: from RHIC to LHC," J. Phys. G G38 (2011) 124144.

[59] E. Pereira de Oliveira Filho (ALICE Collaboration), "Measurements of electrons from heavy-flavour hadron decays in pp, p-Pb and Pb-Pb collisions with ALICE at the LHC," arXiv:1404.3983 [hep-ex] (2014).

[60] B. Abelev, et al. (ALICE Collaboration), "Harmonic decomposition of two particle angular correlations in Pb-Pb collisions at $\sqrt{s_{\mathrm{NN}}}$ = 2.76 TeV," Phys. Let. B 708 (2012) 249-264.

[61] STAR Collaboration, "Measurement of the Bottom Quark Contribution to Nonphotonic Electron Production in p+p Collisions at $\sqrt{s_{\mathrm{NN}}}$ = 200 GeV," Phys. Rev. Lett. 105, 202301 (2010).

[62] S. Chatrchyan et al. (CMS Collaboration), "Multiplicity and transverse momentum dependence of two- and four-particle correlations in pPb and PbPb collisions," Phys. Lett. B 724 (2013) 213.

[63] S. Chatrchyan et al. (CMS Collaboration), "Observation of long-range, near-side angular correlations in proton-proton collisions at the LHC," JHEP 1009 (2010) 091.

[64] B. Abelev, et al. (ALICE Collaboration), "Long-range angular correlations on the near and away side in p-Pb collisions at $\sqrt{s_{\mathrm{NN}}}$ = 5.02 TeV," Phys. Let. B 719 (2013), pp. 29-41.

[65] B. Abelev, et al. (ALICE Collaboration), "Long-range angular correlations of π, K and p in p–Pb collisions at $\sqrt{s_{\mathrm{NN}}}$ = 5.02 TeV," Phys. Let. B 726 (2013) 164–177.

[66] K. Werner, et. al., "Evidence for flow in pPb collisions at 5 TeV from v2 mass splitting," arXiv:1307.4379 [nucl-th] (2013).

[67] P. Bożek, W. Broniowski, G. Torrieri, "Mass Hierarchy in Identified Particle Distributions in Proton-Lead Collisions," Phys. Rev. Lett. 111, 172303 (2013).

[68] P. Bożek, W. Broniowski, "Correlations from hydrodynamic flow in p-Pb collisions," Phys. Lett. B 718 (2013), p. 1557-1561.

[69] K. Dusling, R. Venugopalan, "Comparison of the color glass condensate to dihadron correlations in proton-proton and proton-nucleus collisions," Phys. Rev. D 87, 094034 (2013).

[70] L. Evans, et al., "LHC Machine," J. Inst. 3 S08001 (2008).

[71] http://en.wikipedia.org/wiki/File:Location_Large_Hadron_Collider.PNG (on Sep/2014).

[72] http://home.web.cern.ch/topics/large-hadron-collider (on Sep/2014).

[73] http://pt.wikipedia.org/wiki/Organização_Europeia_para_a_Pesquisa_Nuclear (on Sep/2014).

[74] http://home.web.cern.ch/about/accelerators (on Sep/2014).

[75] B. Abelev, et al. (ALICE Collaboration), "The ALICE experiment at the CERN LHC," J. Inst. 3 S08002 (2008).

[76] B. Abelev, et al. (ALICE Collaboration), "ALICE: Physics Performance Report, Volume I," J. Phys. G: Nucl. Part. Phys. 30 (2004) 1517 - 1763.

[77] B. Abelev, et al. (ALICE Collaboration), "ALICE: Physics Performance Report, Volume II," J. Phys. G: Nucl. Part. Phys. 32 (2006) 1295 - 2040.

[78] B. Abelev, et al. (ALICE Collaboration), "Centrality determination of Pb-Pb collisions at $\sqrt{s_{NN}}$ = 2.76 TeV with ALICE," Phys. Rev. C 88, 044909 (2013).

[79] B. Abelev, et al. (ALICE Collaboration), "Measurement of electrons from beauty hadron decays in pp collisions at $\sqrt{s}$ = 7 TeV," Phys. Lett. B 721 (2013) 13-23.

[80] B. Abelev, et al. (ALICE Collaboration), "Beauty production in pp collisions at $\sqrt{s}$ = 2.76 TeV measured via semi-electronic decays," arXiv:1405.4144 [nucl-ex] (2014).

[81] http://root.cern.ch

[82] M. Gyulassy, et al., "HIJING: a Monte Carlo model for multiple jet production in pp, pA and AA collisions," Phys. Rev. D 44 (1991) 3501.

[83] M. Goossens, et al., "GEANT detector description and simulation tool," CERN program library long write-up W5013 (1994), http://cdsweb.cern.ch/record/1073159.

[84] A. Fassò, et al. "FLUKA: present status and future development," Proceedings of the IV International Conference on Calorimeters and their Application, World Scientific, Singapore (1994).

[85] B. Abelev, et al. (ALICE Collaboration), "Measurement of electrons from semileptonic heavy-flavour hadron decays in pp collisions at $\sqrt{s}$ = 7 TeV," Phys. Rev. D 86, 112007 (2012).

[86] X. Lin, "Non-Photonic Electron Angular Correlations with Charged Hadrons from the STAR Experiment: First Measurement of Bottom Contribution to Non-Photonic Electrons at RHIC," PhD thesis, Central China Normal University, Wuhan China, 2007.

[87] MinJung Kweon, Private Communication.

[88] D. Thomas, "Jet-like heavy-flavour particle correlations in proton-proton and lead-lead collisions in ALICE," PhD thesis, Utrecht University, the Netherlands, 2014.

[89] P. Z. Skands, "The Perugia Tunes," arXiv:0905.3418 [hep-ph] (2009).

[90] R. Maciula, A. Szczurek, Private Communication.

[91] G. Kramer, Private Communication.

[92] E. Pereira de Oliveira Filho (ALICE Collaboration), "Measurements of the correlation between electrons from heavy-flavour hadron decays and light hadrons with ALICE at the LHC," arXiv:1404.4243 [hep-ex] (2013).

[93] E. Pereira de Oliveira Filho (ALICE Collaboration), "Electron-Hadron Correlations in pp Collisions at $\sqrt{s}$ = 2.76 TeV with the ALICE experiment," arXiv:1211.3793 [hep-ex] (2012).

[94] F. Colamari (ALICE Collaboration), "Measurement of azimuthal correlations between D mesons and charged hadrons with ALICE at the LHC", arXiv:1408.6038v2 [hep-ex] (2014).

[95] S. Senyukov (ALICE Collaboration), "The upgrade of the ALICE Inner Tracking System", Nucl. Inst. and Meth. in Phys. Res. Sect. A: Accelerators, Spectrometers, Detectors and Associated Equipments, 723 (2013) 164-167.